Biomechanics of Intestinal Crypt Morphogenesis

Axel Allen Almet

Merton College

University of Oxford

A thesis submitted for the degree of

Doctor of Philosophy

Michaelmas 2019

Abstract

The intestinal epithelium exhibits remarkable rates of self-renewal to protect the small intestine and colon from damage during digestion and facilitate nutrient absorption. This monolayer of epithelial cells is maintained by the crypts of Liehberkühn, test-tube-shaped glands that are robust in morphology and structure, undergoing significantly large deformations, despite comprising a heterogeneous composition of cells with varying proliferative capacities and mechanical properties. While the genetic and molecular processes governing crypt morphogenesis have been studied in detail, there is a lack of understanding regarding the evident contribution of biomechanical factors, leading to a poor understanding of crypt morphogenesis as a whole. Additionally, it is not known how the crypt's unique, yet incredibly robust, proliferation structure arises. However, morphoelastic rod theory allows one to consider the interplay between growth and tissue mechanics in a unified framework, where we can exploit the slenderness aspect of the crypt and model the tissue as a growing, elastic rod.

In this thesis, we use the framework of morphoelastic rods, which extends the classical Kirchhoff rod theory to account for local tissue growth, to explore various aspects of morphogenesis, growth, and homeostasis that are motivated by the crypt. We restrict ourselves to a planar geometry to model the transverse deformations of the crypt epithelium. Morphogenesis is modelled by the buckling and subsequent deformation of an elastic rod tethered to an underlying foundation, representing the crypt and the supporting extracellular matrix and stroma.

First, we consider an abstracted model of the crypt, a morphoelastic rod supported by an elastic foundation. We consider crypt morphogenesis in the context of buckling, exploring how growth and spatial heterogeneous properties—two key aspects of the crypt—impact mechanical pattern formation. We investigate the buckling and post-buckling behaviour of the simplified crypt model, extending previous linear stability analyses with a weakly nonlinear analysis and complementing the analysis with numerical continuation of the full nonlinear system. We analyse how incorporating spatial heterogeneity in growth, rod and foundation stiffness affects the underlying bifurcation structure.

Then, we specialise the framework to simulate tissue morphogenesis more realistically. We develop different models for the processes that are believed to play

a role in crypt morphogenesis, but were not previously included, such as tissue relaxation, chemical signalling, self-contact, and so on. We use simulation results to determine which of these models contribute most significantly to a realistic crypt morphology. By combining several of these processes, we show that a realistic crypt morphology, which is highly-invaginated but narrow in structure, can be generated.

To close, we consider a simplified 1D geometry to analyse how the unique growth structure of the crypt rises in development and subsequently is maintained in homeostasis. We develop a minimal mechanochemical model for tissue growth that captures the proliferation structure observed in the crypt, where proliferation activity is maximal away from the crypt base and the crypt top and is thus bimodal in shape. We finish by identifying the necessary conditions for dynamic tissue homeostasis, in which the proliferation structure is fixed with respect to the observable reference frame, but there is a continuous flux of tissue material due to the balance between growth and cell death, modelled through the sloughing of material.

Acknowledgements

It's safe to say that this DPhil did not go to plan. While it was, at times, frustrating, in the end, undertaking this DPhil was an immensely rewarding experience. Completing this thesis would not have been possible without the help of several people.

Firstly, I thank my supervisors, Professors Derek Moulton, Helen Byrne, and Philip Maini. I don't think I could have been supervised by a better trio of people in Oxford. To Derek, for reading my terrible drafts of everything so thoroughly, for all of your help on the technical side of things, and for believing that everything is explained better with a figure. This thesis would not have existed without you. To Helen, for reminding me of the bigger picture and for finding the funding which allowed me to come to Oxford. To Philip, for returning feedback so promptly, no matter the location or time zone, and for all the times you sent a kind email of encouragement after a setback. Your kindness and leadership are an inspiration to all and it has made the WCMB a lovely place in which to conduct a DPhil.

I would also like to thank my examiners, Professors Alain Goriely and John King, who took the time to examine this thesis thoroughly, and for the useful discussions that took place during the viva.

I am very grateful to the generous funding I received from the Cancer Research UK Oxford Centre and the Mathematical Institute. In particular, I am thankful for the funding from Cancer Research UK that allowed for academic travel and, indirectly, the chance to return home. I must also thank Merton College for providing me with comfortable and relatively cheap accommodation over the years, a luxury I do not take for granted. In particular, the last two years at Manor Place, with Liisa, Christian, and Lily have been lovely.

I thank my parents, who not only encouraged me to apply for Oxford, but continued to support me from afar. In particular, I thank my mum for always keeping track of Oxford's weather and reminding me to stay warm, and for keeping me well fed when I returned to Melbourne. I know it hasn't been easy, and I am so grateful for your love and support.

Finally, and most importantly, to my partner, Liisa. This DPhil would not have gone nearly as well without your love, support, generosity, and patience. Thank you for being my rock when I was struggling, for reading drafts of my work so

enthusiastically, for always being a sounding board for ideas and biological concepts, and for always believing in me. Your strength, kindness, and brilliance are a constant source of inspiration to me and I have learnt so much from you. Our numerous trips and weekends together have brought some much-needed balance over the past two-and-a-half years, while our lifestyle has kept us healthy and happy, which is not always possible in a place like Oxford. You have enriched my life far beyond what I could have imagined and brought me so much joy. I cannot wait for the next chapter in our adventure to unfold.

Contents

x

1 Introduction

1.1 Motivation

The crypts of Liehberkühns are a canonical example of growth and homeostasis in biology. These test-tube-shaped invaginations renew and maintain a protective epithelial layer, called the intestinal epithelium, for the small intestine and colon. In the context of disease, colonic cancer originates in the crypts [88], while during inflammation, crypts facilitate rapid regeneration of the epithelium [154]. Therefore, crypt function is crucial to a healthy gut. While the numerous genetic and biochemical signalling pathways governing crypt homeostasis have been slowly deciphered, in part due to the insight gained from mathematical and computational modelling, there are many aspects of crypt morphogenesis and homeostasis that have not been fully explored.

The first significant aspect is the crypt's highly-invaginated morphology. Crypts exhibit incredibly large deformations, and possess a long, narrow morphology (see Figure 1.1). However, it is not fully understood what may cause these crypts to initially form during development. An amenable framework to study such deformations is continuum mechanics. In continuum mechanics, the governing equations come from first principles and deformations arise naturally due to mechanical forces and torques. We can exploit morphoelasticity theory [74, 147] to

account for biological tissue growth. Morphoelasticity has been used successfully to study the mechanics of many biological processes, such as wound healing [24], vascular artery modelling [43], and brain cortical folding, [29], the latter of which shares many similarities with crypt invagination. However, such ideas have not been widely applied to the crypt. Several continuum-mechanics-based models for crypt and/or villi buckling do exist in the literature [14, 19, 56, 124, 125], but they lack the biological specificity required to be of value to experimentalists. This thesis aims to use a continuum mechanics framework in order to identify essential components that may contribute to crypt morphogenesis.

The second aspect concerns the notions of growth and homeostasis. The homeostatic structure of the crypt is robust and consists of functionally-distinct subpopulations of stem cells, transit-amplifying cells, and differentiated cells, with varying proliferative capacities and mechanical properties. Even though key biochemical signalling pathways, such as the Wnt signalling pathway, have been proposed to govern proliferative capacity, the observed proliferative capacity does not correspond to the observed concentration of Wnt signalling [69, 162]. Moreover, in homeostasis, the crypt population appears to be static and unchanging. However, when individual cells are labelled and tracked over time, there is a clear migration of cells out from the base to the top, indicating continuous turnover [84, 107]. To date, no continuum models appropriately capture this dynamic feature of tissue homeostasis. Therefore, a secondary aim of this thesis is to investigate the role of mechanical processes in shaping the crypt's unique proliferative structure and subsequently maintaining it in homeostasis.

Most crypt models in the literature are cell-based in nature. One reason continuum models of the crypt are less prevalent may be because it is difficult to incorporate individual cell detail. Biological tissues, such as the crypt, are spatially heterogeneous in many ways, including their growth capacity and stiffness, and these properties can evolve over time. In order to develop specialised continuum models for the crypt that account for deformation at the tissue scale, one must consider a range of chemical, biological and mechanical processes spanning subcellular and

cellular scales. This in turn introduces significant model complexity. In order to ameliorate model complexity, when appropriate, the number of spatial dimensions considered may be reduced. Filamentary structures are particularly well-suited for such dimensional reductions. Filaments, by definition, have one length scale much longer than the other two—such as the size of a single crypt cell compared to the length of the crypt epithelium—and hence are well suited to a spatially 1D description. Kirchhoff theory for elastic rods has been applied to a diverse range of filamentary systems, such as DNA coiling [172], neurite motility [145], plant tendril twisting [78], and many more. The theory of morphoelastic rods, formulated by Moulton et al. [120], extends Kirchhoff theory to account for axial growth and can be used to model biological tissue growth. In this thesis, we will explore the steps necessary to specialise the morphoelastic rod framework to that of an intestinal crypt.

The remainder of this chapter is structured as follows. First, we outline the biological background, highlighting crypt structure and the key signalling pathways known to contribute to homeostasis. We then discuss relevant studies of buckling and growth, with the intention of framing crypt morphogenesis as a buckling problem. Following this, we discuss previous modelling approaches for the crypt, which can be distinguished as discrete (individual-based) or continuum, along with their strengths and limitations, and a summary of the advances they have enabled. We continue with a general description of morphoelastic rod theory, which will be employed throughout this thesis. We close this chapter by outlining the structure for the following thesis chapters.

1.2 Biological background

The intestinal epithelium undergoes continuous, rapid renewal to maintain a protective epithelial barrier for the small intestine and colon during digestion and to facilitate nutrient absorption [1, 183]. This monolayer is maintained by the crypts of Liehberkühn, uniformly-spaced invaginations lining the gut which are vast in number. Each gland houses a pool of multipotent stem cells that coordinate cell proliferation, cell death, migration, and mechanical processes to facilitate constant

renewal of the epithelium. A human colonic crypt houses approximately 2000 cells [140] and is approximately five times as long as it is wide (Figure 1.1(a)). Despite this continuous turnover, crypts are robust in structure, their proliferative structure being conserved across each crypt (see Figure 1.1(b)).

Within the small and large intestines, stem cells are found in the crypt bases, a feature that has established the crypt as a canonical example for stem cell dynamics [141]. Furthermore, these stem cell pools are the only places where cells within the gut can persist long enough to accumulate mutations that could lead to cancer [88]. That is, certain mutations within stem cells may confer a competitive advantage, leading to a takeover of the crypt and allowing further mutations to occur [88]. Consequently, crypts are the sites of origin for colorectal cancer [16]. More generally, along the intestinal epithelium, proliferative cells are localised in the crypts. Hence, when gut tissue is affected by injury or inflammation, crypts are crucial to restoring barrier function by regenerating new, healthy tissue [98]. It is clear that understanding crypt dynamics and how these may be disrupted is of incredible clinical significance.

While considerable research attention has been directed towards the crypt, many fundamental questions remain unresolved. Much research has focussed on how the structure of proliferating and non-proliferating cells is maintained during homeostasis [69, 162], but it is not clear how this structure arises initially. Moreover, while crypt morphogenesis involves great physical changes and deformations, most attention has focussed on subcellular mechanisms, gene regulation and protein signalling pathways [69, 162], while little attention has been directed towards elucidating the role of mechanical cues in the gut. Finally, there is increasing evidence that mechanical forces have a role in guiding morphogenesis of the crypt and homeostasis [71, 155], yet the exact mechanisms are unclear.

1.2.1 Crypt development and structure in homeostasis

The intestinal epithelium forms via a well-defined series of events, and crypts do not form until several days after birth [183]. Crypt formation only begins after

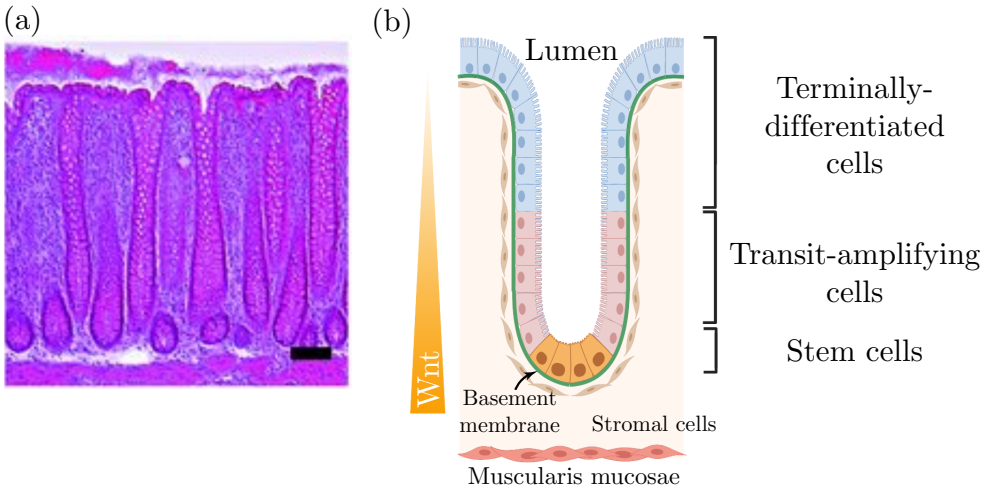

Figure 1.1: Structure and essential components of the colonic mucosa and crypt. (a) Histology of the human colonic mucosa, adapted with permission from Taylor et al. [170]. The scale bar represents 100μm. (b) A schematic of the colonic crypt and the different components contributing to homeostasis.

the formation of villi, protruding glands designed to maximise surface area for nutrient absorption [44, 167, 183][1]. Once the villi have been established, crypt morphogenesis occurs in the regions between villi. It is not fully understood what triggers crypt formation, but it has been shown that crypt formation is marked by apical constriction in the inter-villous tissue [65, 167]. In the colon, the villi-like structures are shed, leaving flat regions of epithelial tissue between crypts.

During homeostasis, crypts possess a unique yet remarkably robust population hierarchy of cell types, with slight variations between small intestinal and colonic crypts. These variations can be attributed to the functional differences between the small intestine and colon—the function of the former is primarily nutrient absorption, while the latter is primarily for water absorption and waste processing. In the base reside a pool of stem cells, with active cell cycle times ranging between 24 and 48 hours. Unusually, these cells are not actively proliferating, but rather reside in a paused state [35]; this non-cycling behaviour was initially thought to be

[1] As a side note, it is not completely clear whether villus formation is primarily driven by mechanical processes due to differential growth [158] or chemical signal patterning [181].

characteristic only of the conserved ring of quiescent stem cells around the crypt base, which only activate during injury [185], but has since been to apply to the whole crypt base. As stem cell progenitors migrate out of the base, these so-called transit-amplifying cells begin to cycle faster, between 12 and 24 hours, albeit for a finite number of divisions [114]. As the transit-amplifying cells move further away from the base, they differentiate into non-dividing, mature cells with specialised functions designed to aid gut health [183]. Eventually, these differentiated cells are shed into the lumen, the inner intestinal cavity, and undergo apoptosis [1, 183]. Unusually, in the small intestine, differentiated Paneth cells reside in the base alongside stem cells in an alternating arrangement. These cells have been shown to provide signalling factors that enhance stem cell renewal [150]. In the colonic crypt base, terminally-differentiated goblet cells have been identified, which are thought to have a similar role [148]. It is not known why the crypt's internal structure is so robust, given the enormous amounts of tissue renewal taking place. Nor are the mechanisms that generate this population structure fully understood. However, a study by Itzkovitz et al. [93] using optimal control theory showed that a sharp transition from symmetric stem-cell-driven cell population growth to transit-cell-driven cell population growth, indicated by asymmetric division, minimises the time taken for the mature crypt population to develop, suggesting an optimising role for rapid transit-amplifying cell divisions.

In addition to the complex internal structure of the crypt, external factors contribute to maintaining its structure and function. Directly lining each crypt is the basement membrane, a thin layer of extracellular network proteins. The basement membrane provides an adhesive surface on which epithelial cells can polarise and migrate, and a channel of communication between the crypt and the surrounding environment [175]. Further underneath is a heterogeneous composition of non-epithelial stromal cells that provide external signalling factors to support the stem cell niche and guide cell differentiation, as well as structural stability for the crypt [45, 97, 142]. More recently, it has been shown that the stroma undergoes significant remodelling during inflammation and injury [103, 118, 165]. Situated

underneath the tissue stroma is a thin layer of smooth muscle, referred to as the muscularis mucosae [1]; as a whole, the epithelium, stroma, and smooth muscle layer constitute the intestinal mucosa, the innermost layer of the gastrointestinal tract. The mucosa structure is illustrated in Figure 1.1.

1.2.2 Important contributors to crypt growth and maintenance

The crypt has long been viewed as a canonical example of stem cell dynamics; as such, the underlying signalling pathways contributing to crypt homeostasis have been studied extensively. Several significant pathways have been discussed in detail in comprehensive reviews such as Kershaw et al. [100] and Spit et al. [162]. We will briefly discuss arguably the most important signalling pathway, namely the Wnt signalling pathway. Other important signalling pathways that we do not mention here include BMP signalling, which regulates proliferation by driving terminal differentiation, and Notch signalling, which governs cell differentiation fate [69, 162].

Wnt signalling is responsible for regulating proliferative capacity [39], differentiation [137], and adhesion properties [126]. From a clinical perspective, colorectal cancer onset is most commonly linked with dysregulation of Wnt signalling [21]. In each healthy crypt, there is a decreasing gradient of Wnt signalling originating from the base [67]. It is not entirely clear how this gradient is formed or maintained, for there are multiple sources of Wnt signalling, such as Paneth cells within the small intestine [150] and cKit$^+$ cells within the colon [148], and extrinsic sources from the surrounding stroma [45, 97, 104]. However, it has been shown that Wnt signal ligands do not spread via diffusion, but rather through cell-cell contact and that they are diluted in concentration through cell division [61].

While Wnt signalling is proposed to be the primary regulator of proliferation, the proliferative structure in the crypt does not correspond to Wnt signalling concentration. Although Wnt signal concentration is maximal in the crypt base, where the stem cells are situated, proliferation activity is highest in the transit-amplifying cell region, which is towards the middle of the crypt. It is not understood

why this is the case, nor why this proliferative structure is so robust amongst the millions of crypts lining the gut.

1.2.3 The role of mechanics in the crypt

Although the majority of research attention has been directed towards genetic and signal transduction processes, which occur at the subcellular scale, it is becoming increasingly clear that mechanical forces have considerable influence on crypt morphogenesis and homeostasis, at the cellular and tissue scales. At the cellular level, tissue is created by the proliferation of stem cells and their progenitors. These newly-created cells, in turn, exert forces on neighbouring cells, which creates mechanical competition that leads to a 'conveyor belt' of cell migration out of the crypt base. This mechanical competition also leads to cell death in the form of anoikis (cell extrusion) to relieve internal tissue stress. Moreover, cell types differ in mechanical properties, such as their mechanical stiffness, cell-substrate adhesion, or cell-cell adhesion. These differences may, in turn, affect the forces that cells exert on each other.

At the tissue level, the role of mechanics is even more evident. Crypts are highly-invaginated structures; such significant deformation can only be generated by an interplay between tissue growth and mechanical forces [167]. However, perhaps the most compelling evidence for the role of mechanics in the crypt is the process of crypt fission. Crypt fission occurs during development and in homeostasis and is marked by a splitting of the crypt base, which pulls the underlying basement membrane and stroma upwards [31]. This bifurcation continues to deform, leading to the branching of two new crypts. This unique deformation process, akin to buckling, gives strong evidence for the role of mechanics in shaping crypt tissue.

The lack of attention directed towards understanding the role of mechanics in the crypt may stem from the difficulty in characterising the mechanical properties of biological tissue. Although technology has advanced considerably so that it is now possible to measure forces at the cellular and tissue level *in vitro* [139, 166], it is impossible to perform such measurements *in vivo*. However, mathematical and

computational modelling provides a tractable framework in which one can develop and validate possible models of mechanics within the crypt.

1.3 Modelling challenges

Crypt morphogenesis is but one of many remarkable examples of mechanical pattern formation. The marked transition from a trivial 'base state' to a more complex morphology can be found in myriad structures across biology and engineering. While these structures may be functionally distinct, they are typically governed by the same underlying physical principles. By abstracting the crypt and extracting its fundamental physical processes, we can draw analogies with previous studies of buckling in the modelling literature.

From a modelling perspective, considering crypt morphogenesis as a buckling problem opens many doors, as the literature for buckling and mechanical pattern formation is extensive and mature. There are a wide range of analytical tools from which one can draw, such as linear stability analysis [86, 120], weakly nonlinear analysis [86], and imperfection sensitivity [90], and numerical tools such as numerical continuation [36]. While crypt formation has previously been treated as a buckling problem [56, 124], there are several notable aspects of crypt formation that are worth investigating in more detail.

The first and foremost aspect is the impact of tissue growth. In the crypt and other biological systems, mechanical pattern formation is driven by internal tissue growth, rather than an externally-applied force. Therefore, in this scenario, buckling occurs at a critical growth that is characterised by both the geometrical and mechanical properties of the system [120]. Investigating the similarities and differences between growth-induced buckling and standard load-induced buckling is itself of mathematical interest. In particular, how does the presence of growth change the underlying bifurcation structure?

Second, the crypt is a highly-deformed structure with a length that is, on average, five times its width [170]. Such deformations extend well beyond the onset of buckling. As such, standard linear stability analyses that are used to

predict the onset of buckling are inadequate to characterise such large deformations. Therefore, to fully characterise crypt evolution, nonlinear analysis techniques such as weakly nonlinear analysis and numerical solutions are required to investigate the *post-buckled* behaviour.

Finally, the crypt is a spatially-heterogeneous material. The crypt tissue is heterogeneous, consisting of cells with varying proliferative capacities and mechanical properties, such as cell stiffness and cell-substrate adhesion. Generally, spatially heterogeneity in material parameters is often neglected in continuum mechanics, as it reduces analytical tractability in models. As such, it is not fully understood what impact spatial heterogeneity in material parameters (such as growth and stiffnesses) may have on the underlying bifurcation structure and post-buckled behaviour.

1.3.1 Buckling

Buckling has been studied since the 18th century, when Euler first calculated the famous buckling load for a column under vertical compression [60]. Historically, in engineering studies, buckling has been associated with structural failure. Therefore, the focus of many buckling studies in the literature is the *onset* of buckling, which can be determined through a linear stability analysis. Our focus on the subsequent deformation after buckling thus differs from these engineering studies, as we wish to understand the post-buckled behaviour of the crypt due to growth. By analysing the post-buckled behaviour, we can gain insight into the full growth evolution and understand which parameters are most influential in driving morphogenesis.

One of the best known models for the study of buckling is a bilayer system, most commonly represented by a rod tethered to an underlying foundation. This setup, dating back to the works of Timoshenko [173] and Biot [22], continues to be relevant to many systems, particularly in biology. Indeed, when Edwards and Chapman [56] proposed the first continuum mechanics model of the crypt, it was of an elastic rod supported by a foundation. The rod-on-foundation model has also found use in describing other biological processes, such as the folding of brain tissue [29], the formation of seashell spines [37], to name but two examples. A common aspect of this

system is the restriction of deformations to the x-y plane. While this appears to be an oversimplification, when modelling the transverse deformations of 2D sheets, the governing equations often reduce to these of the planar system [29, 47, 48, 85, 125]. As such, following the works of Edwards and Chapman [56] and Nelson et al. [124], we will model the transverse deformations of the crypt by considering a growing rod upon a foun dation that is confined to a planar geometry, where the foundation represents the mechanical effects of the supporting extracellular matrix and tissue stroma. Later, we will demonstrate how this framework can be used model the crypt's unique growth structure and crypt homeostasis.

A common feature of systems that undergo buckling is a pitchfork bifurcation [86, 90, 131]. The pitchfork bifurcation is indicative of the inherent symmetry of the system; when buckling, the system can, in theory, buckle 'up' or 'down' with equal preference. Moreover, in several systems, these pitchforks can be supercritical, indicating a smooth change from the unbuckled to buckled state, or subcritical, where the change from unbuckled to buckled is discontinuous. While such structures have been extensively studied for systems that buckle under an externally-applied force [89, 90], it is not known whether similar bifurcation structures arise when growth is modelled. In particular, understanding whether subcritical pitchfork bifurcations can occur due to growth is important as it implies that small changes in growth can lead to large deformations, which suggests rapid morphological changes during morphogenesis.

It was arguably the introduction of imperfection sensitivity, which quantified the predisposition of structures to buckle at drastically reduced loads due to small structural imperfections, that highlighted the need to understand post-buckling behaviour in more detail [4, 90]. First pioneered by Koiter [105], the analysis was developed to understand why thin-walled shell structures buckled at significantly lower loads than those predicted by standard linear analysis techniques. One useful feature of imperfection sensitivity analysis is that it reveals which buckled mode will be selected due to the (spatially-varying) imperfection. For systems that exhibit a pitchfork bifurcation in the absence of imperfections, this indicates

that the underlying imperfection 'breaks' the symmetric pitchfork, predisposing the system to a particular solution branch [4, 90]. In this thesis, it will be of interest to investigate whether the spatial heterogeneities that are present in the crypt can be interpreted as structural imperfections, thus rendering them amenable to imperfection sensitivity analysis.

While many of the techniques developed to study buckling and post-buckling have existed for a long time, buckling and mechanical pattern formation continues to be an active research area. In particular, following initial computations of mechanical instability due to growth alone [18], many recent applications of buckling in a biological context have appeared, where the buckling is driven by internal growth [6]. This has only been possible due to recent developments in the continuum mechanics field, namely, the development of morphoelasticity [74].

1.3.2 Descriptions of tissue growth

Growth is a fundamental process that shapes numerous biological structures and has been modelled for a long time [6]. One significant continuum mechanics model of growth was proposed by Rodriguez et al. [147]. In this work, growth is incorporated into nonlinear elasticity theory by decomposing the deformation gradient tensor into sequential growth and elastic tensors. This multiplicative decomposition, which has become standard in the mechanics literature, is the fundamental assumption of what is now known as morphoelasticity, an extension of continuum mechanics to incorporate volumetric growth.

A branch of morphoelasticity, which was originally developed for 3D nonlinear elasticity theory, that is of particular relevance is the theory of morphoelastic rods. Originally presented by Moulton et al. [120], morphoelastic rod theory extends classical Kirchhoff rod theory to account for axial growth along filamentary structures, using a 1D version of the multiplicative decomposition principle introduced in Rodriguez et al. [147]. As tissue growth occurs primarily along the crypt axis, modelling proliferation through axial growth is appropriate in this case. It is this morphoelastic rod framework that forms the theoretical foundation for this thesis.

An alternative model of tissue growth is that of surface growth [159, 176, 189, 190], which is in contrast to the volumetric growth typically considered in morphoelastic frameworks. Surface growth is typically modelled as an accretive process, where material is deposited over time, updating the unstressed, reference configuration. While this type of growth is not used to model tissue growth in this thesis, this concept of an evolving reference configuration will be explored when we discuss the concept of tissue homeostasis in Chapter 4.

One of the fundamental challenges in growth modelling is determining the most appropriate 'growth law' [74]. That is, what are the minimal contributions that capture the essential growth structure of the biological system in question? For the crypt, no such growth laws exist in the modelling literature. However, a common mechanism that is often proposed to regulate growth is mechanical feedback. In Chapter 4, we will explore whether mechanical feedback can generate the observed proliferative structure of the crypt.

Mechanical feedback on growth

It has long been hypothesised that biological tissue grows in response to mechanical stress [5]. Consequently, a number of mathematical and computational models that incorporate mechanical feedback on tissue growth have been applied to a variety of biological systems, such as plant tissue [5], tumour spheroids [6], *Drosophila* wing disc formation [157], and bone tissue [42]. In several computational models of the crypt, mechanical feedback in the form of contact inhibition is included to regulate cell proliferation, allowing the cell population to reach a steady state during homeostasis [52, 54]. However, the role of mechanical stress in shaping and maintaining the crypt's proliferative structure has not been investigated in any detail. One of the goals of this thesis is to determine whether mechanical feedback can help to explain how the unique proliferative structure of the crypt arises and is maintained.

In 1D, the simplest mechanosensitive growth law takes the following form [168]:

$$\dot{\gamma}\gamma^{-1} = \mu(n - n^*), \tag{1.1}$$

where the overdot denotes the derivative with respect to time; γ describes local growth; μ describes the strength of mechanical feedback; n is the stress; and n^* is the homeostatic stress. For this growth law, it is clear that growth reaches a steady state when $n = n^*$; this state is often referred to in the literature as mechanical homeostasis [59, 168]. However, in the crypt, the presence of Wnt signalling and other signalling pathways means that there is a constant 'background' contribution to tissue growth. Therefore, one goal of this thesis is to investigate how signalling pathways, such as the Wnt pathway, and mechanical regulation combine to maintain tissue homeostasis in the crypt, which occurs when cell proliferation and cell death balance each other.

1.4 Mathematical and computational models of the crypt

The crypt has become a canonical example for studying stem cell dynamics. In order to understand the role of stem cells in maintaining crypt homeostasis, it is vital that they and their respective lineages can be monitored over time. Indeed, experimental techniques are continuously being refined to track different cell types in the crypt at finer temporal and spatial resolutions [84, 107]. As colorectal cancer originates in crypts, it is important also to understand how alterations in cell properties, such as proliferative capacity and biomechanical properties, may confer selective advantages in mutant cell clones, perturbing homeostasis. Despite this, monitoring cell lineages *in vivo* and altering cell properties via gene knockout experiments can be time-consuming and costly. However, this is not an issue for mathematical and computational models, where individual cells can be tracked and their properties can be varied systematically through model parameters. Consequently, considerable modelling efforts have been directed towards the crypt, employing a variety of geometries and modelling approaches. A timeline of notable models from the literature is shown in Figure 1.2, while common crypt model geometries are shown in Table 1.1. In terms of approaches, models can be broadly classified into four

categories: continuum non-spatial (typically compartmental models); discrete non-spatial (typically stochastic processes); discrete spatial (either on-lattice or off-lattice); and continuum spatial (typically continuum mechanics models). Each approach has its strengths and limitations; we discuss these in the following sections.

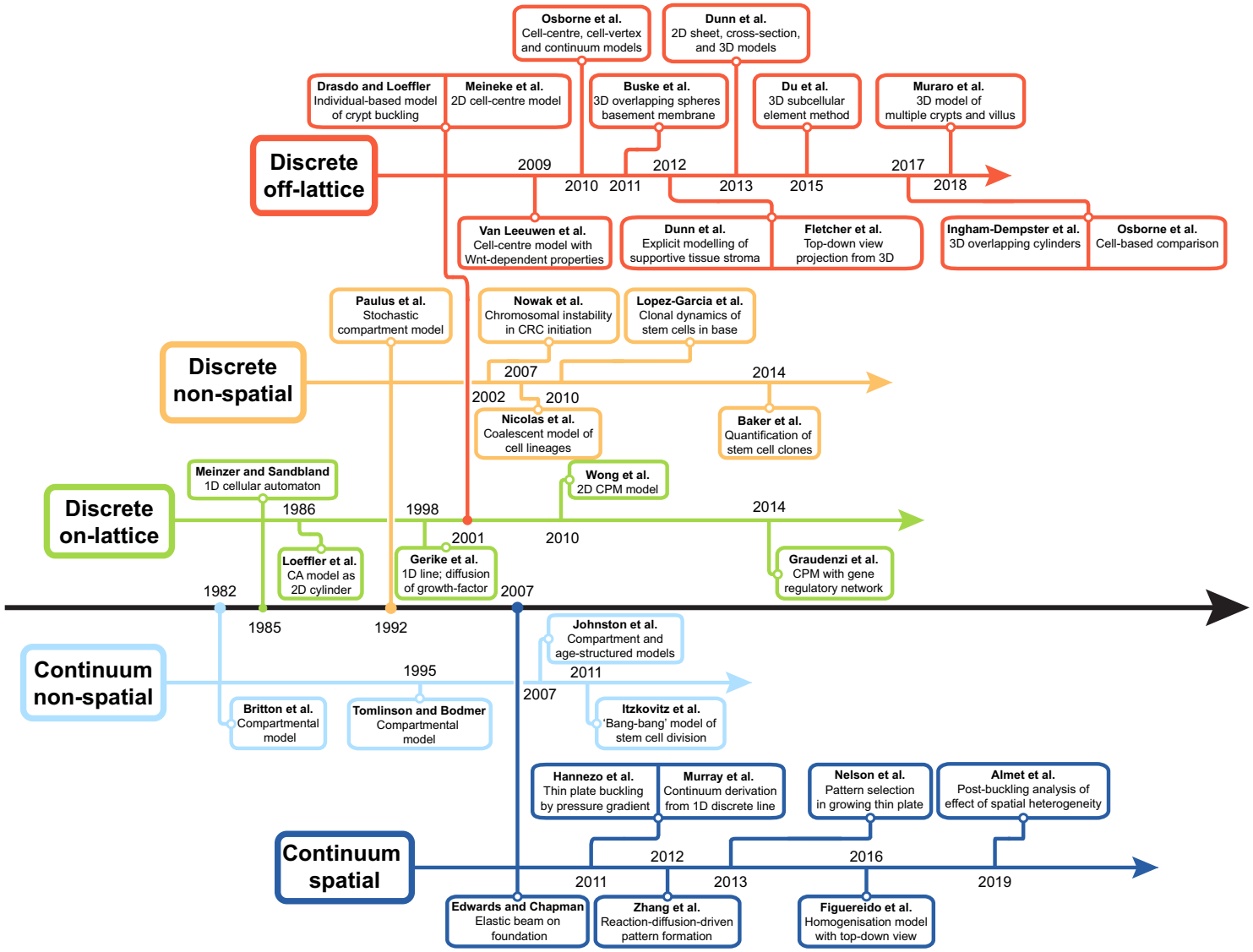

Figure 1.2: A history of the different modelling approaches that have been applied to the crypt.

1.4.1 Non-spatial models

As the name suggests, non-spatial models only consider the temporal dynamics of the crypt. As such, these frameworks tend to focus on population-level quantities, such as cell number (or cell density in a continuum setting), or on regions that are not large in space, such as the crypt base.

Discrete non-spatial

Discrete non-spatial models generally consider cell number and focus on problems relating to clonal evolution. These models focus on questions relating to stem cell homeostasis within the base, for example, the robustness of the stem cell pool to genetic mutations. A variety of stochastic theories can be employed, such as branching processes, to study how cell clones may evolve over time. These theories are most useful when considering small cell numbers, such as the number of stem cells in the crypt base. These models are also a popular choice for studying the effects of mutation accumulation within cells [23, 106, 116, 127, 128]. Recent work using these models has suggested that intestinal stem cells divide symmetrically during homeostasis and follow neutral drift dynamics; that is, in healthy crypts, clonal competition is effectively random [112, 160]. The main benefit of using these models is that they are straightforward to parametrise, as cell clone data have become more readily available in recent years as imaging technologies have advanced [13, 180]. However, their simplicity, particularly their neglect of spatial effects, means that quantitative insight is obtained at the cost of mechanistic insight.

Continuum non-spatial

Compartmental models decompose the cell population into distinct subpopulations and account for transitions between these compartments. Arguably, the first model of the crypt was a compartmental model, by Britton et al. [27]. In Johnston et al. [96], the first age-structured model of crypt dynamics was introduced, relaxing the assumption of 'synchronous' division that is an artefact of compartmental models. Non-spatial continuum models capture population dynamics during

homeostasis and because cell populations are assumed to be spatially well mixed, steady state behaviours can be studied. Using this analysis, Johnston et al. [96] demonstrated that modelling transitions between cell populations, which represented cell differentiation, as a saturating mechanism allows the population to destabilise and grow unboundedly due to mutations. However, it is difficult to gain insight beyond the population-level conclusions, as it is very hard to incorporate details about individual cells, and spatial heterogeneity and mechanical processes are neglected.

1.4.2 Spatial models

Spatial models attempt to capture the highly-specialised geometry of the crypt and model the inherent spatial aspects of processes such as proliferation, death, and migration. It is therefore no surprise that spatial models comprise the largest class of crypt models in the literature. When developing spatial models of biological tissues, such as the crypt, two important decisions must be made: what is the spatial geometry and are cells are viewed as discrete entities or a coarse-grained, continuous quantity? The different geometries that have been applied to the crypt are presented in Table 1.1. As might be expected, each geometric abstraction comes with its respective benefits and drawbacks.

Geometry	Representative works	Notable applications	Strengths	Weaknesses
1D line 	Gerike et al. [70]; Murray et al. [122]	Growth-factor-driven proliferation [70]; Mutant accumulation [188]; Population dynamics [122]	Easy to use; Can derive continuum approximations	Spatially restricted; Over-simplified; Cannot model cell sorting
2D cross -section 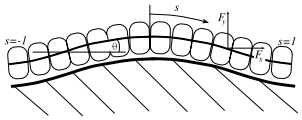	Drasdo and Loeffler [50]; Edwards and Chapman [56]; Dunn et al. [52];	Signal-driven morphogenesis [187]; Crypt buckling [50, 52, 56, 124]; Mechanical effects of basement membrane and stroma; [50, 52, 53, 56, 124]; Cell migration [52, 53]	Models tissue deformation well	Spatially restricted; Limited scope for mutations and clonal evolution; Cannot model cell sorting
2D sheet, top-down view 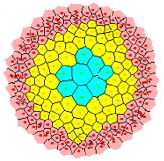	Fletcher et al. [64]; Hannezo et al. [85]; Figueiredo et al. [62]	Stem cell hypotheses [64]; Monoclonal conversion [64]; Buckling morphogenesis [85, 125]; Aberrant crypt foci [62]	Can model multiple crypts; Can model 3D effects in 2D	Over-simplified cell-cell interactions; Difficult to model cell sorting
2D rolled-out cylinder 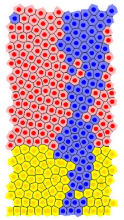	Loeffler et al. [111]; Meineke et al. [115]; Van Leeuwen et al. [178]; Osborne et al. [134]	Dynamics during homeostasis [82, 115, 178]; Monoclonal conversion [117, 134]; Mutant takeover [117, 134];	Well-suited for clonal dynamics; Produces many observed features	Difficult to model mechanical heterogeneity; Difficult for cells to rearrange
3D crypt 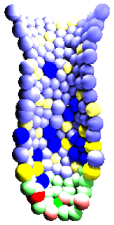	Buske et al. [30]; Dunn et al. [54]; Du et al. [51]; Ingham-Dempster et al. [92]; Pin et al. [136]	Anoikis distribution [92]; Stem cell niche maintenance [51]; Cell lineages [30, 136, 171]; Post-irradiation recovery [54]; Cell migration [53]; Post-division cell separation [34]	Can model crypt base; Cells can rearrange; Can inform correct cell numbers	Current models have fixed geometry; Can be computationally expensive

Table 1.1: The different geometries that have been used to model the crypt. Images have been reproduced with permission from (top to bottom): Zhao and Michor [188]; Edwards and Chapman [56]; Fletcher et al. [64]; Osborne et al. [134]; and Buske et al. [30].

Discrete spatial models

Discrete spatial models are generally referred to as cell-based models. This broad class of models treat each cell individually. Consequently, features such as cell lineages, mitotic indices, and migration velocity can be tracked over time and validated against analogous experimental data [183]. Moreover, cellular processes can be specified with a wide range of complexity, from simple, logic-based rules [82] to direct coupling of cellular behaviour to mathematical models that describe subcellular signalling pathways [178].

Cell-based models can be classified as either of on-lattice or off-lattice type. In on-lattice models, cells are constrained to move along a regularly-spaced grid of lattice 'cells', and may occupy one or multiple lattice sites. Off-lattice models relax this assumption, so that cells can move freely through Euclidean space, with cell shapes either fixed or defined via partitions, such as the Voronoi tessellation, that remodel as the distances between cells vary [9].

The first multicellular model of the crypt was an on-lattice, cellular automaton model, by Loeffler et al. [111]. The crypt was modelled as a 2D rectangular tissue with periodic vertical boundaries, representing an 'unfolding' of the crypt surface. This geometry was used in a series of papers [110, 111] and has become popular for tracking cell populations and different cell lineages [115, 117, 133, 134, 178]. In the cellular automaton model, each cell occupied at most one lattice site. Loeffler, Paulus, Potten, and colleagues used this approach to investigate possible migration mechanisms induced by cell division and compared their simulation results to experimental mitotic labelling data. While this model has been used in recent applications [8, 10, 25], the off-lattice implementation of this 2D sheet has become more prevalent [115]. However, we do note the work of Zhao and Michor [188], who simplified the 2D rectangle to a 1D lattice to investigate how proliferation kinetics affected the rate at which cells acquired the mutations necessary for colorectal cancer. This geometric reduction retains the average behaviour of cells migrating along the crypt axis, but sacrifices detail on lateral cell movement. In general, cellular automaton models are computationally efficient and straightforward to

implement, but are spatially restricted and highly idealised, as individual cells are restricted in movement and mechanical effects are ignored.

An extension of cellular automaton models, where cells occupy at most one lattice site, is the Cellular Potts model, originally proposed by Graner and Glazier [81]. This model allows cells to span multiple lattice sites, as determined through a Hamiltonian energy function describing constraints on cell volume, area, and adhesive capacity. One of the key strengths of the Cellular Potts model is that cell shapes evolve dynamically. Coupling this with adhesion constraints allows cell sorting to be simulated straightforwardly. This is an important feature of confluent tissues, particularly the crypt, that is absent from many multicellular models. However, as is the case with on-lattice models, it is not clear how other forces and mechanical effects may be incorporated.

Off-lattice models relax the lattice-based assumption of on-lattice models, and can be categorised into cell-centre and cell-vertex models. Cell-centre models consider cells as points in space, encapsulated by a region defined either through a spatial partitioning or fixed shape. As such, cell-vertex models view each cell as a collection of points encapsulating a cell region. To date, there has only been one cell-vertex implementation of the crypt [134]; it was primarily used as a point of comparison between a cell-centre model and a continuum model of the crypt, as there is negligible difference between cell-centre and cell-vertex models of the crypt, aside from the increase in computational complexity.

Off-lattice, cell-centre models are a popular framework for studying the crypt, and exist in a variety of geometries. In 2D, cell areas are modelled through the Voronoi region, which allows cell-cell connectivity to be defined straightforwardly through its dual, the Delaunay triangulation. Force balances are imposed at each point through an over-damped version of Newton's Second Law. Overlapping object models treat each cell as a point in space, with a radius of interaction specified by a fixed shape, typically spheres [30] or cylinders [92]. These have natural generalisations to 3D. Moreover, one could extend these to accommodate variable cell shapes by using the subcellular element method [51], or deformable cell model

[179]. However, overlapping object models do not have well-defined connectivities, rendering the implementation of spatially-dependent forces difficult.

The first off-lattice cell-centre model for the crypt was presented by Meineke et al. [115]. This paper modelled the crypt using the same 2D geometry as Loeffler et al. [111]. However, by relaxing the lattice-based assumption, cell migration behaviour reflective of the crypt emerged with fewer contrived modelling assumptions than for the on-lattice counterpart. The framework of Meineke et al. was extended later by Van Leeuwen et al. [178]; a Wnt signal profile was prescribed along the crypt axis and a Wnt-dependent cell cycle was included. This work set the stage for a number of investigations on monoclonal conversion, such as in Mirams et al. [117] and Osborne et al. [134]. One drawback of the cylindrical model is that the crypt base is neglected. An alternative, top-down geometry, was employed by Fletcher et al. [64] in order to explicitly model the crypt base. Here, forces are defined via a law that accounts for the 3D crypt geometry, but is projected down to the 2D model geometry. It was shown that the monoclonal conversion results depend on the assumed geometry of the model.

Tessellation-based models are generally implemented in 2D and become computationally expensive in 3D. Hence, 3D models are, by and large, of overlapping object type. The first 3D model of the crypt was that of Buske et al. [30], who modelled each cell as a deformable sphere. Additionally, they accounted for the different cell types that appear within intestinal crypts, and used a simple, rule-based model to relate cell fate specification to local levels of Wnt and Notch. The crypt surface was modelled using a surface of revolution. Adhesion to the surface was enforced by a triangular fibre network, representing the basement membrane, which determined cell death through anoikis. In the majority of 3D crypt models, cells are treated as deformable spheres that interact via distance-based forces. However, Ingham-Dempster et al. [92] showed that when cells are modelled as cylinders rather than spheres, different spatial distributions of cell death events are observed. In Du et al. [51], a subcellular element model is presented, where cells are modelled as

collections of deformable spheres, resulting in more realistic simulated cell shapes and greater spatial control of subcellular properties.

One aspect of the aforementioned cell-based models is that the crypt geometry is fixed. However, there are a select few models with a deformable crypt geometry. The first deformable crypt model was proposed by Drasdo and Loeffler [50]. In this paper, the crypt is presented as a U-shaped chain of individual cells. Notably, a bending force, based on spontaneous curvature, is applied in order to stabilise the crypt shape. Simulation results showed that a stable crypt shape can be disrupted by decreasing the bending stiffness and increasing cell proliferation rates simultaneously. Following this work, Dunn et al. [52] presented the first deformable crypt model that explicitly modelled the presence of the underlying tissue stroma. A curvature-based force is presented to model the effects of the underlying basement membrane, which anchors the epithelium to the tissue stroma. The authors showed that it is possible to deform the flat epithelium into a buckled crypt shape. However, this is only possible by imposing a spatially-heterogeneous target curvature, rather than the shape 'naturally' emerging.

1.4.3 Continuum spatial

One of the most common features of discrete, individual-based models is the assumption of a pre-determined, fixed geometry. That is, the crypt geometry does not evolve naturally over time. Despite their infrequent use, an evolving tissue geometry is possible within continuum spatial models. These frameworks can also capture mechanical deformations in a way none of the other frameworks can. By adopting a continuum mechanics approach, crypt morphogenesis can be viewed as the buckling and further deformation of a thin elastic material, a rod in 1D and a plate in 2D. Edwards and Chapman [56] were the first to consider a continuum mechanics model of crypt formation. They treated the crypt epithelium as a growing elastic beam supported by a foundation force, representing attachments to the underlying extracellular matrix and stroma. A linear stability analysis was conducted, investigating how crypt formation is affected by parameters relating

to tissue growth, foundation stiffness, and substrate relaxation. This work was extended by Nelson et al. [124], who performed a more extensive buckling analysis and considered heterogeneities to growth and beam stiffness. In an analogous 2D setting, Nelson et al. [125] combined Foppl-von-Kárman thin plate theory with a nonlinear elasticity description for soft tissue growth [147] to investigate pattern formation due to growth and substrate heterogeneity. Hannezo et al. [85] also considered crypt-villus formation within the Foppl-von Kárman framework, who modelled tissue growth through a pressure gradient along the sheet caused by differences in cell division and cell death rates.

Part of the reason that continuum mechanics models of the crypt are scarce is the challenge of accounting for tissue growth and, in particular, the residual stresses induced by growth. Only more recently has it been possible to construct well-defined mathematical models of biological tissue growth within a continuum mechanics framework [74, 147]. Moreover, biological tissues contain a number of spatial heterogeneities, at the cellular and subcellular levels, which are inherently difficult to incorporate into continuum models as, by construction, there is no cellular unit. However, in order to faithfully model the crypt from a mechanical perspective, it is vital that spatial heterogeneities and nonlinearities in geometry can be readily captured. As previously discussed, this becomes more feasible when one simplifies the geometry to a 1D setting by exploiting the 'slenderness' ratio of the crypt epithelium; that is, the size of a single cell compared to the length of the epithelium. As this ratio is small, the Kirchhoff theory of elastic rods is an attractive candidate for considering crypt deformations, where heterogeneities and nonlinear geometries can be readily modelled. The morphoelastic rod theory, originally developed by Moulton et al. [120], extends this theory to include axial tissue growth. The goal of this thesis will therefore be to develop a morphoelastic rod model of the crypt, the theory of which we will now outline.

1.5 Morphoelastic rod theory

Throughout this thesis, we will draw upon the morphoelastic rod framework that was initially developed in [120]. Accordingly, we will describe the general mathematical theory, before specialising the model to be of greater biological relevance to the crypt. For brevity, we do not present the complete, generalised framework; instead we only state the equations needed for future analysis. In particular, we restrict attention to extensible and unshearable rods in quasi-static mechanical equilibrium. We note that this general framework also encapsulates the previous works of Edwards and Chapman [56] and Nelson et al. [124].

The shape of a rod is described with respect to its centreline, denoted by the smooth space curve $\mathbf{r}(S)$, where S is the material parameter in an unstressed configuration. Typically, S is taken to be the arc length in this configuration. The current arc length s is subsequently defined by

$$s = \int_0^S \left| \frac{\partial \mathbf{r}(\sigma)}{\partial \sigma} \right| d\sigma. \tag{1.2}$$

At each material point S along the centreline, we define a local orthonormal basis $\{\mathbf{d}_1, \mathbf{d}_2, \mathbf{d}_3\}$, generally referred to as the *director basis*. The basis vectors will be defined such that $\mathbf{d_3}$ is aligned with the tangent vector of the rod at S, while $\mathbf{d}_1$ and $\mathbf{d}_2$ are taken to lie in the plane of the rod cross-section at S along the principle axes of inertia. A schematic representation of the director basis construction is shown in Figure 1.3.

The geometry of the rod can be completely described by the following equations, which are a generalisation of the Frenet-Serret equations [40, 76, 77, 120]:

$$\frac{\partial \mathbf{r}}{\partial S} = \alpha \mathbf{d}_3, \tag{1.3}$$

$$\frac{\partial \mathbf{d}_i}{\partial S} = \mathbf{u} \times \mathbf{d}_i, \qquad i = 1, 2, 3. \tag{1.4}$$

Here, α is the *elastic stretch*, and we have defined the basis vector $\mathbf{d}_3$ to align with the tangent direction. The *Darboux vector* $\mathbf{u} = u_1\mathbf{d}_1 + u_2\mathbf{d}_2 + u_3\mathbf{d}_3$ describes the bending and twisting of the rod: u_1 and u_2 are associated with the former and u_3 with the latter.

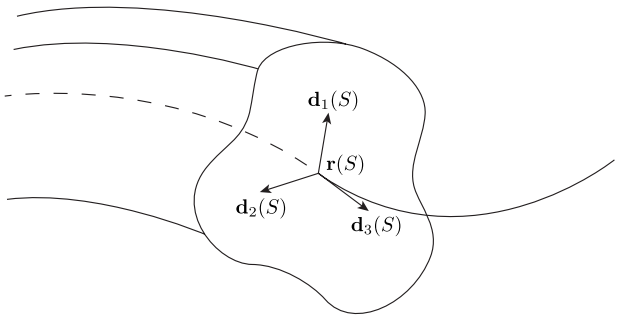

Figure 1.3: Definition of the local director basis. The vectors $\mathbf{d}_1$ and $\mathbf{d}_2$ lie in the cross-section at the material position S, while $\mathbf{d}_3$ is normal to the cross-section. See Section 1.5 for more details.

Rod growth is incorporated into the framework by applying a multiplicative decomposition approach [18, 120, 147]. In order to do this, we consider three different configurations of the rod: the pre-grown and stress-free configuration, hereafter called the 'initial configuration', which is parametrised by the arc length S_0; the grown (and still stress-free) virtual configuration, parameterised by S and referred to as the 'reference' configuration; and the current configuration, parametrised by s. This framework is summarised in Figure 1.4. In the initial, reference, and current configurations, the total rod lengths are L_0, L, and l, respectively (Figure 1.4). The rod arc length is assumed to evolve through some growth process, described by the *growth stretch*[2] $\gamma(S_0) = \partial S/\partial S_0$, followed by an elastic response, encapsulated by the elastic stretch $\alpha = \partial s/\partial S$. We can therefore write the *total stretch* of the rod λ from initial to current configuration (see Figure 1.4) as

$$\lambda = \alpha\gamma \qquad \Longleftrightarrow \qquad \frac{\partial s}{\partial S_0} = \frac{\partial s}{\partial S}\frac{\partial S}{\partial S_0}. \tag{1.5}$$

This is the 1D analogue of the multiplicative decomposition of the deformation gradient tensor employed in 3D morphoelasticity [18, 120, 147].

We follow Moulton et al. [120] and initially define the kinematics and mechanics with respect to the reference configuration, before using (1.5) to recast the equations

[2]Here we follow standard terminology [79] in referring to γ as the growth 'stretch', the rationale being that growth acts to 'stretch' the arc length by adding new material. That is, the word 'stretch' does not refer to a 'stretching' of old material, but rather an increase in reference arc length by the addition of new material.

in the initial configuration, where it is analytically and computationally easier to perform calculations.

Mechanics

A balance of linear and angular momentum leads to the following equilibrium equations for the resultant force and moment, $\mathbf{n}$ and $\mathbf{m}$, respectively:

$$\frac{\partial \mathbf{n}}{\partial S} + \mathbf{f} = \mathbf{0}, \tag{1.6}$$

$$\frac{\partial \mathbf{m}}{\partial S} + \frac{\partial \mathbf{r}}{\partial S} \times \mathbf{n} + \mathbf{l} = \mathbf{0}. \tag{1.7}$$

Here, the quantities $\mathbf{f}$ and $\mathbf{l}$ represent the body force and couple per unit reference length, respectively. The model is considered in the absence of any body couple—that is, no force is exerted on the surface of the rod—and therefore $\mathbf{l} = \mathbf{0}$. The body force $\mathbf{f}$ is to be specified later by a constitutive assumption.

We close the system by introducing constitutive relations describing the elastic properties of the rod and its behaviour due to bending, stretching and twisting. Following Coleman et al. [40], Goriely and Tabor [76, 77], and Moulton et al. [120], $\mathbf{m}$ is related to the Darboux vector $\mathbf{u}$ by

$$\mathbf{m} = EI_1(u_1 - \widehat{u}_1)\mathbf{d}_1 + EI_2(u_2 - \widehat{u}_2)\mathbf{d}_2 + \mu J(u_3 - \widehat{u}_3)\mathbf{d}_3, \tag{1.8}$$

where E is the Young's Modulus; μ is the shear modulus; I_1 and I_2 are respectively the first and second moments of area; and J is a parameter depending on the shape of the rod cross-section and I_1 and I_2. The vector $\widehat{\mathbf{u}} = (\widehat{u}_1, \widehat{u}_2, \widehat{u}_3)$ is the unstressed Darboux vector, describing the rod shape when it is experiencing no stress. In general, it is assumed that the rod is naturally straight and hence $\widehat{\mathbf{u}} = \mathbf{0}$. However, in Chapter 3, we will explore the effects of an evolving and hence non-zero $\widehat{\mathbf{u}}$.

We can model rod extensibility by relating the axial stress to the elastic stretch α by

$$n_3 = \mathbf{n} \cdot \mathbf{d}_3 = EA(\alpha - 1). \tag{1.9}$$

Here, A is the cross-sectional area of the rod. Note that this is analogous to Hooke's law.

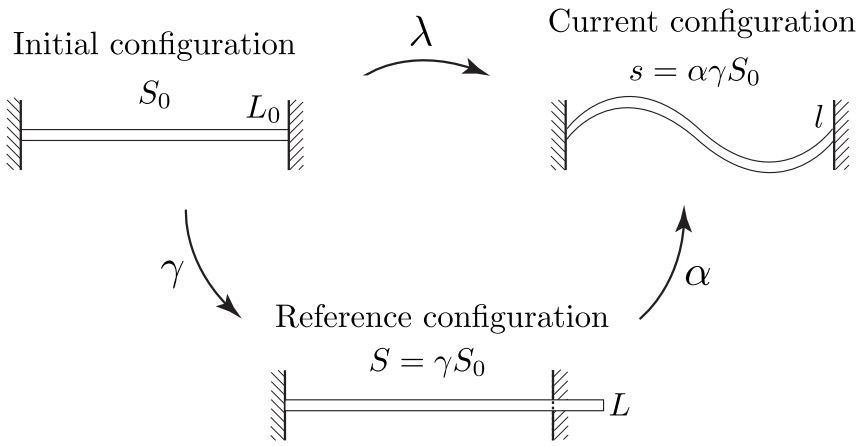

Figure 1.4: The different morphoelastic rod configurations. A rod that is initially confined to a (finite) interval grows in a virtual, unstressed reference configuration, before being mapped to the current configuration, where it is subject to boundary conditions and loads. The rod is parametrised by a different arc length in each configuration. The respective rod lengths have been indicated. The parameters γ, α and λ denote the growth, elastic, and total stretches, respectively.

Our objective is to explore several important aspects of crypt morphogenesis and homeostasis within the morphoelastic rod framework. For example, in the context of buckling and morphogenesis, we will explore how spatial variations in growth, γ, and rod stiffness, E, which are both known properties of the crypt, impact the onset of buckling and post-buckled behaviour. Other examples include: different growth laws, modelled through the incremental growth $\dot{\gamma}\gamma^{-1}$, which reflect mechanochemical contributions, and different laws for the foundation force $\mathbf{f}$, which can be used to model tissue relaxation, and how these different growth and foundation forces may affect the resulting morphologies during morphogenesis. Such modelling choices have not been investigated in detail previously.

One subtle issue that has not been explored in detail is how these different processes and material properties should be parametrised. In this framework, there are two main parametrisation choices: by the initial arc length S_0, the Lagrangian representation, or the current arc length s, the Eulerian representation. Modelling a Lagrangian or Eulerian representation reflects the underlying assumption about the material property. For instance, in the former case, modelling heterogeneous stiffness by $E = E(S_0)$ reflects stiffness as an 'inherent' property of the rod. In

the latter case, modelling stiffness as $E = E(s)$ reflects stiffness that remains fixed with respect to current position. A key question is whether the simulated morphologies are markedly different for Lagrangian and Eulerian representations. We will explore this concept in Chapter 3.

1.6 Discussion

Colonic crypts are of great clinical significance, for they serve as the sites of origin of colorectal cancer [143] and facilitators of regeneration from injury [154], which is particularly important in the context of inflammatory diseases. In both cases, disrupting crypt homeostasis—subcellular processes, cellular properties, and morphology—is key. However, while much is known at the genetic and molecular level, very little is known about the emergent effects of these processes, coupled with biomechanical factors at the cellular and tissue scales, on crypt morphogenesis. Is what is observed in the crypt due to the underlying genetic and molecular mechanisms, or the result of forces and spatial effects? Understanding how these biomechanical effects are coordinated and give rise to a healthy crypt is crucial to understanding how the gut transitions from healthy to diseased. Mathematical and computational modelling provide valuable frameworks in which different aspects of crypt morphogenesis can be investigated in a systematic and detailed manner. However, each model comes with its own set of assumptions, and, consequently, its own set of strengths and limitations. At present, no single model captures all the important aspects of the crypt. However, by exploring different aspects of the crypt within a unified continuum mechanics framework, we can gain further insight into the role of mechanics in shaping crypt morphogenesis and homeostasis.

In this thesis, we aim to address three particular questions:

1. **What drives the initial formation of crypts?** Moreover, what is the impact of material heterogeneities on both the initial onset of crypt formation, and its subsequent evolution? To answer these questions, we will consider the crypt in the context of mechanical pattern formation and analyse the buckling and post-buckled behaviour of an idealised crypt model.

2. **How does the crypt generate a narrow, highly-invaginated morphology?** From a modelling perspective, what are the essential modelling choices that are needed to replicate these observed morphologies? These modelling choices must also capture the underlying processes—which may be of biological, chemical, or a mechanical nature—governing crypt morphogenesis.

3. **How is the crypt's unique growth structure generated and subsequently maintained?** In particular, can we replicate the unique growth structure using mechanical models? Consequently, can we use these mechanical models to identify the essential conditions needed for homeostasis in the crypt?

1.7 Thesis structure

This thesis is structured as follows. In Chapter 2, we consider a planar morphoelastic rod tethered to an elastic foundation as an abstracted model for a buckling crypt. We perform a comprehensive post-buckling analysis to understand how material parameters affect growth-induced pattern forming, particularly when spatial heterogeneity is considered. Following this, in Chapter 3, we develop several new models for the processes that play an important role in crypt morphogenesis and homeostasis (as well as other epithelial structures) and adapt pre-existing models from the literature. Through numerical simulation, we investigate the effect of these different models on the growth evolution and morphologies. Then, in Chapter 4, we specialise the morphoelastic rod framework to that of a crypt, and investigate how the crypt's unique growth structure arises and is maintained in homeostasis. We close with a discussion of the main results and future extensions in Chapter 5.

1.8 List of publications

Parts of Chapter 1 have been used in a literature review article, which has been accepted for publication [3]. A significant portion of Chapter 2 and Appendix A has been published in Almet et al. [2].

2

Post-buckling behaviour of a morphoelastic rod

2.1 Introduction

In this chapter, we treat crypt formation during morphogenesis as a buckling problem, investigating how growth can lead to mechanical pattern formation. We consider a 1D model system of a growing planar rod on an elastic foundation, serving as an abstracted framework for the intestinal crypt. The rod is subject to growth in the axial direction and clamped boundary conditions, which drive buckling at a critical growth. We use the morphoelastic rod framework originally presented in Moulton et al. [120] and outlined in Section 1.5 to extend the results of Edwards and Chapman [56] and Nelson et al. [124] and analyse unexplored features that are of general relevance. A focal point for our analysis is the behaviour of the crypt beyond the initial buckling.

We aim to extend previous analyses in two main ways. First, we aim to extend the previous linear stability analyses, which predicts the onset of buckling, and perform a weakly nonlinear analysis, considering growth evolution well beyond the onset of buckling. In other words, we are interested in the post-buckled behaviour of the rod, particularly at large deformations. By analysing the rod growth at large deformations, we can begin to understand how varying model parameters,

such as the foundation stiffness or rod length, impact the resulting morphology. We will show that the system undergoes a pitchfork bifurcation at the onset of buckling, which depends on two parameters that quantify the finite length of the rod and the stiffness of the foundation. Second, we investigate how both the buckling and post-buckling behaviour changes in the presence of spatial heterogeneity in material properties, obtaining explicit relations for how the pitchfork bifurcation that arises is impacted by heterogeneity, and exploring the shape evolution in the nonlinear post-buckled regime.

Both of these features—large deformation beyond buckling and heterogeneity—pose significant mathematical challenges. To capture post-buckling behaviour requires analysis of a nonlinear system of equations, as opposed to the linear stability analysis that can be used to detect buckling. Furthermore, including heterogeneity complicates the use of many analytical tools, either rendering the system analytically intractable or complicating attempts to unfold bifurcations. Here, rather than rely fully on computational techniques, our approach is to analyse post-buckling behaviour and the effect of heterogeneity through a combination of a weakly nonlinear analysis and numerical solution. This approach yields a broad understanding of the role of heterogeneities in growth, material properties, and adhesion, and reveals features of post-buckling pattern formation not described in previous analyses.

The remainder of this chapter is structured as follows. In Section 2, we outline the framework of a planar morphoelastic rod tethered to an elastic foundation. Then, in Section 3 we summarise the linear stability analysis before extending to a weakly nonlinear analysis. The results of the weakly nonlinear analysis and numerical analysis of the full nonlinear model are presented in Section 4, first in a homogeneous setting, then with the addition of different material heterogeneities. Finally, we close by discussing the implications of our results and directions for future model extensions that we will consider in Chapter 3.

2.2 Model setup

As a model system to investigate post-buckling in growing slender structures, we consider in this paper an extensible and unshearable planar rod in quasi-static mechanical equilibrium. The rod is constrained geometrically by clamped-clamped boundary conditions, and is also adhered to an elastic (Winkler) foundation. Growth of the rod is modelled under the morphoelastic rod framework that we described in Section 1.5.

Let the rod's centerline be given by (x, y), and let θ denote the angle between the tangent vector, $\mathbf{d}_3 = \cos\theta \mathbf{e}_x + \sin\theta \mathbf{e}_y$, and the x-axis. This is expressed by

$$\frac{\partial x}{\partial S_0} = \alpha\gamma \cos\theta, \qquad \frac{\partial y}{\partial S_0} = \alpha\gamma \sin\theta, \tag{2.1}$$

(The scale factor $\alpha\gamma$ accounts for the fact that we parametrise the system by the initial arclength parameter S_0, as opposed to the current arclength parameter s.) Defining the resultant force and moment in the rod by $\mathbf{n} = n_x\mathbf{e}_x + n_y\mathbf{e}_y$ and $\mathbf{m} = m\mathbf{e}_z$, the balance of linear and angular momentum give

$$\frac{\partial n_x}{\partial S_0} + \gamma f_x = 0, \qquad \frac{\partial n_y}{\partial S_0} + \gamma f_x = 0, \tag{2.2}$$

$$\frac{\partial m}{\partial S_0} + \alpha\gamma(n_y \cos\theta - n_x \sin\theta) = 0. \tag{2.3}$$

Here $\mathbf{f} = f_x\mathbf{e}_x + f_y\mathbf{e}_y$ is the external body force, which is assumed to be solely due to the underlying foundation.

To this system we add a constitutive equation relating moment to flexure:

$$m = \frac{EI}{\gamma}\frac{\partial\theta}{\partial S_0}, \tag{2.4}$$

The parameter E is the Young's modulus of the rod, and is taken for now to be constant, and I denotes the (second) moment of inertia. For an extensible rod, we take the axial stress to be related to the elastic stretch α via a linear constitutive relation

$$n_x \cos\theta + n_y \sin\theta = EA(\alpha - 1), \tag{2.5}$$

where A is the cross-sectional area of the rod.

The foundation is assumed to be a Winkler foundation occupying an interval along the x-axis, as is the rod. Initially the foundation is a distance y_0 from the rod centreline and the rod is glued to the x-axis; that is, a point $(S_0, 0)$ along the x-axis is attached to a point (S_0, y_0) on the rod. We can set $y_0 = 0$ without loss of generality. No remodelling takes place, so these two points are still connected in the reference (grown) configuration, and are now at $(S/\gamma, 0)$ and (x, y) respectively. Therefore the body force acting on the rod (as a force per initial length) is

$$\mathbf{f} = f_x \mathbf{e}_x + f_y \mathbf{e}_y = -\frac{Ek_f}{\gamma} \left[(x - S_0)\mathbf{e}_x + y\mathbf{e}_y \right], \tag{2.6}$$

where we assume the foundation stiffness is proportional to that of the rod, with the dimensionless positive parameter k_f comparing the stiffness of the foundation to that of the rod. The factor of $1/\gamma$ indicates that the body force is parametrised with respect to the initial configuration, and that no remodelling occurs after growth.

The system is closed with the clamped boundary conditions at $S_0 = 0$ and L_0^*:

$$x(0) = 0, \quad x(L_0^*) = L_0^*, \qquad y(0) = y(L_0^*) = 0, \qquad \theta(0) = \theta(L_0^*) = 0. \tag{2.7}$$

2.2.1 Non-dimensionalisation

Next, we non-dimensionalise the system using the standard Kirchhoff scaling [40, 76, 77] and circumflexes to denote non-dimensional quantities:

$$(S_0, x, y) = (A/I)^{1/2} \left(\widehat{S}_0, \widehat{x}, \widehat{y} \right), \quad (n_x, n_y) = EA \left(\widehat{n}_x, \widehat{n}_y \right), \quad m = E(AI)^{1/2} \widehat{m}. \tag{2.8}$$

Dropping the circumflexes of independent and dependent variables for notational convenience, Equations (2.1)–(2.3) simplify to

$$\frac{\partial x}{\partial S_0} = \alpha\gamma \cos\theta, \qquad \frac{\partial y}{\partial S_0} = \alpha\gamma \sin\theta, \tag{2.9}$$

$$\frac{\partial n_x}{\partial S_0} = k(x - S_0), \qquad \frac{\partial n_y}{\partial S_0} = ky, \tag{2.10}$$

$$\frac{\partial \theta}{\partial S_0} = \gamma m, \qquad \frac{\partial m}{\partial S_0} + \alpha\gamma(n_y \cos\theta - n_x \sin\theta) = 0. \tag{2.11}$$

The constitutive law for extensibility now reads

$$n_x \cos\theta + n_y \sin\theta = \alpha - 1. \tag{2.12}$$

The dimensionless boundary conditions are

$$x(0) = 0, \quad x(L_0) = L_0, \qquad y(0) = y(L_0) = 0, \qquad \theta(0) = \theta(L_0) = 0, \tag{2.13}$$

where the remaining (non-dimensional) parameters are

$$L_0 = L_0^*(A/I)^{1/2}, \qquad k = \frac{k_f I}{A^2}. \tag{2.14}$$

Note that the non-dimensional rod length L_0 depends on the ratio of two length characteristics of the rod: its initial total length L_0^* and the thickness, characterised by $(I/A)^{1/2}$. For instance, for a rod with circular cross-section of radius r, we have $I = \pi r^4/4$, $A = \pi r^2$, and hence $L_0 = 2L_0^*/r \gg 1$.

2.3 Stability Analysis

In this section, we present the analytical tools that we will use to investigate the buckling and post-buckling behaviour of the morphoelastic rod. We first adapt and summarise the linear stability analysis from [120], used to calculate the growth bifurcation value, γ^*, before unfolding the bifurcation with a weakly nonlinear analysis.

2.3.1 Linear stability analysis

We first determine the critical growth stretch γ^* and corresponding buckling mode using a linear stability analysis. The calculations in this section are also present in Moulton et al. [120], but are summarised here for completeness and to motivate the weakly nonlinear analysis. Inspecting the system (2.9)–(2.13), for all $\gamma > 1$ there exists a base solution corresponding to a straight, compressed rod; that is, with $\theta \equiv 0$ and the total stretch $\lambda = \alpha\gamma = 1$ (implying an elastic compression $\alpha = 1/\gamma$):

$$x^{(0)} = S_0, \qquad y^{(0)} = 0 \qquad n_x^{(0)} = \frac{1-\gamma}{\gamma}, \qquad n_y^{(0)} = \theta^{(0)} = m^{(0)} = 0. \tag{2.15}$$

Expanding each variable about the base solution so that, for example, $x = x^{(0)} + \delta x^{(1)} + O(\delta^2)$, where δ is an arbitrary small parameter, and considering $O(\delta)$ terms, leads to the linearised system

$$x^{(1)\prime} - \gamma n_x^{(1)} = 0, \qquad y^{(1)\prime} - \theta^{(1)} = 0, \tag{2.16}$$

$$n_x^{(1)\prime} - k x^{(1)} = 0, \qquad n_y^{(1)\prime} - k y^{(1)} = 0, \tag{2.17}$$

$$\theta^{(1)\prime} - \gamma m^{(1)} = 0, \qquad m^{(1)\prime} + \frac{(\gamma - 1)}{\gamma}\theta^{(1)} + n_y^{(1)} = 0, \tag{2.18}$$

where $' = \partial/\partial S_0$. We observe that $\{x^{(1)}, n_x^{(1)}\}$ are decoupled from $\{y^{(1)}, n_y^{(1)}, m^{(1)}, \theta^{(1)}\}$, and that (2.16)-(2.18) can be expressed as two ordinary differential equations for $x^{(1)}$ and $y^{(1)}$,

$$\mathcal{L}x^{(1)} := x^{(1)\prime\prime} - b^2 x^{(1)} = 0, \tag{2.19}$$

$$\mathcal{M}y^{(1)} := y^{(1)\prime\prime\prime\prime} + 2a y^{(1)\prime\prime} + b^2 y^{(1)} = 0, \tag{2.20}$$

where the coefficients a and b are defined by

$$a = \frac{\gamma - 1}{2}, \qquad b = (k\gamma)^{\frac{1}{2}}. \tag{2.21}$$

Solving Equation (2.19) subject to $x^{(1)}(0) = x^{(1)}(L_0) = 0$ leads to the trivial solution $x^{(1)} \equiv 0$ (and subsequently $n_x^{(1)} \equiv 0$). Turning to Equation (2.20), our linearised boundary conditions are

$$y^{(1)} = y^{(1)\prime} = 0 \qquad \text{at} \qquad S_0 = 0,\ L_0. \tag{2.22}$$

Seeking solutions of the form $y^{(1)} \sim e^{i\omega S_0}$ (valid on an infinite domain) leads to the following oscillation frequencies

$$\omega_{\pm}^2 = a \pm \left(a^2 - b^2\right)^{\frac{1}{2}}. \tag{2.23}$$

We remark that in order for non-damped oscillations to exist over the (finite) domain, we require $a \geq b$. Applying the four boundary conditions for $y^{(1)}$, specified by Equation (2.22), yields the solution

$$y^{(1)} = C_1 \left[\cos(\omega_+ S_0) - \cos(\omega_- S_0) + C_2 \sin(\omega_+ S_0) + C_3 \sin(\omega_- S_0)\right], \tag{2.24}$$

where the constants C_2 and C_3 are given by

$$C_2 = \frac{\omega_-(\cos(L_0\omega_-) - \cos(L_0\omega_+))}{\omega_- \sin(L_0\omega_+) - \omega_+ \sin(L_0\omega_-)}, \qquad C_3 = \frac{\omega_+(\cos(L_0\omega_+) - \cos(L_0\omega_-))}{\omega_- \sin(L_0\omega_+) - \omega_+ \sin(L_0\omega_-)}, \tag{2.25}$$

and the critical growth value γ^* must satisfy the relation

$$a \sin(L_0\omega_+) \sin(L_0\omega_-) + b \cos(L_0\omega_+) \cos(L_0\omega_-) - b = 0. \tag{2.26}$$

If (2.26) is satisfied, then the buckled solution is given by (2.24), but with arbitrary constant C_1. For later convenience, we thus define the function $\hat{y}$ to be the determined part of this function, i.e.

$$\hat{y} := C_1^{-1} y^{(1)}. \tag{2.27}$$

The smallest value of $\gamma > 1$ that satisfies (2.26) occurs when $a = b$ (and, hence, $\omega_1 = \omega_2$), giving

$$\gamma^*_{\text{inf}} = 1 + 2k + 2\left(k + k^2\right)^{\frac{1}{2}}, \tag{2.28}$$

where $k = k_f I/A^2$. Although it appears that γ^*_{inf} does not vary with any length scale, this is not entirely true. For example, for a rod with circular cross-section of radius r, then from (2.14), $k \propto k_f$. However, for a rectangular cross-section with height h and width w, $k \propto k_f h/w$. Additionally, this value of γ only leads to oscillations if the rod length L_0 is infinite, and results in the trivial solution over a finite domain. Therefore the critical growth value γ^* is the first value of $\gamma > \gamma^*_{\text{inf}}$ that solves (2.26).

2.3.2 Weakly nonlinear analysis

Having summarised the above results from [120] that are key for us, we now carry out a weakly nonlinear analysis. For a given root of (2.26), the buckled solution is only determined to within the arbitrary constant C_1. In order to understand the behaviour of the buckled rod as it continues to grow, it is necessary to determine how the buckling amplitude C_1 depends on γ, which we accomplish through a weakly nonlinear analysis. We unfold the bifurcation by introducing the ansatz

$$\gamma = \gamma^* + \varepsilon\gamma^{(1)}, \tag{2.29}$$

where ε is a fixed small parameter (whereas δ is small, but arbitrary) and $\gamma^{(1)} = O(1)$ is a control parameter describing the proximity to the growth bifurcation point γ^*. Substituting (2.29) into (2.11), re-expanding θ and m and retaining higher-order terms in θ reveals that the nonlinearities will be balanced by growth if $\varepsilon = O(\delta^2)$. Setting $\varepsilon = \delta^2$ and re-expanding our variables about the trivial solution (2.15) as a power series in δ leads to the following system of differential equations for each order $O(\delta^n)$, $n \geq 1$,

$$x^{(n)\prime} - \gamma^* n_x^{(n)} = h_{x^{(n)}}, \qquad y^{(n)\prime} - \theta^{(n)} = h_{y^{(n)}}, \tag{2.30}$$

$$n_x^{(n)\prime} - k x^{(n)} = h_{n_x^{(n)}}, \qquad n_y^{(n)\prime} - k y^{(n)} = h_{n_y^{(n)}}, \tag{2.31}$$

$$\theta^{(n)\prime} - \gamma^* m^{(n)} = h_{\theta^{(n)}}, \qquad m^{(n)\prime} + \frac{(\gamma^* - 1)}{\gamma^*}\theta^{(n)} + n_y^{(n)} = h_{m^{(n)}}. \tag{2.32}$$

Here, the functions $h_{x^{(n)}}, h_{y^{(n)}}, h_{n_x^{(n)}}, h_{n_y^{(n)}}, h_{\theta^{(n)}}$, and $h_{m^{(n)}}$ denote inhomogeneities due to lower order terms. As was the case in Section 2.3.1, the system decouples into two linear operators acting on $x^{(n)}$ and $y^{(n)}$,

$$\mathcal{L}x^{(n)} = h'_{x^{(n)}} + \gamma^* h_{n_x^{(n)}} =: H_{x^{(n)}}, \tag{2.33}$$

$$\mathcal{M}y^{(n)} = h'''_{y^{(n)}} + 2a h'_{y^{(n)}} + h''_{\theta^{(n)}} + \gamma^*\left(h'_{m^{(n)}} - h_{n_y^{(n)}}\right) =: H_{y^{(n)}}. \tag{2.34}$$

For general $n \geq 1$, the boundary conditions for $y^{(n)}$ are now given by

$$y^{(n)} = 0, \qquad y^{(n)\prime} = h_{y^{(n)}} \qquad \text{at} \qquad S_0 = 0,\ L_0. \tag{2.35}$$

Observe that the homogeneous problems, (2.19) and (2.20), along with the boundary conditions—$x^{(1)}(0) = x^{(1)}(L_0) = 0$ and (2.22), respectively—are self-adjoint. When $n = 1$, we recover the linearised system described by Equations (2.16)–(2.18), i.e. $H_{x^{(1)}} = H_{y^{(1)}} \equiv 0$. At $n = 2$ we find that $H_{y^{(2)}} \equiv 0$, giving us no further information on the buckling amplitude C_1; however, as $x^{(1)}$ is trivial, the Fredholm Alternative Theorem is immediately satisfied thus a non-trivial solution for $x^{(2)}$ exists. Hence, we must consider $O(\delta^3)$ terms to obtain the amplitude equation for C_1. This leads us to consider the inhomogeneities $H_{y^{(3)}}$, which can be expressed solely in terms of

$x^{(2)}$ and $y^{(1)}$ and their derivatives. Then, by the Fredholm Alternative Theorem, a solution for $y^{(3)}$ exists if and only if the following solvability condition is satisfied:

$$\int_0^{L_0} \left(\mathcal{M}y^{(3)}\right) \widehat{y}\, dS_0 = \int_0^{L_0} \left(H_{y^{(3)}}\right) \widehat{y}\, dS_0 = 0, \tag{2.36}$$

where $\hat{y}$ solves the homogeneous problem, defined by (2.27). The only unknown quantity in (2.36) is the coefficient C_1; hence this solvability condition for $y^{(3)}$ provides a relation between the buckling amplitude C_1 and the distance from the critical buckling growth parameter, expressed by $\gamma^{(1)}$. Simplifying this condition (see Section A.1) leads us to deduce that

$$C_1 \left(K_1 C_1^2 + K_2 \gamma^{(1)}\right) = 0. \tag{2.37}$$

The constants K_1, K_2 are tedious to compute analytically, but nevertheless only depend only on the material parameters k and L_0, and through them the critical growth γ^*. It can also be shown (Section A.1) that $K_2 > 0$ for all parameter choices. Equation (2.37) shows that the system exhibits a pitchfork bifurcation, a known property of similar systems [90, 124]. The three branches of the pitchfork are given by

$$C_1 = 0, \qquad C_1^2 = -\frac{K_2}{K_1}\gamma^{(1)}. \tag{2.38}$$

This suggests that the bifurcation will be supercritical if $K_1 < 0$, and subcritical if $K_1 > 0$. Dynamical stability analysis of these solution branches confirms that this is indeed the case; the details of this analysis can be found in Appendix A.4. In the next section, we explore the dependence of K_1 on k and L_0 and its effect on the buckling and post-buckling behaviour.

2.4 Buckling and post-buckling behaviour

Having established a relationship for the post-buckling amplitude, we now explore the effect of material parameters and heterogeneity on the buckling and post-buckling behaviour. First we examine the form of bifurcation in a homogeneous setting, effectively by analysing how the critical buckling growth γ^*, the buckling mode, and the pitchfork constants K_1 and K_2 vary with the two free parameters in the

non-dimensional system, L_0 and k. We then adapt the weakly nonlinear analysis to incorporate heterogeneity and investigate the impact of non-uniformity in foundation stiffness, rod stiffness, and growth. In each case, we complement the analytical work by solving the full nonlinear system (2.9)–(2.13), using the numerical package `AUTO-07p` [49]. `AUTO-07p` uses pseudo-arclength continuation to trace solution families and solves the system with an adaptive polynomial collocation method.

2.4.1 Effect of length and foundation stiffness

In Figures 2.1–2.2, we plot bifurcation diagrams for varying values of the dimensionless foundation stiffness k and the dimensionless rod length L_0, respectively, for increasing growth. The horizontal axis in each case is the growth parameter γ, and the vertical axis plots the non-trivial branches, $\pm\|y\| := \pm\max_{S_0}|y(S_0)|$, which is closely related to the value of the constant C_1 but more representative of the post-buckling amplitude. The solid lines are determined from the weakly nonlinear analysis, while the dashed lines are numerical results. We also plot the buckled shape $(x(S_0), y(S_0))$ at the specified points for each branch.

As k increases, the buckling occurs for increased mode number, reflecting the energy trade-off that as the foundation stiffness is increased, a large amplitude is penalised more by a high foundation energy, and hence higher bending energy is sacrificed to have a lower amplitude. An increased value of k also leads to an increase in γ^*, which shows that the foundation is serving to stabilise the rod against buckling. This can again be understood in terms of an energy trade-off, but in this case it is the compressive energy in the grown but unbuckled state that is being sacrificed. It is important to note that this feature could not occur in an inextensible rod, for which the trivial state does not exist for any $\gamma > 1$.

Considering length L_0 leads to similar changes in both critical buckling growth and mode number. However, while the buckling mode increases for increasing length, the critical buckling growth *decreases*. Recalling the scaling $L_0 = L_0^*(A/I)^{1/2}$, this reflects the notion that a short or thick rod can endure more growth before buckling,

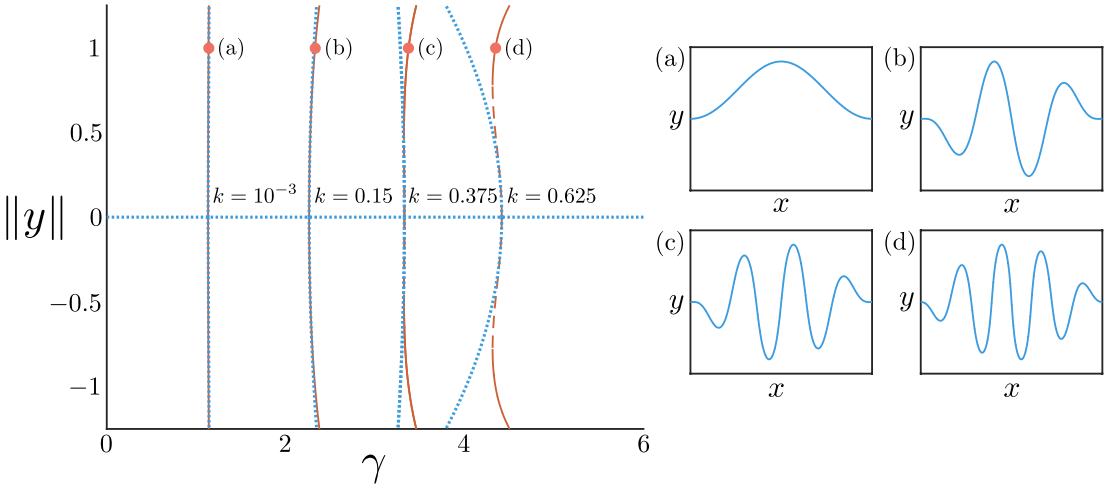

Figure 2.1: Bifurcation diagram for varying foundation stiffness. Bifurcation diagram plotting $\pm\|y\| = \pm\max_{S_0}|y(S_0)|$ against γ from weakly nonlinear analysis (blue, dotted lines) and numerical continuation (red) of the full model (2.9)–(2.13); stable solutions are marked with solid lines, while dashed lines represent unstable solutions. Each non-trivial branch denotes a continuation in γ for a fixed value of k. The buckled shape $(x(S_0), y(S_0))$ is plotted at the point $\|y\| = 1$ (orange dot) for (a) $k = 10^{-3}$, (b) $k = 0.15$, (c) $k = 0.375$, and (d) $k = 0.625$. The dimensionless rod length is fixed to be $L_0 = 20$ for all cases.

and will buckle at lower mode. We note also that as $L_0 \to \infty$, $\gamma^* \to \gamma^*_{\text{inf}}$, the critical growth value for buckling on an infinite domain (2.28).

Perhaps most notable is the transition from supercritical to subcritical bifurcation evident in both diagrams. We find initially that subcritical bifurcations occur for large enough k or small enough L_0. We find through numerical continuation that the subcritical branches then fold back, a feature not captured by the weakly nonlinear analysis at order $O(\delta^3)$. A linear stability analysis (see Section A.4) confirms that the portion of the subcritical branch before folding back is unstable, while the portion after the fold-back is stable. (As would be expected, the curved branches are stable in the supercritical case.) This implies that a subcritical bifurcation signifies a discontinuous jump from the trivial flat state to the finite amplitude stable branch, as well as the presence of a hysteresis loop if γ is subsequently decreased. Moreover, as we will show in the next section, multiple transitions between supercritical and subcritical pitchfork bifurcations can actually occur.

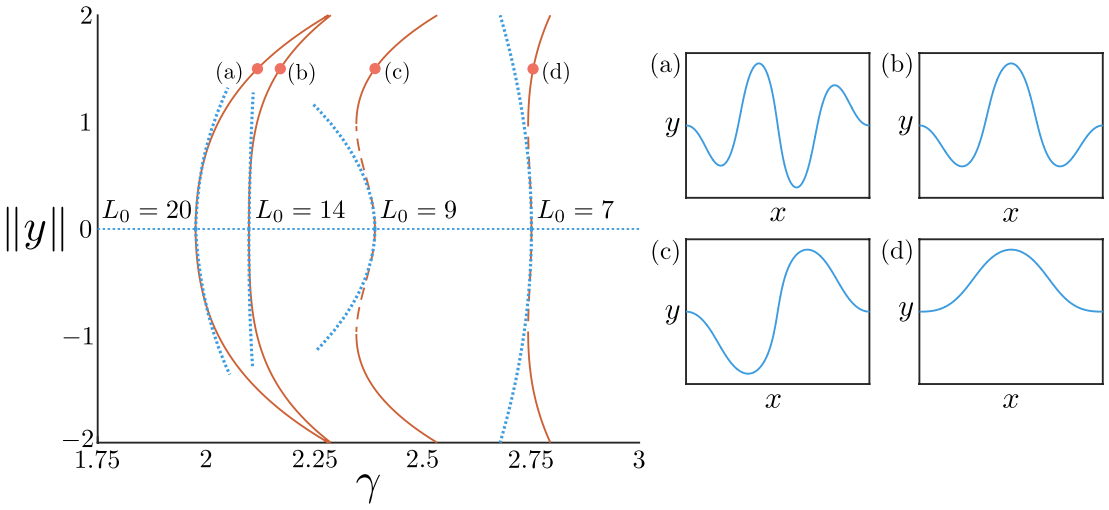

Figure 2.2: Bifurcation diagram for varying rod length. Bifurcation diagram plotting $\pm\|y\| = \pm\max_{S_0}|y(S_0)|$ against γ from weakly nonlinear analysis (blue, dotted lines) and numerical continuation (red) of the full model (2.9)–(2.13); stable and unstable solutions are marked with solid and dashed lines respectively. The buckled shape $(x(S_0), y(S_0))$ is plotted at the point $\|y\| = 1.5$ (orange dot) for (a) $L_0 = 20$, (b) $L_0 = 14$, (c) $L_0 = 9$, and (d) $L_0 = 7$. The dimensionless foundation stiffness k is set to $k = 0.1$ for all cases.

2.4.2 Locating the pitchfork transition

For given parameters k and L_0, the weakly nonlinear analysis enables us to determine the type of pitchfork bifurcation simply by computing the sign of K_1. Figure 2.3 shows the regions in k-L_0 space where supercritical and subcritical pitchforks occur. Note that despite having an explicit expression for K_1, the actual computation of its value was done numerically as it requires root finding for the eigenvalue γ^*. Hence, to produce Figure 2.3 we computed K_1 over a discrete grid in the k-L_0 plane. The transition boundary was then verified at several points through numerical path following in `AUTO-07p`.

Unexpectedly, we do not find a simple monotonic transition boundary, as seen in similar studies [89], but rather an intricate pattern with an oscillatory structure. This structure implies that multiple transitions between super- and subcritical buckling can occur for a fixed k and varying L_0 (or vice versa); that is, simply increasing the length of the rod monotonically can create repeated transitions between super- and subcritical bifurcation. For an infinite rod, the transition can

be computed as $k \approx 0.38196$ (see Section A.2); this point is included as a dashed, horizontal line in Figure 2.3, and it appears that as $L_0 \to \infty$, the oscillations dampen and the transition boundary approaches this constant value. By contrast, as L_0 decreases, the oscillation amplitude increases, although the slenderness assumption of the rod breaks down as $L_0 \sim O(1)$.

This intricate structure, which to our knowledge has not been reported before, has interesting potential implications. The defining characteristic of the subcritical regime is a discontinuous bifurcation: a small change in growth beyond the critical value leads to a potentially large jump in amplitude; while the bifurcation is smooth in the supercritical regime. Hence, the fact that the transition boundary oscillates in the parameter space implies a sort of non-robustness to the instability. The effects of subcritical bifurcations have been studied in the biological contexts of biochemical Turing patterns [26], epidemics [149], and even neuroscience [108]. The phenomenon seems to be less-well studied in mechanical models of morphogenesis, despite clear analogies with engineering structures where subcritical buckling is well-documented, e.g. [113]. This may be in part due to the difficulty in observing the actual instability event in biological morphogenesis, hence classifying the form of bifurcation is not straightforward. Subcritical bifurcation in a mechanical context has however been observed in a model of the buckling of a lipid bilayer vesicle between two plates [144]. It remains an interesting open question whether or not the transition region in Fig. 2.3 could be physically realised. Of course the model system presented here is highly idealised, and the complexities of the structure may either not exist in a real system or be detectable within experimental error; nevertheless the framework could in principle be tailored to a particular biological setting to explore the form of bifurcation in greater detail.

2.4.3 Parameter heterogeneity

Thus far, we have assumed spatial homogeneity in model parameters. However, in many biological systems, heterogeneities are inherent in the system. This raises the question of how a given heterogeneity is manifest in the buckled pattern. To explore

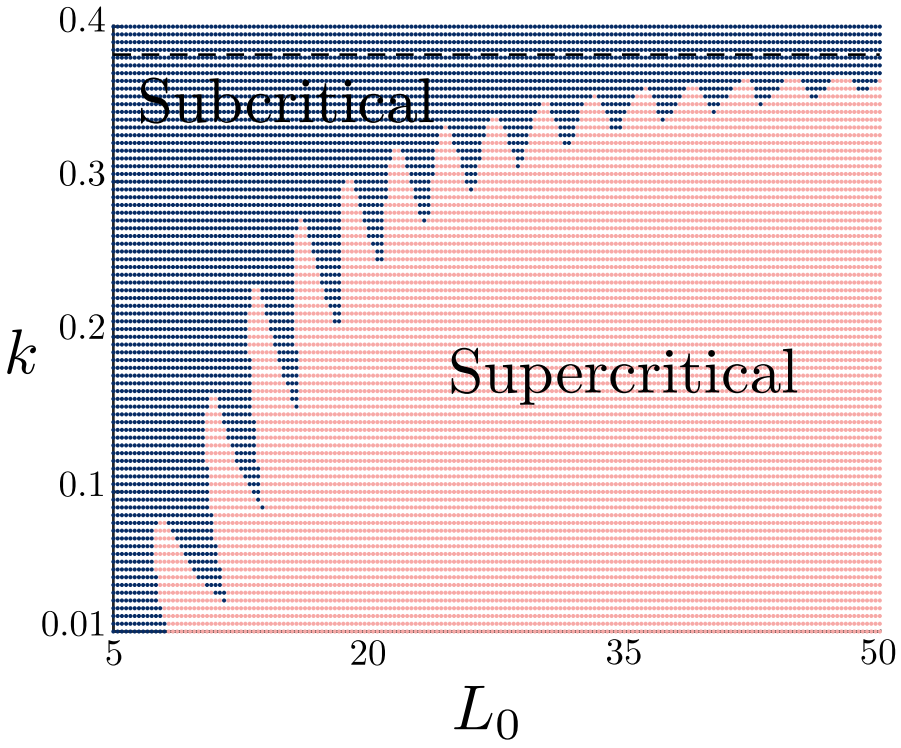

Figure 2.3: Phase diagram of pitchfork bifurcations. The regions have been determined by computing the sign of K_1 at each point on a discretised grid of k and L_0. Subcritical pitchfork bifurcations ($K_1 > 0$) have been labelled with dark blue crosses, while supercritical pitchfork bifurcations are labelled with an orange dot ($K_1 < 0$). The dashed line corresponds to the transition value of k in the infinite-length case, $k \approx 0.38196$ (see Appendix A.2).

this, we initially consider three distinct forms of heterogeneity in: the foundation stiffness, the rod stiffness, and the growth. Each heterogeneity has a clear biological interpretation. For example, in the intestinal crypts, these heterogeneities would correspond to: the different types of extracellular matrix secreted by the cells comprising the underlying tissue stroma (foundation heterogeneity), the mechanical properties of epithelial cells in the crypt (stiffness heterogeneity), and the variations in the proliferative capacity of these cells (growth heterogeneity). In order to understand the effect of each type of spatial heterogeneity, we examine heterogeneity for each parameter in isolation.

With parameter heterogeneity, it becomes increasingly difficult to obtain analytically tractable results with a weakly nonlinear analysis, especially if the amplitude of the heterogeneity is pronounced. Nevertheless, when the parameters are close

to homogeneous, we can extend the weakly nonlinear analysis and, in particular, ask how the heterogeneity impacts the pitchfork bifurcations observed in the homogeneous case. We complement this analysis with numerical solutions of the full system defined by Equations (2.9)–(2.13). For computational convenience, heterogeneity is incorporated via a sequence of numerical continuations in the growth and heterogeneity parameters.

We model heterogeneity as a spatial deviation from a baseline homogeneous state. In general, for an arbitrary parameter μ, we consider

$$\mu(S_0) = \mu_0 + \widehat{\epsilon}\mu_0\xi(S_0). \tag{2.39}$$

Here, the constant μ_0 corresponds to the baseline homogeneous value, and the function $\xi(S_0)$ captures the spatial variation, modulated by the amplitude factor $\widehat{\epsilon}$ and constrained only by the requirement that $\mu \geq 0$.

With heterogeneity introduced, the weakly nonlinear analysis can be viewed as a two-parameter unfolding, both in the distance from the critical buckling growth, via $\gamma = \gamma^* + \varepsilon\gamma^{(1)}$, and in the distance from homogeneity, characterised by $\widehat{\epsilon}$. We are thus faced with balancing three small parameters: ε, $\widehat{\epsilon}$, and the order of the expanded variables, which we denoted by δ, e.g. as in $y = \delta y^{(1)} + O(\delta^2)$. In the homogeneous case the correct balance is given by $\epsilon = \delta^2$. With $\widehat{\epsilon} > 0$, numerous balances could be sought, and a full analysis of the two-parameter unfolding is beyond the scope of this paper. Our approach involves starting from homogeneity, and increasing the order of $\widehat{\epsilon}$ to see when and how it first impacts on buckling. Hence, we again take $\epsilon = \delta^2$, and consider $\widehat{\epsilon} = \delta^\beta\eta$, with $\beta > 1$ and η an $O(1)$ control parameter.

The three cases we wish to consider for heterogeneity are:

- **Foundation heterogeneity**, for which $\mu = k$;
- **Rod stiffness heterogeneity**, for which $\mu = E$, the Young's modulus[1];

[1] In this case heterogeneity is incorporated prior to non-dimensionalization, and scaling proceeds using the baseline value. Note also that we do not vary the Young's modulus E present in the definition of the foundation force (2.6), so that we may distinguish the material properties in the foundation from material properties of the rod itself.

- **Growth heterogeneity**, for which $\mu = \gamma$.

Perturbing each of these parameters via (2.39) has a similar effect on the weakly nonlinear analysis. In each case, it is easy to show that for $\beta > 2$, the heterogeneity does not affect the weakly nonlinear analysis up to $O(\delta^3)$, and therefore does not affect the buckling amplitude C_1. Consequently, the bifurcation relation (2.38) is unaffected. When $\beta = 2$, the heterogeneity first has an impact (up to $O(\delta^3)$) and, hence, it is for this case that we adapt the analysis. At $O(\delta^3)$, the corrective term $y^{(3)}$ now satisfies

$$\mathcal{M}y^{(3)} = H^{\text{old}}_{y^{(3)}} + \eta H^{\text{new}}_{y^{(3)}}. \tag{2.40}$$

The first term on the right hand side, $H^{\text{old}}_{y^{(3)}}$, corresponds to the inhomogeneities in the homogeneous case, while $H^{\text{new}}_{y^{(3)}}$ describes the effects of the heterogeneity (2.39).

For each parameter considered, evaluating the solvability condition (2.36) leads to a new equation for C_1:

$$C_1\left(K_1 C_1^2 + K_2\gamma^{(1)} + K_3\eta\right) = 0. \tag{2.41}$$

The constants K_1 and K_2 are identical those in Equation (2.37) (see Appendix A.1). The heterogeneity is fully encapsulated in the term K_3, defined straightforwardly by

$$K_3 = C_1^{-1}\int_0^{L_0} H^{\text{new}}_{y^{(3)}}\ \widehat{y}\ dS_0. \tag{2.42}$$

The heterogeneous model, hence, undergoes a translated pitchfork bifurcation, where the branches are given by

$$C_1 = 0, \qquad C_1^2 = -\frac{K_2}{K_1}\gamma^{(1)} - \frac{K_3}{K_1}\eta. \tag{2.43}$$

Observe that since ξ appears in $H^{\text{new}}_{y^{(3)}}$ only, and hence in K_3 only, it does not affect the type of pitchfork that occurs, but merely translates it. That is, setting $C_1 = 0$ in the non-trivial branch gives $\gamma^{(1)} = -(K_3/K_2)\eta$; recalling (2.29), the critical growth γ^* is now shifted to

$$\gamma^* = \gamma_0^* - \delta^2\frac{K_3}{K_2}\eta, \tag{2.44}$$

where γ_0^* is the critical growth stretch for the rod in a homogeneous setting, as determined from the linear stability analysis in Section 2.3.1. Hence, we see that the material heterogeneity (2.39) results in an $\mathcal{O}(\delta^2)$ shift in γ^*. Since $K_2 > 0$, the direction and degree of the shift is determined by K_3. Generally, K_3 provides the 'metric' for whether the heterogeneity has a net effect of strengthening or weakening the effect of the material parameter.

In order to investigate greater amplitudes of heterogeneity and the post-buckling shape evolution, we perform numerical continuation on the full model. As an illustrative example, we apply the same form of heterogeneity for each of the three parameters: $\xi(S_0) = \cos(2\pi S_0/L_0)$ and $\widehat{\epsilon} = 0.9$, characterising a significant decrease in the middle region and increase in the outer regions. Figure 2.4 depicts the resultant rod shapes. As evident in Figure 2.4, the heterogeneity has a markedly different effect for each material parameter.

Foundation stiffness heterogeneity Here, the modified foundation is softer in the middle and stiffer near the endpoints, causing a significant increase in amplitude in the middle of the rod, where the resistance to deformation is weaker. This phenomenon can be generally understood and quantified by applying the weakly nonlinear analysis. Note from Equation (2.20) that the operator M on the left hand side of Equation (2.40) is the linearised (beam) equation, i.e. the vertical force balance for an extensible rod upon a foundation. Consequently, the term $H^{\text{new}}_{y^{(3)}}$ captures additional forces due to the imposed heterogeneity. In the case $k(S_0) = k_0(1 + \delta^2\eta\xi(S_0))$, at $O(\delta^3)$ this term takes the particularly simple and instructive form:

$$H^{\text{new}}_{y^{(3)}} = -k_0\gamma^*\xi\ y^{(1)}. \tag{2.45}$$

The heterogeneity thus acts as an amplifying force where $\xi(S_0) < 0$, and a resistive force where $\xi(S_0) > 0$. This is apparent in Figure 2.4(b): the magnitude of $y^{(1)}$ is largest in the middle, with $\xi(S_0) < 0$, reducing the effects of $H^{\text{old}}_{y^{(3)}}$ and leading to an increase in amplitude.

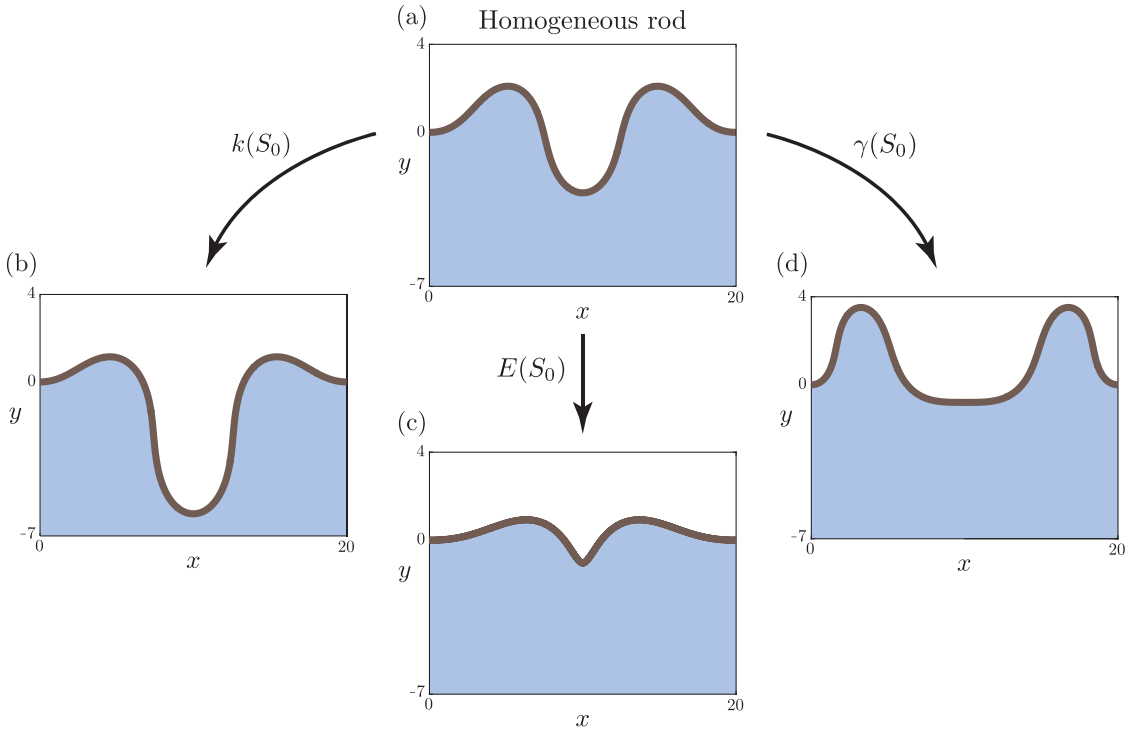

Figure 2.4: The effect of heterogeneity on the post-buckled shape $(x(S_0), y(S_0))$ **and the underlying foundation**. The baseline foundation stiffness k_0 and rod length L_0 have been set to $k_0 = 0.04$ and $L_0 = 20$, respectively. (a) The growth stretch γ (γ_0 for $\gamma(S_0)$) has been continued until $\|y\| = 2.75$ for the homogeneous case. The heterogeneity function $\xi(S_0)$ has been set to $\xi(S_0) = \cos\left(\frac{2\pi S_0}{L_0}\right)$ for each of (b) foundation stiffness heterogeneity $k(S_0)$, (c) rod stiffness heterogeneity $E(S_0)$, and (d) growth heterogeneity $\gamma(S_0)$. The heterogeneity amplitude $\widehat{\epsilon}$ has been continued to $\widehat{\epsilon} = 0.9$ from the homogeneous state ($\widehat{\epsilon} = 0$).

Rod stiffness heterogeneity In the case of rod stiffness, the dominant trend is compression in the middle region, leading to a significant decrease in amplitude and arclength, and formation of a near cusp-like point, reflecting the reduced energy cost of both bending and stretching in the middle region. We have also examined the competing energies within the system: bending versus stretching versus foundation (defined in Appendix A.5). Figure 2.5 shows that both the bending and foundation energy are reduced as $\widehat{\epsilon}$ increases, despite the cusp-like formation, while the stretching energy increases. The total energy remains roughly constant through most of this tradeoff, but eventually, at large values of $\widehat{\epsilon}$, the stretching penalty outweighs the benefit to the bending and foundation energies and a sharp rise in the total energy occurs for $\widehat{\epsilon} \gtrsim 0.7$.

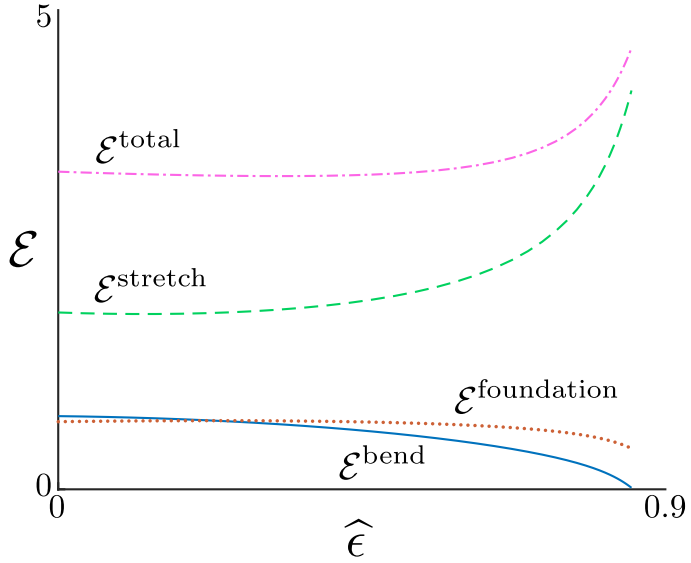

Figure 2.5: Energy plot for heterogeneous rod stiffness. The bending energy $\mathcal{E}^{\text{bend}}$ (blue, solid), stretch energy $\mathcal{E}^{\text{stretch}}$ (green, dashed), $\mathcal{E}^{\text{foundation}}$ (brown, dotted), and total energy $\mathcal{E}^{\text{total}}$ (pink, dot-dashed) have been plotted. The parameters are the same as those in Figure 2.4. We see that $\mathcal{E}^{\text{stretch}}$ increases while $\mathcal{E}^{\text{bend}}$ and $\mathcal{E}^{\text{foundation}}$ decrease for increasing heterogeneity.

Growth heterogeneity In the case of growth heterogeneity, note that for the form of heterogeneity considered, $\xi(S_0) = \cos(2\pi S_0/L_0)$, the *net growth*, defined by

$$\overline{\gamma} = \frac{1}{L_0}\int_0^{L_0} \gamma(S_0)dS_0, \tag{2.46}$$

is unchanged from the homogeneous case, $\gamma(S_0) = \gamma_0$. Thus, for varying $\widehat{\epsilon}$, there is no change in net growth, merely a redistribution of material from the middle region to the sides. Accordingly, Figure 2.4(d) shows a significant change in shape: the middle region flattens while the left and right regions, with increased material, show an increase in amplitude and curvature. The loss of material from the middle also has the effect of increasing the elastic stretch α, resulting in a transition from compression to tension. An intuitive explanation for this can be seen by examining the flat solution (2.15): a growth stretch of $\gamma < 1$ implies that the horizontal force $n_x^{(0)} > 0$, i.e. the rod is in a state of tension. For growth heterogeneity, we observe behaviour in energy that is qualitatively opposite from rod stiffness heterogeneity:

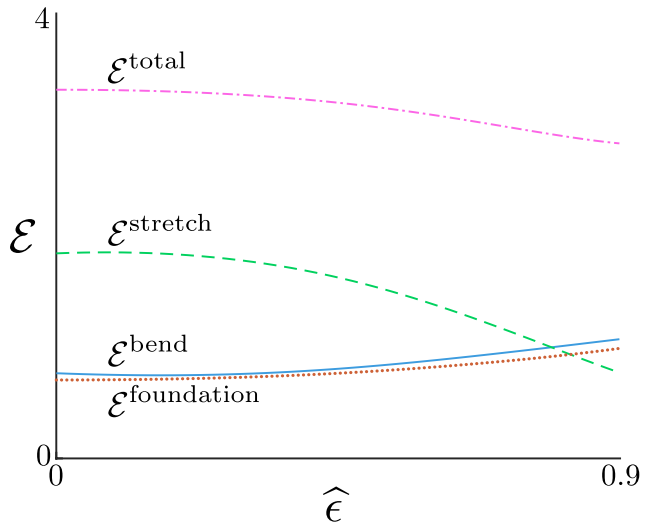

Figure 2.6: The effect of growth heterogeneity on energy for $\xi(S_0) = \cos\left(\frac{2\pi S_0}{L_0}\right)$. The bending energy $\mathcal{E}^{\text{bend}}$ (blue, solid), stretch energy $\mathcal{E}^{\text{stretch}}$ (green, dashed), $\mathcal{E}^{\text{foundation}}$ (brown, dotted), and total energy $\mathcal{E}^{\text{total}}$ (pink, dot-dashed) have been plotted. The parameters are the same as those in Figure 2.4. As growth heterogeneity increases, $\mathcal{E}^{\text{stretch}}$ decreases drastically, with $\mathcal{E}^{\text{bend}}$ and $\mathcal{E}^{\text{foundation}}$ increasing slightly.

as heterogeneity is increased, both bending and foundation energies increase, while stretching and total energies decrease. The flattening of the middle region caused by loss of material to the edges reduces the compressive energy locally, due to the transition to tension in the middle region, while the redistribution of material to the sides leads to a net increase in bending and foundation energy, as shown in Fig. 2.6.

It is worth comparing these results to similar studies. In Nelson et al. [124], bending stiffness heterogeneity and growth heterogeneity were considered. In the case of growth heterogeneity, Nelson et al. concluded that net growth affects the post-buckling behaviour more than heterogeneity, whereas we have found a significant change in morphology due to growth heterogeneity, even with no change in net growth. This discrepancy may be partially due again to the inextensibility assumption present in [124]. More likely though, the behaviour may be attributable to viscous relaxation. Nelson et al. have modelled the foundation as viscoelastic springs, thus incorporating a stress relaxation not present in our model. Indeed, they presented an example (see Fig. 11 of [124]) in which a change in morphology

does initially occur due to growth heterogeneities, but the difference is then lost once stresses are allowed to relax. Some form of viscous relaxation is almost certainly present in development of the colorectal crypt, and incorporating such effects in our framework is the subject of Chapter 3.

The role of extensibility

It is important to note that many of the above trends are reliant on the assumption of rod extensibility. In an inextensible model, axial compression is not permitted, as the arclength is fixed, which is equivalent to the geometric constraint $\alpha \equiv 1$. For explicit comparison, we consider the same stiffness heterogeneity in an inextensible rod. Consequently, only bending is affected by the heterogeneity (2.39). In Figure 2.7, we compare the shape evolution with increasing $\widehat{\epsilon}$ in both inextensible and extensible models, for $\xi(S_0) = \cos(\pi S_0/L_0)$ and $\xi(S_0) = \cos(2\pi S_0/L_0)$. For the inextensible models, we take an equivalent foundation stiffness, $k = 0.04$, but set $\gamma = 1.1$ to obtain a similar initial amplitude. In an inextensible rod, the arclength is fixed and thus the response to heterogeneity is to alter the shape towards aligning points of minimal and maximal curvature with material points of maximal and minimal stiffness, respectively. Hence in Figure 2.7(a) the inextensible rod shifts to have maximal amplitude on the soft region on the right side, whereas the extensible rod (Fig. 2.7(b)) compresses on the right side, thus producing a completely different morphology with minimal amplitude. In Figure 2.7(c), the inextensibility leads to a localisation of curvature in the soft middle region, as opposed to the strong compression in the extensible case, shown in Figure 2.7(d). These simulations illustrate the dramatic effect that extensibility can have on shape morphology and the response to material heterogeneity.

We note that Nelson et al. [124] also considered bending stiffness heterogeneity, finding that localised regions of softened bending stiffness leads to a localisation of buckling. This result is similar to Figure 2.7 for the inextensible case, where the rod shape shifts towards points of softened rod stiffness.

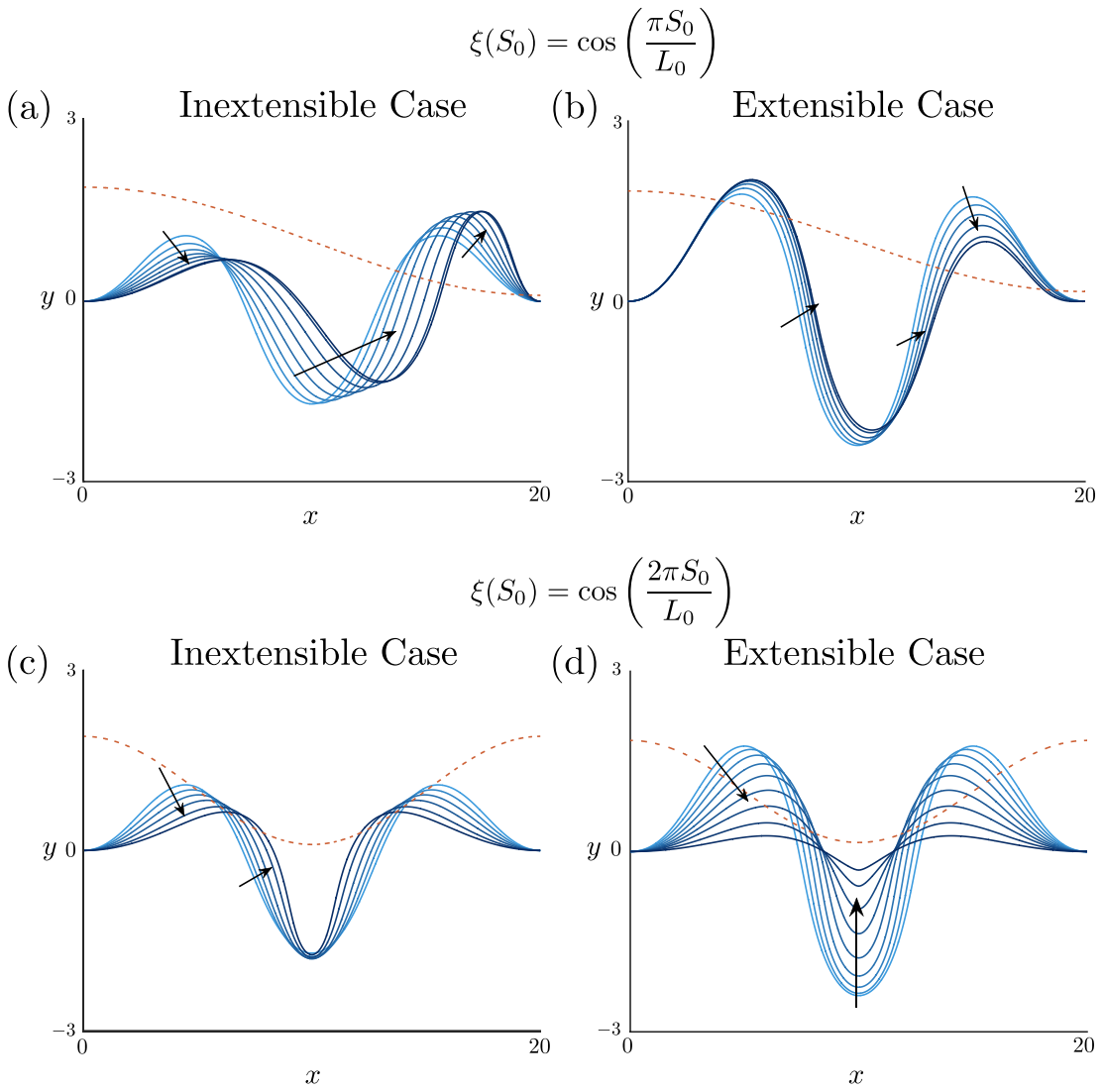

Figure 2.7: The effect of extensibility on rod shape. The specified heterogeneities are (a)–(b) $\xi(S_0) = \cos\left(\frac{\pi S_0}{L_0}\right)$ and (c)–(d) $\xi(S_0) = \cos\left(\frac{2\pi S_0}{L_0}\right)$. The dimensionless foundation stiffness and rod length have been set to $k = 0.04$ and $L_0 = 20$, respectively. The growth parameter γ was set to $\gamma = 1.1$ and $\gamma = 1.8$ for the inextensible and extensible cases respectively. Continuation in $\widehat{\epsilon}$ is over the interval $\widehat{\epsilon} \in [0, 0.85]$. The resulting forms of $E(S_0)$ (brown, dashed line) have also been plotted. Arrows in the plots indicate the evolution of the rod shape (blue, sold lines) in the increasing direction of the continuation parameter, while darker blue lines correspond to higher values of $\widehat{\epsilon}$. When rod stiffness is asymmetric, competition in curvature causes the inextensible rod to redistribute its material more so than the extensible rod. In the symmetric case, extensibility leads to compression at the locations of maximal curvature, which is not seen for the inextensible rod.

Foundation imperfection

The heterogeneities we have considered thus far, while having significant impact on the post-buckling shape evolution, have had a relatively minor effect on the

bifurcation itself, only serving to translate the pitchfork, and by modest amounts. This is in contrast to typical results in a Koiter imperfection sensitivity analysis [4, 90], in which material imperfections may shift the bifurcation to occur at significantly reduced loads and in an imperfect fashion (a 'broken pitchfork'). Here, the small change in bifurcation can be understood within the framework of our model by considering the form of heterogeneity imposed. As derived in section 2.3.2, the base (homogeneous) equation for the pitchfork bifurcation is

$$K_1 C_1^3 + K_2 C_1 \gamma^{(1)} = 0.$$

Perturbations to the system in the form of heterogeneities have the potential to change this to

$$K_1 C_1^3 + K_2 C_1 \gamma^{(1)} + K_3 C_1 + K_4 = 0.$$

The cases we have examined lead to $K_4 = 0$ and $K_3 \neq 0$, which merely translates the pitchfork (as $C_1 = 0$ is still a solution branch). Breaking the pitchfork would require $K_4 \neq 0$. The reason that the additional term obtained has a factor of C_1 is that we have only considered *multiplicative* heterogeneity, i.e. we have imposed heterogeneity in terms that multiply dependent system variables: foundation stiffness k multiplies x and y in the force balance, stiffness E multiplies θ' as well as α, and growth γ appears in the system multiplicatively in multiple places (as evident in Equations (2.1)-(2.3)). Thus, at the relevant order in an asymptotic expansion, a perturbation to these parameters always appears multiplicatively with the base solution $y_1 = C_1 \hat{y}$, and thus the additional term in the solvability condition that provides the bifurcation condition is of the form $K_3 C_1$.

In order to produce a non-zero added term K_4, independent of C_1, we must consider *additive* heterogeneity. One possible type of additive heterogeneity, commonly considered in imperfection analyses, is in the shape of the foundation; that is, we consider the foundation to have spatially-varying imperfections present. That is, we modify the force balance equations (2.10) to

$$\frac{\partial n_x}{\partial S_0} = k(x - S_0), \qquad \frac{\partial n_y}{\partial S_0} = k(y - \widehat{\epsilon}\xi(S_0)), \tag{2.47}$$

where $\xi(S_0)$ is the shape of the imperfection and $\widehat{\epsilon}$ captures the magnitude. This form of heterogeneity first affects the weakly nonlinear analysis when $\widehat{\epsilon} = O(\delta^3)$. Setting $\widehat{\epsilon} = \delta^3\eta$, where η acts as a control parameter away from homogeneity, the solvability condition (2.36) is shifted by a factor independent of C_1, and the bifurcation now satisfies

$$K_1 C_1^3 + K_2 C_1 \gamma^{(1)} + K_4 \eta = 0. \tag{2.48}$$

The constant K_4 is defined by

$$K_4 = k\gamma_0^* \int_0^{L_0} \xi \widehat{y} dS_0. \tag{2.49}$$

(The constants K_1 and K_2 are the same as in the homogeneous case (2.37).) Note the loss of both the trivial amplitude branch and the symmetric nature of the non-trivial amplitude branches. Therefore, with this underlying imperfection, the model undergoes an asymmetric (or imperfect) pitchfork bifurcation, with the branch selected determined by the sign of K_4. As η is increased, so is the deviation from the homogeneous amplitude equation (2.37), and hence the splitting of the initially-symmetric non-trivial branches is amplified. Note also that K_4 involves a simple inner product with ξ and the buckling mode $\widehat{y}$. The heterogeneity thus has maximum effect when the imperfection to the foundation is of the same shape as the buckling mode, i.e. when $\xi \propto \widehat{y}$. Figure 2.8 displays the bifurcation diagram for $\pm\|y\|$ against γ for various values of η, both from the weakly nonlinear analysis (dashed curves) and numerical solution of the full system (solid curves). We have taken the heterogeneity $\xi(S_0) = \widehat{y}(S_0)$. As expected, increasing η further splits the branches and increases the predisposition to the upper branch[2]. Due to the scaling $\widehat{\epsilon} = \delta^3$, large values of η are needed to observe a noticeable difference in the bifurcation. In Figure 2.8 we have taken $\eta = O(10^5)$, which grossly violates the asymptotic assumption that $\eta = O(1)$; since in this plot $\delta = 10^{-2}$, even with $\eta = 10^5$, $\widehat{\epsilon} = 10^{-1}$, i.e. the perturbation is still small, and we find that the weakly

[2]Setting $\xi(S_0) = -\widehat{y}(S_0)$ biases the buckled rod to the lower amplitude branch, as seen by setting $D_1 = -1$. (Note that numerical continuation, increasing γ from the flat rod state, cannot be used to detect the split branches.)

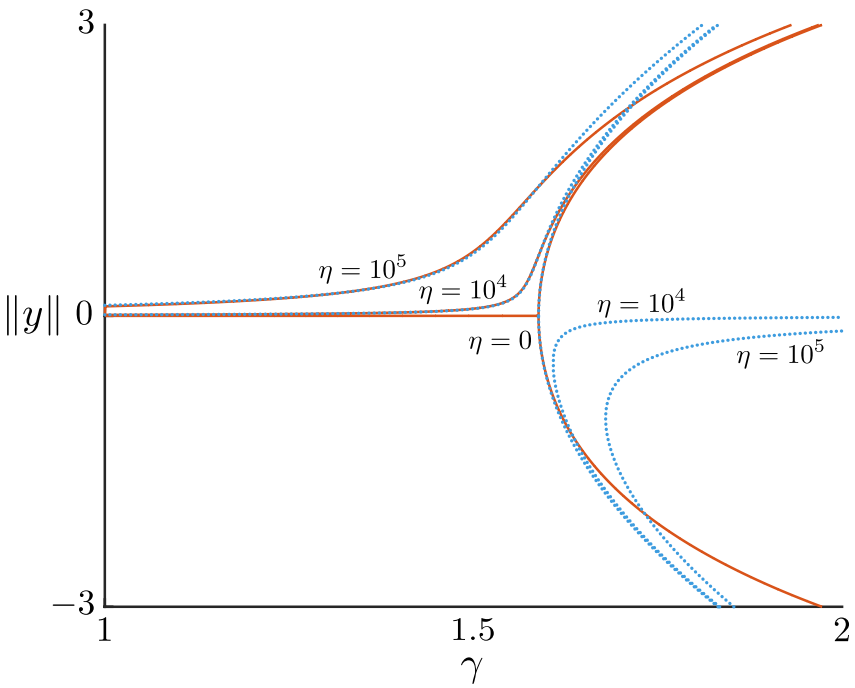

Figure 2.8: Bifurcation diagram for additive foundation heterogeneity (2.47). The foundation stiffness and rod length have been set to $k = 0.04$ and $L_0 = 20$, respectively, while the foundation heterogeneity $\xi(S_0)$ has been prescribed to $\xi(S_0) = \widehat{y}(S_0)$, as defined by Equation (2.27). The amplitudes $\pm\|y\| = \pm\max_{S_0}|y(S_0)|$ against γ from weakly nonlinear analysis (blue, dotted lines) and numerical continuation (red, solid lines) have been plotted for different values of η. For numerical calculations, the small parameter δ is set to $\delta = 0.01$ for all cases. Increasing η further biases the rod to $\gamma = 1$ to the upper non-trivial amplitude branch.

nonlinear analysis matches the full model reasonably well. Also evident is that as heterogeneity is increased, a larger deflection is observed for a given γ. This is consistent with typical results that imperfection deforms load-deflection curves so that higher deflections occur under smaller loads [90].

As a final point of interest, we wish to measure which form of heterogeneity has the greatest impact on the bifurcation. As a 'metric' for comparison, following the typical engineering analysis of load-deflection, here we consider the compressive force as a function of growth. To examine this, we define the *net axial stress*

$$\overline{n_3} = \frac{1}{L_0}\left|\int_0^{L_0} n_3 dS_0\right| = \frac{1}{L_0}\left|\int_0^{L_0} n_x\cos\theta + n_y\sin\theta dS_0\right|. \tag{2.50}$$

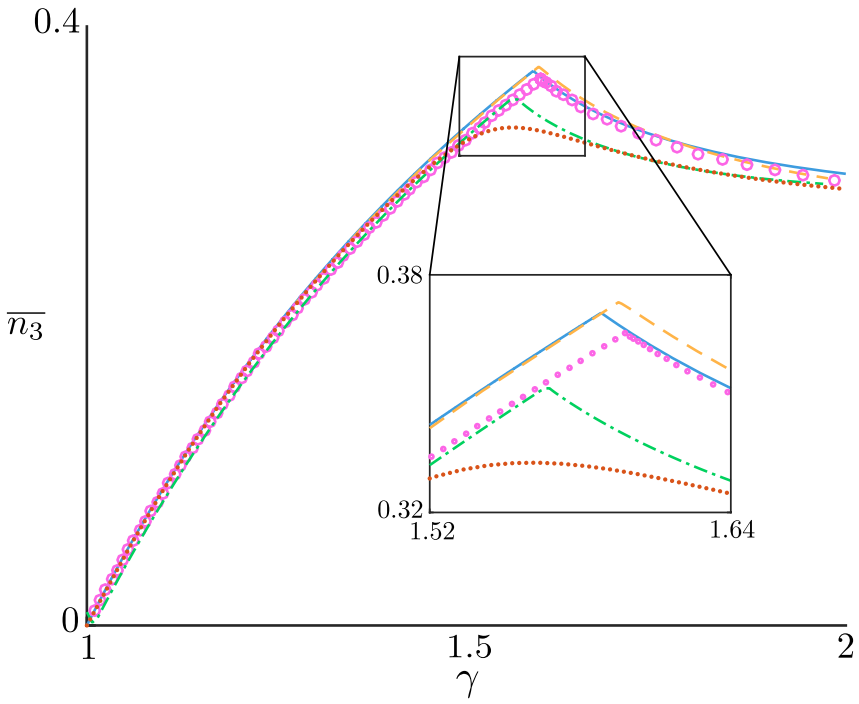

Figure 2.9: Effect of the considered heterogeneities on compressive stress. The net axial load $\overline{n_3}$ is plotted against γ. As before, the foundation stiffness and rod length have been set to $k = 0.04$ and $L_0 = 20$, respectively, while the foundation heterogeneity $\xi(S_0)$ has been prescribed to $\xi(S_0) = \widehat{y}(S_0)$ (see Eq. (2.27)). The homogeneous case (blue, solid line) is compared against the foundation stiffness heterogeneity (orange, dashed lines); rod stiffness heterogeneity (pink, open circles); growth heterogeneity (green, dash-dotted lines); and foundation imperfection (2.47) (brown dots). For numerical calculations, the small parameter δ is set to $\delta = 0.01$ and η is set such that $\widehat{\epsilon} = 0.1$ for all cases. The additive foundation heterogeneity is quickest to relieve the axial stress induced by rod growth.

In Figure 2.9, we compare the net axial stress with increasing growth for each of the four heterogeneities considered. In each case we have imposed $\xi = \hat{y}$, and due to the different nature of the perturbation schemes, we have chosen the scale factors such that the total perturbation from the uniform state is equivalent across the four cases. The perfect buckling case appears as the solid blue line, with the sharp cusp appearing at γ^* and signifying that buckling occurs at a critical compressive stress, which is relieved partially through the buckling. Each of the heterogeneities produces a similar curve, though we see that the additive heterogeneity in foundation shape just considered has the most significant effect, followed by growth heterogeneity. Both foundation and stiffness heterogeneity follow the perfect case very closely;

zooming in on the cusp region (see inset) shows that these forms lead to a delayed bifurcation, and, in the case of foundation stiffness, the bifurcation occurs at slightly larger stress before subsequently compensating and dipping below the perfect case.

Why do crypts always invaginate downwards?

The predisposition to a particular solution branch shown in Figure 2.8 leads to an interesting hypothesis about crypt invagination. In the intestines, crypts always invaginate downwards, away from the lumen (inner cavity) while in the small intestine, villi always protrude outwards into the lumen [183]. While functional differences between the two glands—the crypts house and protect a stem cell pool, while the villi maximise surface area for nutrient absorption [1]—may suggest why these directional biases are useful or necessary, it is not known how these preferential directions for deformation occur. However, it has been observed that during gut development, villi formation occurs first, which is followed by crypt formation in the regions between villi [167]. As villi protrude out towards the lumen, the intervillous tissue regions curve away from the lumen and are thus convex in shape [167]. This suggests an inherent imperfection in the 'foundation', where the foundation is represented by the underlying extracellular matrix and stroma, such that $\xi(S_0) \propto -\hat{y}(S_0)$. This leads to a natural preference for crypts to invaginate downwards, away from the lumen. It is worth noting that these biases may be exacerbated by the differences in considered tissue geometries, as the gastrointestinal tract is cylindrical in shape, whereas our analysis is considered along a 1D line.

2.5 Discussion

We have investigated the buckling and post-buckling behaviour of a planar morphoelastic rod attached to an elastic foundation, an abstracted model of a buckling intestinal crypt. We extended the original linear stability analysis by Moulton et al. [120] by conducting a weakly nonlinear analysis, complemented with numerical solutions of the full, nonlinear model. We first considered a homogeneous setting, and then explored the effect of heterogeneity in material parameters.

In the homogeneous case, we obtained a classic pitchfork bifurcation, with buckling occurring at a critical growth. The nature of the bifurcation (its location and type—supercritical or subcritical) could be characterised via two dimensionless parameters, one (L_0) relating to length of the finite rod, and another (k) comparing the relative stiffness of foundation and rod. Increasing length was found to destabilise the rod, causing bifurcation at a smaller value of growth and with increased mode number. Increasing the foundation stiffness, on the other hand, stabilises the rod, increasing the critical growth and the mode number. The influence of foundation stiffness on the buckling mode and the onset of instability shows how variations in system parameters, even in a heterogeneous setting, can have a dramatic impact on the resulting morphology. Such results may have strong relevance in the crypt, where its invaginated structure is crucial to functionality.

The general trends we have found in the homogeneous case are consistent with previous analyses of a similar nature, e.g. [131]. The type of bifurcation, however, was non-standard: the boundary between supercritical and subcritical bifurcations exhibited an unexpected complexity. In a biological context, where monotonically increasing growth is a natural driver of the formation and subsequent evolution of spatial patterns, this transition has critical importance, signifying where a smooth shape evolution (supercritical) can be expected, as opposed to a discontinuous jump from a flat state (subcritical). Here the effect of a finite domain is also apparent, as the complexity of the transition becomes less pronounced as L_0 increases.

Multiplicative heterogeneity with respect to three different material properties was then considered: the foundation stiffness, the rod stiffness, and growth. A modified weakly nonlinear analysis showed that in each case the heterogeneity served to translate the bifurcation point, but did not alter its nature. Explicit relations for the shift in bifurcation allowed us to determine how the form of the heterogeneity influences the direction and degree of the translation. For example, the simplest relation appeared with heterogeneity in the foundation stiffness, in which case the greatest effect occurs when the heterogeneity is aligned with the square of the buckling mode. This reflects the intuitive notion that weakening

the foundation attachment in regions where the uniform rod deforms maximally has the strongest impact.

To complement the weakly nonlinear analysis, the full nonlinear system was solved with numerical continuation; this enabled us to investigate the post-buckling behaviour for more pronounced heterogeneity and at large growth values. A common feature was an induced 'asymmetry' of the buckled shape. With heterogeneous foundation stiffness, softer (stiffer) parts of the foundation give rise to increased (decreased) rod amplitudes, as might be expected. With heterogeneity in rod stiffness, the situation is less straightforward. Softer parts of the rod are more easily curved, and thus it might be reasonable to expect such regions to correspond to higher amplitude; however, compression is also less costly in the soft regions. In all cases we have examined, the rod flattens through compression in the soft regions, a deformation that increases stretching energy, but is compensated by a decrease in both bending and foundation energies. Here, the assumption of extensibility is crucial, as compression is not permitted in an inextensible model. Indeed, a direct comparison of an inextensible and extensible model post-buckling revealed significant morphological differences, highlighting the importance of a critical assessment of when the inextensible assumption is warranted. In the case of non-homogeneous growth, we showed that even with zero net growth, heterogeneity, interpreted as a redistribution of rod material from spatial regions with decreased γ to those with increased γ, can significantly impact the post-buckling behaviour. The general trend is not surprising: the rod flattens in regions where material is lost. What is perhaps surprising is that the distribution of material seems to play as important a role in the shape evolution as the total amount of material added through growth.

Having examined the effect of heterogeneity on post-buckled shape, two natural and related questions follow from this: (i) can one tailor the heteregeneities to achieve a desired shape? And (ii) given a particular shape, can one infer the form and type of any material heterogeneity present? These questions, with significant relevance both from morphogenetic and tissue engineering perspectives, are related to the mathematical inverse problem. Such a problem is inherently complex, as the

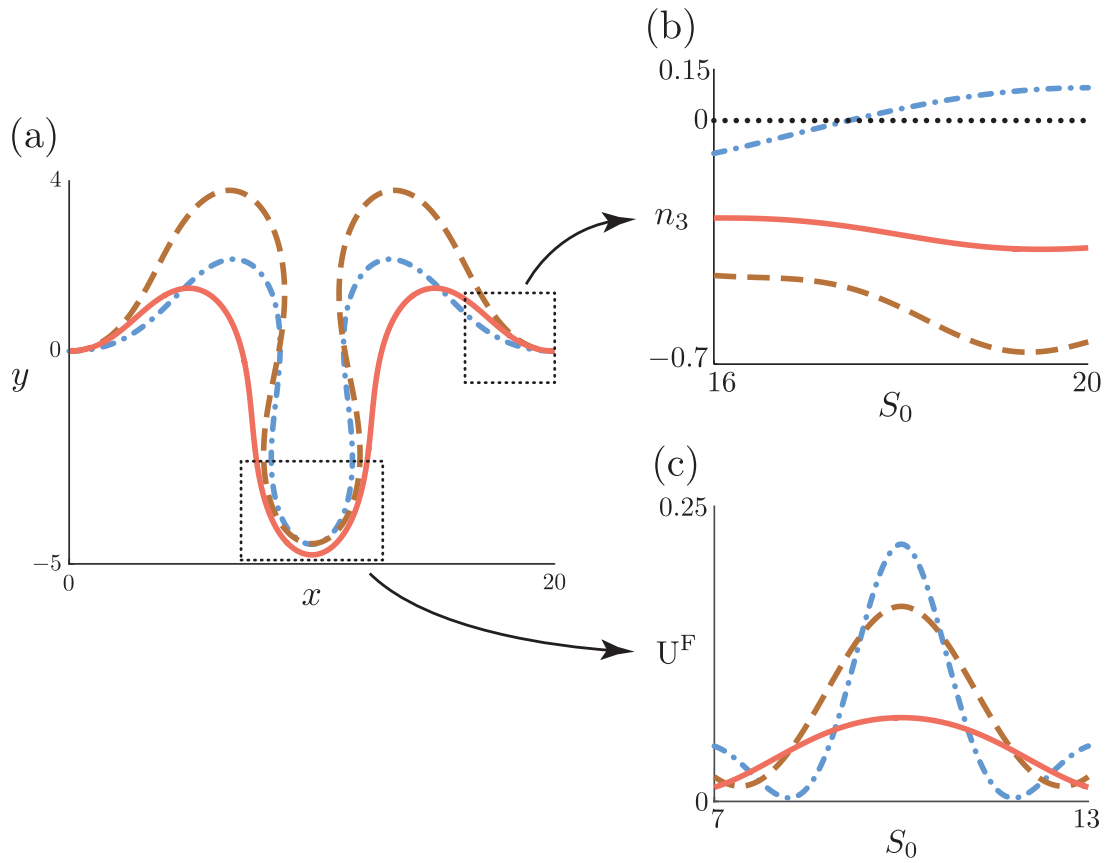

Figure 2.10: Inverse problem example. (a) Different forms of heterogeneity in rod stiffness (brown, dashed), and growth (blue, dot-dashed) are chosen to approximately match the morphology produced by foundation stiffness heterogeneity (red, solid). (b) Despite the similar shape and amplitude in the edge region, growth heterogeneity gives rise to tension ($n_3 > 0$). (c) Foundation stiffness heterogeneity decreases the foundation energy density U^{F} in the central region where the foundation has been weakened.

shapes considered are (partial) solutions of a high-order nonlinear boundary value problem, only achieved in the forward direction through numerical path continuation. In order to develop some intuition, here we provide a simple but illustrative example: we take a candidate shape with embedded heterogeneity—foundation heterogeneity following Figure 2.4(b)—and we try to match that shape, in a trial-and-error manner, by varying the heterogeneity in either the rod stiffness or the growth (as well as the net growth), guided by the results of Section 2.4.3; we then consider characteristics other than the shape itself and seek distinctive differences, i.e. *signatures* of the heterogeneities (more details provided in Appendix A.6).

The result of this exercise is summarised in Figure 2.10. In Figure 2.10(a) we plot

the 'matched' shapes; clearly the match is imperfect, highlighting already the non-trivial nature of tailoring the heterogeneity to achieve a specific shape. Figure 2.10(b) shows the axial stress n_3 in the outer region. We observe that growth heterogeneity produces disparate regions of tension, $n_3 > 0$ (where growth is reduced), and compression, $n_3 < 0$ (where growth is increased). In contrast, the rod remains in compression for foundation and rod stiffness. In distinguishing foundation stiffness heterogeneity, the foundation energy density U^{F}, defined explicitly in Appendix A.5, provided the clearest indicator. Figure 2.10(c) plots U^{F} in the middle section of the rod, where the shapes are qualitatively most similar, and we find a significant decrease in the case of foundation heterogeneity.

In a thought experiment where the morphology is given and the task is to determine the heterogeneity, these differences could in principle be detected by cutting experiments that release residual stress, as is done for instance in arteries [38] and solid tumours [164]. However, while this example suggests the possibility of distinguishing between forms of heterogeneity and using heterogeneity to tailor properties, it is clear that this is not a straightforward problem, and a more rigorous treatment would be needed to reach firm conclusions. Moreover, we observed no features that clearly distinguished the case of rod stiffness heterogeneity from the other two heterogeneities. In a 3D setting, more measurable quantities are available, for example, stress in transverse directions, which could potentially yield measurable differences in behaviour. On the other hand, the general complexity of the inverse problem will increase as the number of variables increases. In any case, modelling studies and computational and/or analytical results such as those provided by a weakly nonlinear analysis can provide important insights in a tissue engineering context, e.g. determining the right 'ingredients' to generate desired tissue morphologies; as well as for building intuition for how different regions of a heterogeneous elastic tissue with evolving material properties will behave. This is of particular relevance to intestinal tissue health, where deformation of the epithelium plays a significant role in facilitating wound healing [154] and adenoma expansion [143].

In the final section, we have examined a fourth type of heterogeneity, with a view to establishing why the impact of heterogeneity on the bifurcation itself was relatively minor in the previous scenarios. Here we made the key distinction between multiplicative and additive heterogeneity. A multiplicative heterogeneity appears in a term that multiplies dependent variables in the system; due to the nature of the perturbative expansion, such terms only serve to shift the pitchfork bifurcation. An additive heterogeneity, for which a perturbation is applied to a term that does not multiply dependent variables, can have a significant effect, creating an imperfect bifurcation (broken pitchfork) and creating a larger deviation from the perfect, homogeneous, case. Here we considered an imperfectly-straight foundation, and showed that the effect is maximal when the form of the imperfection matches that of the buckling mode. These results suggested that crypts always invaginate downwards because the inherent imperfections along the epithelium that arise after villi formation.

This framework provided a preliminary setting in which we could an perform analysis that was motivated by observations on the intestinal crypt and other, physiologically similar structures. The buckling and subsequent deformation we considered could be interpreted as a proxy for crypt morphogenesis, in which the intestinal epithelium undergoes significant deformation, leading to crypt formation. However, in order to properly link the insights and results gained from Chapter 2 to processes such as morphogenesis or homeostasis, greater biological detail needs to be included. That is, we need to account for the various biological, chemical, and mechanical processes that may be present in the crypt. These include processes such as: chemical signalling, tissue relaxation, cell-type-dependent heterogeneity, and cell turnover. However, there are no established models of these processes within the morphoelastic framework. Moreover, many of these processes are not unique to the crypt, and are essential aspects of epithelial structures in general (and even non-epithelial structures). Thus, in Chapter 3, we aim to build on the analysis in Chapter 2 by developing models that capture the various features that may be present in a growing epithelial tissue, such as the crypt.

We note that the spatial forms of heterogeneities that were considered in this chapter were for illustrative purposes. While we briefly discussed how one may tailor these heterogeneities to a given morphology, the spatial profiles were not reflective of any particular growth or stiffness properties in the crypt. A natural extension to the work in Chapter 2 is to then model spatial heterogeneous properties that are actually indicative of the different properties of the crypt. The question of how to appropriately extend this work brings up several points of discussion. First, all material properties that were considered were static and fixed in form. For instance, it is clear that in biological tissue, growth is an evolving process over time. Other features that may evolve over time could be the intrinsic rod curvature or the foundation attachments, which could be used to model tissue relaxation, an important feature of many biological tissues. Second, all heterogeneity was modelled as a function of the initial arc length, S_0, i.e. a Lagrangian parametrisation. In biological tissue, a Lagrangian parametrisation reflects the notion that the heterogeneity as an inherent property of cells. However, if we are modelling heterogeneity based on observations from biological experiments, then these profiles are observed in the current Eulerian configuration, which is parametrised by the current arc length s. We aim to explore the effect of modelling evolving properties and different spatial parametrisations on rod morphology in the next chapter.

3

Fundamentals of continuum epithelia modelling

3.1 Introduction

In Chapter 2, we explored (mechanical) pattern formation and the effects of spatially heterogeneous tissue mechanics within a growing rod tethered to an elastic foundation. This model served as an abstracted description of tissue-on-substrate bilayers, such as the intestinal crypt. We treated the buckling and subsequent deformation of the rod as an analogy for crypt morphogenesis. We now wish to build upon the insights gained from Chapter 2 and make the link between the growth-induced deformation of the rod and epithelial morphogenesis more concrete, by modelling the different processes that are suspected to play a role in morphogenesis.

Notable processes that drive morphogenesis include: biochemical signalling, which leads to spatial heterogeneity in growth; tissue relaxation, in which the system adapts to changes in stress; cell type specification, which governs different material properties; cell turnover, which balances growth and induces a homeostatic state, where the morphology is unchanging; and self-contact, which allows continued invagination and prevents the growing material from self-penetrating. However, for many of these processes, which span the cellular and subcellular spatial scales, there are no established models within a continuum mechanics framework. As

such, it is not clear how to best incorporate each process, nor how significant of an effect each will have on the resulting morphology.

We now proceed as follows. In Section 3.2, we briefly summarise the generalised morphoelastic rod framework for the inextensible case. In Section 3.3, we outline possible models of the different components that may contribute to crypt morphogenesis. While we are ultimately interested in modelling the intestinal crypt, these models can be applied to a number of epithelial bilayer systems, such as the hair follicle [68], Barrett's Esophagus [161], and even non-epithelial structures, such as the brain [75] and seashell spine formation [37]. In Section 3.4, we perform a range of simulations, varying parameter values and model choices, such as for the foundation. We close with a discussion of the biological implications of our results.

3.2 Model set-up

Our aim is to extend the framework considered in Chapter 2 to model the growth and subsequent large deformation of a buckling epithelial tissue attached to a substrate, considering the effects of relevant biomechanical factors that may contribute to its morphogenesis and homeostasis. In order to shift our focus from the analysis of buckling and post-buckled bifurcation structure that we examined in Chapter 2, to the various additional processes involved in epithelial morphogenesis, we will assume the rod is inextensible.

3.2.1 Mechanics

We build upon the general framework for growing elastic rods described in Chapter 2. As before, the rod's shape is described by its centreline curve in 2D Cartesian geometry, such that $\mathbf{r} = x\mathbf{e}_x + y\mathbf{e}_y$. For an inextensible rod, the elastic stretch $\alpha = \frac{\partial s}{\partial S} \equiv 1$. Therefore, by the multiplicative decomposition (1.5), the total stretch, λ, is equal to the growth stretch γ:

$$\alpha = \frac{\partial s}{\partial S} = 1 \qquad \Longrightarrow \qquad \lambda = \gamma(S_0, t) = \frac{\partial s}{\partial S_0}. \tag{3.1}$$

In morphogenesis, tissue growth is not a fixed quantity, but rather evolves over time. Therefore, we model tissue growth via an evolution equation for γ of the generalised form:

$$\frac{\dot{\gamma}}{\gamma} = \mathcal{G}, \tag{3.2}$$

where the overdot represents partial differentiation with respect to t. The quantity $\dot{\gamma}\gamma^{-1}$ on the left hand side of Equation (3.2) describes the *incremental change* in growth. This quantity is a closer analogue to proliferation than γ, which describes the total amount of material accumulated over the entire growth history. Hence, we can relate $\dot{\gamma}\gamma^{-1}$ to biologically meaningful contributions contained within the function $\mathcal{G}$. The function $\mathcal{G}$ can depend on a number of variables, such as spatial position, time, stresses, strains, chemical signalling, and so on.

In order to describe both the resistive effects of the underlining extracellular matrix and supporting stroma, as well as how attachments may change over time, we model the combined mechanical effects of the extracellular matrix and stroma via a foundation force. We generalise the linear elastic foundation model used in Chapter 2, treating the foundation as a smooth curve $\mathbf{p} = p_x\mathbf{e}_x + p_y\mathbf{e}_y$, which is either elastically or viscoelastically attached to the growing rod. The resistive effects of the attachments are specified through a constitutive law for stress induced by the foundation and described by the function σ, while any remodelling of the attachment shape, $\mathbf{p}$, can be specified by an appropriate evolution equation. Within this framework, all foundation forces are prescribed via the body force, $\mathbf{f}$, using the following constitutive law:

$$\mathbf{f} = \frac{\sigma}{\Delta}(\mathbf{p} - \mathbf{r}) + \mathbf{f}^{\text{ext}}, \tag{3.3}$$

where $\Delta = \|\mathbf{p} - \mathbf{r}\|_2$ is a measure of the rod strain with respect to the foundation, where $\|\cdot\|_2$ denotes the Euclidean two-norm, and $\mathbf{f}^{\text{ext}}$ describes any additional external forces, such as self-contact or spatial competition due to neighbouring epithelial tissue. Note that we assume that there is no twisting effect induced by $\mathbf{p}$; hence, $p_z \equiv 0$. Let $\mathbf{n} = n_x\mathbf{e}_x + n_y\mathbf{e}_y$ and $\mathbf{m} = m\mathbf{e}_z$ denote, respectively, the

resultant force and bending moment in the growing rod. The equations describing geometric constraints and balance of linear and angular momentum are:

$$x' = \gamma \cos\theta, \tag{3.4}$$

$$y' = \gamma \sin\theta, \tag{3.5}$$

$$n_x' = \gamma \frac{\sigma}{\Delta}(x - p_x), \tag{3.6}$$

$$n_y' = \gamma \frac{\sigma}{\Delta}(y - p_y), \tag{3.7}$$

$$m' = \gamma(n_x \sin\theta - n_y \cos\theta). \tag{3.8}$$

Here, the primes $'$ denote (partial) differentiation with respect to the initial arclength parameter S_0 (hence the presence of factors of γ in Equations (3.4)–(3.8)). The bending moment m is assumed to depend on curvature via the standard constitutive relation

$$m = E_b \gamma^{-1} \theta', \tag{3.9}$$

where E_b is the (nondimensional) bending stiffness parameter. To close the system, we assume the rod is clamped horizontally at the boundaries:

$$x(0) = 0, \quad y(0) = 0, \quad \theta(0) = 0, \qquad x(L_0) = L_0, \quad y(L_0) = 0, \quad \theta(L_0) = 0. \tag{3.10}$$

As the rod is inextensible, it is no longer appropriate to scale the resultant rod force with respect to the extensibility assumption (2.5). Therefore, scaling the system by the standard Kirchhoff scaling (2.8) does not result in the most effective reduction in the number of parameters. Instead, throughout this chapter, the model is scaled using the following nondimensionalisation [37]:

$$\begin{aligned}
(S_0^*, x^*, y^*, \Delta^*, p_x^*, p_y^*) &= L_0^*(S_0, x, y, \Delta, p_x, p_y) \\
(n_x^*, n_y^*) &= E(I/L_0^{*^2})(n_x, n_y), \\
\sigma^* &= E(I/L_0^{*^3})\sigma, \\
m^* &= E(I/L_0^*)m, \\
t^* &= \tau t.
\end{aligned} \tag{3.11}$$

Here, L_0^* is the initial rod length; E is the Young's Modulus; $I = wh^3/12$ is the (second) moment of inertia, for an assumed rectangular cross-section with width w and height h; and τ is a typical timescale for tissue growth, on the order of a day (i.e. $\tau = 24$ hours). Henceforth, we take $L_0 = 1$.

Simulating morphogenesis

In this framework, morphogenesis is modelled as the subsequent deformation after growth-induced buckling. Given that tissue growth occurs on longer timescales than elastic deformations, we assume that at every time step during the growth evolution, the system is in quasi-static mechanical equilibrium. Hence, for all simulations, we first update growth via Equation (3.2), then update any other mechanisms that evolve in time, such as viscoelasticity or intrinsic curvature relaxation. The corresponding force balance equations, Equations (3.4)–(3.8), are then solved to obtain the resulting morphology.

For a linear elastic foundation, we have shown previously that the shape upon buckling is dependent on both the foundation stiffness and initial rod length (see Chapter 2 or Almet et al. [2]). As we have scaled the spatial coordinates by the initial rod length L_0^*, the stiffness of the foundation determines the buckling mode. This will be an important aspect to note, as we begin to explore the effect of different foundation models on tissue patterning.

3.3 Biological specifications

In this section, we discuss the factors that may contribute to epithelial morphogenesis and how they may be incorporated into mathematical models. We focus on biological processes that are believed to play a role in driving morphology. In the context of our mechanical framework, they can be modelled through material properties such as the bending stiffness, through tissue growth itself, or through the development of new constitutive laws.

3.3.1 Sources of tissue relaxation

Tissue relaxation is defined as a dynamic functional adaptation to applied stresses or strain. It may also be a response to the stresses and strains induced by growth of the tissue itself. This is a well-established feature of soft biological tissues [66, 87]. Therefore, in order to develop a realistic model of a buckling epithelial tissue, some form of tissue relaxation must be present. However, there are several ways in which relaxation could occur. It may occur in the epithelium itself, through a plastic remodelling of its intrinsic shape or, given that epithelial tissue is typically tethered to a basement membrane and surrounding tissue stroma, relaxation may occur through the mechanical interactions between the epithelium and the surrounding media. Therefore our first task is to explore and contrast alternative mechanisms of tissue relaxation within the morphoelastic rod framework.

Relaxation through the foundation

As stated, the contributions of the basement membrane and stroma are reduced to a foundation force, $\mathbf{f}$. In continuum models of the crypt, the basement membrane and stroma are often modelled by a constitutive law describing the bulk behaviour of the underlying attachments to the epithelium [56, 124, 125], although models that describe both explicitly do exist [85]. Nevertheless, there are several possible choices, ranging on a spectrum from completely static, in terms of stress and foundation attachment evolution, to complete remodelling of the foundation attachments.

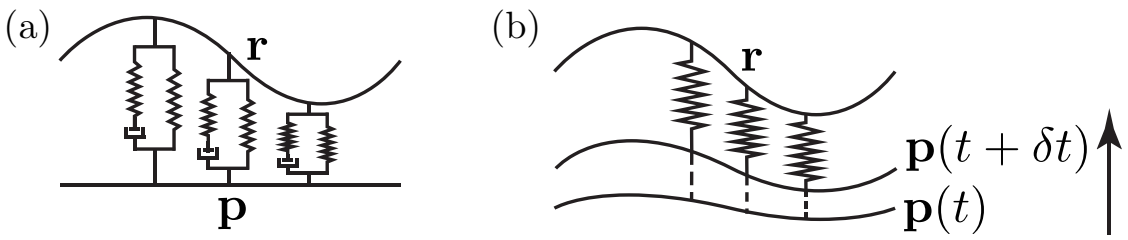

Figure 3.1: The two different models of foundation relaxation. (a) The attachments are viscoelastic, modelled using a standard linear solid model, but the foundation shape $\mathbf{p}$ does not change over time. (b) The attachments are linearly elastic, but the shape of the attachments, $\mathbf{p}$, remodels over time.

Stress relaxation. It is well documented that cells and biological tissue are able to adapt to stress [66]. A fundamental modelling question is whether this relaxation occurs within the tissue itself or with respect to the external environment to which the tissue is anchored. In the context of modelling tissue as a 1D elastic rod, internal tissue relaxation can be modelled through the evolution of the intrinsic rod curvature, corresponding to plastic relaxation.

We first consider relaxation of the external foundation force, which represents the tethering of the epithelium to the extracellular matrix and surrounding tissue stroma. We consider two distinct models, illustrated in Figure 3.1. As the foundation force encapsulates the mechanical effect of the surrounding biological tissue and extracellular matrix components, it is natural to assume that the foundation may behave viscoelastically. We note that the works of Edwards and Chapman [56] and Nelson et al. [124] have both explored the effects of viscoelasticity within the crypt, through the prescription of a Maxwell foundation. However, key aspects of viscoelasticity are stress relaxation and the phenomenon of creep, where strain continues to relax under a constant stress [86], which a purely Maxwell-type law fails to capture. Our approach is to prescribe a foundation law through the body force vector, $\mathbf{f}$, and a constitutive law satisfied by the foundation attachments, and then project into its separate components, e.g. the x and $y-$components, to obtain the force terms in the rod balance equations (3.4)–(3.8). We describe the viscoelasticity of the foundation stress using a standard linear solid model [109] (Fig. 3.1(a)). For simplicity, at present we assume that the foundation curve $\mathbf{p}$ does not evolve over time. The standard linear solid model is constructed by connecting a Maxwell unit in parallel with another elastic spring. In dimensional terms, both the Maxwell unit and the spring contribute to the total foundation stress, with equal strains:

$$\sigma^* = \sigma_E^* + \sigma_M^*, \qquad \Delta_E^* = \Delta_M^*, \qquad \dot{\mathbf{p}} = 0, \tag{3.12}$$

where σ_E^* is the stress of the non-damped spring, obeying the constitutive equation

$$\sigma_E^* = E_1 \Delta^*, \tag{3.13}$$

where E_1 is the spring stiffness, and σ_M^* is the stress of the Maxwell unit, satisfying

$$\frac{1}{E_2}\dot{\sigma}_M^* + \frac{1}{\eta_\sigma}\sigma_M^* = \dot{\Delta}^*, \tag{3.14}$$

with a spring stiffness of E_2 and a viscous relaxation rate η_σ^{-1}. Substituting (3.13) and (3.14) into (3.12) yields the dimensional evolution equation for σ^*:

$$\frac{1}{E_2}\dot{\sigma}^* + \frac{1}{\eta_\sigma}\sigma^* = \frac{E_1}{\eta_\sigma}\Delta^* + \left(\frac{E_1+E_2}{E_2}\right)\dot{\Delta}^*. \tag{3.15}$$

We write $E_1 = (1-\beta)Ek_f$ and $E_2 = \beta E k_f$, where E is the rod stiffness, k_f quantifies the bulk foundation stiffness, and $\beta \in [0,1]$ quantifies the weighting in elastic response between the Maxwell and non-damped spring. This is so that the buckling mode is equivalent to that for a linear elastic foundation constitutive law (2.6). Applying the nondimensionalisation (3.11) to Equation (3.15) yields

$$\dot{\sigma} + \beta\nu\sigma = \beta(1-\beta)k\nu\Delta + k\dot{\Delta}, \tag{3.16}$$

where

$$\nu = \frac{Ek_f\tau}{\eta_\sigma}, \qquad k = \frac{k_f L_0^{*4}}{I}. \tag{3.17}$$

In terms of the weighting parameter, β, the case $\beta = 0$ results in an elastic foundation, while $\beta = 1$ corresponds to a Maxwell foundation. An elastic foundation is also obtained in the limiting cases $\nu \to 0$ and $\nu \to \infty$. The initial foundation attachments are made along the $x-$axis, i.e. $\mathbf{p}(S_0, 0) = S_0\mathbf{e}_x$. Hence, the force balance equations for a standard linear solid foundation are

$$n_x' = \gamma\frac{\sigma}{\Delta}(x - S_0), \qquad n_y' = \gamma\frac{\sigma}{\Delta}y, \tag{3.18}$$

where σ evolves according to Equation (3.16).

Foundation attachment remodelling. Alternatively, we can consider an evolution law for the foundation shape, $\mathbf{p}(S_0, t)$, itself. This law has been used previously to describe seashell spine formation [37] and cytoskeleton remodelling within a cell [121]. We assume that $\mathbf{p}(S_0, t)$ relaxes to the current rod shape, $\mathbf{r}(S_0, t)$, as

shown in Figure 3.1(b). The foundation stress, σ, and evolution equation for $\mathbf{p}$ are given in dimensional form by

$$\sigma^* = Ek_f\Delta^*, \qquad \dot{\mathbf{p}}^* = \frac{1}{\eta}(\mathbf{r}^* - \mathbf{p}^*), \tag{3.19}$$

where $\mathbf{p}^*(S_0^*, 0) = S_0^*\mathbf{e}_x$. Therefore, after nondimensionalisation, the force balance equations in this case are given by

$$n_x' = k\gamma(x - p_x), \qquad n_y' = k\gamma(y - p_y), \tag{3.20}$$

where the foundation attachment components p_x and p_y evolve according to:

$$\dot{p_x} = \rho(x - p_x), \qquad \dot{p_y} = \rho(y - p_y), \qquad \text{where} \qquad \rho = \frac{\tau}{\eta_{\mathbf{p}}}, \tag{3.21}$$

with initial conditions $p_x(0) = S_0$, $p_y(0) = 0$.

It is possible to combine the viscoelastic law (3.16) with a remodelling foundation as described by Equations (3.21); we refrain from doing so here in order to compare the relaxation effects of each model on the morphology and internal stresses, namely, the stress relaxation parameter, ν, for the viscoelastic foundation, and ρ for the remodelling foundation law.

Relaxation within the epithelium

Aside from relaxation within the foundation, we can consider relaxation of the epithelium stress-free shape through the evolution of an intrinsic rod curvature. We relax the assumption that the rod has zero intrinsic curvature, i.e. that the epithelium will be flat in the absence of any forces. Following Moulton et al. [120], we modify the moment-curvature relation (3.9) to include an intrinsic curvature, $\hat{\kappa}$

$$m = E_b(\kappa - \hat{\kappa}) = E_b(\theta'\gamma^{-1} - \hat{\kappa}), \tag{3.22}$$

where $\hat{\kappa}$ relaxes to the current curvature, $\kappa = \theta'\gamma^{-1}$, via the following evolution equation

$$\dot{\hat{\kappa}} = \chi(\kappa - \hat{\kappa}) = \chi(\theta'\gamma^{-1} - \hat{\kappa}), \qquad \text{where} \qquad \chi = \frac{\tau}{\eta_{\hat{\kappa}}}. \tag{3.23}$$

We take the intrinsic curvature to be initially zero, i.e. $\hat{\kappa}(0) = 0$, as the pre-buckled rod is flat. This type of plastic remodelling of the intrinsic curvature has been used in previous models of plant stem growth [72, 132, 153].

3.3.2 Modelling tissue growth

Previously, in Section 2.4.3, we demonstrated that spatially heterogeneous growth, modelled through the growth stretch $\gamma(S_0, t)$, can significantly impact the morphology by redistributing material along the rod. As epithelial invaginations often have a highly-specialised and consistent proliferative structure [1], we expect that these variations in proliferative capacities affect the resulting growth evolution and morphology. Therefore, it is important to capture these proliferative structures with an appropriately-specialised growth law. In our framework, growth is specified by the evolution equation, Equation (3.2). Here, we discuss some of the key processes that contribute to $\mathcal{G}$, and how they may be incorporated.

Chemical signalling

Chemical signalling plays a significant role in morphogenesis. For example, Wnt signalling is known to be the primary driver of proliferation within intestinal crypts [146]. However, as the timescale of chemical reactions is much faster than that of tissue growth, it is reasonable to assume that, on the timescale of tissue growth, the concentration of any chemical signalling is effectively in steady state [187]. The simplest growth law to model spatial dependence on Wnt signalling would be the following:

$$\frac{\dot{\gamma}}{\gamma} = W, \tag{3.24}$$

where W is the (steady-state) sensitivity to Wnt signal ligand. A key challenge in modelling chemical concentration is deciding how the tissue interprets chemical signals such as Wnt—is it an inherent property of cells at birth, or is it a dynamically-varying signal? In other words, in the crypt, would Wnt signal sensitivity be a function of the initial arc length parameter, $W = W(S_0)$, corresponding to an inherent material property of cells, or is sensitivity a function of the current position, via the current arc length parameter $W = W(s)$. Figure 3.2 shows schematically how this choice affects the spatial distribution of these material properties over time, as the rod grows. In what follows, we will show that the choice of spatial parametrisation can have a significant effect on the resulting morphology.

3.3.3 Mechanical properties

In Section 2.4.3 we demonstrated that rod stiffness heterogeneity can have a significant impact on morphology, depending on the extensibility assumption. The effect of rod stiffness heterogeneity is important in a biological context, as cells within a tissue vary not only in their proliferative capacity, but also in their mechanical properties. Examples include the increase of rigidity of epithelial cells due to maturation over time [20], or the reduced stiffness of metastatic cells [184]. From the results of Chapter 2, we suspect that accounting for these differences in mechanical stiffness in a model of epithelia affects the resulting morphology significantly.

For an inextensible rod, the mechanical properties of the rod are characterised by the bending stiffness, E_b, which regulates the ease with which the rod can bend. In this chapter, we will focus on the effect of heterogeneity within the bending stiffness, E_b, rather than heterogeneity within the foundation stiffness k, as it describes the mechanical properties of the epithelial tissue itself. Many epithelial glands, such as the intestinal crypt, hair follicles, or skin epidermis, house stem cells in the base which are mechanically less rigid than the differentiated cells that are positioned at the top of these glands. It is therefore natural to investigate the effect of these regions of softened tissue on buckled morphologies. However, as we discussed in the previous section, it is not entirely clear whether these properties, which model the cellular properties within the tissue, should be parametrised with respect to the Lagrangian frame, $E_b = E_b(S_0)$, representing stiffness as an inherent

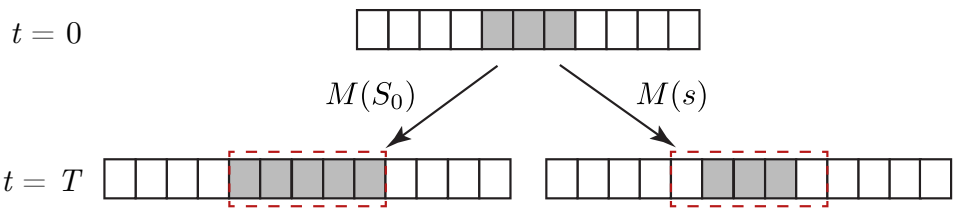

Figure 3.2: Possible frames of reference for material properties. If the material property, M, is parametrised by the initial arc length parameter S_0, $M = M(S_0)$, then the material property values at $t = 0$ propagate as the rod grows to $t = T$. However, if $M = M(s)$, then the material properties at $t = T$ is updated so that the values are the same as at $t = 0$. The red dashed boxes indicate the regions of the rod that have grown at $t = T$.

property of cells, or with respect to the Eulerian frame, $E_b = E_b(s)$, representing cells remodelling in stiffness according to their current position.

We will consider Gaussian forms for the Lagrangian parametrisation of the nondimensional bending stiffness:

$$E_b(S_0) = 1 - b\exp\left[-\left(\frac{S_0 - 0.5}{\sigma_b}\right)^2\right], \tag{3.25}$$

and for the Eulerian parametrisation,

$$E_b(s) = 1 - b\exp\left[-\left(\frac{s - 0.5l}{\sigma_b}\right)^2\right], \tag{3.26}$$

where $b \in [0, 1)$ controls the amount of stiffness variation, while σ_b specifies the width of the region of softened tissue, and $l = \int_0^1 \gamma dS_0$ is the total rod length. Figure 3.2 shows how these parametrisations will lead to different distributions of stiffness along the rod. From a modelling perspective, we aim to understand which of the parameters b and σ_E contribute most to shaping the growing morphologies, and to compare different spatial parametrisations; that is, parametrising $E_b = E_b(S_0)$ or $E_b = E_b(s)$.

3.3.4 Population control

A drawback of using a continuum framework is the difficulty in incorporating biological detail at the cell level. For instance, how does one specify cell type and heterogeneity in cell properties, such as proliferation and mechanical stiffness? Moreover, it can be difficult to incorporate control of cell populations through mechanisms such as cell death. Here, we will present methods to incorporate cell death within the morphoelastic framework, and discuss how the definition of a continuous quantity can serve as a proxy for cell type.

Cell turnover

A key feature of the crypt is turnover through cell death. This arises through either apoptosis of differentiated cells at the top of the crypt, where cells are 'sloughed' via ejection into the lumen, or through anoikis, where overcrowding can

drive cellular extrusion from the monolayer and detachment from the basement membrane [57, 182].

To simulate sloughing, we 'discount' the ends of the rod, shifting the points at which the clamped boundary conditions, (3.10), are applied. The new boundaries are denoted by $S_0 = 1 - L_\mu \geq 0$ and $S_0 = L_\mu \leq 1$. We now only apply the balance equations (3.4)–(3.8) within the region $[1 - L_\mu, L_\mu]$, ignoring regions outside these boundaries. That is, cell death at the boundary is accounted for by shrinking the reference domain.

We denote by the quantity μ the amount of material sloughed. Then we can relate μ to L_μ and γ by the relation

$$\mu = \int_0^{1-L_\mu} \gamma dS_0 + \int_{L_\mu}^1 \gamma dS_0. \tag{3.27}$$

We can specify criteria to determine cell death through μ based on biologically-motivated mechanisms for cell death. Alternatively, differentiating Equation (3.27) with respect to time yields a differential equation for L_μ, in terms of a sloughing rate $\dot{\mu}$ and $\dot{\gamma}$, which is specified by Equation (3.2):

$$\dot{\mu} = -\dot{L}_\mu \left[\gamma(1 - L_\mu, t) + \gamma(L_\mu, t)\right] + \int_0^{1-L_\mu} \dot{\gamma} dS_0 + \int_{L_\mu}^1 \dot{\gamma} dS_0. \tag{3.28}$$

Having cell turnover allows us to achieve a quasi-steady state in the growth evolution, so that the morphology can attain a steady state even as growth processes continue to evolve.

Specifying cell type

A typical drawback of continuum models is the difficulty in specifying subcellular and cell-level detail. This means that material properties must either be imposed, or phenomenological evolution equations must be specified. One approach to rectify this is to specify cell type through a continuous proxy, such as age. At a cell level, age can be assumed to be regulated by the growth activity of a cell. For instance, stem cells, when proliferating actively, can delay ageing through continuous cycling and division, whereas transit-amplifying cells and mature, differentiated

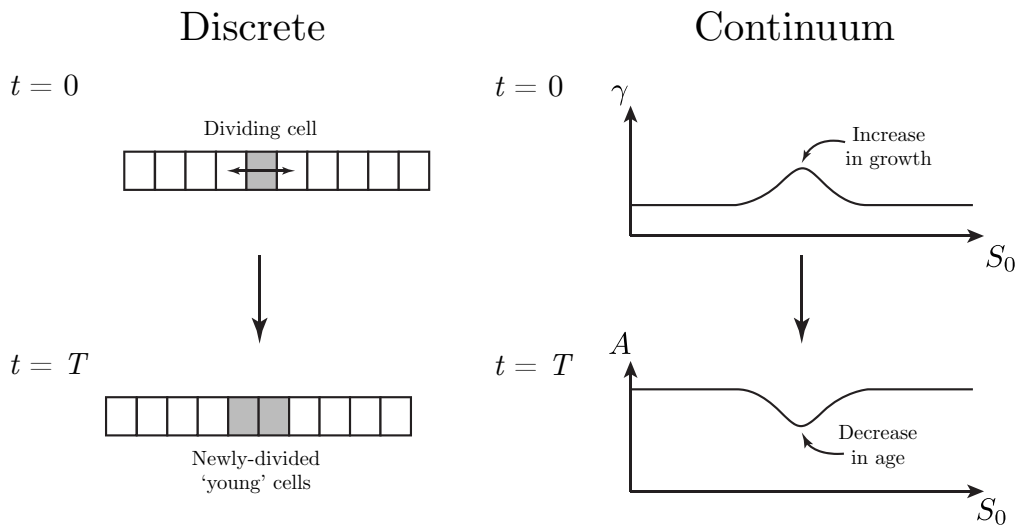

Figure 3.3: Ageing within the continuum framework. Local growth leads to a decrease in age.

cells will experience more rapid turnover. Therefore, at a continuum level, one may propose the following law:

$$\dot{A} = a - \frac{\dot{\gamma}}{\gamma} A, \tag{3.29}$$

where $A = A(S_0, t)$ denotes the age at material position S_0 and time t, and a is the 'base rate' of ageing compared to the growth timescale. Equation (3.29) describes the concept that all cells within the tissue are cycling through a 'clock' at a rate which is modulated by the cell's proliferative activity. For instance, if $\dot{\gamma}\gamma^{-1}$ is high, corresponding to high proliferative activity, then the cell will age slower than one with minimal proliferation. This concept is illustrated in Figure 3.3. Introducing ageing as a proxy for cell type may allow more biologically realistic criteria for cell death to be specified through Equation (3.27).

3.3.5 Facilitating realistic crypt morphologies

The morphologies of epithelia present a unique modelling challenge. For example, in the human colon, crypts are roughly five times as long as they are wide [170]. This means consideration of the growth evolution of the rod well beyond the point of buckling. Evolving the system this far into the post-buckled regime increases the chance of self-contact occurring significantly. Typically, in models assuming

planar deformation, such as ours, simulations will be stopped long before self-contact occurs, as evolving the system any further risks the formation of 'loops' that result in the material self-penetrating. However, it is biologically unrealistic that this geometric feature is a biological stopping criteria for the growth of epithelia. Moreover, epithelial glands experience spatial competition due to the presence of neighbouring tissue. Therefore, we also require models that can account for both self-contact and spatial competition induced by neighbouring epithelial tissue.

Modelling self-contact

In order to observe deformations akin to those witnessed for epithelial tissue, it is important that growth is allowed to continue on biologically realistic timescales, without being hindered by geometric constraints such as self-contact. Self-contact is an important feature of long biological filaments that undergo significant deformation, such as DNA supercoiling and polymer knotting [41, 172]. While the mechanics of self-contact is well outlined in the literature [41, 46, 73, 80, 152, 163, 172, 177], it is a complex and computationally intensive feature to add. Our purpose is to allow deformations to continue *ad infinitum*, which requires a clear description of self-contact, both at a point and along a region. For the sake of clarity, we only outline the main mathematical principles behind this framework; the full details are described in Appendix B.

In this framework, self-contact is assumed to be both frictionless and symmetric. The principle is as follows and is illustrated schematically in Figure 3.4. Initially, the planar rod grows in the absence of self-contact, until it is close to self-penetrating. At this point, self-contact occurs at an isolated point, $S_0 = S_c$, which is defined such that $x(S_c) = x_0 > 0$, where x_0 the half-width of the self-contact opening. We incorporate this constraint into the total energy of the system, which can be decomposed:

$$\mathcal{E} = \mathcal{E}^{\text{rod}} + \lambda_c(x(S_c) - x_0), \tag{3.30}$$

where $\mathcal{E}^{\text{rod}}$ is the total energy of the rod in the absence of self-contact and λ_c is a Lagrange multiplier that enforces the self-contact condition. The resulting

force balance equations are obtained by minimising the total variation of $\mathcal{E}$. In Appendix B, we show that modelling self-contact in this manner leads to a jump in the horizontal force component n_x about $S_0 = S_c$, indicating that self-contact acts as a repulsive horizontal force to maintain planarity. Note that our assumption of symmetric self-contact means that we need only consider self-contact at one point along the half-interval, rather than two points along the full interval.

After further growth, the self-contact point may expand to a finite region of self-contact, denoted by $[S_c^{(1)}, S_c^{(2)}]$, which is defined such that $x(S_0) = x_0$ in the self-contacted region. By modelling the expansion of the self-contact point, we aim to capture the 'zippering' process of tissues such as the crypt, which become enclosed during developmental growth, but continue to invaginate downwards. This type of self-contact is modelled by replacing the point contact condition in (3.30) with a pointwise Lagrange multiplier:

$$\mathcal{E} = \mathcal{E}^{\text{rod}} + \int_{S_c^{(1)}}^{S_c^{(2)}} \lambda_c(S_0)(x(S_0) - x_0)dS_0. \tag{3.31}$$

Minimising the total variation of $\mathcal{E}$ reveals that self-contact is enforced through a pointwise horizontal repulsion force along $[S_c^{(1)}, S_c^{(2)}]$. Consequently, along the self-contact region, the bending moment $m(S_0) = E_b\gamma^{-1}\theta'(S_0) = 0$. More complete details are given in Appendix B. Hence, the transition from self-contact at a point to self-contact along a region is marked by the condition $m(S_c) = 0$.

Spatial competition

While we have focussed on modelling the growth of a single epithelial gland, epithelial glands do not grow in isolation. Rather, multiple, adjacent tissue structures form simultaneously, and are tightly packed [183]. It is hence worth exploring the consequences of spatial competition induced by neighbouring epithelial structures on the growth of the gland in consideration. The presence of adjacent glands, such as crypts, combined with the resistive effects of underlying extracellular matrix networks and substrates, prevent the tissue from bulging outwards excessively. We illustrate this concept schematically in Figure 3.5. As a proof of concept,

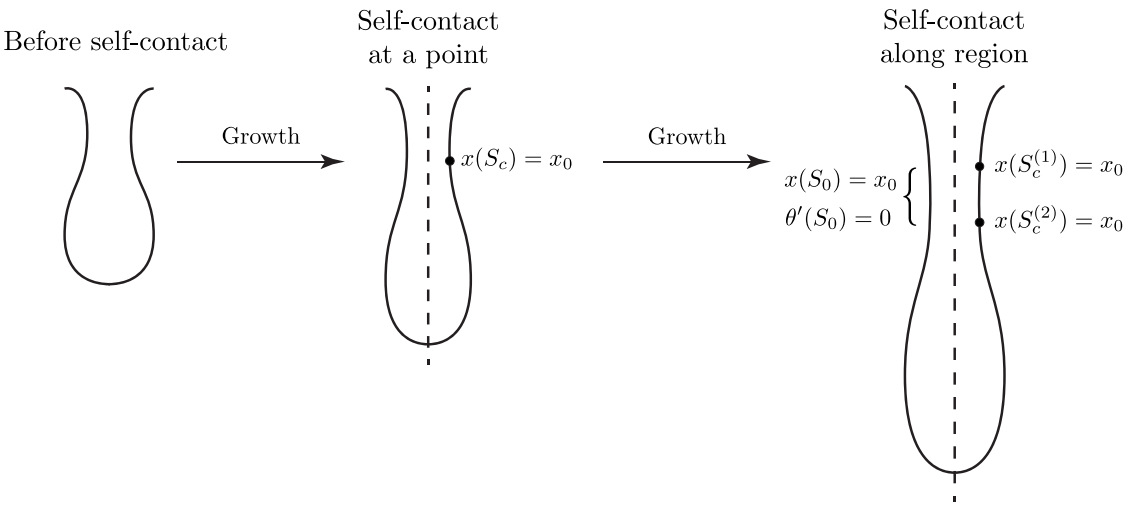

Figure 3.4: The key features of the self-contact model. This ensures that as growth continues, the planarity assumption is not violated. The self-contact width is given by $2x_0 > 0$. Eventually, the self-contact point expands to a region.

we model this competition through a horizontal repulsion force, modifying the horizontal force balance as such:

$$n'_x = \gamma \frac{\sigma}{\Delta}(x - p_x) + \gamma q \left[\frac{1}{(x-1)^2} \mathrm{H}(1-x) - \frac{1}{x^2} \mathrm{H}(x) \right], \tag{3.32}$$

where the second term on the right hand side describes a repulsion force, where $\mathrm{H}(x)$ is the Heaviside step function. The force pushes the rod away from the vertical boundaries, $x = 0$ and $x = 1$, and towards the invagination's axis of symmetry, $x = 1/2$. The functions x^{-2} and $(x-1)^{-2}$ have been chosen so that regions along the rod that are farther from $x = 0$ and $x = 1$ experience a reduced repulsive effect compared to regions that are closer to $x = 0$ and $x = 1$. The step functions have been incorporated in order to prevent further deformation if any internal region of the rod crosses $x = 0$ or $x = 1$. The rate of spatial decay of the repulsive force is controlled by the parameter q, which we assume to be equal from both the left and right neighbouring structures.

We note that the type of spatial competition induced by the force law in Equation (3.32) is possible even in the absence of self-contact. Another feature that may be relevant following the onset of contact is the entrapment of material, such as extracellular fluid, that becomes enclosed by the gland. For example, in the crypt, the opening that connects to the inner intestinal lumen is very small, approximately

6μm [69], suggesting that any material enclosed by the crypt remains entrapped after self-contact. Therefore, we consider a model of self-contact where the enclosed area after self-contact is constant. Letting A_c denote the area enclosed by self-contact and assuming a symmetric morphology about $x = 1/2$, by Green's Theorem, for the case of self-contact at a point, this constraint can be formulated as such:

$$A_c = \int_{S_c}^{1} xy' dS_0 = A_0 > 0, \tag{3.33}$$

where A_0 is prescribed by the area enclosed at the first moment of self-contact. For self-contact along a region, we replace S_c by $S_c^{(2)}$. The imposition of a constant self-encapsulated area is also considered by Jambon-Puillet et al. [94], who modelled the folding of an elastic rod at a liquid-fluid interface due to compression. We show in Appendix B that the constraint (3.33) introduces a normal pressure, akin to that modelled in Flaherty et al. [63].

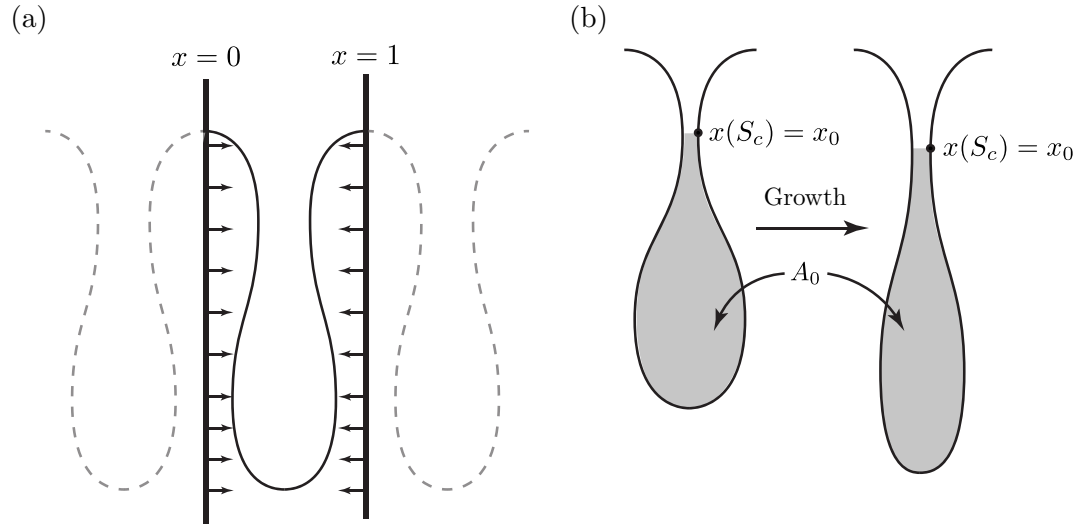

Figure 3.5: Mechanical effects induced by neighbouring tissue. (a) In the crypt, it is likely that the presence of adjacent crypts enforces spatial constraints on the growing crypt. By symmetry, we model these effects as repulsive forces from the domain boundaries, $x = 0$ and $x = 1$. (b) We can also impose that the self-encapsulated area is constant after self-contact. As the rod grows, while the self-contact point $S_0 = S_c$ may change over time, the self-encapsulated area A_0 does not change once self-contact occurs.

3.4 Results

In this section, we present simulation results for the effects of the different models we have proposed within the morphoelastic rod framework for a growing, epithelial tissue. In all cases, the foundation stiffness scaling parameter k_f has been set to $k_f = 0.01$, which produces a mode 1 shape upon buckling. This shape represents the morphogenesis of a single epithelial gland, such as the crypt or hair follicle. As our over-arching motivating example is the intestinal crypt, we use dimensional parameters based on estimates from histological images of human colonic crypts [170]. Accordingly, the slenderness scale has been chosen such that we assume a rectangular cross-section of height $h = 15\mu m$, width $w = 10\mu m$, and initial rod length $L_0^* = 125\mu m$. Unless specified, all material parameters, i.e. growth γ, the bending stiffness E_b, and foundation stiffness k, are homogeneous. For homogeneous growth, the growth stretch γ is updated according to the equation $\dot{\gamma} = 1$.

For all simulations, morphogenesis is triggered through growth-induced buckling. As we assume the rod is inextensible, buckling occurs at $t = 0$. All time derivatives are discretised using the Forward Euler method. For each time step, the governing equations (3.4)–(3.8) are solved numerically using the MATLAB package `bvp4c`, which employs a fourth-order spatial collocation method [101, 156]. The initial guess used for all simulations is obtained by solving the model for a linear elastic foundation [2, 120]. The time step increment δt is chosen such that there is no jump in solution branch and stability as the simulation progresses; as such, δt is set in the range $\delta t = 0.01 - 0.05$.

As data related to the mechanical properties of epithelial tissue are extremely limited, we gauge the efficacy of our modelling choices on morphological characteristics and aspects that we can measure, such as the internal stresses. Assuming a symmetric solution about $x = 1/2$, with $y(1/2) < 0$, Figure 3.6 illustrates the morphological features that we extract. These include:

- The local peak,

$$P_y = \max\{y(x) : x \in [0, 1]\}.$$

- The invagination depth,

$$D_y = \min\{y(x) : x \in [0,1]\}.$$

- The invagination width

$$\frac{W_y}{2} = \frac{1}{2} - \min\left\{x(S_0) : \theta(S_0) = \frac{\pi}{2}\right\}.$$

- The aspect ratio $A_y = W_y/D_y$.

We use criteria based on these measurements to evaluate model choices. For example, a typical crypt morphology contains a narrow, highly-invaginated structure, with minimal, to no, peaks. Consequently, in an accurate model, we would expect the peaks P_y to be small, the invagination depth D_y to be large, and the aspect ratio A_y to be small. Moreover, as the rod grows over time and D_y increases, A_y should decrease over time, while P_y should not increase significantly.

We also track the net axial stress, originally defined in Equation (2.50), for $L_0 = 1$:

$$\overline{n}_3 = \left|\int_0^1 n_3 dS_0\right| = \left|\int_0^1 n_x \cos\theta + n_y \sin\theta dS_0\right|, \tag{3.34}$$

and the net foundation stress, $\overline{\sigma}$, which is defined in a similar manner:

$$\overline{\sigma} = \left|\int_0^1 \sigma dS_0\right|. \tag{3.35}$$

We measure these components rather than the horizontal and vertical forces, because of the highly nonlinear geometry of the resulting morphologies. For example, the axial stress n_3 provides a measure of the compressive or tensile stresses that cells experience along the direction of the epithelium.

3.4.1 Comparison of foundation relaxation models

We now explore the effect on overall morphology of the different foundation relaxation mechanisms (i.e. stress relaxation and attachment remodelling). We focus on the effect of varying separately the respective stress and foundation relaxation

parameters, ν and ρ. For a viscoelastic foundation, the parameter ν describes the competition between the growth timescale and the viscoelastic stress relaxation timescale. Large ν indicates shorter viscoelastic timescales (compared to the growth timescale), resulting in rapid relaxation of the viscous attachments. For a remodelling elastic foundation, for large ρ, the foundation attachments quickly relax to the current rod shape.

In both cases, for a given value of ν or ρ, we consider two regimes. First, when the foundation is relaxing during growth, which we simulate according to $\dot{\gamma} = 1$ up to to $t = 1$, and subsequently, when we pause growth ($\dot{\gamma} = 0$) and allow the foundation to continue evolving up to $t = 2$.

Foundation stress relaxation For the viscoelastic foundation, the parameter β quantifies the weighting of the stiffnesses between the Maxwell and the purely elastic units. For $0 < \beta < 1$, the viscoelastic attachments will exhibit creep under a constant applied stress. However, it is unclear how this parameter will affect the system during, and after, growth. In Figure 3.7, we plot the net axial stress, $\overline{n}_3$, and the net foundation stress, $\overline{\sigma}$, for different β. There is very little difference in the evolution of the stresses for different values of the parameter β. That is, under constant growth, the effect of introducing creep through β is minimal. Henceforth,

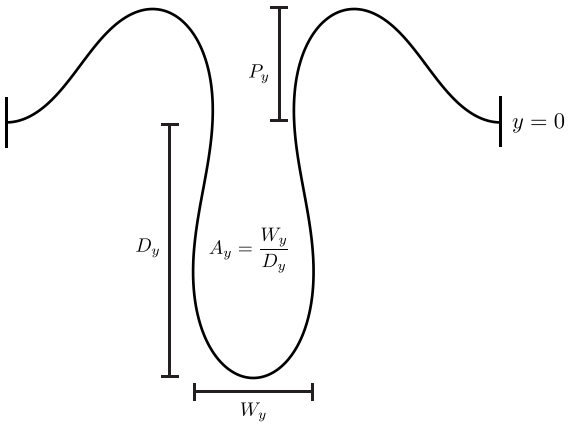

Figure 3.6: Morphological features of interest. For each grown morphology, we measure the local peaks P_y, the invagination depth D_y, the invagination width W_y, and the aspect ratio of the invagination, $A_y = W_y/D_y$.

for the viscoelastic stress case, fixed $\beta = 0.5$, balancing the contributions between the Maxwell and purely elastic units.

Figure 3.8 displays the effect of increasing the foundation stress relaxation, ν, on the resultant morphology. As the rod grows (Fig. 3.8(a)), increasing ν enables a larger invagination depth D_y to develop, while diminishing the growth of local maxima P_y. However, the same is not observed when growth is paused. In Figure 3.8(b), growth is halted and the foundation stress σ is allowed to relax. We observe that unless ν is large, the relaxation of σ leads to an overall decrease in post-buckled amplitude, reducing D_y and increasing P_y significantly. We note that for $\nu = 0.01$, self-contact occurred during the pure relaxation phase. The differences in behaviour can be explained by the discrepancies between the growth timescale of the rod and viscous timescale of the foundation attachments. As the rod continues to grow, the elastic force increases in magnitude. Once growth is arrested, if the viscous attachments have not relaxed sufficiently quickly, the effects of the elastic force dominate, pulling the rod back to the initial attachment location.

Figure 3.9 displays the corresponding net axial forces, $\overline{n}_3$, and foundation stress, $\overline{\sigma}$, during growth and post-growth foundation relaxation. Consistent with previous

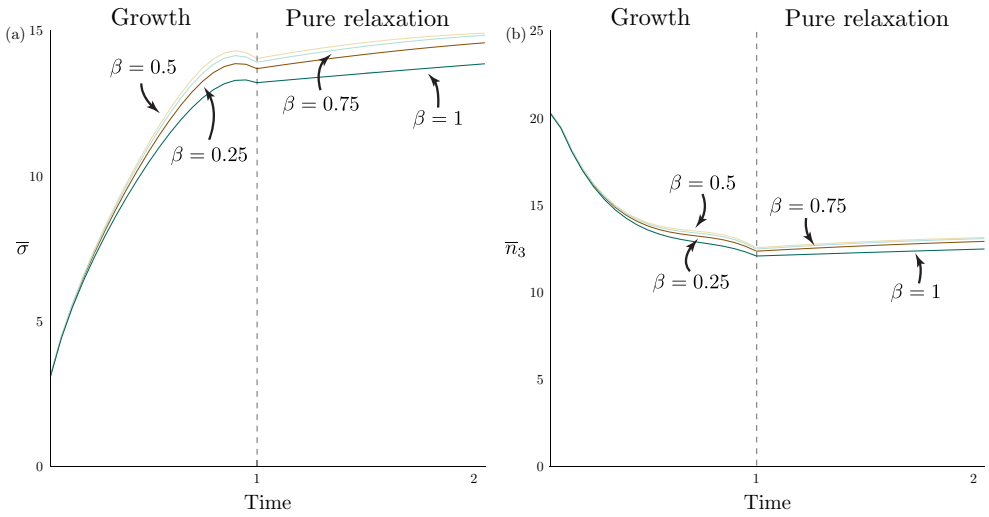

Figure 3.7: Viscoelastic creep does not influence internal or external foundation stress. (a) The net foundation stress $\overline{\gamma}$ has been plotted for various values of β, during growth, $0 \leq t \leq 1$, and pure relaxation of foundation stress, $1 < t \leq 2$. (b) The net axial stress within the rod, $\overline{n}_3$. The choice of the parameter β does not have a significant effect on stress behaviours.

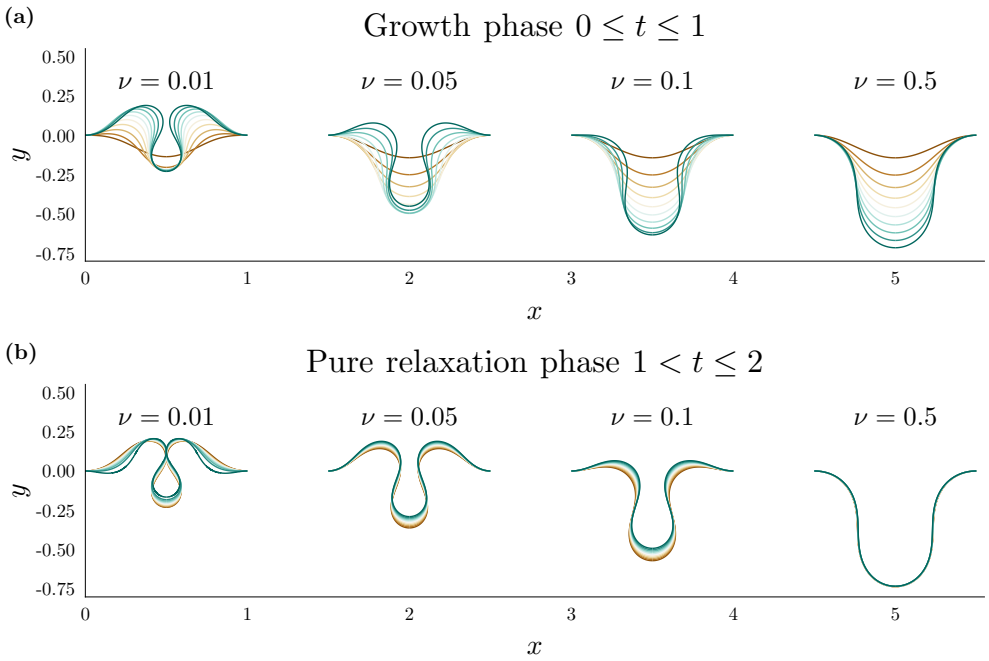

Figure 3.8: Increasing the rate of viscoelastic foundation stress relaxation deepens rod invagination. (a) The resultant morphology at times $t = 0.1, 0.2, \ldots, 0.9$, $t = 1$ has been plotted for $\nu = 0.01, 0.05, 0.1$, and 0.5, with homogeneous growth and stiffnesses. Each plot along the x-axis is a separate simulation. The viscoelastic weighting parameter β has been set to $\beta = 0.5$. Solutions are plotted at the same times, with each time corresponding to a displayed line colour. Dark brown lines denote earlier times, while dark green lines denote later times. Increasing the rate of stress relaxation in Equation (3.16) results in deeper invagination lengths. (b) Growth has been paused, and the foundation stress σ continues to evolve up to $t = 2$.

results, growth-induced buckling relieves stress within the rod [2]. Moreover, as ν is increased, the net amount of axial stress and foundation stress both decrease. However, once growth has stopped and σ continues to evolve, for all cases except $\nu = 0.01$, the net axial stress does not change significantly, nor does the net foundation stress, $\overline{\sigma}$. The behaviour for $\nu = 0.01$, can be attributed to the rod undergoing self-contact during the pure foundation relaxation phase, which introduces a horizontal repulsion force about the point of self-contact. As the foundation stress continues to relax, the repulsion force increases in magnitude to maintain self-contact, resulting in the observed increase in net axial stress after growth.

Foundation attachment remodelling We now examine the effect of relaxation through the foundation attachments, as per Equation (3.19). Figure 3.10 shows the growth evolution of rod shapes for various values of the parameter ρ, which

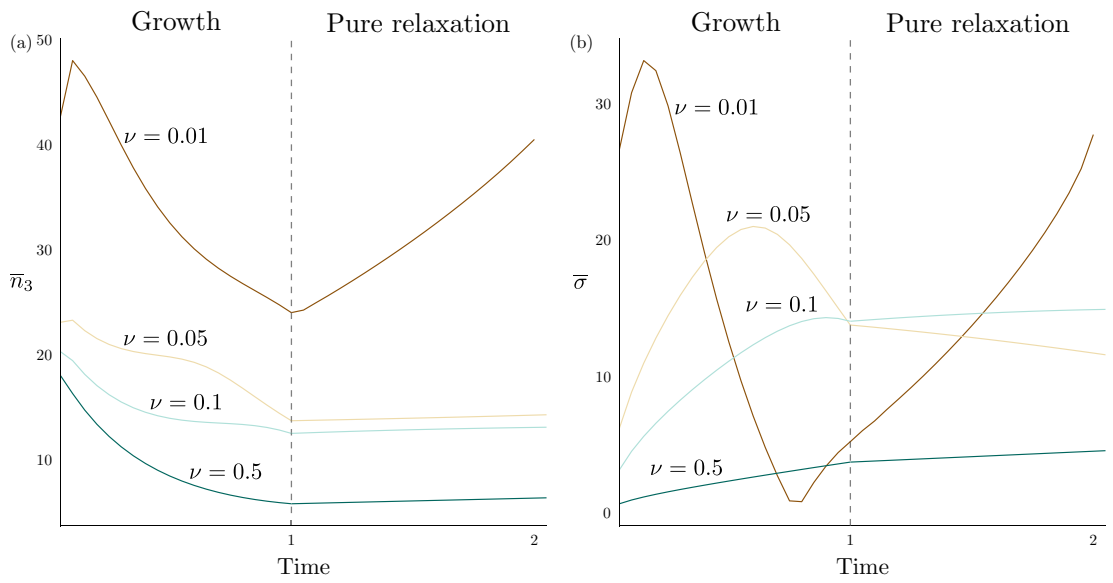

Figure 3.9: Viscoelastic foundation stress relaxation relieves internal stress. (a) The net axial stress $\overline{n}_3$ is plotted for $\nu = 0.01, 0.05, 0.1$ and $\nu = 0.5$ during growth and pure foundation relaxation. (b) The foundation stress $\overline{\sigma}$, where σ evolves according to Equation (3.16).

characterises the rate of foundation attachment relaxation. In Figure 3.10(a), the rod is grown until $t = 1.0$ for each specified value of ρ. Increasing ρ has a similar effect to increasing the foundation stress relaxation parameter ν; as the foundation can relax to the current rod shape more rapidly, the resistance to deformation imposed by the elastic foundation diminishes. Therefore less growth is required to increase the overall rod amplitude. In Figure 3.10(b), we arrest growth and allow the foundation attachments $\mathbf{p}$ to relax. For all values of $\rho > 0$, if there is any change, we observe an increase in rod invagination depth D_y and a decrease in rod local maxima height P_y. This behaviour is in contrast to that for the viscoelastic foundation model, where P_y increased significantly after growth. Moreover, the effect of increasing ρ saturates—for $\rho \geq 5$, the invagination depth D_y and width W_y do not increase significantly.

Figure 3.11 demonstrates that the remodelling foundation law relieves stress within the rod and external foundation stress, both during growth and relaxation. The net axial and foundation stresses are tracked during the growth and relaxation phases of the shape evolution. In Figure 3.11(a), increasing ρ decreases the net

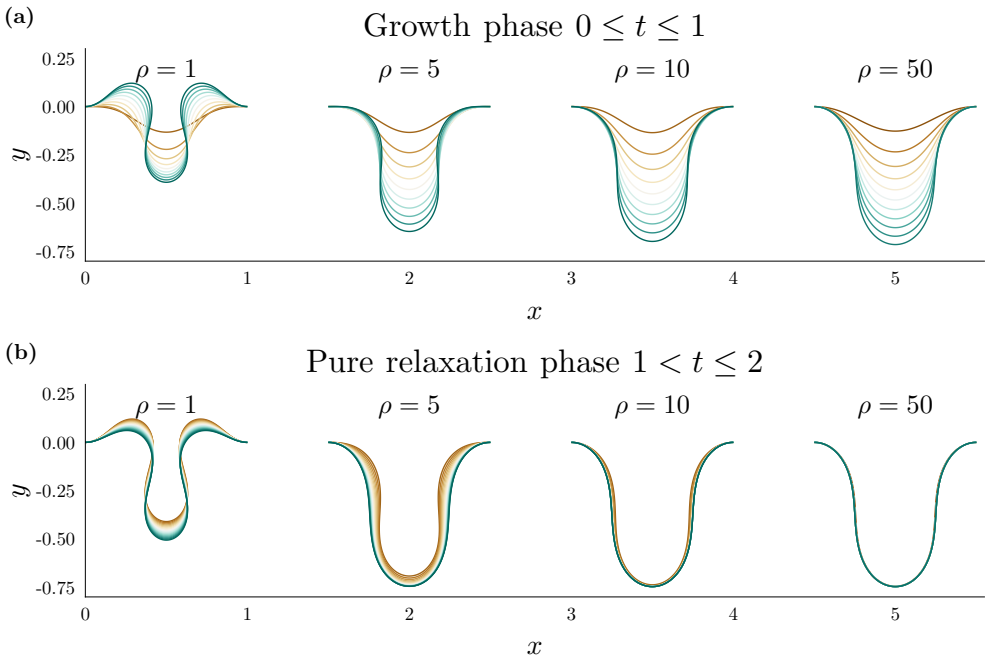

Figure 3.10: Foundation attachment remodelling increases rod invagination. (a) The rod morphology has been plotted for $\rho = 1, 5, 10$, and 50, with homogeneous growth and stiffnesses, over times $t = 0.1, 0.2, \ldots, 1.0$. Each plot along the x-axis is a separate simulation. Line colours correspond to the same times; dark brown lines denote earlier times, while dark green lines denote later times. Increasing the rate of attachment relaxation results increases the invagination depth D_y and decreases the local maxima height P_y. (b) Growth has been paused, and the foundation attachments $\mathbf{p}$ are allowed to relax up to $t = 2$. For all values of ρ, the rod invagination deepens.

amount of axial stress within the rod, as well as the rate of decay, during both growth and pure relaxation. The same behaviour is observed in the foundation stress, where the rapidly-relaxing foundation shape leads to a decrease in foundation stress. As we have modelled the attachments to be linearly elastic, the foundation stress scales with the distance between the rod shape and foundation shape. Hence, if the foundation shape can relax rapidly to the current rod shape, the foundation stresses will correspondingly be reduced.

Comparing foundation models Figure 3.12 compares the rod morphologies after growth to a fixed time and relaxation, for an elastic, viscoelastic, and remodelling foundation. Here, the viscoelastic parameter has been set to $\nu = 0.1$, while the remodelling parameter is set to $\rho = 10$, corresponding to equivalent dimensional timescale ratios. That is, for a viscoelastic foundation, the viscous relaxation

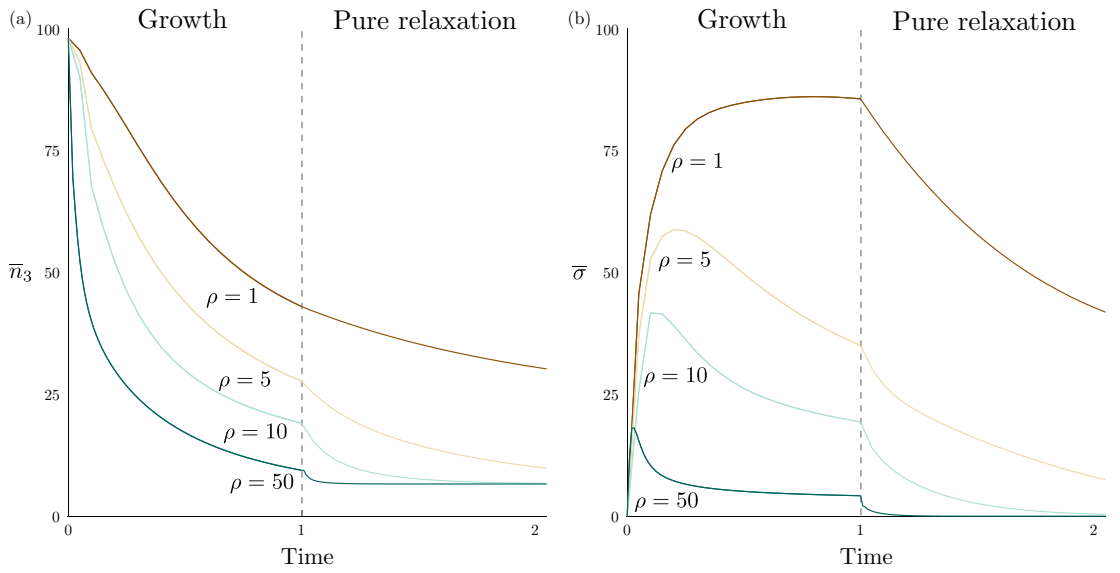

Figure 3.11: Foundation attachment remodelling relieves internal and external stresses. The parameter ρ dictates how rapidly the foundation attachments remodel. (a) The net axial stress, $\overline{n}_3$, during the growth phase, $0 \leq t \leq 1$, and pure relaxation phase, $1 < t \leq 2$. A rapidly-remodelling foundation shape quickens the rate of internal stress relaxation. (b) The net foundation stress, $\overline{\sigma}$, shows that remodelling the foundation attachments also reduces external foundation force.

timescale $\eta_\sigma = 0.1\tau$, where τ is the growth timescale, while for the remodelling foundation, the attachment relaxation timescale $\eta_{\mathbf{p}} = 0.1\tau$. In Figure 3.12(a), the viscoelastic and remodelling foundation morphologies are comparable, although the remodelling foundation law results in quicker invagination. Figure 3.12(b) highlights the main differences in behaviours. After relaxation, the invagination depth of the rod that is attached to a viscoelastic foundation decreases. This demonstrates that an evolving foundation shape may provide a better model to generate deeply-invaginated morphologies, even with a linear elastic constitutive law.

3.4.2 Morphological effects of intrinsic curvature relaxation

The intrinsic epithelium shape has thus far been assumed to correspond to a flat shape. This assumption is modelled in the constitutive relation for the bending moment (3.9): $m = E_b(\kappa - \hat{\kappa})$, where $\kappa = \theta'\gamma$ and $\hat{\kappa} = 0$. If $\hat{\kappa}$ is prescribed to be equivalent to a deeply-invaginated shape, then the resulting force and moment balance will produce this shape (in the absence of a foundation). This then begs

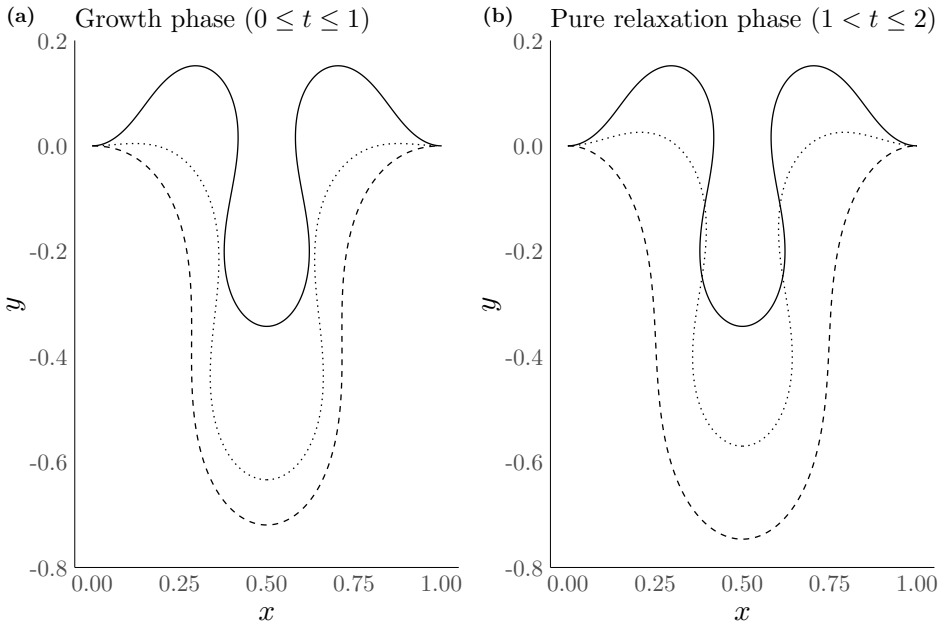

Figure 3.12: Foundation attachment relaxation yields the deepest invaginations. (a) Solutions for the elastic foundation case (solid line); the standard linear solid foundation case (dotted), for $\beta = 0.5$ and $\nu = 0.1$; and the remodelling foundation case (dashed), for $\rho = 10$, have been plotted at $t = 1$. (b) The morphologies after foundation relaxation mechanisms have evolved up to $t = 2$.

the question: it is possible for $\hat{\kappa}$ to evolve naturally to such a shape? Moreover, is it sufficient to describe the evolution of $\hat{\kappa}$ through Equation (3.23), $\dot{\hat{\kappa}} = \chi(\kappa - \hat{\kappa})$? Concluding our study of relaxation, we examine the effect of an evolving intrinsic curvature, $\hat{\kappa}$, according to Equation (3.23). This is equivalent to the epithelium itself exhibiting plastic relaxation. Figure 3.13 displays the resulting morphologies for different values of the intrinsic curvature relaxation parameter χ. In Figure 3.13(a), we grow the rod until $t = 1$ for each value of χ. As χ increases, the invagination depth D_y decreases with the magnitude of this reduction increasing with χ. After allowing $\hat{\kappa}$ to relax to a steady state in Figure 3.13(b), the decrease in D_y and increase in P_y is exacerbated further. Moreover, for $\chi = 1$ and $\chi = 5$, we observe a 'bifurcation' in the base, which leads to an increase in the mode. This behaviour stems from the significant reduction in the bending energy. As $\hat{\kappa}$ relaxes rapidly to the current curvature, the contributions to the total energy due to bending decrease, which leads to a reduction in invagination depth. Moreover, when growth is paused and Equation (3.23) continues to evolve, varying χ changes

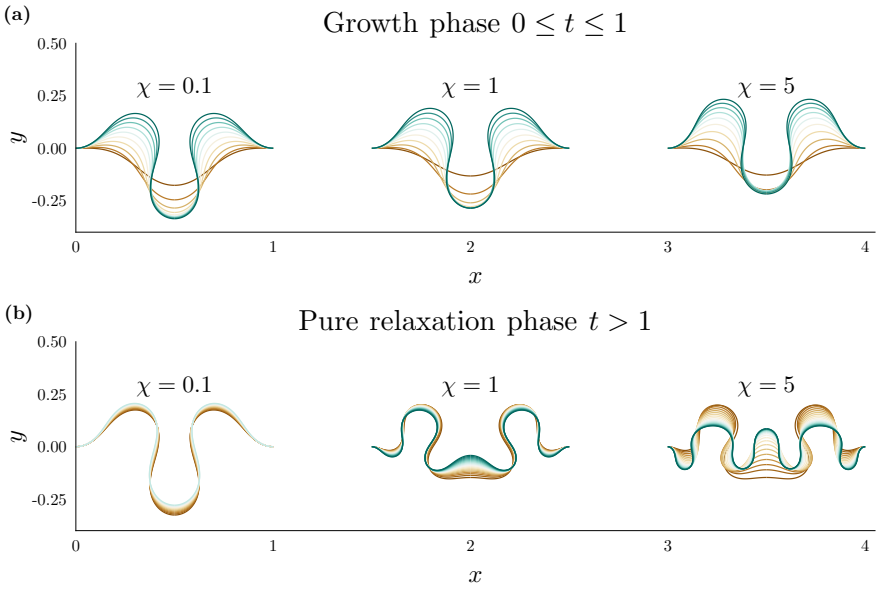

Figure 3.13: The effect of intrinsic curvature remodelling. We consider the cases $\chi = 0.1, 1, 5$, where χ is the parameter which in Equation (3.22)controls how rapidly the intrinsic curvature $\hat{\kappa}$ remodels. For each value of χ: (a) the rod is tethered to an elastic foundation and grown up to $t = 1$; (b) the intrinsic curvature $\hat{\kappa}$ is allowed to evolve to a steady state, according to Equation (3.23). Each plot along the x-axis is a separate simulation. Line colours correspond to the same times; dark brown lines indicate earlier times, while dark green lines indicate later times. A rapidly-relaxing intrinsic curvature counteracts growth-induced invagination.

the profile for $\hat{\kappa}$ at $t = 1$. While this 'fissioning' feature is interesting, it does not lead to a deeper invagination. Therefore, it is unlikely that a relaxation of intrinsic curvature contributes to a realistic crypt morphology.

3.4.3 Exploring contributors to epithelial tissue growth

Having established feasible mechanisms of relaxation for buckling epithelia, we now turn our attention to exploring models of tissue growth. Henceforth, we employ a remodelling foundation law (3.19), with the relaxation parameter set to $\rho = 10$. We aim to establish the mechanisms that generate the most realistic proliferative structures and morphologies for the crypt and related biological systems. We showed in Section 2.4.3 that heterogeneous growth redistributes material towards regions where $\gamma(S_0)$ is large and away from regions where γ is minimal, producing a morphology significantly different from that observed under homogeneous growth. Here, we investigate whether growth-related processes, such

as chemical signalling, are more appropriately defined with respect to the Lagrangian or Eulerian reference frames, which are parametrised by the initial arc length S_0 and current arc length s, respectively.

During simulations, we track the relative growth rate, $\dot{\gamma}\gamma^{-1}$, as defined by Equation (3.2). This provides a better measure of proliferation within the epithelium than the growth stretch, $\gamma(S_0, t)$, which describes the total growth over the entire growth history, at each point S_0.

Chemical signalling parametrisation affects morphology

As a case study, we examine growth due to Wnt signalling within the crypt. As it is established there is a decreasing spatial profile of Wnt proteins along the crypt axis [67], it is appropriate to define the Wnt signal concentration through a Gaussian function. However, from a modelling perspective, it is not clear how rapidly this profile decreases, or whether it is fixed with respect to Eulerian or Lagrangian coordinates, i.e. the current arc length parameter s or initial arc length S_0. In other words, it is not clear how wide the imposed Gaussian function, dictated by the parameter σ_W, should be.

In Figure 3.14, we show how biohemically-regulated growth affects the morphologies that emerge. The simulation results were generated by defining the Wnt signal functions, W, in terms of either initial or current arc length parameters, S_0 and s, in the following manner:

$$\frac{\dot{\gamma}}{\gamma} = W, \tag{3.36}$$

where

$$W(S_0) = \exp\left[-\left(\frac{S_0 - 0.5}{\sigma_W}\right)^2\right], \quad \text{or} \quad W(s) = \exp\left[-\left(\frac{s - 0.5l}{\sigma_W}\right)^2\right], \tag{3.37}$$

where $l = l(t) = \int_0^1 \gamma dS_0$ is the total rod length at time t. If $W = W(S_0)$, then the region of enhanced incremental growth expands as the rod grows, resulting in greater net growth at each time step. Consequently, the rod invaginates at a quicker rate, but the increasing accumulation of material away from the base leads

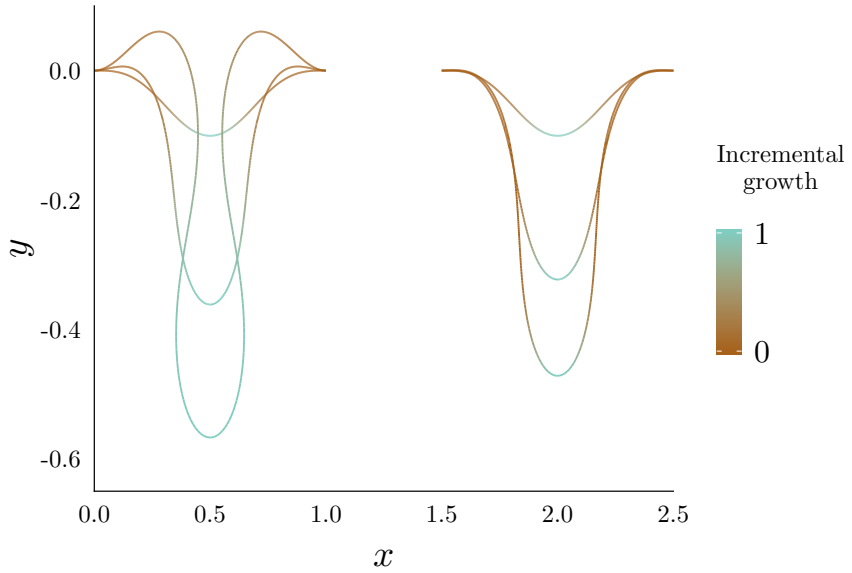

Figure 3.14: Chemical signalling parametrisation affects morphology significantly. The morphologies under chemical-signal-driven growth, $\dot{\gamma}\gamma^{-1} = W$, are shown for the cases $W = W(S_0)$ (left) and $W = W(s)$ (right), as per (3.37). Plots are shown at times $t = 0.1, 1, 2$, where both profiles invaginate down for increasing time. The Gaussian width parameter has been set to $\sigma_W = 0.16$. An Eulerian parametrisation $W = W(s)$ generates a more realistic crypt morphology.

to a significant increase in local peak height, P_y, that coincides with the increase in invagination depth D_y. By contrast, setting $W = W(s)$ models a compartment of enhanced incremental growth that is fixed in size over time. While this leads to a smaller invagination depth D_y for a given growth time, peaks do not develop during this growth phase, i.e. $P_y(t) = 0$, since the growth is always focussed in the central region. This shows a strong morphological difference between the Lagrangian Wnt signal $W(S_0)$ and the Eulerian Wnt signal $W(s)$. In the context of the crypt, Eulerian signalling leads to a more realistic crypt morphology. Moreover, from a biological perspective, chemical signal concentrations can be directly monitored and remodel over time, depending on spatial position [162], suggesting that the Eulerian parametrisation is, in general, a more accurate modelling choice. Therefore, in Chapter 4, we will employ an Eulerian parametrisation to model the Wnt signal profile in the crypt.

3.4.4 Varying mechanical stiffness

The results in Section 2.4.3 demonstrated that for an inextensible rod, heterogeneity in rod stiffness redistributes the rod curvature towards reasons where $E_b(S_0)$ is minimal, corresponding to softened regions of the rod. In the context of crypt morphogenesis, we once again ask whether or not defining E_b as a Lagrangian or Eulerian quantity makes a difference to the resulting morphology.

We consider the effect of heterogeneous epithelial cell stiffness, modelled through the bending stiffness E_b. In particular, we consider the effect of introducing softened tissue regions on buckling and growth evolution. We do this by assuming the following functional forms for the bending stiffness E_b from Equation (3.26):

$$E_b(S_0) = 1 - b\exp\left[-\left(\frac{S_0 - 0.5}{\sigma_b}\right)^2\right]$$

or

$$E_b(s) = 1 - b\exp\left[-\left(\frac{s - 0.5l}{\sigma_b}\right)^2\right]$$

where we vary the parameters b and σ_b, which control the degree of stiffness variation and width of the softened region of epithelial tissue, respectively.

Stiffness parametrisation does not affect morphology for small stiffness variations

We compare simulation results for Lagrangian versus Eulerian heterogeneity, $E_b = E_b(S_0)$ versus $E_b = E_b(s)$. When $E_b = E_b(S_0)$, the mechanical properties of the epithelial tissue propagate along the rod as the rod grows. In a line of individual cells, this is analogous to newly-divided daughter cells inheriting mechanical properties from the parent cell. For the latter, the mechanical properties depend on the current position. To quantify the morphological differences between the parametrisations, we use the following two-norm

$$\mathcal{N} = \|\mathbf{r}_{E_b(s)} - \mathbf{r}_{E_b(S_0)}\|_2 = \sqrt{(x_{E_b(s)} - x_{E_b(S_0)})^2 + (y_{E_b(s)} - y_{E_b(S_0)})^2}, \tag{3.38}$$

where $\mathbf{r}_{E_b(s)} = (x_{E_b(s)}, y_{E_b(s)})$ is the shape of the rod subject to $E_b = E_b(s)$ for a given value of b and σ_b (for $\sigma_E = 0.08$ and $\sigma_E = 0.24$), with a similar definition

for $E_b = E_b(S_0)$. Figure 3.15 illustrates how the differences change as the stiffness variation parameter, b, is varied. A common feature of both cases is the minimal difference in morphology when b is small. Only when $b \gtrsim 0.7$, that is, when the base of the invagination is much softer than the top, do differences in morphology become apparent. Moreover, the differences between the two frames of reference are greater for $\sigma_b = 0.24$. This is because when $\sigma_b = 0.08$, the region of softened tissue is initially very thin. When $E_b = E_b(S_0)$, as the rod grows, this region does not expand greatly. However, for $\sigma_E = 0.24$, as the rod grows, for $E_b = E_b(S_0)$, the region expands such that the rod is nearly 'homogeneously' soft. This is not the case for $E_b = E_b(s)$, when the region of softened tissue is the same at all times. While the differences in morphology are more noticeable for larger values of b and σ_b, the differences between morphologies are not significant. Therefore, in this framework, a heterogeneous bending stiffness does not contribute significantly to a deeply-invaginated morphology. As such, we will not consider heterogeneous stiffness in the next chapter, when investigating the possible links between growth and mechanical stress.

3.4.5 Cell turnover induces a morphological steady state

As epithelial tissues display remarkable rates of self-renewal, it stands to reason that growth processes are continuously active and dynamic. Therefore, other mechanisms must contribute to maintaining the 'steady-state' morphologies observed during homeostasis. Here, we investigate the effect of cell turnover on morphology as represented by the sloughing equation (3.27), which describes how the domain of deformation is altered to balance growth and turnover.

To demonstrate this idea, we consider homogeneous and constant growth and assume that sloughing occurs at a constant rate but only after a fixed time, T. In more detail, we specify the following growth and sloughing rates, $\dot{\gamma}$ and $\dot{\mu}$:

$$\dot{\gamma} = 1, \qquad \dot{\mu} = \frac{1}{2}\left[1 + \tanh(10(t - T))\right], \tag{3.39}$$

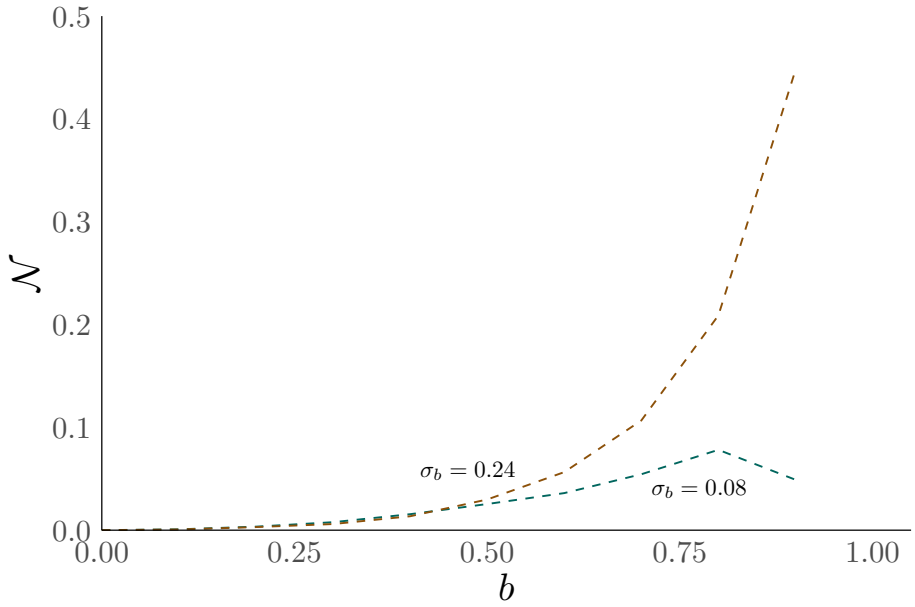

Figure 3.15: Differences between stiffness parametrisations increase with stiffness variation. For heterogeneous stiffness (3.26), the norm $\mathcal{N}$, defined in Equation (3.38), measuring differences between the morphologies for $E_b = E_b(s)$ and $E_b = E_b(S_0)$ at t = 1, for $b = 0, 0.1, \ldots, 0.9$, for $\sigma_E = 0.08$ (dark green, dashed) and $\sigma_E = 0.24$ (dark brown) is plotted. Spatially heterogeneous stiffness only affects morphology significantly when the variation in stiffness is high.

where $T > 0$ describes the time at which cells start to be sloughed from the tissue. The functional form for $\dot{\mu}$ models a rapid transition from zero to non-zero sloughing.

Figure 3.16 shows how the total length, l, changes over time as L_μ evolves according to Equation (3.39) for $T = 2.5$. For $0 < t < 2.5$, there is no cell death and the rod invagination depth increases with the total rod length. For $t \geq 2.5$, cell death acts to balance the material gain from growth γ, and there is no net gain in the total length l. This results in a regime during which the rod morphology does not change significantly, despite the fact that growth continues. This simple example illustrates how our sloughing framework can generate a transition from tissue development, characterised by large morphological changes, to homeostasis, when the morphology is static. Moreover, despite the static morphology there is, nevertheless, a movement of material points, reminiscent of cell migration out of the tissue. This suggests a possible method to parametrise growth and cell death in our model, based on migration data. In Chapter 4, we will develop a

more complete framework of tissue homeostasis, from which this sloughing process emerges as a condition of homeostasis.

3.4.6 Ageing as a proxy for cell properties

One noticeable aspect of our investigations of growth and mechanical stiffness is that heterogeneity has been imposed from the outset and, while spatial profiles of heterogeneous growth and stiffness may rearrange over time, the functional forms of growth and stiffness are fixed. However, in the context of epithelia, these heterogeneous stiffness and growth properties are not present at the beginning of development, but rather emerge over time. Moreover, these properties likely correspond to those of different 'cell types' which, in the context of the crypt, are robust and well established. Hence, it is a valuable exercise to understand how cell types may be incorporated within the morphoelastic framework and affect the growth evolution of the tissue.

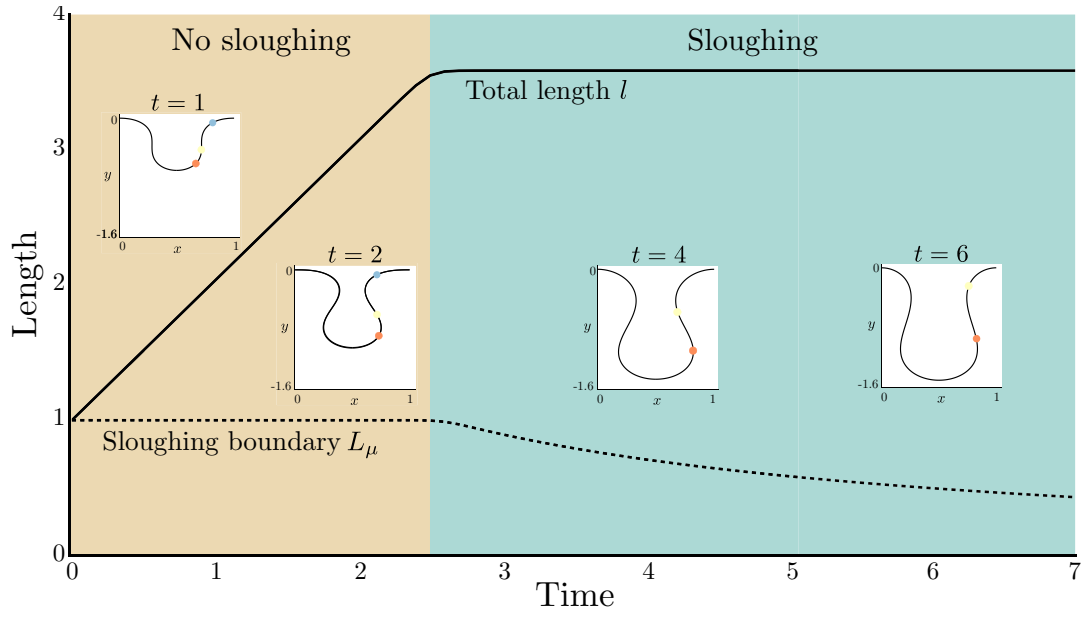

Figure 3.16: Cell sloughing balances active growth. The total rod length l and sloughing boundary, L_μ, as determined by (3.27), are shown over time for homogeneous growth and time-dependent sloughing (3.39). The morphologies at $t = 1, 2, 4, 6$ are also plotted. The positions of the material points that are initially at $S_0 = 0.6$ (orange circle), $S_0 = 0.7$ (yellow circle), and $S_0 = 0.9$ (blue circle) have been marked. Sloughing prevents further invagination, resulting in a quasi-steady state, while also inducing 'migration' of material points.

To this end, we endow each material point with an age, $A(S_0, t)$, which evolves according to Equation (3.29),

$$\dot{A} = a - \frac{\dot{\gamma}}{\gamma} A,$$

where we set the base ageing rate $a = 1$ and growth evolves according to an Eulerian chemical signal, $\dot{\gamma}\gamma^{-1} = C(s)$. The profiles of $A(S_0, t)$ and $\dot{\gamma}\gamma^{-1}(S_0, t)$ have been plotted along the growing rod morphology (x, y) in Figures 3.17(a)–(b). The external signal profile causes a spatially-varying age structure to emerge over time. In the base of the tissue, where $C(s)$ is highest, high proliferative activity causes this region of tissue to age slowly, while material points towards the ends of the rod age faster. Figure 3.17(b) shows that modelling age through Equation (3.29) results in the expected age structure. Therefore, we now have an internal structure which we can couple to other mechanical properties, allowing a stiffness gradient to emerge over time, or to other biological properties, such as cell death. For example, the sloughed region in Equation (3.27) can be modelled as a function of both the age and ageing rate of cells, to model differences in apoptosis between young and mature cells within the tissue.

3.4.7 Self-contact reveals the importance of spatial competition

For most of the previous results, simulations have been paused before the rod has undergone self-contact. However, modelling a fully-invaginated crypt requires extending simulations beyond the point of self-contact. We thus consider the effect of allowing self-contact to occur, and thus allowing deformations to continue for longer times, has on the rod morphology. Ultimately, as we are aiming to model intestinal crypts, which exhibit long invagination depths D_y, but are narrow in width W_y, resulting in a small aspect ratio A_y, we are interested in which of the different self-contact models can produce morphologies reminiscent of the crypt.

To ameliorate issues relating to numerical convergence of the self-contacted solutions, we reduce the mechanical effect of the foundation by setting $k = 50$ which,

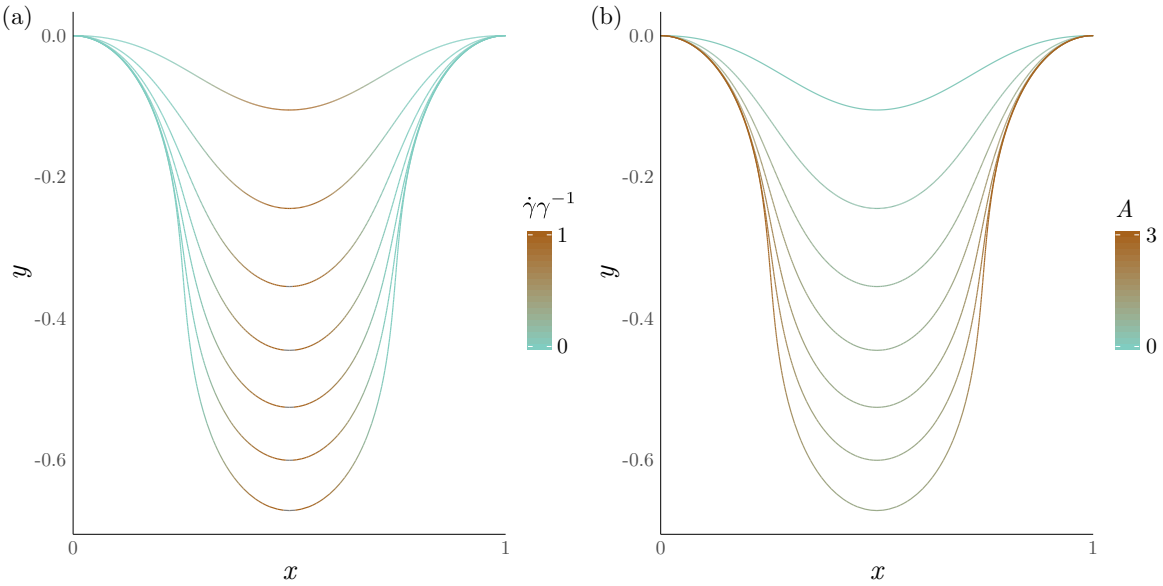

Figure 3.17: Ageing allows cell type to be incorporated. (a) The incremental growth $\dot{\gamma}\gamma^{-1}$ is tracked for Wnt-based growth (3.37). (b) The growth-dependent age $A(S_0, t)$, obtained by solving (3.29) for $a = 1$, is plotted over time. The morphologies, which are invaginating downwards, have been plotted at times $t = 0.1$ and $t = 0.5, 1.0, \ldots, 3.0$. In both (a) and (b), the morphologies are invaginating downwards as time increases.

in turn, allows for larger deformations to be considered. We compare three distinct self-contact mechanisms: self-contact without any additional constraints; self-contact with the imposed constraint of a constant enclosed area, modelled through (3.33); and self-contact with additional horizontal repulsion, modelled through (3.32). Figure 3.18 illustrates the effect of the different self-contact mechanisms on the rod morphology at $t = 5$. Self-contact alone, represented by the green, dotted line in Figure 3.18, results in the shallowest rod invagination, with the widest invagination. In the absence of additional constraints, for long growth times, the foundation has rapidly relaxed to the rod shape. As the attachments remodel in the x and y directions at the same rate, there is no mechanical preference for the rod invagination to expand in the x or y direction. As such, self-contact alone can result in excessive horizontal bulging, which is not observed in crypt morphologies. This effect is ameliorated when imposing the constraint of a constant self-encapsulated area (orange, dashed line in Figure 3.18), reducing both the invagination depth and width, due to the normal force exerted on the self-contacted area. While the

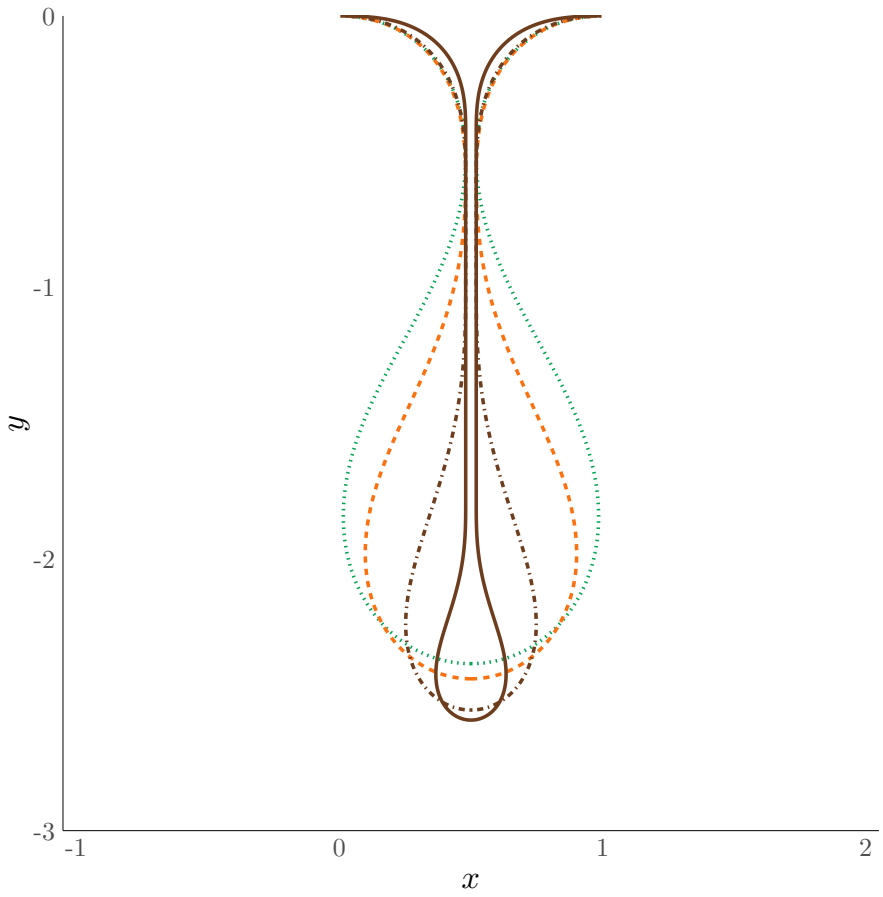

Figure 3.18: Morphologies for different self-contact mechanisms. Profiles $(x(S_0), y(S_0))$, are taken at time $t = 5$ to simulate large deformations. The morphologies are shown for: self-contact alone (green, dotted), self-contact with a constant self-contacted area (orange, dashed), self-contact with horizontal repulsion for $q = 1$ (brown, dot-dashed) and self-contact with horizontal repulsion for $q = 10$ (brown, solid). Self-contact alone results in excessive horizontal bulging, while imposing a constant self-contacted area or modelling spatial repulsion results in more narrow structures.

invagination depth D_y is smaller than that for self-contact alone, the reduction in W_y is greater, resulting in a reduced aspect ratio A_y. However, we note that the resultant normal force strength cannot be varied, but rather is determined by solving the relevant force balance equations. However, when modelling horizontal repulsion, the strength of the repulsive force can be varied explicitly through the parameter q. We observe that increasing q biases the rod to deform more along the $y-$axis than the $x-$axis. Thus, increasing q reduces the invagination aspect ratio significantly.

When modelling self-contact, two possible questions arise. First, is it possible to transition from self-contact along a point to self-contact along a region? This

feature is important as it is observed in the crypt that continued invagination results in a 'zippering up' of the tissue, in which the crypt becomes self-encapsulated, but continues to invaginate, stretching out the self-contacted region. Second, if self-contact along a region is possible, how long is the transition from point contact to region contact? For this set of model parameter values, simulations reveal that it is indeed possible to transition to solutions involving region contact for each of the self-contact models considered. The respective times, relative to the time the rod first undergoes self-contact, are plotted for each self-contact model in Figure 3.19. Self-contact alone is observed to require the longest time to reach region contact. This occurs because, in the absence of additional spatial constraints, it is just as mechanically favourable for the rod invagination to widen as it is to deepen. Therefore, more growth is required for the bending moment at the self-contact point, $m(S_c)$, to eventually decay to zero, which is the criterion for the transition to contact along a region. Contrastingly, when the rod grows and a constant enclosed area is imposed, the region about the self-contact point flattens, resulting in a rapid transition to $m(S_c) = 0$, indicating region contact. Modelling a horizontal repulsion has a similar effect and is either slower or faster than the constant area model, depending on the repulsive strength q.

Additionally, in the case of the horizontal repulsion model, varying the repulsive strength also varies the initial time taken for self-contact at a point to occur, as shown in Figure 3.20. This is not the case for the constant self-contact area model, where the time to self-contact is the same as that for self-contact alone and is equivalent to the $q = 0$ case. Increasing q rapidly reduces the time, until the effect saturates for larger q. These results, combined with the results shown in Figures 3.18–3.19, demonstrate that incorporating spatial competition has a significant effect on the rod morphology for large deformations, as well as time to self-contact events. In the context of the crypt, this suggests that the presence of neighbouring tissue, such as adjacent crypts, contributes to its narrow and highly-invaginated structure.

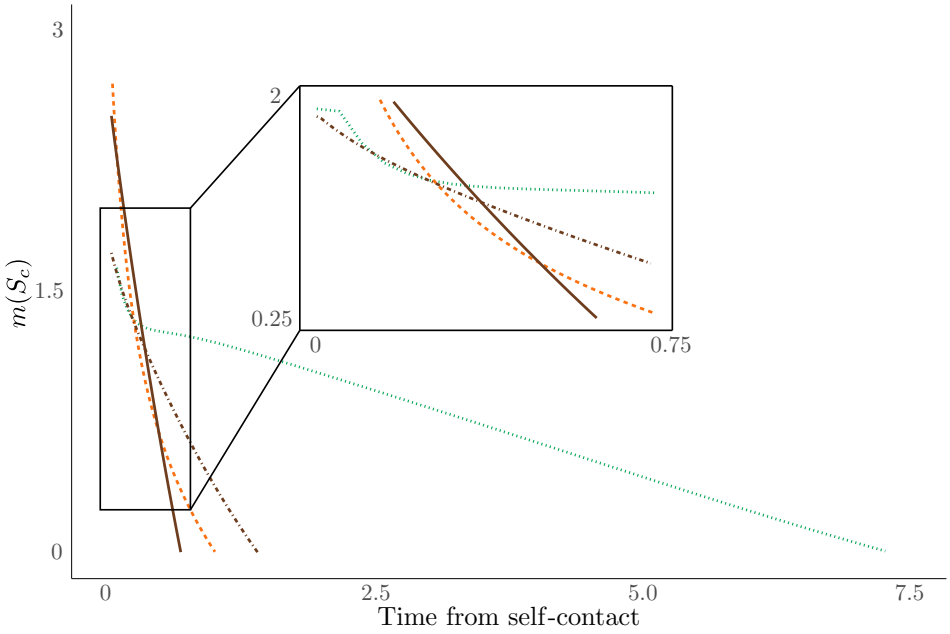

Figure 3.19: The time taken to reach self-contact along a region for different self-contact mechanism. Times are plotted relative to the time when the rod first undergoes self-contact at a point. Self-contact along a region occurs when the bending moment at the self-contacted point, $m(S_c)$, reaches zero. The cases considered are: self-contact alone (green, dotted), self-contact with a constant self-contacted area (orange, dashed), self-contact with horizontal repulsion for $q = 1$ (brown, dot-dashed) and self-contact with horizontal repulsion for $q = 10$ (brown, solid). The transition to region contact is quickened with additional spatial constraints.

3.4.8 Putting it all together: simulating crypt morphogenesis

Thus far, we have investigated potential modelling assumptions and the resulting morphological effects for a number of different processes, but with each process explored in isolation. Having demonstrated which features may be most relevant for modelling crypt morphogenesis, we conclude by providing two examples in which different features are combined to yield interesting and more realistic properties.

Generating a crypt morphology

As we have gauged morphologies based on their similarities to the morphology of the crypt, we first ask whether we can generate a realistic crypt morphology. In particular, we consider the remarkable morphological feature of the crypt: it forms an invagination that is five times as long as it is wide without excessive

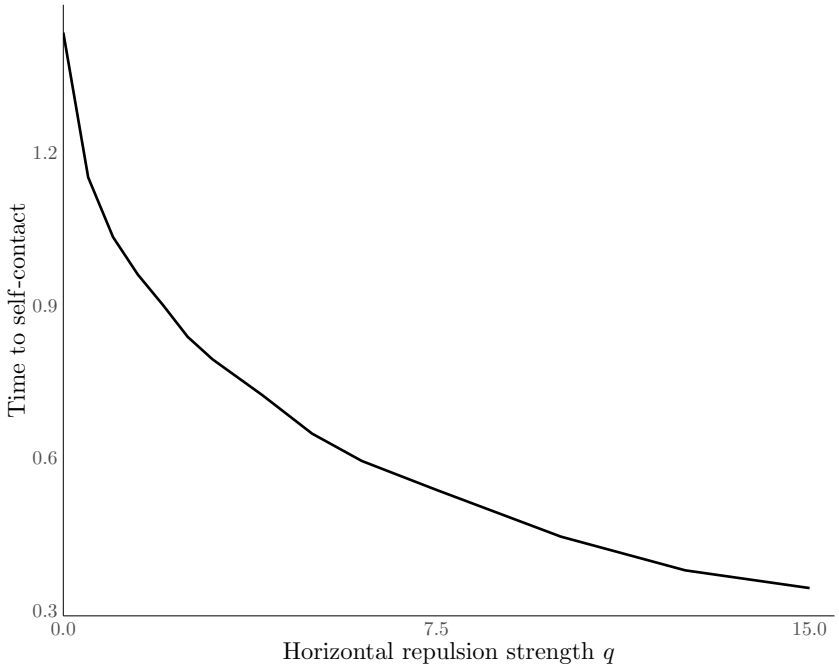

Figure 3.20: Horizontal spatial repulsion quickens the time to initial self-contact. Note that the case $q = 0$ corresponds to the times for self-contact alone and self-contact with a constant self-contacted area.

horizontal bulging.

Based on previous results, we simulate the growth of a rod with the following components:

- A remodelling foundation, where, for proof of concept, the stiffness is set to $k = 50$ and the remodelling parameter is set to $\rho = 10$. This choice is based on the results of Figure 3.10, in which we found that a rapidly-remodelling foundation produced a deeper invagination than that of a viscoelastic foundation, as compared in Figure 3.12.

- Eulerian Wnt-driven growth $\dot{\gamma}\gamma^{-1} = W(s)$, where $W(s)$ is defined analogously to (3.37) for $\sigma_C = 0.16$. This localises growth at the tip of the invagination and prevents local peaks from developing, as was shown for $W = W(S_0)$ in Figure 3.14.

- Horizontal spatial repulsion (3.32), where the repulsion strength is set to $q = 10$. This ensures that the rod does not bulge excessively in the x-direction

at large deformations, as demonstrated in Figure 3.18.

Figure 3.21 shows the resulting morphology over time. We see that it is indeed possible to generate a realistic crypt morphology. However, this is only possible if, in addition to the modelled processes above, the rod is allowed to undergo self-contact. Moreover, the time taken to generate a realistic crypt invagination depth results in the rod undergoing self-contact along a region. After extended growth for region contact, the region of non-zero curvature localises to the tip of the invagination. This feature is not unlike that observed by Demery et al. [46], who modelled the folding of a thin film upon a liquid substrate. Figure 3.21 demonstrates that this set of morphogenetic processes is sufficient to generate realistic crypt morphologies within the morphoelastic rod framework, where each of these processes alone does not the observed morphology.

Cell-type-dependent sloughing

In Section 3.4.5, we demonstrated how a quasi-homeostatic state, where the morphology was unchanging but growth was still evolving, could be obtained when the sloughing rate, $\dot{\mu}$, balanced the growth rate $\dot{\gamma}$. In this example, we imposed that sloughing began when $t > T$, where T was an imposed time with no biological significance. However, a more natural way of imposing sloughing is to model sloughing based on the biological properties of the actual cells (or points along the tissue, as is the case in our continuum setting). That is, cells will die when they pass a certain age. As we observed in Figure 3.17, the age $A(S_0, t)$ for Wnt-based growth $\dot{\gamma}\gamma^{-1} = W(s)$ is highest at the ends of the rod and minimal in the base. Following this observation, as a proof of concept, we propose the following age-dependent sloughing law:

$$\frac{\dot{\gamma}}{\gamma} = W(s), \qquad \dot{\mu} = \frac{1}{2}\left[1 + \tanh(10(A(L_\mu) - A^*))\right], \tag{3.40}$$

where $A(L_\mu)$ is the age of the rod at $S_0 = L_\mu$ and A^* is the threshold boundary age at which sloughing begins to occur. The sloughing law (3.40) models sloughing to begin only when $A(L_\mu) > A^*$. The resulting evolution of the sloughing boundary,

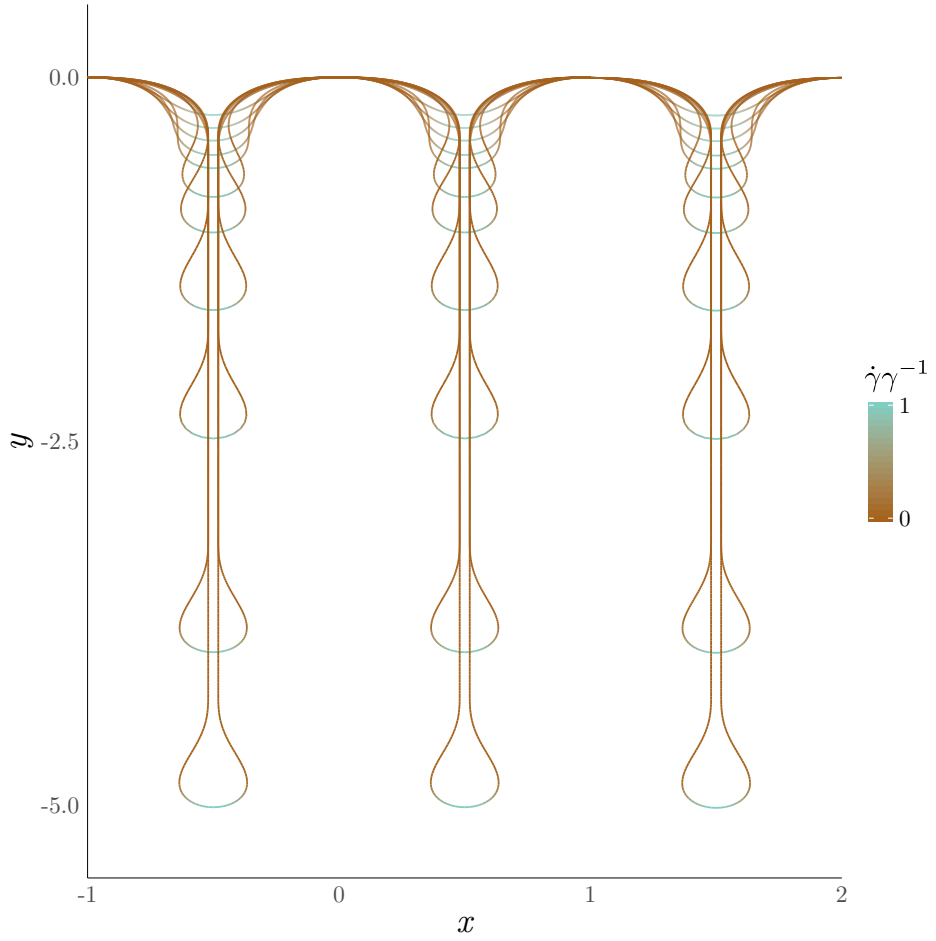

Figure 3.21: A simulation of crypt morphogenesis. Here, the horizontal repulsion strength has been set to $q = 10$ and growth evolves according to $\dot{\gamma}\gamma^{-1} = W(s)$, where $W(s)$ is given by (3.37). The profiles have been plotted at $t = 0.5, 1, 1.5, \ldots, 5, 5.25$, where $t = 5.25$ is the earliest time to reach an invagination depth that reflects a typical crypt morphology and the rod invaginates downwards as t increases. We have plotted the reflections of the rod solutions about $x = 0$ and $x = 1$ to underlie the implicit assumption that neighbouring crypts are growing simultaneously. Note that the rod has undergone self-contact along a region.

L_μ, and the total rod length, l, are plotted in Figure 3.22. For this coupling between growth and death, we observe that the decrease in L_μ also decreases l. That is, when $A(L_\mu) > A^*$, the sloughing rate $\dot{\mu} = 1$, which exceeds the increase in material due to growth. Therefore, the rod morphology begins to shrink in amplitude due to sloughing. While we do not observe a static morphology, this example demonstrates how we can straightforwardly couple sloughing to processes that represent biological properties, such as the age $A(S_0, t)$. For future work,

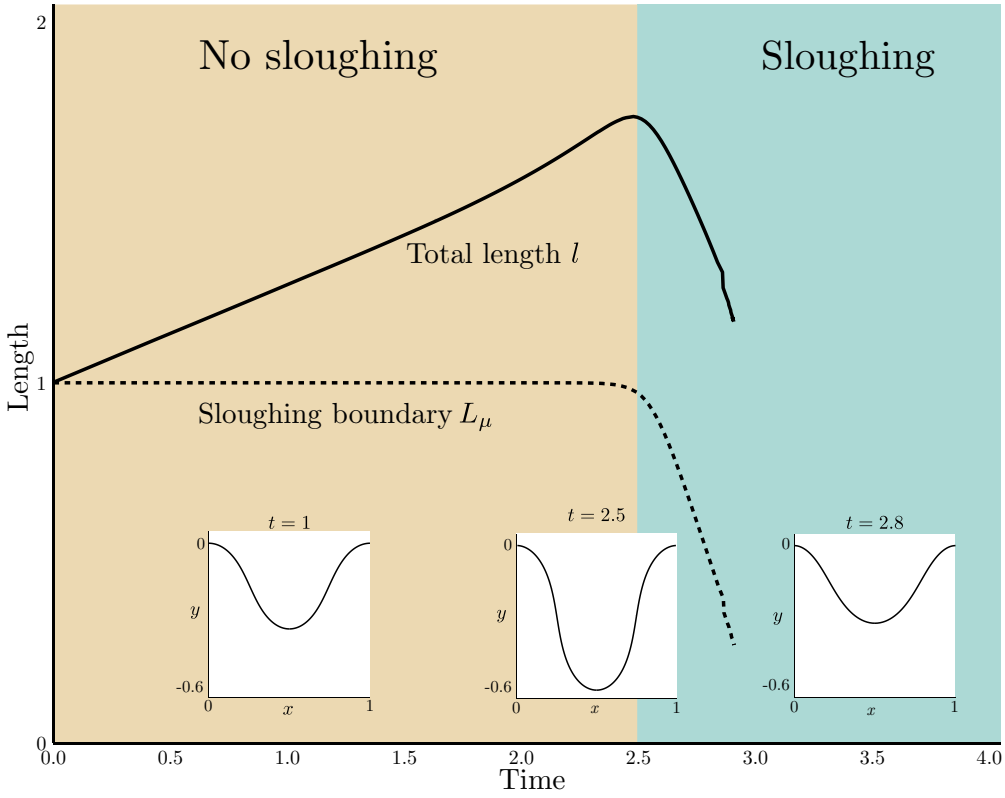

Figure 3.22: Evolution of sloughing boundary for age-dependent sloughing. The total rod length, l, and sloughing boundary, L_μ, are shown over time for Wnt-based growth and age-dependent sloughing (3.40), where sloughing only begins once $A(L_\mu) > A^*$. The morphologies at $t = 1, 2.5, 2.8$ are also plotted. Here, the sloughing rate is faster than the growth rate, which decreases the invagination depth once sloughing begins.

it would be worthwhile to explore which couplings between processes result in a static morphology, such as that in Figure 3.16.

3.5 Discussion

In this chapter, we have considered a number of modelling choices within a morphoelastic framework of epithelial tissue that accounts for the complex interplay between tissue growth, internal stresses, external forces due to a substrate, and mechanical deformation. Building upon the work of Chapter 2, we considered how various chemical, biological, and mechanical processes can be incorporated within the morphoelastic rod framework to simulate crypt morphogenesis more faithfully.

We first investigated how different mechanisms of tissue relaxation, either within the epithelium or in relation to its external environment, affect the resulting

morphology. For a viscoelastic foundation, increasing the relaxation rate, ν, of the viscoelastic attachments deepened the rod invagination during growth. However, when growth was paused and the foundation attachments continued to relax, the invagination depths shortened for smaller relaxation rates. For higher viscoelastic relaxation rates, the rod invagination did not change. For a remodelling foundation, increasing the attachment remodelling parameter, ρ, also resulted in a deeper invagination during growth. However, in contrast to the viscoelastic foundation, allowing the attachments to continue to relax after growth increased the invagination depth, for all values of ρ. Modelling relaxation within the rod led to different behaviour from each foundation relaxation models. When we introduced an evolving intrinsic curvature, increasing the rate at which the intrinsic curvature remodelled to the current rod curvature shortened the invagination depth. When growth was paused and the intrinsic curvature continued to evolve, the rod base fissioned. Hence, for generating a long crypt invagination, a remodelling foundation is the most appropriate model for tissue relaxation.

We then investigated how defining material properties, such as growth or stiffness, with respect to the Lagrangian or Eulerian reference frames, may impact the resulting morphology. In a biological context, modelling material properties with a Lagrangian parametrisation reflects the notion that the quantity is an inherent property of cells, which then spreads along the tissue due to growth, while an Eulerian parametrisation implies that cellular properties remodel over time and are position-based. Motivated by the importance of Wnt signalling in the crypt, we showed that changing the spatial parametrisations of chemical signal affects the emergent morphology significantly. Moreover, an Eulerian parametrisation of the chemical signal generated the most realistic, crypt-like morphology. However, this was not the case for mechanical stiffness, where the differences in morphology between Lagrangian and Eulerian stiffnesses was only relevant when the variation in stiffness is high. Thus, we conclude that, for the crypt, an Eulerian Wnt signal is required to generate a realistic crypt morphology, but it is not important to model heterogeneous stiffness.

Following on from heterogeneity, we showed how biological processes such as cell death and ageing (as a proxy for cell type), which play an important role in epithelial development and maintenance, can be modelled within the continuum framework—something which, to our knowledge, has not been done previously. We modelled cell death through a sloughing mechanism that shrunk the initial domain to accommodate for growth. Selecting a sloughing rate that balanced the growth rate led to a morphological steady state, even as growth continued evolving. This concept of an 'observable' steady state but with dynamic growth is an important one that we will revisit in more detail in Chapter 4, when we construct a framework to model non-static tissue homeostasis. We then showed that modelling age via Equation (3.29) produced the correct age structure for heterogeneous growth, where the 'youngest' points along the rod were growing most rapidly.

As all previous simulations had been stopped long before self-contact, we investigated the morphological effects of allowing continued deformation after self-contact. Modelling such deformations allowed us to consider morphogenesis on biologically-realistic timescales. In particular, we investigated whether prolonged growth would result in the 'zippering' feature observed in crypts. When modelling self-contact alone, the rod exhibited excessive horizontal bulging. However, when additional constraints were incorporated, such as a constant self-encapsulated area or spatial competition due to neighbouring tissue, the resulting morphologies were both more invaginated and narrower. This indicated the importance of spatial competition, that may be present within or around the growing tissue.

Finally, we combined several of the model components that were previously considered in isolation to demonstrate more concrete examples of morphogenesis. First, we considered a rod subject to an Eulerian chemical signal, supported by a remodelling foundation and subject to significant spatial repulsion. We showed that when simulating the system over long times—in dimensional terms, growth continued for almost a week—the resulting morphology was similar to that observed of a crypt. That is, we produced a narrow invagination that was five times as long as it was wide. Second, we extended the preliminary investigation of sloughing in

Section 3.4.5 by coupling the sloughing rate to the age structure of a rod subjected to heterogeneous growth, demonstrating how sloughing can be modelled to depend on biological properties and arise more naturally. However, in this case, as the sloughing rate did not balance the growth rate, a morphological steady state was not achieved. Rather, the invagination began to shrink over time due to the imbalance between growth and sloughing. We will show in Chapter 4 why the sloughing and growth rate need to balance when we construct a model for dynamic tissue homeostasis.

We have demonstrated that care is needed when translating biological processes to a modelling framework, in particular to a continuum setting, and we have investigated in detail the impact of modelling choices and ingredients on the resulting morphology. While tissue morphogenesis is a complex process, by developing mathematical models for the different components and investigating their morphological effect, we can suggest which components contribute most significantly to the morphogenesis of the system in question. As the crypt is our motivating example, our results were framed in the context of crypt morphogenesis; that is, which of these processes may contribute to a deep, narrow invagination? From the results of this chapter, the model components required to simulate crypt morphogenesis are: a rapidly-relaxing foundation; a concentrated position-based Wnt signal; and, for large deformations, horizontal repulsion induced by neighbouring crypts.

In the next chapter, we will shift our focus from simulating realistic crypt morphologies to modelling the unique growth structure of the crypt and the crypt in homeostasis. In order to investigate these concepts of growth and homeostasis in detail, we will uncouple the rod from the 2D geometry and consider a 1D unbuckled rod. However, based on the results of this chapter, our starting framework will be a rod that is tethered to a remodelling foundation, while the starting point for growth will be due to an Eulerian Wnt signal.

4

Growth and homeostasis in the crypt

4.1 Introduction

In Chapter 2, we investigated how spatial heterogeneity within the material properties of a growing, deformable rod impacted pattern formation initiated by growth. In Chapter 3, we considered different biochemical and mechanical processes that act within an epithelial tissue, and investigated how these models may be incorporated within our continuum framework. We now take these findings and specialise them for the colonic crypt. In this way, we aim to answer two key questions relating to the crypt.

The first question concerns one of the unique and robust aspects of the crypt, namely its proliferative structure. In the base of the crypt reside a pool of stem cells, which produce progenitors that migrate upwards. Transit-amplifying cells are the first progenitor cell type to emerge, proliferating rapidly for a fixed number of divisions as they migrate from the base. Transit-amplifying cells will differentiate into non-proliferating specialised cells, which reside at the top of the crypt. Despite this hierarchical structure being robust, it is not fully understood how it emerges. Wnt signalling is known to be a primary driver of proliferation within the crypt [39] and forms a decreasing spatial profile from the crypt base to the top [67]. If proliferation within the crypt is driven solely by Wnt and proliferation responds

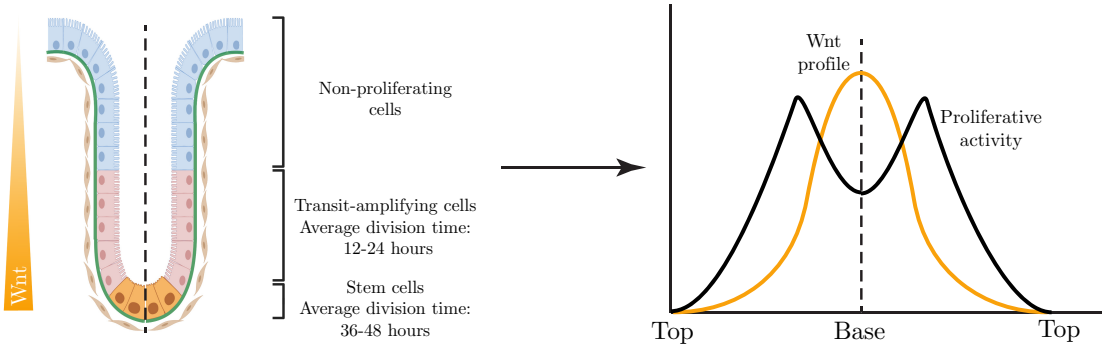

Figure 4.1: The internal proliferative structure of the crypt. The proliferative structure is bimodal shape, i.e. maximal away from the crypt base, which contradicts the proposal that Wnt signalling is the primary governor of proliferation, as it is maximal at the base (assuming growth is a linear function of Wnt signalling).

linearly to Wnt, then we would expect proliferative activity to be highest in the base and thus observe a 'unimodal' curve of proliferative capacity, we showed in Chapter 3. However, the bulk of proliferative activity is driven by transit-amplifying cell proliferation, leading to a 'bimodal' shape. This concept is illustrated in Figure 4.1. Therefore, the first significant goal of this chapter is to develop a parsimonious growth law that gives rise to the proliferative structure observed in the crypt, by determining what additional mechanisms may regulate the rate of proliferation. Specifically, we wish to determine whether or not this structure can be captured with a growth law that incorporates regulation through mechanical stimuli.

The second question concerns the concept of tissue homeostasis, which we define as a state in which the rate of cell proliferation throughout a crypt is balanced exactly by the rate of cell death to maintain a 'morphological' steady state, where the stress and material velocity have fixed profiles in the current configuration. Previously, in Section 3.4.5, we demonstrated that introducing sloughing shrinks the initial domain, which can balance material increase due to growth and render the rod morphology static. However, while the observed system appeared to be static, there was a continuous flux of tissue material. The of homeostasis is important to the crypt and other biological systems, for disruption of homeostasis marks the onset of disease. Thus, it is important to identify conditions under which homeostasis in the crypt is maintained. However, to our knowledge, such a 'dynamic' tissue homeostasis model

has not been rigorously considered in a continuum framework. The challenge with modelling tissue homeostasis is indeed its non-static feature, as there are actively-evolving growth and removal processes. Hence, tissue homeostasis of the type described above cannot be defined simply as the evolution towards a steady state, in which dependent variables do not change over time. Tissue homeostasis also stands in contrast to the principle of mechanical homeostasis, where growth remodels towards a preferred mechanical stress state [59, 168]. Within the crypt, Wnt signalling is always present as a heterogeneous 'background' regulator of growth that competes with other mechanisms are contributing to the convergence to a homeostatic stress state. Thus, the second goal of this chapter is to develop a mathematical model that, building on the growth law developed, captures tissue homeostasis within the crypt and to derive the necessary conditions under which homeostasis occurs. Moreover, we will show how the the sloughing mechanism defined in Chapter 3 emerges naturally as a consequence of the constructed homeostasis model.

One important aspect of the work in Chapters 2–3 is that we have focussed on studying the effects of different models on the resulting morphology. As pattern formation within the morphoelastic rod framework is initiated through buckling, the patterns subsequently give rise to geometric nonlinearities. This leads to an increase in computational cost, particularly when exploring the coupling of different processes. In order to maintain a level of computational tractability, we will uncouple these processes from the nonlinear geometry caused by buckling by focussing on a straight, unbuckled rod.

In this chapter, we explore different feedback mechanisms within the context of a growing elastic rod. First, in Section 4.2, we cast the morphoelastic rod framework in a simplified 1D setting. In Section 4.3, using this framework, we combine numerical simulations and analytical results for special parameter cases to develop a minimal growth law that gives rise to the unique growth structure that characterises the crypt. In particular, we determine which form of mechanical feedback most appropriately couples to Wnt signalling. Then, in Section 4.4, we explore how homeostasis can be achieved by considering the balance between growth,

cell death, stress, and velocity. By defining homeostasis as the condition when growth is fixed with respect to the Eulerian configuration, we derive the governing equations in homeostasis and demonstrate how homeostatic growth in the crypt depends on key mechanical parameters.

4.2 Model set-up

We wish to preserve the key features of a morphoelastic rod without having to account for the 2D morphology induced by buckling and further deformations. That is, we wish to examine how growth relates to stress in a tractable setting. Geometrically, we consider a deformed crypt and 'unfold' it, restricting attention to processes that act along a 1D line and ignoring the 2D morphology. This situation is illustrated in Figure 4.2. Using asterisks to denote dimensional quantities, independent and dependent variables have been scaled by the following nondimensionalisation:

$$(S_0^*, s^*, p^*) = L_0^*(S_0, s, p), \qquad n^* = Ehwn, \qquad t^* = \tau t, \tag{4.1}$$

where L_0^* is the initial rod length; E is the Young's modulus; h and w are the height and width of the rod cross-section, where we have assumed a rectangular cross-section; and τ is the characteristic growth timescale.

In order to allow the rod to grow in a fixed domain, we take the rod to be extensible. In this geometry, the position of the rod centreline is given by the current arc length parameter, s. Recall that s relates to the initial arc length parameter, S_0, via the morphoelasticity decomposition (1.5):

$$\lambda = \alpha\gamma \qquad \Longleftrightarrow \qquad \frac{\partial s}{\partial S_0} = \frac{\partial s}{\partial S}\frac{\partial S}{\partial S_0},$$

where α denotes the elastic stretch and γ is the growth stretch. Hence, the kinematics of the rod are described completely by this decomposition:

$$s' = \alpha\gamma. \tag{4.2}$$

Here, the prime $'$ denotes differentiation with respect to the initial material arc length, S_0. Following the results of Section 3.4.1, we assume that the rod is attached to an

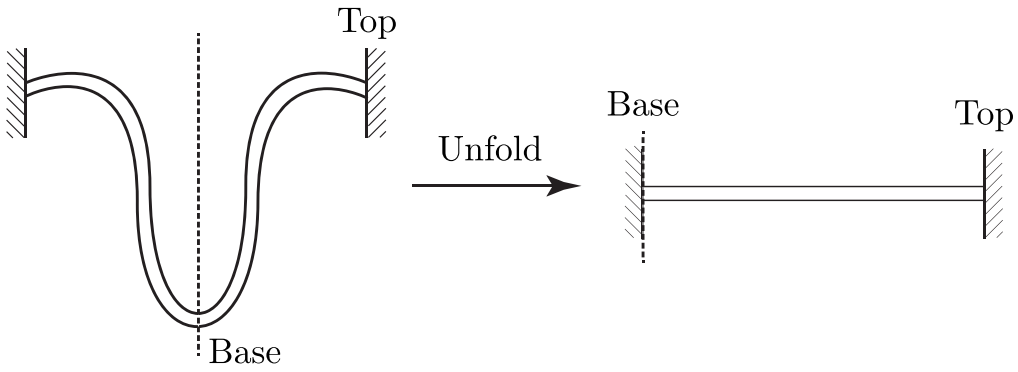

Figure 4.2: Geometric simplification of the crypt. We exploit the symmetry of the crypt morphology and split a deformed crypt at the base, mapping it to a straight line. In doing so, we uncouple the rod growth from the geometry.

underlying foundation that remodels to the current position. Therefore, we model the position of the foundation attachments as a smooth curve, $p(S_0, t)$, of linearly elastic attachments. The force balance for the internal rod stress, $n(S_0, t)$, is given by:

$$n' = k\alpha\gamma(s - p), \qquad \text{where} \qquad \dot{p} = \rho(s - p), \quad p(S_0, 0) = S_0, \tag{4.3}$$

where the overdot represents partial differentiation with respect to time t. Note the presence of the $\alpha\gamma$ factor, as we have defined the foundation force with respect to the current configuration. The parameters k and ρ denote the foundation stiffness and remodelling rate of the foundation, respectively, and are given by:

$$k = \frac{k_f L_0^{*^2}}{hw}, \qquad \rho = \frac{\tau}{\eta_p}, \tag{4.4}$$

where k_f quantifies the stiffness of the foundation with respect to the rod stiffness and η_p is the relaxation rate of the foundation attachments.

We must also specify a constitutive law for the elastic stretch α and an evolution for the growth stretch γ. We relate α to the internal stress n using a Hookean constitutive law analogous to that employed in Chapter 2 (Equation (2.12)), so that

$$n = \alpha - 1, \tag{4.5}$$

By allowing the rod to be extensible, we can probe the effects of growth and other processes on stresses while the rod remains straight and unbuckled. In line with

Chapter 3, the growth law takes the form

$$\frac{\dot{\gamma}}{\gamma} = \mathcal{G}, \tag{4.6}$$

where the left hand side represents the incremental growth, the continuum analogue of proliferative activity, and the function $\mathcal{G}$ comprises possible chemical and mechanical contributions to growth.

In order to close the system, defined by Equations (4.2)–(4.3), we must have two boundary conditions. For simplicity, we assume that the rod is fixed at both boundaries:

$$s(0) = 0, \qquad s(1) = 1. \tag{4.7}$$

Substituting the extensibility assumption (4.5) into Equations (4.2)–(4.3), we obtain the system:

$$s' = (1+n)\,\gamma, \tag{4.8}$$

$$n' = k\,(1+n)\,(s-p), \qquad \dot{p} = \rho(s-p), \quad p(S_0, 0) = S_0, \tag{4.9}$$

subject to the clamped boundary conditions (4.7).

4.2.1 Mechanochemical growth

In this chapter, we aim to develop a mechanochemical growth that recapitulates the proliferation profile along the crypt axis. With this in mind, we assume that growth satisfies an evolution equation of the form:

$$\frac{\dot{\gamma}}{\gamma} = \mathcal{G}(W(s), n - n^*), \tag{4.10}$$

where $W(s)$ is the sensitivity to Wnt signalling, modelled as an imposed profile with respect to the current configuration; n is the rod stress; and n^* is the homeostatic stress.

4.3 Developing a minimal growth law for the crypt

It has been proposed that proliferative capacity in the crypt is governed primarily by Wnt signalling, which decreases monotonically in concentration from the crypt base to the top [67]. However, proliferation due to Wnt alone does not generate the observed proliferative structure. Therefore, we conclude that additional regulators modulate proliferative activity in the crypt. A natural candidate is mechanical feedback. We will demonstrate in the following sections that Wnt signalling, coupled with mechanical stress, can produce a proliferative structure consistent with biological observations.

For numerical simulations, we discretise all time derivatives using a Forward Euler discretisation, with a time step size of $\delta t = 0.05$. First, growth γ is updated via the evolution equation (4.10). Then, we solve the resulting quasi-static force balance equations (4.8)–(4.9) using the MATLAB package `bvp4c`, which employs a spatial collocation method [101, 156]. Afterwards, the foundation attachment positions, p, are updated by discretising the evolution equation (4.9).

Unless otherwise specified, the following model parameters are held fixed in subsequent sections: the foundation stiffness, $k = 1000$, the foundation remodelling parameter, $\rho = 10$, and the Wnt spatial profile parameter, $\sigma_W = 0.16$.

4.3.1 Wnt signalling localises growth and stress

In Section 3.4.3, we showed that a Wnt signal profile that is parametrised with respect to the current arc length s produces a realistic crypt morphology. Hence, as a first step, we consider the case when growth depends on a pre-existing Wnt signal profile only, so that:

$$\frac{\dot{\gamma}}{\gamma} = W(s), \tag{4.11}$$

where $W(s)$ represents the cell sensitivity to the concentration of Wnt ligand along the crypt. As Wnt decreases from the crypt base to the top, we define $W(s)$ to be decreasing function over the interval $s \in [0, 1]$ such that $W(0) = 1$ and $W(1) = 0$. Note that defining $W = W(s)$ models the Wnt profile as an

environmental cue for growth. Following Chapter 3, we model the Wnt signal concentration using a Gaussian function:

$$W(s) = \exp\left[-\left(\frac{s}{\sigma_W}\right)^2\right], \tag{4.12}$$

where $\sigma_W > 0$ specifies how rapidly Wnt decreases in concentration for increasing s. We generally consider values of σ_W such that the Wnt signal is concentrated at the base and rapidly decreases for increasing s [114].

To determine the effect of Wnt-driven incremental growth on rod evolution, in Figure 4.3 we plot the growth evolution, $\gamma(S_0, t)$, and the rod stress, $n(S_0, t)$, against the current arc length s. As expected, the heterogeneous growth law concentrates growth towards the base, $s = 0$, as shown in Figure 4.3 (a). This localised growth leads to increased compression near $s = 0$, shown in Figure 4.3 (b). As stem cells in the crypt base are not actively proliferating in homeostasis [35] and transit-amplifying cells, situated outside the base, drive proliferation within the crypt, we can conclude that Wnt signalling is not the sole spatial determinant of growth within the crypt. Moreover, Figure 4.3 (b) indicates that cells in the base, $s = 0$, where growth is highest, experience the largest amount of mechanical stress. This correlation between stress and enhanced growth suggests the possible role of mechanical stress as a regulator of growth within the crypt. We therefore propose the following hypothesis: Wnt combined with mechanical stress regulates proliferation, with the inhibitory mechanism dominant in the crypt base, and the Wnt stimulus dominant in the transit-amplifying region.

4.3.2 Special case: an infinitely-stiff foundation

In Figure 4.3, we observed that a Wnt profile that is concentrated near $s = 0$ leads to increased compression about $s = 0$, where stem cells reside in the crypt. Given that stem cells are not the primary contributors to tissue growth within the crypt during homeostasis, it is reasonable to postulate that there is a subsequent inhibitory mechanism that restricts proliferative activity within the base, leading to the bimodal spatial profile observed within the crypt. The notion that proliferation of

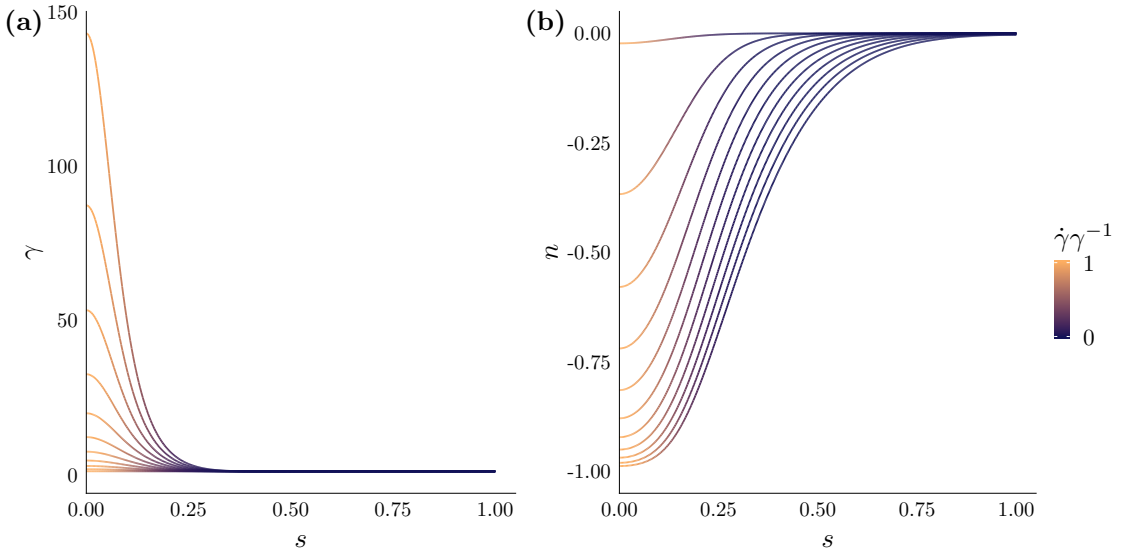

Figure 4.3: A Wnt-based growth law leads to concentrated growth and stress. Solutions are plotted at times $t = 0.05, 0.5, 1, \ldots, 4.5, 5$. (a) Growth $\gamma(S_0, t)$ against current arc length s for Wnt-based growth, as modelled by Equations (4.11)–(4.12). (b) Rod stress $n(S_0, t)$ against s. In both cases, the incremental growth $\dot{\gamma}\gamma^{-1}$ has been coloured in, with darker blue regions indicating minimal values of $\dot{\gamma}\gamma^{-1}$ and orange regions corresponding to higher values of $\dot{\gamma}\gamma^{-1}$. The concentrated Wnt signal profile leads to growth localising and increased compression in the base.

basal stem cells is restricted is perhaps best supported by the presence of quiescent, '+4' stem cells, which only activate during injury [15, 102, 185]. One possible mechanism for this reactivation following injury may be that the loss of epithelial tissue acts to 'release' the compressive stress inhibiting these stem cells, allowing them to proliferate. This observation from the literature, combined with the regions of increased compression in the base that we observe due to growth in the base, leads us to postulate that mechanical feedback is one such inhibitory mechanism. Therefore, we aim to investigate whether growth laws that incorporate mechanical feedback may generate the desired proliferative structure.

In order to develop intuition for appropriate mechanosensitive growth laws, we first restrict ourselves to the special case of an infinitely rigid foundation, $k \to \infty$, where material points do not move. In this case, the solutions for the current arc length s and the rod stress n are given exactly by

$$s(S_0) = S_0, \qquad n(S_0, t) = \frac{1 - \gamma(S_0, t)}{\gamma(S_0, t)}. \tag{4.13}$$

The solution for this limiting case gives a closed-form expression for rod stress, $n(S_0, t)$, which is typically unsolvable analytically when k is finite and growth is heterogeneous. We will refer to this solution repeatedly when considering different mechanisms of mechanical feedback.

Ever-present mechanical feedback

The first law we consider that incorporates mechanical feedback models growth as a linear combination of Wnt, $W(s)$, and mechanical rod stress, n:

$$\frac{\dot{\gamma}}{\gamma} = W(s) + \mu(n - n^*), \tag{4.14}$$

where μ is a parameter describing sensitivity to mechanical stress, and thus the relative impact of mechanical feedback, and $n^* \leq 0$ is the homeostatic stress. The law (4.14) models the constant regulation of Wnt signalling due to mechanical feedback. Note that if $n(S_0, t) - n^* > 0$, indicating relative tension, incremental growth $\dot{\gamma}\gamma^{-1}$ is increased, while if $n(S_0, t) - n^* < 0$, indicating relative compression, $\dot{\gamma}\gamma^{-1}$ is decreased.

The spatial dependence of the Wnt signal parameter, $W(s)$, means that in general, analytical solutions to the growth law (4.14) cannot be found for the majority of parameter values. To gain insight, we consider the $k \to \infty$ limit, where $S_0 = s$. Substituting for $s(S_0, t)$ and $n(S_0, t)$ from Equation (4.13) into Equation (4.14) yields a first-order, linear ODE for $\gamma(S_0, t)$ in time:

$$\dot{\gamma} = W(S_0)\gamma + \mu\left((1 - \gamma) - n^*\gamma\right). \tag{4.15}$$

Equation (4.14) can be solved straightforwardly with the use of an integrating factor. Recalling the initial condition $\gamma(S_0, 0) = 1$, we deduce that

$$\gamma(S_0, t) = \frac{\mu}{\mu(1 + n^*) - W(S_0)} + \frac{\mu n^* - W(S_0)}{\mu(1 + n^*) - W(S_0)} \mathrm{e}^{-(\mu(1+n^*) - W(S_0))t}. \tag{4.16}$$

This, in turn, gives rise to the following expression for incremental growth, $\dot{\gamma}\gamma^{-1}$:

$$\frac{\dot{\gamma}}{\gamma} = \frac{(W(S_0) - \mu n^*)(\mu(1 + n^*) - W(S_0))\mathrm{e}^{-(\mu(1+n^*) - W(S_0))t}}{\mu + (\mu n^* - W(S_0))\mathrm{e}^{-(\mu(1+n^*) - W(S_0))t}}. \tag{4.17}$$

Observe that the long-term behaviour of $\dot{\gamma}\gamma^{-1}$ at a fixed S_0 can be decomposed into two parameter regions: if $\mu(1+n^*) > W(S_0)$, then $\dot{\gamma} \to 0$ as $t \to \infty$ and consequently, $\gamma(S_0, t)$ tends to a finite limit. Otherwise, if $\mu(1+n^*) < W(S_0)$, then $\dot{\gamma}\gamma^{-1} \to W(S_0) - \mu(1+n^*)$ and growth diverges to infinity. This behaviour is summarised in Figure 4.4.

The growth law (4.14) has two features that may be interpreted as biologically unrealistic. The first is demonstrated in Figure 4.5, in which we plot the incremental growth $\dot{\gamma}\gamma^{-1}$ against the initial arc length S_0 for increasing time. The figure shows that if we set the threshold stress $n^* < 0$, then at $t = 0$, mechanical feedback results in incremental growth that exceeds that of Wnt-based growth, as the system is initially in relative tension, i.e. $n(S_0, 0) - n^* > 0$. The second can be observed in Figure 4.6, where we plot the profiles of γ and $\dot{\gamma}\gamma^{-1}$ against time, for fixed values of Wnt. We observe that as the growth law (4.14) does not the alter the monotonicity of the spatial profile of $\dot{\gamma}\gamma^{-1}$, the spatial profiles of both growth γ and incremental growth $\dot{\gamma}\gamma^{-1}$ are qualitatively similar to the case of Wnt-only growth (4.11).

These observations lead us to hypothesise that points along the rod that are exposed to higher Wnt signal concentration will always exhibit greater incremental growth, even in the presence of mechanical feedback. Therefore, it will be impossible to reproduce the 'bimodal' spatial profile of proliferation that is observed in the crypt with this growth law. This can be summarised by the following:

Claim: Let $\gamma(t)$ be defined by Equation (4.16), in the $k \to \infty$ limit. Define $\gamma_w(t) := \gamma(t)\big|_{W(S_0)=w}$ and $\mathcal{G}(w) = \dot{\gamma}_w \gamma_w^{-1}$. Then $\mathcal{G}(w)$ is a strictly increasing function of w.

Proof: For $\mathcal{G}(w)$ to be a strictly increasing function, we must show that for $w_1 > w_2$, $\mathcal{G}(w_1) > \mathcal{G}(w_2)$ for all time $t > 0$:

$$\frac{\dot{\gamma}_{w_1}}{\gamma_{w_1}} > \frac{\dot{\gamma}_{w_2}}{\gamma_{w_2}}. \tag{4.18}$$

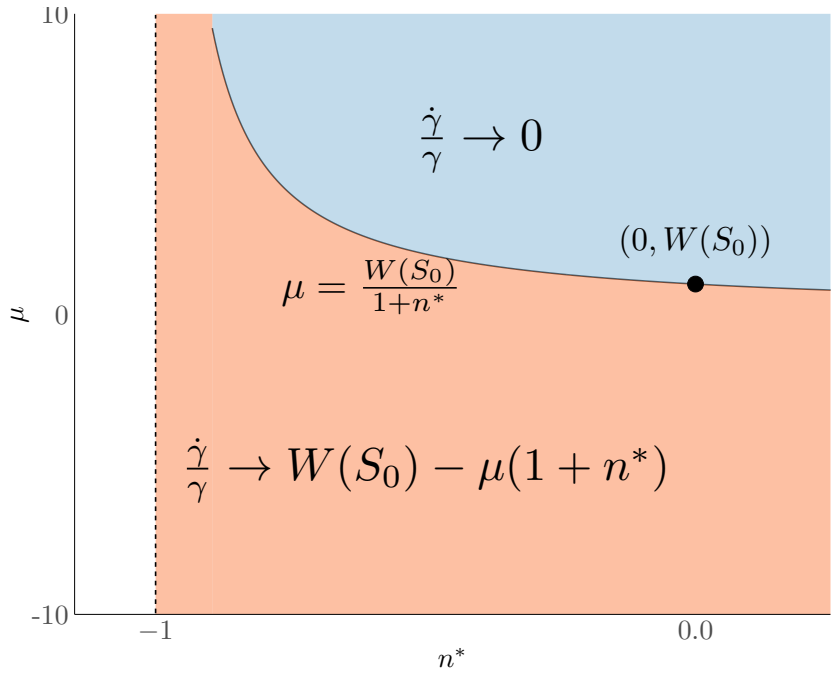

Figure 4.4: Long-time behaviour of growth at a fixed point S_0 that is subject to an ever-present mechanical feedback and infinitely-stiff foundation (as determined by Equation (4.16)). In the blue region, $\mu > W(S_0)(1+n^*)^{-1}$ and mechanical stress dampens the growth induced by Wnt, leading to zero incremental growth at S_0 and growth $\gamma(S_0, t)$ tending to a finite limit as $t \to \infty$. In the orange region, $\mu < W(S_0)(1+n^*)^{-1}$ and incremental growth tends to a finite limit, leading to growth blowing up at S_0.

By (4.17), $\dot{\gamma}_{w_2}\gamma_{w_2}^{-1}$ is given by the following expression:

$$\frac{\dot{\gamma}_{w_2}}{\gamma_{w_2}} = \frac{(w_2 - \mu n^*)(\mu(1+n^*) - w_2)\mathrm{e}^{-(\mu(1+n^*)-w_2)t}}{\mu + (\mu n^* - w_2)\mathrm{e}^{-(\mu(1+n^*)-w_2)t}}. \tag{4.19}$$

By assumption, as $w_1 > w_2$, then it follows that $w_2 - \mu n^* < w_1 - \mu n^*$ and $\mathrm{e}^{-(1+n^*)-w_2)t} > \mathrm{e}^{-(1+n^*)-w_1)t}$. Therefore, we can bound $\dot{\gamma}_{w_2}\gamma_{w_2}^{-1}$ above with the following inequality:

$$\frac{\dot{\gamma}_{w_2}}{\gamma_{w_2}} < \frac{(w_1 - \mu n^*)(\mu(1+n^*) - w_2)\mathrm{e}^{-(\mu(1+n^*)-w_2)t}}{\mu + (\mu n^* - w_1)\mathrm{e}^{-(\mu(1+n^*)-w_1)t}}. \tag{4.20}$$

Therefore, to prove that the inequality (4.18) holds, we must show that:

$$(\mu(1+n^*) - w_2)\mathrm{e}^{-(\mu(1+n^*)-w_2)t} < (\mu(1+n^*) - w_1)\mathrm{e}^{-(\mu(1+n^*)-w_1)t}. \tag{4.21}$$

We may re-arrange (4.21) to obtain the simplified inequality:

$$\mathrm{e}^{(w_1-w_2)t} > \frac{w_2 - \mu(1+n^*)}{w_1 - \mu(1+n^*)}. \tag{4.22}$$

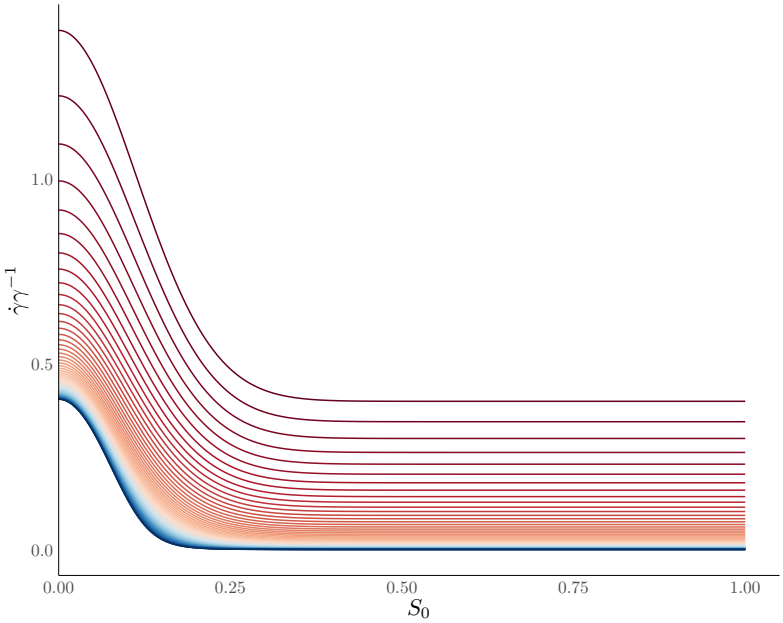

Figure 4.5: Ever-present mechanical feedback dampens growth for an infinitely-stiff foundation. The relative growth $\dot{\gamma}\gamma^{-1}$ against S_0 has been plotted for times $t = 0.05, 0.1, \ldots, 9.95, 10$. Dark red lines indicate earlier times, while dark blue lines indicate later times. The mechanical feedback parameters are $\mu = 1$ and $n^* = -0.4$. Here, mechanical stress dampens incremental growth everywhere.

Observe that as $w_1 > w_2$, the quantity on the right hand side of (4.22) is always less than one. Furthermore, as $(w_1 - w_2)t > 0$, $\mathrm{e}^{(w_1-w_2)t} \geq 1$. Therefore, by our assumption, (4.21) holds. Hence, the inequality (4.18) is true for all time $t > 0$. That is, the incremental growth subject to the mechanical feedback law (4.14) is an increasing function of the Wnt concentration, for an infinitely-stiff foundation.

This claim and subsequent proof demonstrate that, for the $k \to \infty$ case, incremental growth is always highest where Wnt signal sensitivity is highest; this feature is not altered by the presence of mechanical feedback. This is because mechanical feedback acts in a 'global' manner, affecting incremental growth at all points simultaneously. Therefore, while the effect of mechanical feedback may vary across the spatial position S_0, it is triggered at the same time, $t = 0$, for all $S_0 \in [0, 1]$. Hence, the growth law (4.14), which enforces mechanical feedback everywhere from $t = 0$, should be modified such that mechanical feedback is activated at different points at different times.

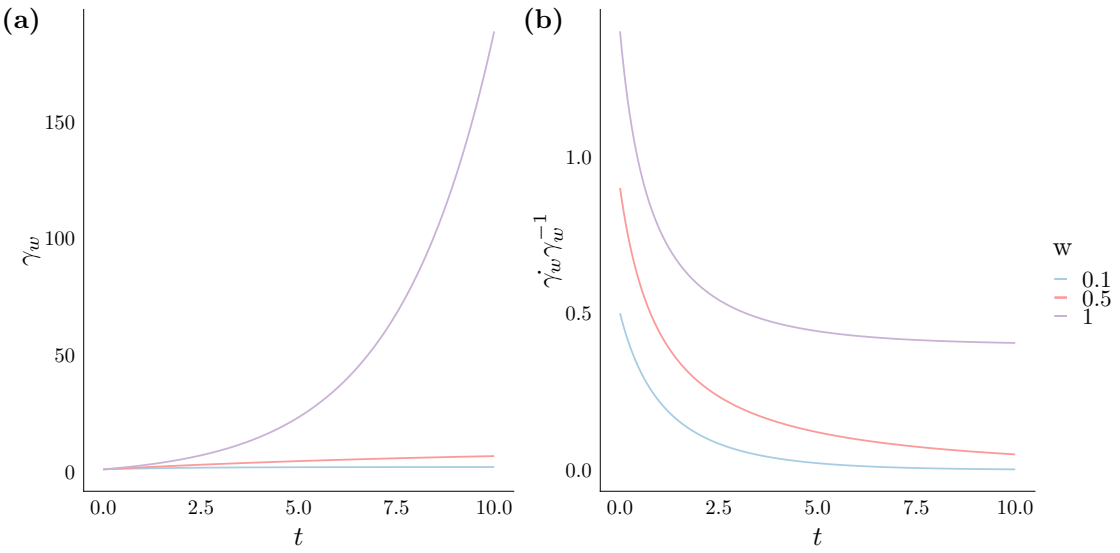

Figure 4.6: Growth at fixed Wnt values for linear mechanical feedback. (a) The behaviour of $\gamma(t)$ for fixed values of Wnt, $W(s) = w$, for $w = 0.1,\ 0.5,\ 1$. (b) The behaviour of $\dot{\gamma}_w\gamma_w^{-1}$. Profiles are plotted up to $t = 10$, for mechanical feedback parameter values of $\mu = 1$ and $n^* = -0.4$. Mechanical feedback that is always present from $t = 0$ can lead to a monotonic decay in incremental growth rates.

Threshold-dependent mechanical feedback

We now consider a variation on the mechanical feedback law (4.14), where mechanical feedback is triggered only when the rod is sufficiently compressed:

$$\frac{\dot{\gamma}}{\gamma} = W(s) + \mu(n - n^*)\mathrm{H}(n^* - n). \tag{4.23}$$

Here, $\mathrm{H}(x)$ is the Heaviside step function. The introduction of the Heaviside function results in a spatially-dependent delay of mechanical feedback, as it will now only occur at points S_0 such that $n(S_0) < n^*$.

Infinite foundation stiffness, $k \to \infty$

As before, in the case of an infinitely-stiff foundation, $k \to \infty$, we can solve Equation (4.23) analytically. Under this growth law, growth evolution is now described by two phases. Initially, growth is driven purely by Wnt signalling, i.e.

$$\dot{\gamma} = W(S_0)\gamma. \tag{4.24}$$

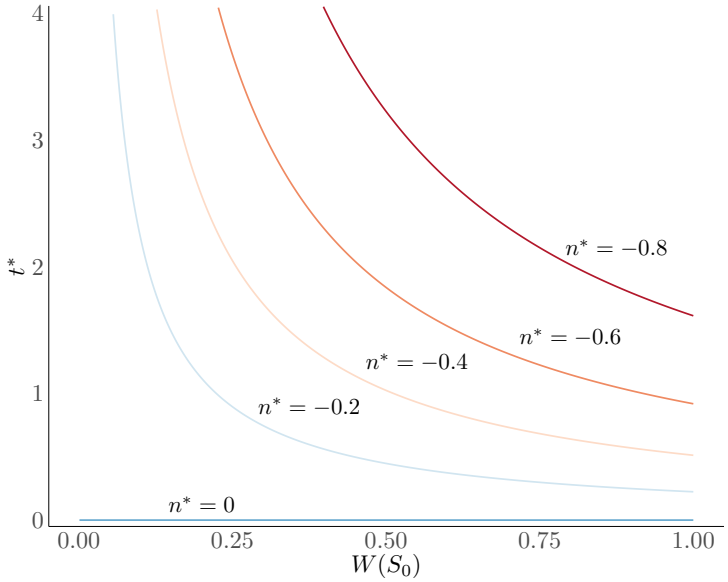

Figure 4.7: Activation times of mechanical feedback, t^*. Regions with greater Wnt signal concentrations are impacted by mechanical feedback earlier than regions with minimal Wnt signal. Decreasing the stress threshold, n^*, also delays activation of mechanical feedback.

Combining the solution to (4.24) with the expression for $n(t)$ given by (4.13) gives:

$$\gamma(S_0, t) = \mathrm{e}^{W(S_0)t}, \qquad n(S_0, t) = \frac{1 - \mathrm{e}^{W(S_0)t}}{\mathrm{e}^{W(S_0)t}}. \tag{4.25}$$

Mechanical feedback first occurs when $n(t) = n^*$. Solving $n(t^*) = n^*$ using Equation (4.25) gives the switching time, t^*, and corresponding growth:

$$t^* = \frac{1}{W(S_0)} \log\left(\frac{1}{1+n^*}\right), \qquad \gamma(S_0, t^*) = \frac{1}{1+n^*}. \tag{4.26}$$

Observe that t^* is smaller—indicating an earlier occurrence of mechanical feedback—where $W(S_0)$ is higher, i.e. the Wnt signal concentration is higher, or where n^* is smaller. In Figure 4.7, we plot t^* against $W(S_0)$ for various values of n^*. This figure shows that in regions of the rod where Wnt is higher, mechanical feedback will activate earlier, due to the increase in compression induced by growth. This feature is lost when $n^* = 0$; in this case, the threshold-dependent mechanical feedback law (4.23) is equivalent to the global mechanical feedback law (4.14). For $n^* < 0$, though, the time at which mechanical feedback begins to occur is spatially non-homogeneous.

For $t \geq t^*$, at a fixed Wnt signal value, Equation (4.23) reduces to the linear ODE (4.15). Solving this with the condition (4.26) gives the following expression for $\gamma(S_0, t)$:

$$\gamma(S_0,t) = \frac{\mu}{\mu(1+n^*) - W(S_0)} - \frac{W(S_0)\mathrm{e}^{-(\mu(1+n^*)-W(S_0))(t-t^*)}}{(1+n^*)(\mu(1+n^*)-W(S_0))}. \tag{4.27}$$

Hence, the incremental growth is given by

$$\frac{\dot{\gamma}}{\gamma} = \frac{W(S_0)(\mu(1+n^*)-W(S_0))\mathrm{e}^{-(\mu(1+n^*)-W(S_0))(t-t^*)}}{\mu(1+n^*) - W(S_0)E_s\mathrm{e}^{-(\mu(1+n^*)-W(S_0))(t-t^*)}}. \tag{4.28}$$

The key feature of this threshold-based mechanical feedback law is the presence of the switching time from Wnt-driven growth to mechanically-regulated growth, t^*, which depends on the Wnt signal concentration, $W(S_0)$. As the Wnt signal gradient $W(S_0)$ is heterogeneous, $t^* = t^*(S_0)$. This is in contrast to the ever-present mechanical feedback law, where $t^* \equiv 0$. As such, we expect that in regions for which mechanical feedback has switched on, growth will dampen such that regions that are subjected to only Wnt-based growth, albeit with a weaker signal, may exhibit greater incremental growth. This leads to us making the following claim.

Claim: Let $\gamma(t)$ be defined by (4.27). Suppose that $w_1 > w_2$. Define $\mathcal{G}(w) := \dot{\gamma}_w\gamma_w^{-1}$, where $\gamma_w(t) := \gamma(t)\big|_{W(S_0)=w}$. Then there exist values of t and μ such that

$$\mathcal{G}(w_1) < \mathcal{G}(w_2). \tag{4.29}$$

Proof: Our strategy is to find a time t such that $\mathcal{G}(w_1)$ exhibits mechanoregulated growth, while $\mathcal{G}(w_2)$ exhibits purely Wnt-driven growth. That is, we consider t for which

$$\frac{1}{w_1}\log\left(\frac{1}{1+n^*}\right) < t < \frac{1}{w_2}\log\left(\frac{1}{1+n^*}\right). \tag{4.30}$$

By this assumption and our expression for $\gamma(t)$, as given by Equation (4.17), we seek values of μ such that

$$\frac{\dot{\gamma}_{w_1}}{\gamma_{w_1}} < \frac{\dot{\gamma}_{w_2}}{\gamma_{w_2}} \qquad \Longleftrightarrow \qquad \frac{w_1(\mu(1+n^*)-w_1)\mathrm{e}^{-(\mu(1+n^*)-w_1)(t-t^*)}}{\mu(1+n^*) - w_1\mathrm{e}^{-(\mu(1+n^*)-w_1)(t-t^*)}} < w_2, \tag{4.31}$$

where t satisfies the inequality (4.30) and $t^* = \frac{1}{w_1}\log\left(\frac{1}{1+n^*}\right)$. Re-arranging this inequality yields:

$$t > t^* + \frac{1}{\mu(1+n^*) - w_1}\log\left(\frac{w_1(\mu(1+n^*) - w_1 + w_2)}{w_2\mu(1+n^*)}\right). \tag{4.32}$$

Imposing that $t > t^*$ leads to the following conditions on μ:

$$\begin{aligned} \mu &> \frac{w_1}{1+n^*}, \qquad \text{if} \qquad \mu(1+n^*) - w_1 > 0; \\ \mu &< \frac{w_1}{1+n^*}, \qquad \text{if} \qquad \mu(1+n^*) - w_1 < 0. \end{aligned} \tag{4.33}$$

Therefore, we choose μ such that the following inequality holds:

$$\begin{aligned} t^* + \frac{1}{\mu(1+n^*) - w_1}\log\left(\frac{w_1(\mu(1+n^*) - w_1 + w_2)}{w_2\mu(1+n^*)}\right) & \\ < t & \\ < \frac{1}{w_2}\log\left(\frac{1}{+n^*}\right) & \\ = t^* + \left(\frac{w_1 - w_2}{w_1 w_2}\right)\log\left(\frac{1}{1+n^*}\right). & \end{aligned} \tag{4.34}$$

This, in turn, imposes an upper bound on μ, where μ must satisfy the inequality:

$$\frac{w_1}{w_2}\left(1 - \frac{w_1 - w_2}{\mu(1+n^*)}\right) < \left(\frac{1}{1+n^*}\right)^{\frac{w_1 - w_2}{w_1 w_2}(\mu(1+n^*) - w_1)}. \tag{4.35}$$

Observe that the left hand side of (4.35) tends to a finite limit as $\mu \to \infty$, w_1/w_2, while the right hand side is an increasing exponential function in μ. Therefore, the inequality (4.35) is satisfied for a sufficiently large value of μ. The proof demonstrates that, for an infinitely-stiff foundation, there is always a finite value of μ such that, under this threshold-dependent mechanical feedback law (4.23), a bimodal[1] distribution of incremental growth can be produced. Moreover, the lower bound on μ shows how the range of values of μ for which a bimodal distribution will be observed depends on both the maximal Wnt signal value–in our case, $\max_{s\in[0,1]} W(S_0) = 1$—and the threshold stress for mechanical feedback, n^*. For smaller values of n^*, μ must be higher in order to ensure that regions along the rod

[1]Note that as we consider growth along the half-length of the crypt (see Figure 4.2, the resulting incremental growth profile in this 1D geometry is unimodal. We refer to this profile as bimodal because its even extension, which is used to capture the proliferative structure of the crypt, means that incremental growth is bimodal in shape.

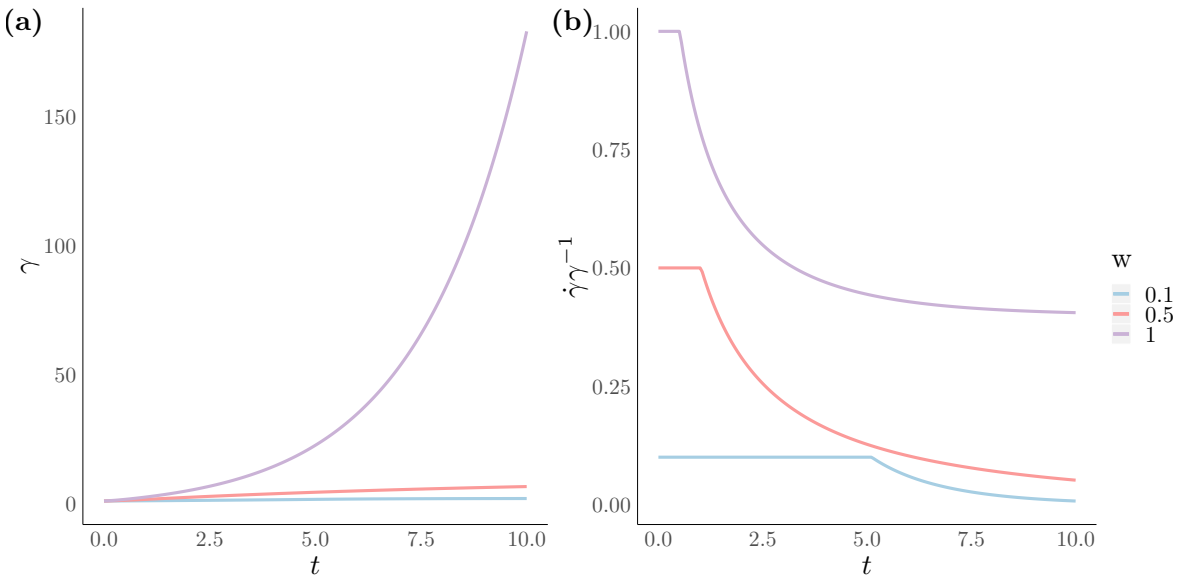

Figure 4.8: Growth at fixed Wnt values for threshold-based mechanical feedback, for $\mu = 1$, $n^* = -0.4$. (a) Growth $\gamma(t)$ and (b) incremental growth $\dot{\gamma}\gamma^{-1}(t)$ for fixed Wnt signal values, $W(S_0) = 0.1,\ 0.5,\ 1$. A non-zero n^* delays the onset of mechanical regulation of growth. However, μ is not high enough to dampen growth at $W(S_0) = 1$ so that it falls below the solutions for $W(S_0) = 0.1$ and $W(S_0) = 0.5$.

that are subject to a higher Wnt signal concentration, and hence grow faster initially, will be dampened sufficiently by mechanical feedback. This feature is demonstrated in Figures 4.8–4.9, $\gamma_w(t)$ and $\dot{\gamma}_w\gamma_w^{-1}(t)$ are plotted for several fixed Wnt signals, for $\mu = 1$ and $\mu = 10$, respectively. In Figure 4.8, when $\mu = 1$, there is a delay in mechanoregulation of incremental growth, due to the non-zero stress threshold n^*, such that $\dot{\gamma}_w\gamma_w^{-1}$ is driven by only Wnt longer for the solutions corresponding to $W(S_0) = 0.1$ and $W(S_0) = 0.5$ than the solution for $w = 1$. However, mechanical feedback does not dampen $\dot{\gamma}_w\gamma_w^{-1}$ sufficiently for $W(S_0) = 1$. Contrast this with Figure 4.9, where $\mu = 10$ and so mechanical feedback is strong enough to dampen the incremental growth at $W(S_0) = 1$, such that there exist times when $\dot{\gamma}_w\gamma_w^{-1}(t)$ falls below the solutions for $W(S_0) = 0.1$ and $W(S_0) = 0.5$. In Figure 4.10, we plot the resulting evolution of incremental growth for $\mu = 10$ and $W(S_0)$ defined by (4.12), demonstrating that a bimodal profile is indeed obtained.

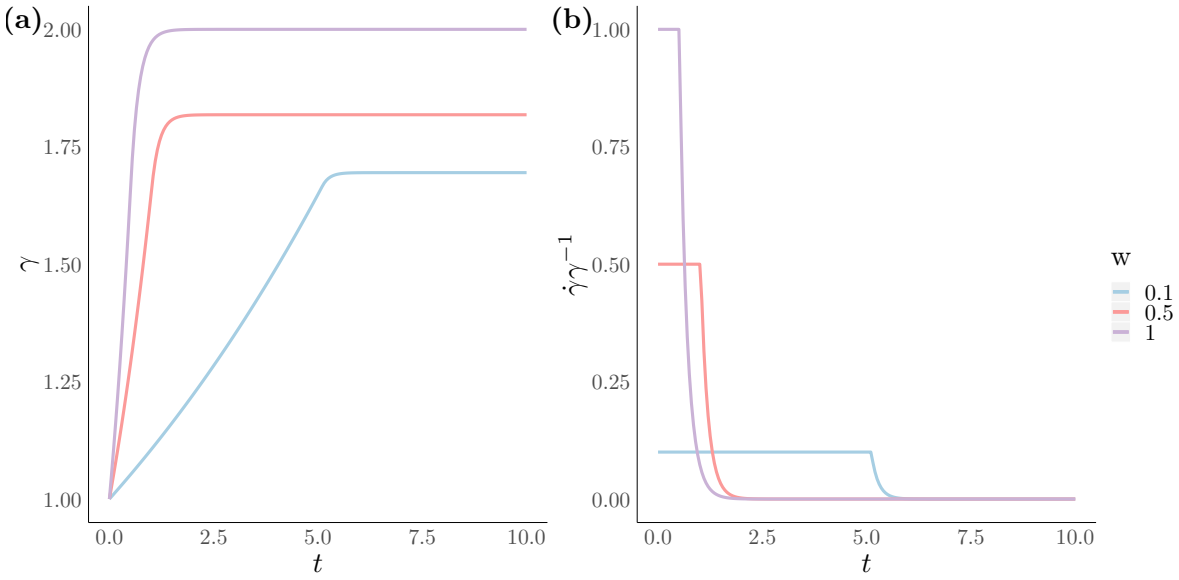

Figure 4.9: Growth at fixed Wnt values for threshold-based mechanical feedback, for $\mu = 10$ and $n^* = -0.4$. (a) Growth $\gamma(t)$ and (b) incremental growth $\dot{\gamma}\gamma^{-1}(t)$ for a fixed Wnt signal values, $W(S_0)$, where $W(S_0) = 0.1,\ 0.5,\ 1$. Here, μ is sufficiently high such that $\dot{\gamma}\gamma^{-1}$ for $W(S_0) = 1$ falls below the solutions corresponding to $W(S_0) = 0.5$ and $W(S_0) = 0.1$ at a finite time.

4.3.3 Finite foundation stiffness

We have shown that it is possible to obtain an incremental growth profile reminiscent of the proliferative structure within the crypt for an infinitely-stiff foundation. However, as infinite stiffness is not physically realistic, we now consider whether such incremental growth profiles are possible for a finite foundation stiffness. In particular, we wish to identify regions of parameter space of (k, μ, n^*)—the foundation stiffness, the sensitivity to mechanical feedback, and the stress threshold for feedback, respectively—in which growth transitions from Wnt-driven, and maximal in the base, to bimodal and maximal away from both the base and the top.

Preliminary simulations (not shown) revealed that changing the value of n^* does not affect the resulting spatial profile over time, but only quickens or delays the onset of mechanical regulation, provided that $-1 < n^* < 0$. Therefore, we fix n^* and perform a parameter sweep over k and μ. For each pair of (k, μ) values, we simulate Equations (4.7)–(4.9) subject to the growth laws (4.14) and (4.23) up to $t = 5$ and examine the resulting spatial profile of incremental growth, $\dot{\gamma}\gamma^{-1}$. Figure

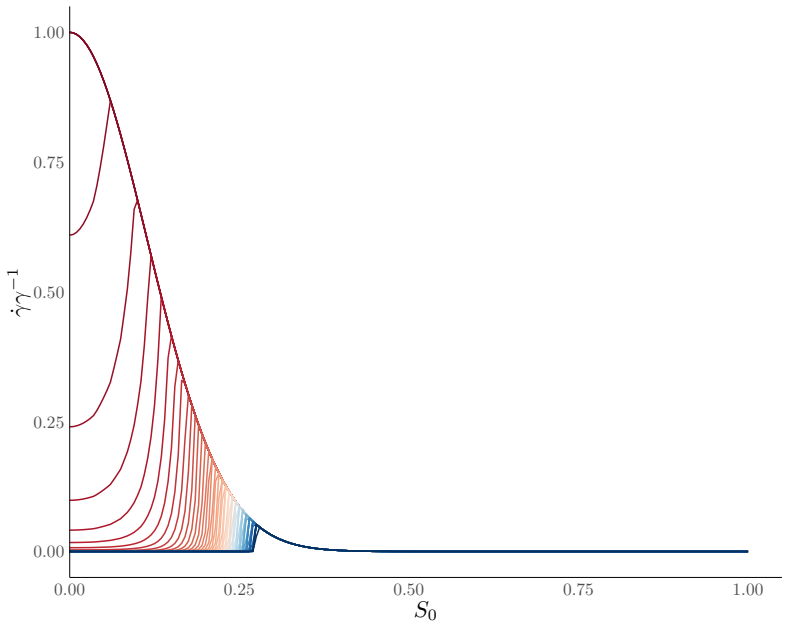

Figure 4.10: Enhanced threshold-dependent mechanical feedback reduces growth in the crypt base. The relative growth $\dot{\gamma}\gamma^{-1}$ against S_0 has been plotted for increasing time. Dark red profiles indicate earlier times, while dark blue profiles indicate later times. Solutions have been solved on an infinitely-rigid foundation. The Wnt gradient has been defined according to Equation (4.12). The mechanical feedback parameters are $\mu = 10$ and $n^* = -0.4$. Introducing stress threshold dependence results in a shift in the position of the local maximum of $\dot{\gamma}\gamma^{-1}$ for sufficiently high values of μ.

4.12 summarises the results of the parameter sweep. We characterise the spatial behaviour of $\dot{\gamma}\gamma^{-1}$, which can be seen to fall into three distinct parameter regimes:

1. **Primarily Wnt-driven:** Here, $\dot{\gamma}\gamma^{-1}$ is maximal at $s = 0$, and is similar in profile to the case $\dot{\gamma}\gamma^{-1} = W(s)$, (see Figure 4.3). This occurs when mechanical feedback is insufficient (μ is too small) to dampen the effect of the Wnt gradient. We note that although our classification of behaviours is based on simulations run up to $t = 5$, the behaviour observed is independent of the simulation end time. We can be certain that this behaviour holds for longer simulation times, because in this framework, stress is bounded below, $n(S_0, t) > -1$, due to the linear relationship between stress and the elastic stretch, (4.5). Therefore, the inhibition of growth due to mechanical feedback is bounded and if μ is too small, then the contribution from mechanical feedback will be negligible.

2. **Non-monotonic from the base:** In this regime, $\dot{\gamma}\gamma^{-1}$ is still maximal at $s = 0$, but mechanical feedback has reduced growth non-monotonically. There are even parameter regions where $\dot{\gamma}\gamma^{-1} < 0$ for $0 < s < 1$. This behaviour arises for the widest range of parameter values, as neither k nor μ are high enough to give rise to bimodal behaviour. This is akin to what is observed in Figure 4.8, when $\mu = 1$ and $k \to \infty$.

3. **Maximal away from the base:** In this case, $\dot{\gamma}\gamma^{-1}$ no longer attains a local maximum at $s = 0$. As such, its even extension is bimodal. This occurs when mechanical stress $n(S_0, t)$ exhibits sufficient spatial variation due to growth (k is sufficiently large) and mechanical feedback is sufficiently strong (μ is sufficiently large) such that mechanical inhibition occurs in the base first, before other regions are affected. If k is small, then (4.9) implies that the rod stress $n(S_0, t)$ is effectively constant. Contrastingly, in the $k \to \infty$ case, then the solution (4.13) implies that $n(S_0, t)$ is minimal where growth γ is maximal, and vice versa. Examples where mechanical feedback sufficiently dampens the Wnt signal can also be seen in Figures 4.9–4.10, for $k \to \infty$ and $\mu = 10$.

Ever-present mechanosensitivity

In Figure 4.11, we plot the phase space of resultant incremental growth profiles obtained by numerically solving Equations (4.8)–(4.9) subject to the growth law (4.14). We observe that the resultant profiles are all primarily Wnt-driven and the monotonicity of $\dot{\gamma}\gamma^{-1}$ does not change for any values of k of μ. These numerical results support the claim we made in the case of an infinitely-stiff foundation, where we proved that it was not possible for $\dot{\gamma}\gamma^{-1}$ to be maximal away from $s = 0$.

Threshold-dependent mechanosensitivity

Figure 4.12 demonstrates the range of the foundation stiffness, k, and mechanical feedback strength, μ, needed to obtain a bimodal growth profile. Sufficient foundation stiffness is required in order to induce heterogeneity in stress, consequently

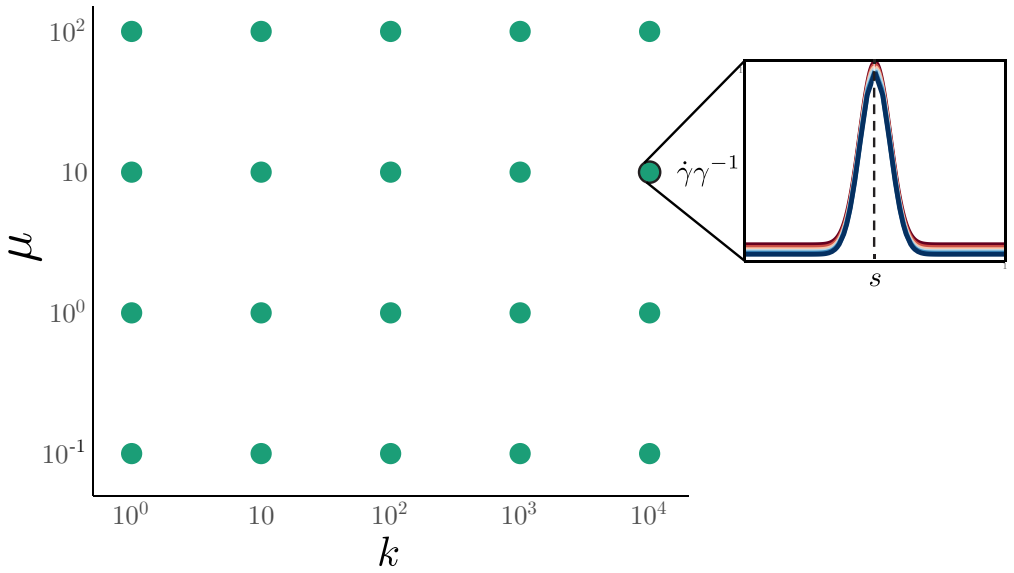

Figure 4.11: Phase space of incremental growth for ever-present mechanical feedback (4.14)**.** Results are obtained by numerical simulations over the parameter space, which are plotted on a log-log scale. Shapes and colours are classified according to the behaviour of the incremental growth profile, $\dot{\gamma}\gamma^{-1}$, up to $t = 5$. Green circles correspond to growth that is primarily Wnt-driven and maximal at $s = 0$. The behaviour of $\dot{\gamma}\gamma^{-1}$ can be described by the two mechanical parameters, k and μ. We have plotted the even extension of the inset incremental growth profile, where $s = 0$ (crypt base) is indicated by the dotted line, to better illustrate possible growth scenarios in the crypt. Incremental growth behaviour does not vary significantly for different values of k and μ.

regulating growth heterogeneously. Additionally, μ must be large enough to ensure that $\dot{\gamma}\gamma^{-1}$ is dampened sufficiently about $s = 0$, such that $\dot{\gamma}\gamma^{-1}$ is locally maximal for $s > 0$. The combination of these provides a plausible mechanical mechanism for producing the proliferative structure observed in the crypt.

4.4 Modelling homeostasis

We have now obtained a minimal, mechanochemical growth law that captures the spatial hierarchy of proliferative activity observed in the crypt. However, one caveat of this mechanosensitive law is that in parameter regions of (k, μ) where bimodal distributions of incremental growth exist, as $t \to \infty$, $\dot{\gamma}\gamma^{-1} \to 0$ everywhere (see Figure 4.12). In these parameter regions, growth decays due to the fixed boundary conditions (4.7). As both ends of the rod are fixed with no flux of material allowed, material points have nowhere to escape and compression continues to build up and

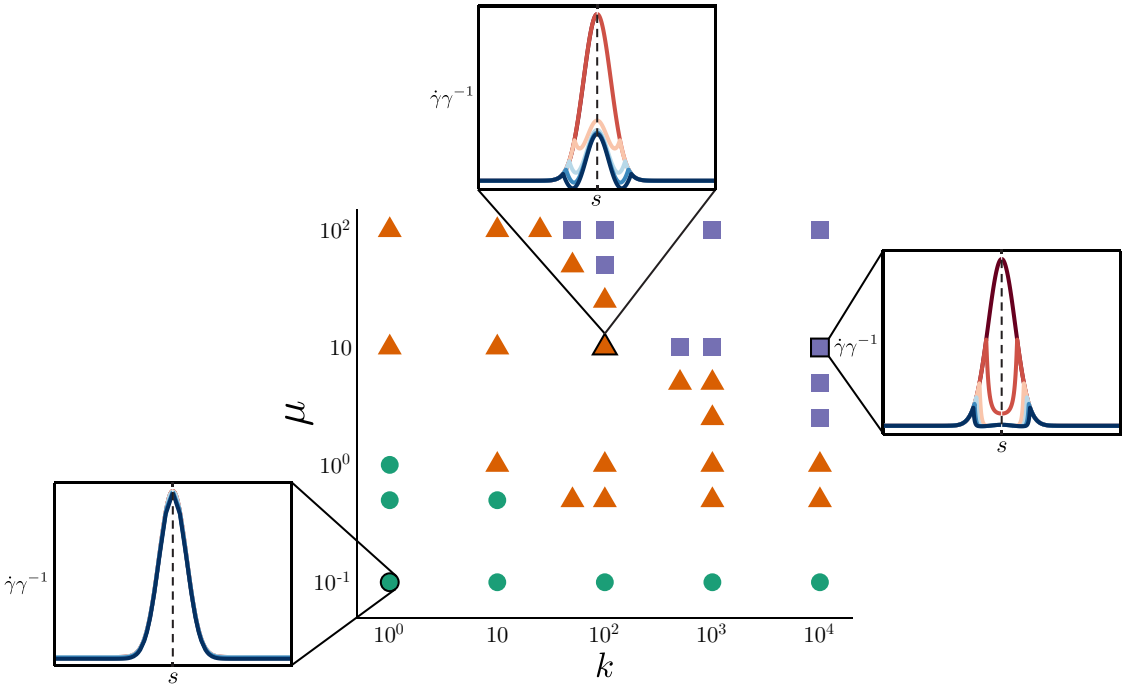

Figure 4.12: Phase space of incremental growth for threshold-based mechanical feedback (4.23)**.** Results are obtained by numerical simulations over the parameter space, which are plotted on a log-log scale. Shapes and colours are classified according to the behaviour of the incremental growth profile, $\dot{\gamma}\gamma^{-1}$, up to $t = 5$. Green circles correspond to growth that is primarily Wnt-driven and maximal at $s = 0$; orange triangles indicate profiles that are maximal at $s = 0$ and non-monotonic; and purple squares indicate those that are maximal away from $s = 0$. In the three subplots, red-coloured profiles indicate earlier times, while blue curves indicate later times. The threshold stress is fixed to $n^* = -0.4$. The behaviour of $\dot{\gamma}\gamma^{-1}$ can be described by the two mechanical parameters, k and μ. Note that we have plotted the even extensions of the incremental growth profiles, where $s = 0$ (crypt base) is indicated by the dotted lines, to better illustrate possible growth scenarios within the context of the crypt. Incremental growth behaviour can be characterised completely by the foundation stiffness, k and strength of mechanical feedback, μ.

inhibit growth until $\dot{\gamma} = 0$. Biologically, this is similar to cells becoming overcrowded due to the presence of neighbouring cells; the resulting increase in stress eventually arrests proliferation everywhere. However, this does not occur in the crypt, as fully-differentiated cells are sloughed into the lumen to undergo apoptosis, which balances proliferation to maintain tissue homeostasis [1]. Thus, we now turn our attention to identifying the conditions under which tissue homeostasis in the crypt occurs and is maintained; that is, that the bimodal shape of $\dot{\gamma}\gamma^{-1}$ stays fixed in time. Henceforth, we will consider threshold-dependent mechanosensitive growth

(4.23), with mechanical parameters set to $k = 10^3$, $\mu = 10$ and $n^* = -0.5$.

Thus far all variables and quantities have been defined with respect to the initial arc length, S_0, which represents the Lagrangian frame of reference. This is a natural way to define quantities such as the growth stretch, $\gamma(S_0, t)$, which describes the total amount that the rod has grown up to time t at S_0. However, from a biological perspective, quantities are observed in the current Eulerian configuration, which in this framework is parametrised by the current arc length, s. In particular, during tissue homeostasis, proliferation, which is modelled through the incremental growth $\dot{\gamma}\gamma^{-1}$, should appear to be unchanging over time in the Eulerian frame. In other words, $\dot{\gamma}\gamma^{-1}$ should be fixed with respect to the current arc length s and independent of time t. Therefore, we define tissue homeostasis by the following condition:

$$\frac{\dot{\gamma}}{\gamma} \equiv g(s), \tag{4.36}$$

where $g(s)$ is the homeostatic incremental growth profile.

Given our definition of homeostasis, it is prudent to consider the system in the Eulerian reference frame. In order to define quantities correctly, we must take particular care with time derivatives. For a Lagrangian variable $f(S_0, t)$, we denote its equivalent Eulerian variable by $\hat{f}(s, t) := f(S_0(s, t), t)$. By the chain rule and the multiplicative decomposition (1.5), the associated space and time partial derivatives are:

$$\frac{\partial \hat{f}}{\partial s} = \frac{\partial f}{\partial S_0}\frac{1}{\alpha\gamma}, \tag{4.37}$$

$$\frac{\partial \hat{f}}{\partial t} = \frac{\partial f}{\partial t} + \hat{v}\frac{\partial f}{\partial s}, \tag{4.38}$$

where $\hat{v}(s, t)$ is the (pull-back) flow velocity and is given by:

$$\hat{v}(s, t) = \hat{\alpha}\hat{\gamma}\frac{\partial \hat{S}_0}{\partial t}. \tag{4.39}$$

We note that the time derivative (4.38) is reminiscent of the material derivative that arises throughout continuum mechanics. The flow velocity itself, $\hat{v}(s, t)$, arises from mapping Lagrangian quantities to the Eulerian reference frame. The current Lagrangian velocity, $v(S_0, t) = \partial s(S_0, t)/\partial t$, which measures the velocity along the

rod at a fixed material point S_0, can be interpreted as a continuum 'migration' velocity; that is, the velocity of a fixed material point along the crypt. This quantity is of interest as it is one of the forms of data obtainable from the crypt and thus provides a link to homeostatic processes [99, 107]. Applying the chain rule to $f(S_0,t) = \hat{f}(s,t)$ shows that

$$\frac{\partial f}{\partial t} = \frac{\partial \hat{f}}{\partial t} + v\frac{\partial \hat{f}}{\partial s}. \tag{4.40}$$

Rearranging (4.40) for $\partial\hat{f}/\partial t$ and equating this definition with Equation (4.38) implies that the current and flow velocities are related as follows:

$$v(S_0,t) = -\hat{v}(s(S_0,t),t). \tag{4.41}$$

4.4.1 Homeostasis framework

We now derive the equations governing homeostasis in a 1D geometry to set the stage for the next section, where we derive the conditions under which homeostasis holds.

We first re-cast the force balance equation with respect to the current arc length s. Applying the multiplicative decomposition (1.5) and the material derivative definition (4.38) to Equations (4.8)–(4.9) yields the resulting Eulerian system:

$$\frac{\partial \hat{S}_0}{\partial s} = \frac{1}{\hat{\alpha}\hat{\gamma}}, \tag{4.42}$$

$$\frac{\partial \hat{n}}{\partial s} = k(s-\hat{p}), \qquad \frac{\partial \hat{p}}{\partial t} = \rho(s-\hat{p}) + \hat{v}\frac{\partial \hat{p}}{\partial s}. \tag{4.43}$$

By Equations (4.36) and (4.38), growth $\hat{\gamma}(s,t)$ in the Eulerian frame evolves according to the following equation:

$$\frac{\partial \hat{\gamma}}{\partial t} = g\hat{\gamma} + \hat{v}\frac{\partial \hat{\gamma}}{\partial s}. \tag{4.44}$$

In homeostasis, we replace the fixed boundary conditions (4.7) with new boundary conditions,

$$\hat{S}_0(0,t) = 0, \qquad \hat{S}_0(1,t) = L_\mu, \tag{4.45}$$

where, in a similar manner to Chapter 3 (see Equation (3.27)), L_μ represents the sloughing boundary. The sloughing boundary L_μ can be related to the

growth and elastic stretches by integrating Equation (4.42) with respect to s over the unit interval:

$$L_\mu(t) = \int_0^1 \frac{1}{\hat{\alpha}\hat{\gamma}} ds. \tag{4.46}$$

Note that $L_\mu(t)$ evolves over time, which distinguishes (4.45) from the fixed 'pre-homeostasis' boundary conditions (4.7), for which $L_\mu(t) \equiv 1$. The presence of the sloughing boundary L_μ implies an evolving Lagrangian domain $S_0 \in [0, L_\mu(t)]$. The idea is that in homeostasis, L_μ will evolve such that the incremental growth profile $\dot{\gamma}\gamma^{-1}$ remains fixed in the observable Eulerian frame.

A subtle issue arises in the Eulerian formulation of $\hat{S}_0(s,t)$. Observe that there are two partial differential equations for $\hat{S}_0$, as specified by Equations (4.39) and (4.42). As both of these equations are of first order, $\hat{S}_0$ is overdetermined. To ensure that $\hat{S}_0$—and consequently the flow velocity $\hat{v}(s,t)$—are defined consistently, we must impose the following compatibility condition:

$$\frac{\partial^2 \hat{S}_0}{\partial s \partial t} = \frac{\partial^2 \hat{S}_0}{\partial t \partial s} \qquad \Longleftrightarrow \qquad \frac{\partial}{\partial s}\left(\frac{\hat{v}}{\hat{\alpha}\hat{\gamma}}\right) = \frac{\partial}{\partial t}\left(\frac{1}{\hat{\alpha}\hat{\gamma}}\right). \tag{4.47}$$

Note that Equation (4.47) holds in general, regardless of whether the system is in homeostasis or not, and is independent of any force balance equation. Therefore, the task is to determine the solutions that arise when Equation (4.47) is coupled with the force balance equation (4.43) during homeostasis.

4.4.2 When does homeostasis hold?

Having reformulated the growth law and force balance equations in the Eulerian configuration, we can now deduce the conditions for which homeostasis is maintained. First, since we have assumed a mechanochemical growth law (4.10), observe that equating (4.10) with the homeostasis definition (4.36) implies that the stress n is a function of s only and can be determined by equating $\mathcal{G}$ with the homeostatic growth profile g:

$$\mathcal{G}(W(s), \hat{n} - n^*) \equiv g(s) \qquad \Longleftrightarrow \qquad \hat{n}(s,t) = \hat{n}(s). \tag{4.48}$$

We can therefore define the homeostatic Eulerian elastic stretch, $\hat{\alpha}$, analogously to the constitutive relation for the elastic stretch α (4.5), which is also independent of time:

$$\hat{\alpha}(s) := 1 + \hat{n}(s), \tag{4.49}$$

and by the Eulerian force balance (4.43), the foundation curve $\hat{p}$ is also a function of s only:

$$\hat{n}'(s) = k(s - \hat{p}) \qquad \Longleftrightarrow \qquad \hat{p}(s) = s - \frac{\hat{n}'}{k}, \tag{4.50}$$

where $' = d/ds$. In other words, in homeostasis, the stress, elastic stretch, and foundation attachments have fixed profiles in the Eulerian configuration. In the case of the foundation, we must have that $\partial\hat{p}/\partial t = 0$; rearranging Equation (4.43) thus gives an expression for the flow velocity $\hat{v}$ in homeostasis, which only depends on s:

$$\hat{v}(s) = -\frac{\rho}{k}\frac{\hat{n}'}{\hat{p}'}. \tag{4.51}$$

This expression for $\hat{v}(s)$ ensures that the force balance (4.43) is satisfied during homeostasis. However, $\hat{v}$ must also be consistent with our compatibility condition (4.47). As $\hat{v} = \hat{v}(s)$, evaluating Equation (4.47) yields a first-order ordinary differential equation for $\hat{v}(s)$:

$$\hat{v}' - \frac{\hat{n}'}{1 + \hat{n}}\hat{v} = -g(s; \hat{n}), \tag{4.52}$$

where we have replaced $\hat{\alpha}$ and its derivative using the constitutive relation (4.49) and write $g = g(s; \hat{n})$ to remind ourselves that growth depends on both current position s and stress $\hat{n}$.

Substituting Equation (4.43) into Equation (4.51) and rearranging for $\hat{p}_s$, we arrive at the following coupled system of three first-order ordinary differential equations that must be satisfied in homeostasis:

$$\hat{n}' = k(s - \hat{p}), \tag{4.53}$$

$$\hat{p}' = -\rho\frac{(s - \hat{p})}{\hat{v}}, \tag{4.54}$$

$$\hat{v}' = \frac{k(s - \hat{p})\hat{v}}{1 + \hat{n}} - g(s; \hat{n}), \tag{4.55}$$

where we assume that $g(s;\hat{n})$ obeys the threshold-dependent mechanical feedback law (4.23),

$$g(s;\hat{n}) = W(s) + \mu(\hat{n} - n^*)\mathrm{H}(n^* - \hat{n}). \tag{4.56}$$

Equations (4.53)–(4.54) ensure that the flow velocity $\hat{v}(s)$ is consistent with the force balance (4.43), while Equation (4.55) ensures that the two differential equations for $\hat{S}_0$, Equations (4.39) and (4.42), are consistent. All solutions of the system (4.53)–(4.55) that are physically consistent—that is, for which $\hat{\alpha}(s) > 0$ and $\hat{v}(s)$ is finite—correspond to profiles in a homeostatic state. However, we are primarily interested in solutions to Equations (4.53)–(4.55) that permit the bimodal shape for $g(s)$ that is representative of the homeostatic proliferative structure observed in the crypt.

We first narrow down the solution space by specifying boundary conditions. Observe that by the definition of $\hat{v}$ from Equation (4.39), the boundary condition $\hat{S}(0,t) = 0$ implies that $\hat{v}(0) = 0$, as $\hat{\alpha}(s,t) \neq 0$ and $\hat{\gamma}(s,t) \neq 0$. Consequently, from Equation (4.43), we deduce that $\hat{p}(0) = 0$. Therefore, we solve the system (4.53)–(4.55) subject to the left boundary conditions:

$$\hat{p}(0) = 0, \qquad \hat{v}(0) = 0. \tag{4.57}$$

We therefore explore the effect of the left boundary condition $\hat{n}(0)$ on the solution space of Equations (4.53)–(4.55), subject to the given boundary conditions (4.57)[2]. We restrict to numerical solutions of Equations (4.53)–(4.55), due to the nonlinearities present. However, we can still deduce certain parameter relationships that must hold in order for a bimodal growth shape. First, it is clear that as $g(s;\hat{n})$ is given by Equation (4.56), for $g(s)$ to satisfy $g(0) \geq 0$, $\hat{n}(0)$ must satisfy the inequality, noting that $W(0) = 1$:

$$n^* - \frac{1}{\mu} \leq \hat{n}(0) < n^*. \tag{4.58}$$

[2]While it appears that the boundary condition $\hat{v}(0) = 0$ results in a singularity, applying L'Hôpital's Rule and re-arranging for $\hat{p}'(0)$ reveals that $\hat{p}'(0) = \frac{\rho}{\rho + g(0)}$, which is bounded.

Second, a local minimum at $s = 0$ is indicative of $g(s; \hat{n})$ being bimodal in shape. Equivalently, we require that $g''(s; \hat{n}) > 0$. Assuming the inequality (4.58) holds, evaluating the second derivative of $g(s)$ at $s = 0$ yields:

$$g''(0) = W''(0) + \frac{\mu k \left(W(0) + \mu(\hat{n}(0) - n^*)\right)}{\rho + W(0) + \mu(\hat{n}(0) - n^*)}, \tag{4.59}$$

where we have used Equation (4.54) to replace $\hat{n}''(0) = \hat{p}'(0) = \rho/(\rho + g(0))$, and used Equation (4.56) to substitute $g(0)$. Thus, in order for $g(s)$ to be locally minimal at $s = 0$, the following inequality for the foundation stiffness k must hold:

$$k > -\frac{W''(0)}{\mu}\left[\frac{\rho}{W(0) + \mu(\hat{n}(0) - n^*)} + 1\right]. \tag{4.60}$$

The inequality (4.60) reveals the importance of several key parameters in maintaining homeostasis. First, larger values of μ (the mechanical feedback strength) permit a wider range of foundation stiffness values that will yield a bimodal incremental growth profile. Second, a more rapidly-remodelling foundation, characterised by the parameter ρ, requires a stiffer foundation, indicating the competition between the foundation stiffness and remodelling of the foundation attachments. Finally, if we define the Wnt signal $W(s)$ as a Gaussian function, as per Equation (4.12), then (4.60) yields

$$k > -\frac{2}{\sigma_W^2 \mu}\left[\frac{\rho}{1 + \mu(\hat{n}(0) - n^*)} + 1\right]. \tag{4.61}$$

Therefore, for smaller values of σ_W, corresponding to Wnt gradients that are more concentrated towards the base, the foundation stiffness k must be larger to maintain homeostasis.

To validate our analysis, we solve the system (4.53)–(4.55) numerically for various values of the foundation stiffness k and foundation remodelling parameter ρ, subject to the left boundary condition $\hat{n}(0) = -0.55$. For each pair of parameter values (k, ρ), we considered the resulting homeostatic incremental growth profile $g(s)$, and, in a similar manner to Figure 4.12, classified profiles as either bimodal or non-monotonic from the base. The results are shown in Figure 4.13. The numerical solutions indicate excellent agreement with the analytical inequality (4.60), with

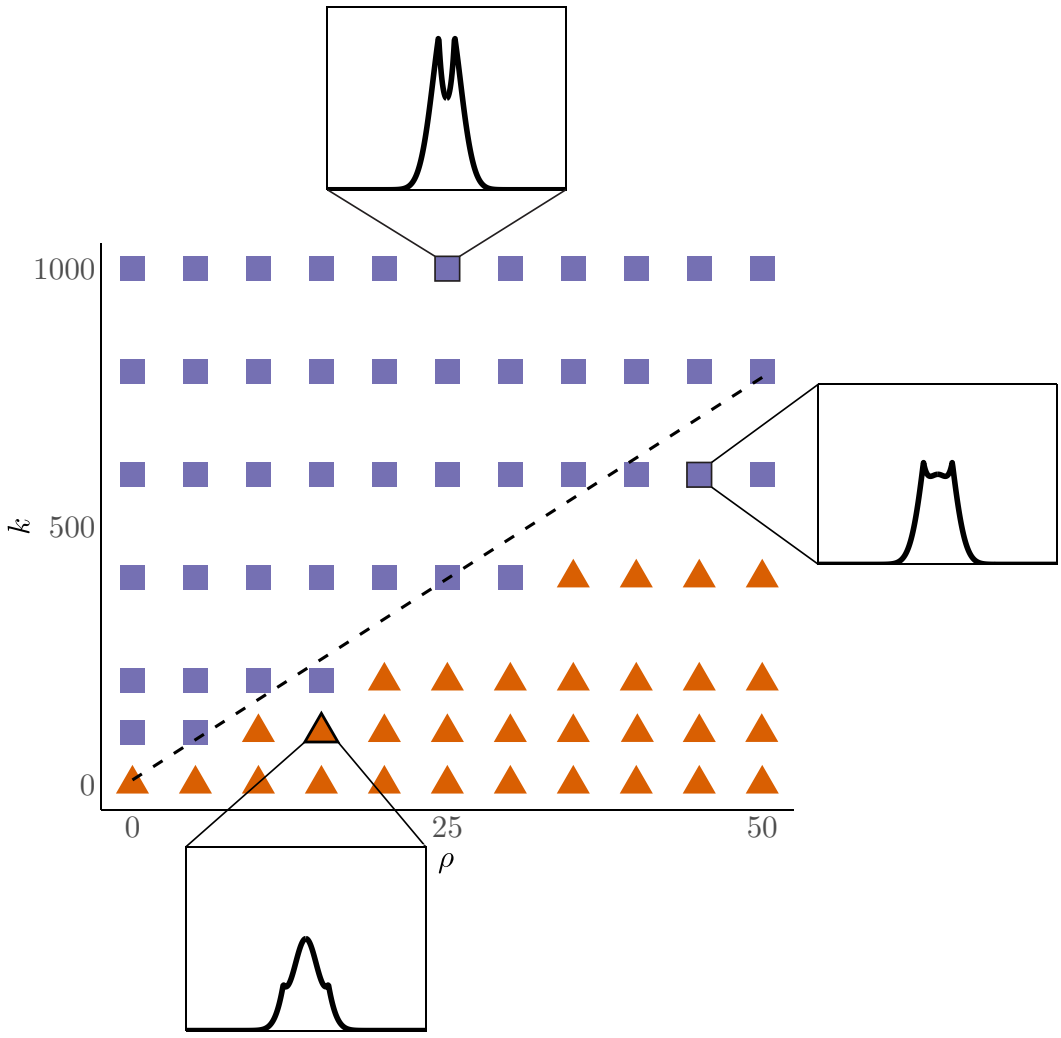

Figure 4.13: Phase space of homeostatic incremental growth profiles. Here, the homeostatic incremental growth $g(s;\hat{n})$ has been generated by solving the homeostasis equations (4.53)–(4.55) for different values of k and ρ. The mechanical feedback parameters have been set to $\mu = 10$ and $n^* = -0.5$. The system has been solved subject to the left boundary condition $\hat{n}(0) = -0.55$. The dashed line represents the predicted separation of bimodal and non-bimodal behaviour, as predicted by the inequality (4.60). The homeostatic incremental growth profile depends on the competition between the foundation stiffness k and foundation remodelling parameter ρ.

exceptions arising from cases where $g(s)$ is bimodal but not a local minimum at $s = 0$. One example of this case is indicated in Figure 4.13, where the profile corresponding to $k = 600$ and $\rho = 45$ is shown.

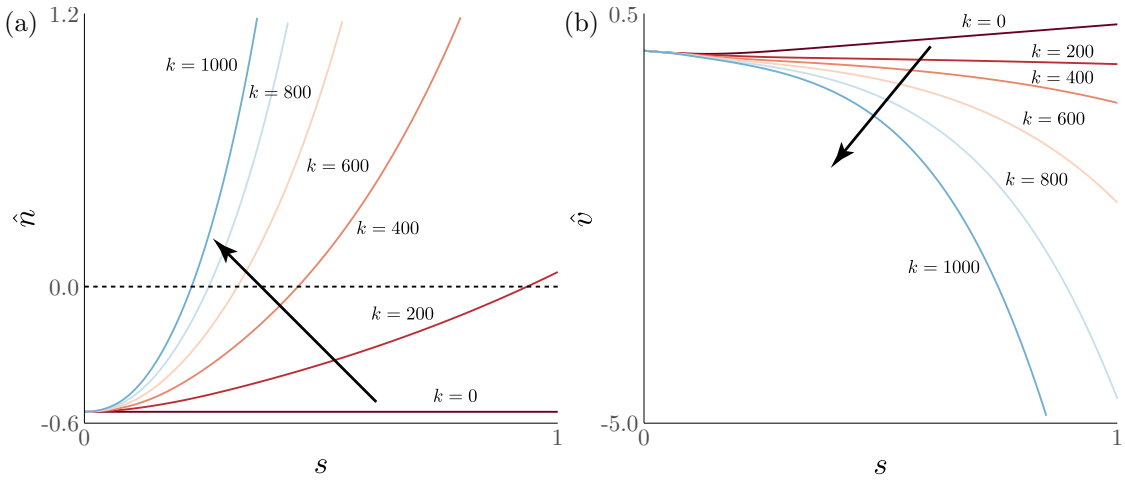

Figure 4.14: Effect of the foundation stiffness k on homeostatic stress and flow velocity. (a) The homeostatic stress profiles $\hat{n}(s)$. (b) The homeostatic flow velocity $\hat{v}(s)$. Both $\hat{n}$ and $\hat{v}$ have been obtained by solving Equations (4.53)–(4.55), subject to $\hat{n}(0) = -0.55$ and $\rho = 35$. Increasing k results in expanding regions of tension while increasing the magnitude of the flow velocity.

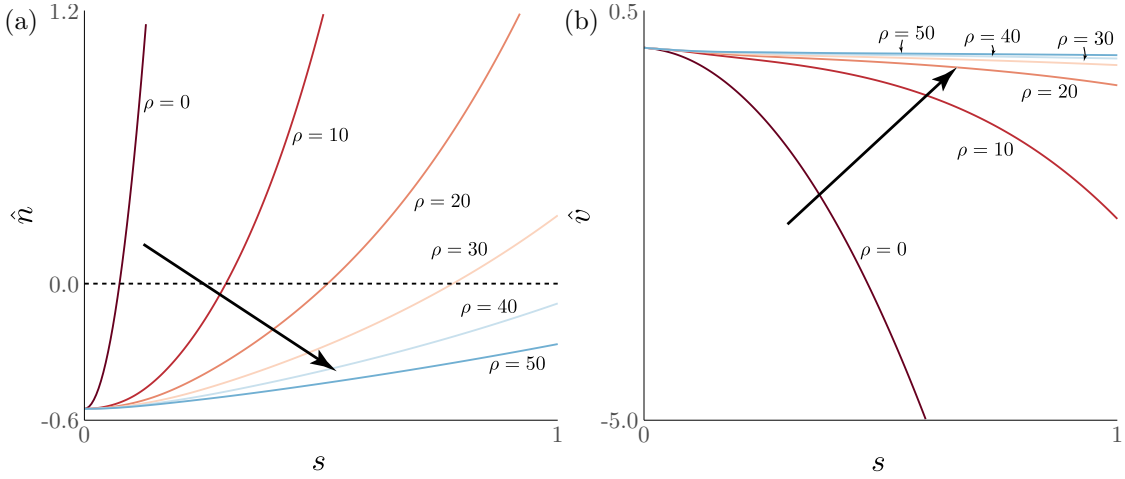

Figure 4.15: The effect of the foundation remodelling parameter ρ on homeostatic stress and flow velocity. (a) The homeostatic stress $\hat{n}(s)$ for fixed k and increasing ρ and (b) The homeostatic flow velocity $\hat{v}(s)$, which are obtained by solving Equations (4.53)–(4.55), subject to $\hat{n}(0) = -0.55$ and $k = 200$. Increasing ρ shrinks the region of the rod under tension and decreases the magnitude of the flow velocity.

4.4.3 Crypt homeostasis requires distinct regions of compression and tension

Figure 4.13 indicates that there are values of the parameters k and ρ for which a homeostatic incremental growth profile can be obtained. We now aim to characterise

the homeostatic stress and flow velocity profiles, $\hat{n}(s)$ and $\hat{v}(s)$ respectively, and the effect of varying the k and ρ. In Figure 4.14, we fix $\rho = 35$ and solve the system (4.53)–(4.55) for increasing foundation stiffness k. When $k = 0$, the homeostatic stress is constant and $\hat{n}(s) = \hat{n}(0) = -0.55$. Therefore, the rod is under constant compression. However, as k begins to increase, particularly for the cases $k = 600, 800$, and $k = 1000$, corresponding to bimodal shapes, stress transitions from compression to tension. Moreover, not only does the region of the rod that is under tension expand for increasing k, but stress also increases along the rod at a faster rate. Correspondingly, the flow velocity $\hat{v}$ becomes increasingly negative, with quicker rates of decrease for larger values of k. As the material velocity v is related to the flow velocity by $v = -\hat{v}$, the increase in magnitude indicates that material is being swept out at an increasing rate to maintain the homeostatic incremental growth profile. Contrastingly, in Figure 4.15, when k is fixed and ρ is varied, we observe the opposite behaviour; that is, increasing ρ reduces the size of the region under tension and decreases the magnitude of the flow velocity.

Figures 4.14–4.15 suggest that the spatial profiles of $\hat{n}(s)$ and $\hat{v}(s)$ are monotonically increasing and decreasing, respectively. Therefore, to characterise the solution space spanned by the parameters k and ρ, it suffices to monitor the boundary values $\hat{n}(1)$ and $\hat{v}(1)$. In Figure 4.16, we plot the 2D contours of $\hat{n}(1)$ and $\hat{v}(1)$ as functions of k and ρ, confirming the trends observed in Figures 4.14–4.15. The magnitude of stress and flow velocities at $s = 1$ are much larger in the parameter regions where a bimodal incremental growth shape arises in regions where non-bimodal shapes are obtained. As all solutions are calculated with $\hat{n}(0) < 0$ and $\hat{v}(0) = 0$, this indicates that in order to maintain the bimodal incremental growth shape observed in the crypt, there must be competing regions of compression towards the base and tension towards the top. Correspondingly, the flow velocity must decrease from the base to the top, indicating that cells migrate at an increasingly faster rate as they move from the base to the top.

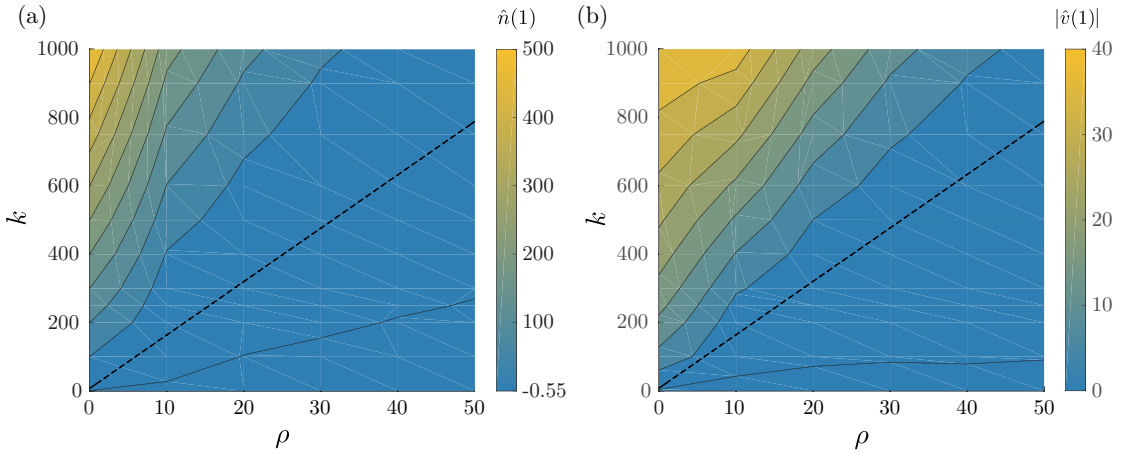

Figure 4.16: Behaviour of the stress $\hat{n}$ and flow velocity $\hat{v}$ at the sloughing boundary $s = 1$ ($S_0 = L_\mu(t)$). (a) The homeostatic stress values $\hat{n}(1)$. (b) The migration velocities $v(1) = |\hat{v}(1)|$. The dotted lines represent the analytical inequality that distinguishes bimodal from non-bimodal shapes (4.60).

4.4.4 Analysis of growth and sloughing during homeostasis

Previously, we did not need to solve for the total growth $\hat{\gamma}(s,t)$, as homeostasis only depends on the incremental growth profile, $g(s)$. However, in order to determine the amount of sloughing that is needed to maintain homeostasis, by definition of L_μ from (4.72), we need to determine the solution to $\hat{\gamma}(s,t)$. In this section, we now derive closed-form expressions for the growth $\hat{\gamma}$ and sloughing boundary L_μ, and consequently the net sloughing rate $\dot{\mu}$ in homeostasis. By determining the solutions to $\hat{\gamma}$ and L_μ, we gain insight into the types of growth and sloughing laws that will lead to homeostasis.

After solving Equations (4.53)–(4.55) and obtaining the resulting homeostatic incremental growth $g(s)$ and flow velocity $\hat{v}(s)$, we can solve for growth $\hat{\gamma}$ in homeostasis, which evolves according to:

$$\hat{\gamma}_t = g(s)\hat{\gamma} + \hat{v}(s)\hat{\gamma}_s. \tag{4.62}$$

Although $\hat{v}(s)$ does not, in general, have a closed-form solution, we see from Equation (4.39) that if $\hat{v} = \hat{v}(s)$ but $\hat{S}_0 = \hat{S}_0(s,t)$ and $\hat{\gamma} = \hat{\gamma}(s,t)$, then we can decompose $\partial\hat{S}_0/\partial t$ and $\hat{\gamma}$ into separable functions of s and t. In particular, we

can express $\partial\hat{S}_0/\partial t$ and $\hat{\gamma}$ using the following forms:

$$\frac{\partial\hat{S}_0}{\partial t}(s,t) = \frac{\Sigma(s)}{\mathrm{T(t)}}, \qquad \hat{\gamma}(s,t) = \Gamma(s)\mathrm{T(t)}. \tag{4.63}$$

We first solve for $\hat{\gamma}$ by substituting the form (4.63) into Equation (4.62). This yields the following:

$$\frac{\dot{\mathrm{T}}}{\mathrm{T}} = g(s) + \hat{v}(s)\frac{\Gamma'}{\Gamma} = \beta \in \mathbb{R}. \tag{4.64}$$

Solving for T and Γ respectively yields the solutions

$$\mathrm{T(t)} = \mathrm{T}_0\mathrm{e}^{\beta\mathrm{t}}, \tag{4.65}$$

$$\Gamma(s) = \Gamma_0 \exp\left(\int_0^s \frac{\beta - g(s')}{\hat{v}(s')}ds'\right). \tag{4.66}$$

We note from the boundary condition (4.57), that as $\hat{v}(0) = 0$, $\Gamma_s(0)$ is singular unless β satisfies the following condition:

$$\beta = g(0) = W(0) + \mu(\hat{n}(0) - n^*)\mathrm{H}(n^* - \hat{n}(0)). \tag{4.67}$$

Therefore, in homeostasis, growth evolves as:

$$\hat{\gamma}(s,t) = \hat{\gamma}_0 \exp\left(g(0)t + \int_0^s \frac{g(0) - g(s')}{\hat{v}(s')}ds'\right), \tag{4.68}$$

where $\hat{\gamma}_0 = \Gamma_0\mathrm{T}_0$ is a constant.

Now, the solution (4.68) implies that $\partial\hat{S}_0/\partial t$ takes the form

$$\frac{\partial\hat{S}_0}{\partial t} = \Sigma(s)\mathrm{e}^{-g(0)t}. \tag{4.69}$$

Substituting (4.69) and (4.68) into Equation (4.39) implies that

$$\Sigma(s) = \frac{\hat{v}(s)}{\hat{\alpha}\hat{\gamma}_0\Gamma(s)} = \frac{\hat{v}(s)\exp\left(-\int_0^s \frac{g(0)-g(s')}{\hat{v}(s')}ds'\right)}{\hat{\gamma}_0(1+\hat{n}(s))}. \tag{4.70}$$

We substitute the solution (4.70) into the form (4.69) and integrate with respect to time, obtaining the general solution for $\hat{S}_0$:

$$\begin{aligned}\hat{S}_0(s,t) &= -\frac{\Sigma(s)}{g(0)}\mathrm{e}^{-g(0)t} \\ &= -\frac{\hat{v}(s)}{g(0)\hat{\gamma}_0(1+\hat{n}(s))}\exp\left(-g(0)t - \int_0^s \frac{g(0) - g(s')}{\hat{v}(s')}ds'\right).\end{aligned} \tag{4.71}$$

With our solutions to $\hat{\gamma}(s,t)$ and the homeostatic elastic stretch, $\hat{\alpha} = 1 + \hat{n}$, we can now calculate L_μ by evaluating the definite integral defined in (4.72)

$$L_\mu(t) = \hat{\gamma}_0^{-1} \mathrm{e}^{-g(0)t} \int_0^1 \frac{\exp\left(-\int_0^s \frac{g(0)-g(s')}{\hat{v}(s')} ds'\right)}{1+\hat{n}(s)} ds. \tag{4.72}$$

Therefore, in homeostasis, the sloughing boundary, $L_\mu(t)$, decays exponentially in time to balance the growth rate, which is determined by $g(0)$, so that the spatial incremental growth profile, $g(s)$, is fixed with respect to the current configuration. An alternative expression for L_μ can be obtained from the solution (4.71), yielding

$$\begin{aligned} L_\mu(t) &= \hat{S}_0(1,t) \\ &= -\frac{\Sigma(1)}{g(0)} \mathrm{e}^{-g(0)t} \\ &= -\frac{\hat{v}(1)}{g(0)\hat{\alpha}(1)\hat{\gamma}_0} \exp\left(-g(0)t - \int_0^1 \frac{g(0)-g(s)}{\hat{v}(s)} ds\right). \end{aligned} \tag{4.73}$$

This expression highlights the relation between L_μ and the boundary flow velocity $\hat{v}(1)$, as $\hat{v}(1)$ measures how quickly material is removed from the rod in homeostasis.

In Chapter 3, we showed how L_μ could be connected to the sloughing rate $\dot{\mu}$, which modelled cell death. We recall that $\dot{\mu}$ relates to the $\dot{L}_\mu$ from Equation (3.28), which we modify to account for crypt half-length in 1D geometry:

$$\dot{\mu} = -\dot{L}_\mu \gamma(S_0 = L_\mu, t) + \int_{S_0=L_\mu}^{S_0=1} \dot{\gamma} dS_0. \tag{4.74}$$

By construction, $\dot{\gamma} = 0$ in the region $[L_\mu, 1]$. Furthermore, $\gamma(S_0 = L_\mu, t) = \gamma(s = 1, t)$. Therefore, we can simplify Equation (4.74) to the straightforward relation:

$$\dot{\mu} = -\dot{L}_\mu \hat{\gamma}(1,t). \tag{4.75}$$

Therefore, the total amount of material removed, μ, can be expressed in terms of the sloughing boundary L_μ. Biologically, one may interpret μ as the total amount of cells removed from the crypt. Differentiating (4.73) with respect to t and substituting the resulting expression into Equation (4.75) yields an expression for the sloughing rate during homeostasis:

$$\dot{\mu} = \frac{\hat{v}(1)}{\hat{\alpha}(1)} = -\int_0^1 \frac{g(s)}{\hat{\alpha}(s)} ds. \tag{4.76}$$

Therefore, in homeostasis, while the sloughing boundary, L_μ, decays exponentially over time, which is determined by the incremental growth at the base, $g(0)$, the sloughing rate, $\dot{\mu}$, remains constant over time. From the second expression of (4.76), determined by integrating Equation (4.55), $\dot{\mu}$ can be interpreted as a 'net proliferation', as determined by the homeostatic incremental growth, $g(s)$.

Note that there is another as-yet unspecified constant, $\hat{\gamma}_0$. However, if we assume that homeostasis began at $t = 0$, then $L_\mu(0) = 1$ and the integration constant $\hat{\gamma}_0$ can thus be found by evaluating the expression (4.68):

$$\hat{\gamma}_0 = \int_0^1 \frac{\exp\left(\int_0^s \frac{g(0)-g(s')}{\hat{v}(s')} ds'\right)}{1+\hat{n}(s)} ds. \tag{4.77}$$

4.4.5 Illustration of homeostasis

To demonstrate the homeostasis framework in full, we solve Equations (4.53)–(4.55) to obtain the homeostatic stress, $\hat{n}(s)$, velocity, $\hat{v}(s)$, and foundation attachments, $\hat{p}(s)$, and consequently, the homeostatic incremental growth profile, $g(s)$. For illustrative purposes, we set the foundation stiffness $k = 10$, the foundation remodelling parameter $\rho = 1$, the mechanical feedback strength $\mu = 10$, and the threshold stress $n^* = -0.5$. We note that in this parameter regime, the resulting homeostatic growth profile $g(s)$ is indeed bimodal. The sloughing boundary, $L_\mu(t)$, is then obtained by directly evaluating the definite integral (4.72).

To demonstrate the differences in behaviours between the Eulerian and Lagrangian reference frames, we also obtain the Lagrangian representation for the current arc length $s(S_0, t)$ by solving the equation $S_0 = \hat{S}_0(s, t)$ numerically for different values of S_0 at each time t. The foundation attachments $p(S_0, t)$ are then found by evaluating $p(S_0, t) = \hat{p}(s(S_0, t))$. We plot the profiles of S_0, $s(S_0, t)$, $p(S_0, t)$ for fixed S_0 values and their Eulerian equivalents for fixed s in Figure 4.17 for increasing time t. To draw analogy with the crypt, we also plot the even extensions of the obtained profiles. Figure 4.17 demonstrates the clear differences between the Lagrangian and Eulerian solutions in homeostasis. In the Lagrangian configuration, we observe a clear migration of the points $s(S_0, t)$ and their corresponding foundation

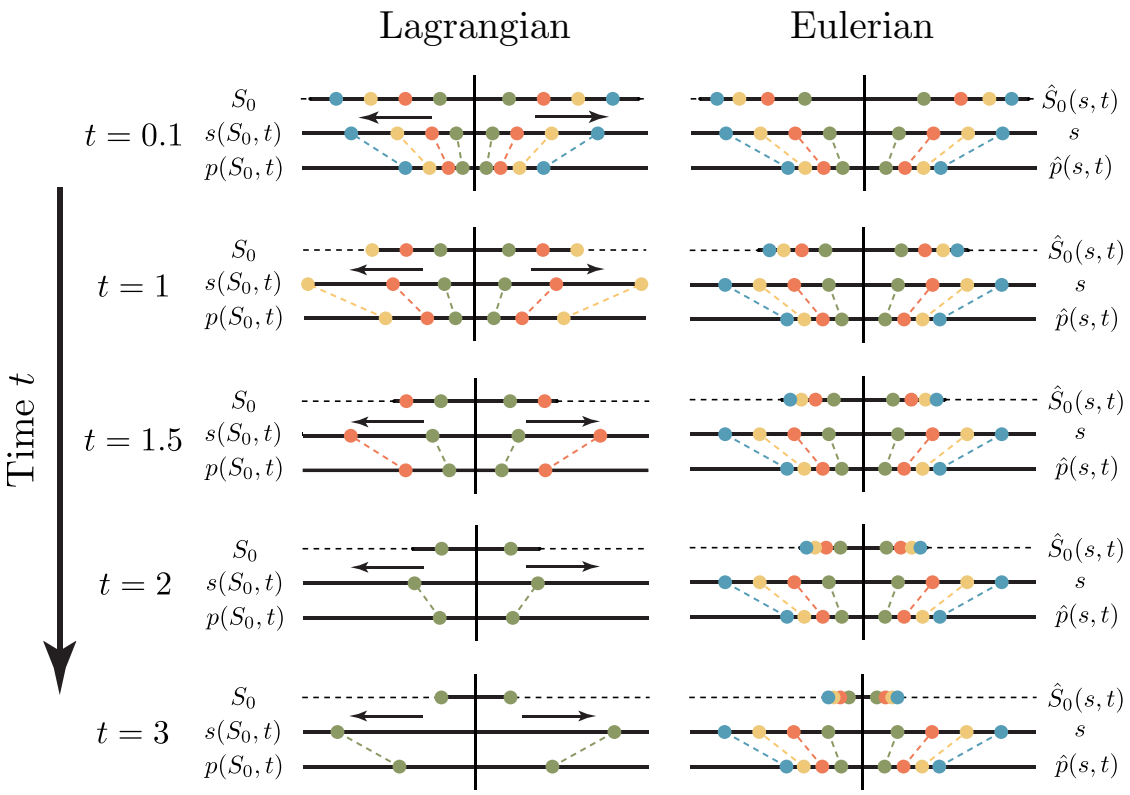

Figure 4.17: A typical homeostasis simulation. The even extension of the profiles have also been plotted, to illustrate homeostasis in the crypt. Left column: the Lagrangian representation of the initial arc length S_0, the current arc length $s(S_0, t)$ and the foundation attachments $p(S_0, t)$. The marked circles correspond to $S_0 = 0.2$ (green), $S_0 = 0.4$ (orange), $S_0 = 0.6$ (yellow), and $S_0 = 0.8$ (blue) and their even extensions. Right column: the Eulerian representations of $\hat{S}_0(s, t)$, s, and $\hat{p}(s)$ for fixed $s = 0.2, 0.4, 0.6, 0.8$ (green, orange, yellow and blue circles respectively) and even extensions. The evolution of the sloughing boundary $S_0 = L_\mu(t)$ is been denoted by the dashed lines. In the Lagrangian configuration, we observe the material points being sloughed out over time, while in the Eulerian configuration, points appear fixed with respect to s over time.

attachments as the sloughing boundary $L_\mu(t)$ shrinks the Lagrangian domain over time. Contrastingly, in the observable Eulerian configuration, for fixed s, the current position and foundation attachments are fixed over time. Thus, in homeostasis, while variables are fixed with respect to the Eulerian configuration, the Lagrangian configuration is evolving continuously to maintain the homeostatic growth profile $g(s)$. It is this aspect of our homeostasis framework that distinguishes it from other homeostasis models, where growth is unchanging and in steady state [59, 168].

4.5 Discussion

We have simplified the morphoelastic rod framework previously considered in Chapters 2–3 to investigate how incremental growth—a continuum analogue of proliferative capacity—may be coupled to mechanical stress, in order to better understand how the crypt's unique proliferative hierarchy may arise. In doing so, we have suggested a mechanical basis for proliferation dynamics within the crypt. Moreover, we have uncovered the key ingredients for a minimal growth law that is representative of the crypt.

First, a concentrated chemical signalling gradient localises growth initially towards the crypt base which, in turn, creates spatial heterogeneity in stress. This is provided by the Wnt signalling pathway, which decreases from the base to the top [67]. Second, threshold-dependent mechanical feedback is required for spatially-heterogeneous mechanical regulation of this Wnt signal. In the crypt, this is akin to cells only experiencing mechanical regulation when they are sufficiently compressed. It ensures that growth is inhibited first in the base, where stem cells would reside. Moreover, we proved that in the special case of an infinitely-stiff substrate, the stress threshold is necessary to generate the 'bimodal' distribution of incremental growth. Finally, we showed that the qualitative impact of mechanical feedback depends on two parameters, the stiffness of the underlying foundation and the sensitivity to mechanical feedback. The former is required to ensure that growth creates heterogeneity in stress. This has also been confirmed in the biological literature: it is well known that extracellular matrix stiffness regulates cell fate [58] and, more recently, it has been shown that intestinal stem cells will either proliferate more rapidly or differentiate in response to different matrix stiffnesses [71]. Additionally, sufficiently high mechanosensitivity ensures that mechanical feedback sufficiently dampens growth in the crypt base. This is consistent with the YAP/TAZ mechanotransduction pathways, which have become increasingly implicated in crypt homeostasis through their regulation of Wnt signalling [11, 12, 17, 83].

Having identified a minimal growth law that replicates the proliferative structure in the crypt, we turned our attention towards modelling homeostasis. To our

knowledge, this is the first treatment of non-static tissue homeostasis, especially within the morphoelastic framework. By defining homeostasis as the condition when incremental growth is fixed in the observable, current configuration, we were able to derive necessary conditions for maintaining homeostasis. In particular, we derived a set of first-order ordinary differential equations that gave rise to the homeostatic stress, foundation attachment, and velocity profiles, which yielded a homeostatic incremental growth profile. Examining the solution space spanned by this set of ordinary differential equations highlighted the importance of the foundation properties, namely the stiffness, k, and remodelling parameter, ρ. Importantly, we showed how the sloughing boundary, $L_\mu(t)$, emerges naturally from this definition, rather than needing to impose it a contrived manner, as we did in Chapter 3. By computing closed-form solutions to growth and sloughing, we demonstrated that the sloughing boundary decays exponentially to offset the rate of material increase due to growth, while the sloughing rate remains constant to balance the net increase in growth. Moreover, the sloughing rate is completely determined by the ratio of the flow velocity and elastic stretch at the top of the crypt. Plotting both the Lagrangian and Eulerian solutions in homeostasis demonstrated that although points in the Eulerian frame appear fixed, in the Lagrangian frame, material points migrate along the crypt at a non-uniform velocity due to sloughing.

In this framework, we have assumed all material properties are homogeneous. In the context of biological tissue, this assumes all cells have equal stiffnesses, mechanosensitivities, and so on. Here, heterogeneity comes from the Wnt signalling gradient alone. It would be worthwhile to investigate the effects of heterogeneities in material properties, such as the mechanical feedback sensitivity, μ, and mechanical feedback stress threshold, n^*. In particular, it would be valuable in understanding how heterogeneities in these properties may be applied to understand colorectal cancer initiation, where mutated cells cease to obey the standard regulatory cues.

The next main challenge is to translate both this growth law and homeostasis framework, which we considered in a 1D geometry, to a 2D morphology. This presents several challenges. In this 1D geometry, growth led to decreasing stress. However, in

a 2D morphology, buckling acts to relieve the axial stress—the 2D analogue of the 1D stress considered in this chapter—induced by growth. Subsequent deformations continue to relieve axial stress. Therefore, axial stress actually increases as the rod deforms, rather than decreasing. Moreover, due to the geometric nonlinearities induced by buckling, the axial stress itself is not completely determined by growth alone, but rather is determined by growth and a balance of bending and stretching. Therefore, the key challenge is to find the simplest function of axial stress that captures the behaviour of stress in this 1D setting. Additionally, we must account for the large deformations observed in the crypt. For example, in Chapter 3, we showed that continued rod invagination leads to self-contact, which introduces spatial discontinuities in stresses.

5 Discussions and conclusions

5.1 Introduction

We close by summarising the results of Chapters 2–4 and discussing ideas for future work. This thesis sought to understand several fundamental aspects of the crypt—its morphogenesis, its internal growth structure, and how homeostasis is maintained—and the role of mechanics in these processes. By using the crypt as our system of focus, we uncovered rich bifurcation structures; gained insight into the processes that contributed to the crypt's deep, invaginated morphology; suggested a hypothesis for the formation of the crypt's proliferative structure; and demonstrated how the stress, foundation attachments, velocity, and sloughing rate due to cell death may couple to maintain homeostasis in the crypt.

5.2 Summary of work

Here, we summarise the key findings from each chapter and discuss the implications of these results in the context of the crypt and, more broadly, for biological tissues.

5.2.1 Chapter 2

In Chapter 2, we viewed crypt morphogenesis as a buckling problem. We started with a simple continuum mechanics model of a buckling crypt, a planar morphoelastic rod

supported by a linearly-elastic foundation, an extension of the classical setup. We investigated how growth alters its post-buckled bifurcation structure in comparison to similar models that do not incorporate growth [32, 33, 89]. Motivated by the evident importance of growth and the heterogeneity of cell types and proliferative capacities in the crypt, we sought to understand how growth affects the onset and subsequent evolution of tissue-scale patterning and how this patterning is affected by spatial heterogeneity in three material parameters: growth, rod stiffness, and foundation stiffness.

First, assuming homogeneous growth and stiffnesses, we extended the linear stability analysis of Moulton et al. [120], performing a weakly nonlinear analysis and supplementing it with numerical continuation of the full nonlinear system. The analysis revealed a pitchfork bifurcation structure which could be supercritical or subcritical, depending on the values of the foundation stiffness and the initial rod length. In the context of morphogenesis, a supercritical pitchfork indicates a smooth transition from flat to buckled morphology due to growth, while a subcritical pitchfork indicates a discontinuous jump in the transition, as well as a hysteresis effect. Exploring the phase space of the pitchfork types revealed that varying either the foundation stiffness or the initial rod length results in multiple transitions between supercritical and subcritical pitchforks, separated by an oscillatory boundary. The non-monotonic nature of the transition boundary suggests a non-robustness in the instability, but, as this is an idealised system, it is not entire clear what this implies in the context of tissue morphogenesis. This behaviour, to the best of our knowledge, has not been previously reported in the literature, although, since the publication of Almet et al. [2], Jin et al. [95] have reported similar behaviour for the buckling of growing tubular tissue.

We then began considering the effects of spatial heterogeneity in growth, rod and foundation stiffness. Numerical solutions revealed that multiplying each of these model parameters by the same spatially-varying heterogeneity function yielded markedly different morphologies. We characterised these morphological differences by extending the weakly nonlinear analysis and considering the resulting changes

in energetic contributions. Despite the marked morphological differences, the new weakly nonlinear analysis revealed that these heterogeneities, which multiplied a 'baseline' material property, had a relatively minor effect on the bifurcation structure, merely translating the pitchfork bifurcation and thus accelerating or delaying the onset of buckling. These results contrasted with previous results on shell buckling, where minor imperfections in shell structures can result in drastic reductions of the buckling load [90]. However, when heterogeneity was incorporated in an additive manner, by modelling underlying foundation shape to be imperfectly-straight, the resulting nonlinear analysis revealed a broken pitchfork, where the underlying foundation shape biased the rod to buckle towards one of the two solution paths, which was more reminiscent of classical imperfection sensitivity studies [90].

Observing these profound effects of heterogeneity, we closed with a brief discussion of the inverse problem, where we asked whether different heterogeneity profiles could produce the same rod morphology and whether different biological experiments could distinguish between these heterogeneities. Identifying heterogeneities in different rod attributes that produced the same (buckled) rod morphology proved to be a non-trivial task. Nevertheless, the most noticeable observed feature was that regions of expansive and resorptive growth were distinguished by regions of axial compression and tension, respectively, which suggested possible biological cutting experiments. By placing cuts in different regions along a tissue, the resulting length change would reveal a region of tension if the post-cut length decreased, indicating a region of minimal growth, while a post-cut increase in length would correspond to a region of compression and indicate high growth.

By framing crypt morphogenesis as a buckling problem and focussing on key aspects of the crypt and analysing the underlying bifurcation structures, we increased our understanding of the impact that spatial heterogeneity has on growth-induced deformation. While many of our questions were motivated by the crypt, there are many processes, such as brain cortical folding [29] or seashell spine formation [37], where growth and heterogeneity are key aspects and thus the results of our analysis generalise straightforwardly to the morphogenesis of other growing bilayer structures.

5.2.2 Chapter 3

In Chapter 3, we developed and investigated various model components that captured a number of biological, chemical, and mechanical features believed to play a fundamental role in crypt morphogenesis and homeostasis. In particular, we considered: tissue relaxation, chemical signalling, mechanical properties, distinguishing cell type, accounting for cell death via the sloughing of material, self-contact, and spatial competition induced by neighbouring tissue or extracellular material. Many of the models developed could be adapted straightforwardly to other monolayers or stratified tissues. By developing and analysing each component in isolation, we highlighted key features and took important steps towards integrating biological specificity within the buckling rod framework.

Analysis of simulation results revealed that modelling tissue relaxation, through either the underlying foundation rod attachments or the rod intrinsic curvature, could have a significant impact on crypt morphology. The different behaviours were particularly pronounced when rod growth was paused and the system continued to relax. For example, while increasing the rate of relaxation for a viscoelastic foundation increased the rod invagination length growth, once growth was paused and the viscoelastic attachments continued to relax, the invagination length subsequently decreased (unless the viscous relaxation rate was sufficiently fast). Similarly, for a remodelling foundation, increasing the remodelling rate increased the invagination depth during growth. However, for this foundation law, pausing growth and allowing the attachments to relax always led to an increase in invagination length. In contrast, a rapidly-evolving intrinsic curvature decreased the invagination depth and, in fact, resulted in the invagination base fissioning when growth was stopped. Comparing these relaxation models, we concluded that a remodelling foundation was most appropriate for generating a realistic crypt morphology.

When modelling material properties such as growth and stiffnesses, for biological tissue such as the crypt, it is not entirely clear whether the property should be modelled with respect to the Lagrangian or Eulerian reference frame. For example, when modelling chemical signals, such as Wnt, in the former case, the

chemical signal is interpreted as an 'inherent property' of the rod (the line of growing cells) and the signal profile propagates along the rod due to growth. In the latter case, the signal profile is fixed with respect to the current configuration and so acts as an environmental cue for growth. Modelling growth for these two cases resulted in significantly different morphologies, emphasising the importance of taking care with model assumptions when formulating continuum models for epithelia. In contrast, modelling rod stiffness with respect to either the Lagrangian or Eulerian reference frame did not produce noticeable differences in morphology. Therefore, an Eulerian Wnt signal was more appropriate for generating a crypt morphology than a Lagrangian representation, while stiffness heterogeneity did not affect the morphology significantly.

To address the paucity of models of cell death, an important component of epithelial homeostasis, we formulated a continuum model for cell death, demonstrating how material sloughing can balance growth to induce a quasi-steady state, where the morphology was static, despite growth evolving. We also showed how cell type can be modelled via age and that the correct age structure emerges when modelling heterogeneous Wnt-based growth, where the youngest points of the rod lie at the base of the invagination, where stem cells would reside, while the oldest points were at the rod endpoints, where differentiated cells would reside.

Motivated by the large deformations exhibited by the crypt, we explored the effect of introducing self-contact in the model to allow growth and deformations for longer times. It was shown that self-contact alone results in excessive horizontal bulging of the rod invagination and an unrealistic crypt morphology. However, including additional spatial constraints, such as a constant self-encapsulated area or additional horizontal repulsion forces due to neighbouring tissue, produced a more realistic crypt invagination. These results suggest that the presence of neighbouring tissue may be a key contributor to the crypt maintaining its narrow shape as it grows.

We closed the chapter by combining several of these models to simulate typical morphogenetic processes. First, we combined the processes that we believed contributed most significantly to a realistic crypt morphology. By simulating

the system with growth due to an Eulerian Wnt signal, a rapidly-remodelling foundation, and a strong repulsion force due to neighbouring tissue, we were able to obtain a realistic crypt morphology, where the invagination depth was five times as long as the initial rod length, with a narrow aspect ratio. Second, we coupled sloughing to ageing which, in turn, was coupled to heterogeneous growth, to model sloughing occurring in a more natural manner than by modelling sloughing to begin after a prescribed time. However, in this case, as the sloughing rate did not balance the growth rate exactly, the morphology was still evolving and the invagination depth shrank over time due to sloughing.

The model investigations performed highlighted the need to develop models for the different processes that contribute to tissue morphogenesis and the need to explore each of these processes in detail. While our results were framed in the context of generating a realistic crypt morphology during development, we note that other models that were not considered may be more appropriate for other biological structures, or even in different crypt processes. For instance, we did not incorporate an evolving intrinsic curvature as it reduced the invagination depth. However, the observed fissioning of the rod base when growth was paused due to curvature relaxation may be relevant to the process crypt fission, which is marked by a similar splitting in the base. Such investigations would be useful for future work.

5.2.3 Chapter 4

Chapter 3 provided a starting point from which we could investigate the concepts of growth and homeostasis in the crypt in greater detail. In Chapter 4, we abstracted the model from the 2D geometry, but retained the remodelling foundation law and Eulerian Wnt signal. Our goals were two-fold. First, we aimed to investigate how the proliferative structure that is unique to the crypt may arise. Second, we aimed to identify necessary conditions for homeostasis in the crypt; that is, under which the crypt can maintain its growth structure.

We demonstrated that mechanochemical growth that couples Wnt signalling and mechanical stress can generate the crypt's proliferative structure. Considering

the special case of an infinitely-stiff foundation, we proved analytically that a mechanochemical law in which mechanosensitivity is ever-present does not generate the correct proliferative structure. By contrast, a law that incorporates *threshold-dependent* sensitivity, where mechanical feedback is only triggered once the rod is sufficiently compressed, generate the desired structure. These claims were shown to extend to the more biologically realistic case of a finite foundation stiffness by numerically solving the full system for different model parameter values. By exploring model parameter space, we found realising that the correct proliferative structure, which is maximal away from both the base ($s = 0$) and top of the crypt ($s = 1$), relied upon two key mechanical properties: the stiffness of the foundation, which induced spatial variation in stress due to the heterogeneous Wnt signal, and the strength of mechanical feedback, which ensured that mechanosensitivity altered the monotonicity of the incremental growth profile, meaning that incremental growth was no longer maximal in the base, where the Wnt signal was maximal.

Following this, we explored the question of how this crypt maintains its proliferative structure over time, despite the continual turnover of cells, a question relating to the principle of tissue homeostasis. In order to answer this, we developed a new continuum framework of tissue homeostasis, which defines homeostasis as the state when the incremental growth spatial profile is independent of time in the current (Eulerian) observable configuration. Using the mechanochemical growth law, we showed that the stress, foundation attachments, and flow velocity must be independent of time, and derived a coupled system that these quantities must satisfy to maintain homeostasis. The derived set of equations ensured that the flow velocity was consistent within the Eulerian formulation of the system and the force balance. In this framework, the incorporation of sloughing that was imposed in Chapter 3 emerged naturally as a necessary condition for homeostasis. Analysing and numerically solving the homeostatic system for different parameter values revealed that the homeostatic growth profile depended on the foundation stiffness and the remodelling rate of the foundation attachments. Examining solutions corresponding to homeostatic crypt growth profiles revealed that the velocity must increase along

the crypt at a non-uniform rate, while the homeostatic stress profile comprises two distinct regions of compression towards the base and tension towards the top. By deriving closed-form solutions for growth and the sloughing boundary, we discovered that the sloughing rate and growth rate must balance exactly. Moreover, the sloughing and growth rates are determined by the incremental growth value in the base, corresponding to the proliferative capacity there.

By considering a 1D geometry but retaining the most important processes from the 2D morphology, we were able to explore different mechanical feedback processes on growth in the crypt in an analytically tractable manner; this would not have been possible in a 2D geometry. In doing so, we demonstrated that a mechanochemical law may give rise to the unique proliferative structure of the crypt. We were also able to construct a model that describes dynamic tissue homeostasis, in which dependent variables and growth are fixed in space in the current Eulerian configuration, but evolve continually in the Lagrangian configuration, in order to maintain a homeostatic growth structure.

5.3 Future work

There are many interesting avenues for extending the work in this thesis. Here, we list a few of what we consider to be the most important directions for future work.

5.3.1 A 2D growth law and homeostasis

We have developed a mechanochemical growth law that can explain the proliferative structure of a straight, unbuckled crypt. In this 1D geometry, stress decreases with increasing growth, leading us to postulate the existence of a threshold-dependent mechanosensitive law, where growth is inhibited where the rod stress falls below a threshold stress. However, as stated in Chapter 4, this law does not necessarily generalise onto a 2D morphology. In 2D, buckling and subsequent rod deformation act to alleviate the compressive stress in the system. Therefore, the axial stress actually increases from the critical buckling stress for increasing growth. However, we note that as the crypt epithelium is a confluent surface, other stresses not

considered in a planar geometry, such as hoop stress, may become important. Therefore, an important future goal is to develop a mechanosensitive law that holds for 2D morphologies.

Translating the homeostasis framework to a 2D morphology is more straightforward. For a 2D morphology, the homeostasis definition is altered such that both the rod shape and incremental profile are also fixed with respect to the Eulerian reference frame. However, as growth occurs only in the axial definition, it is still only parametrised by initial arc length parameter S_0. Therefore, the compatibility conditions for the flow velocity in the Eulerian frame are the same as those for a 1D geometry. However, as there are two force balance equations in 2D, the flow velocity must be compatible with both the horizontal and vertical components of the foundation attachments. While exploring homeostasis for a 2D morphology is beyond the scope of this thesis, an outline of the 2D homeostasis framework is provided in Appendix C.

5.3.2 From development to homeostasis

Throughout this thesis, we considered crypt dynamics during two distinct phases: in development, when the crypt is invaginating and the incremental growth structure is evolving, or in homeostasis, when the morphology was unchanging and the proliferative structure is established. While we developed separate mathematical models to characterise the crypt during these two phases, we did not investigate in detail the transition from development to homeostasis. That question of interest here is: under what conditions does the crypt tend to a homeostatic state, as defined by (4.36)? This question is related to the *stability* of homeostatic states, a concept which is especially important in the context of disease, when crypt homeostasis is disrupted.

5.3.3 Comparison with cell-based models

In future work, we aim to compare the continuum models of the crypt developed in this thesis against pre-existing discrete cell-based models of the crypt. Such model comparisons are important because of the complementary strengths and weaknesses

Crypt feature	Continuum	Discrete (cell-based)
Deformability	✓✓: Can use continuum mechanics theory	✓: Not well-developed
Mechanical effects	✓✓: Very well-placed	
Clonal cell tracking	✓: Possible for a few models	✓✓: Can easily track cell lineages
Subcellular detail	Has not been considered in detail	✓✓: Very well-suited for this
Stochasticity	×	✓
Cell migration	Possible for certain models	✓✓
Population control	✓: Laws to prescribe local growth	✓✓
Interaction with external environment	✓✓: Can prescribe mechanical forces	✓: Computationally expensive
Cellular heterogeneity	✓: Coarse-grained heterogeneity	✓✓: Individual cell heterogeneity
Cell sorting	×: Not possible	✓: Possible in some models
Experimental parametrisation	Possible but has not been implemented	✓: Possible with enough biological detail

Table 5.1: Desirable features of an ideal crypt model, and the current efficacy of continuum and cell-based frameworks to capture them. The two classes of frameworks have complementary strengths and limitations.

of the two frameworks, which are summarised in Table 5.1. It is easier to incorporate intracellular biological detail into cell-based models, but they are less amenable to analysis. Equally, with continuum models, while it is more difficult to incorporate biological detail into continuum models, we can more readily account for tissue deformation due to mechanical forces and torques, allowing us to analyse the impact of these effects. By linking cell-based frameworks and continuum frameworks, we can begin to understand which processes are most important for modelling the crypt, and which can be neglected through continuum approximations and abstractions. In doing so, we can understand the relationships between the two modelling approaches, as well as identify the similarities and differences in their respective behaviours.

5.3.4 Experimental validation

This thesis has focussed on developing and validating mechanical models of crypt morphogenesis. In general, mechanical models are difficult to validate, as key model parameters, such as the rod and foundation stiffness, are difficult to estimate *in vivo* for biological tissue. However, with the advances in crypt organoids, *in vitro* cultures that recapitulate gut tissue structure [151], data for biochemical processes, such as cell-cell signalling, is becoming more readily available. Therefore, one of the most pertinent extensions is to link these models to biological processes that can be validated with experimental data. These processes, such as signalling pathways, are typically of a biochemical nature and exist primarily at the subcellular

scale. Biochemical and biomechanical processes have typically been modelled in isolation and their interactions neglected. In practice, however, these processes are coupled at various spatial scales. In future work, we will investigate how different feedback mechanisms can be modelled.

One possible way to incorporate more biological detail is to couple the mechanical feedback model considered in Chapter 4, which was phenomenological, to a biochemical mechanotransductive pathway. In recent years, the Hippo signalling pathway has become increasingly implicated in crypt homeostasis through the transcription factors YAP and TAZ [11, 17, 83, 162]. YAP and TAZ are well known for their role in mechanotransduction, as they regulate biochemical signals in response to mechanical cues [7, 55]. In the crypt, YAP and TAZ regulate proliferation by mediating Wnt signalling; the proteins bind directly to β-catenin, preventing its translocation to the nucleus and, thereby, inhibiting proliferation [11, 12]. It has also been shown that they affect differentiation by interacting with Notch signalling [91, 155, 174]. Interestingly, YAP and TAZ are not active during homeostasis [11]. Rather, they are most active during pathological conditions, such as crypt regeneration (for example, due to inflammation) and cancer [83, 135, 169, 186]. It would be interesting to explore how parameters, such as the mechanical feedback strength μ or the threshold stress n^*, may be coupled to mathematical models that describe the YAP/TAZ signalling pathways, where homogenisation techniques used in works such as those of O'Dea and King [129, 130] may be useful.

5.3.5 Investigating crypt fission

One of the most attractive features of drawing upon a continuum mechanics framework is the ease of simulating tissue deformability. This is particularly important when investigating crypt fission, the process by which (healthy) crypts replicate [31]—see Figure 5.1. In the context of disease, crypt fission is particularly important as it enables colorectal adenomas to expand [143]; crypt fission is also the dominant mechanism by which the epithelium regenerates following injury [154]. While we have not investigated crypt fission in this thesis, the framework we have

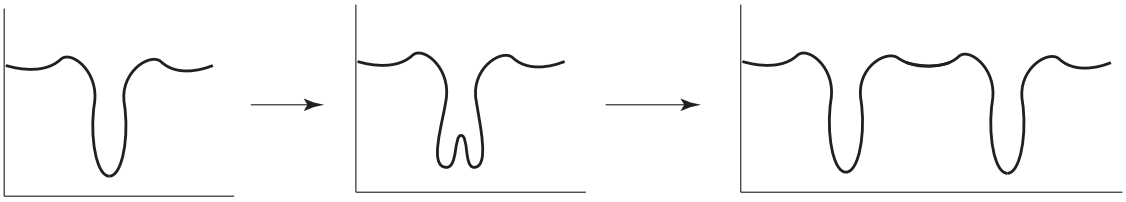

Figure 5.1: The crypt fission process. Crypt fission is marked by a split in a single crypt base, which eventually leads to the formation of two new crypts. The deformations that take place suggest a role for biomechanical factors in initiating crypt fission.

developed provides a suitable starting point to begin investigating such questions. An important step to understanding crypt fission, that could be answered with this framework, is how to classify the initial bifurcation event. That is, do we classify the initiation of crypt fission as an example of snap buckling [123], localised folding [138], period doubling [28], or something else altogether? Understanding crypt fission is arguably the next big challenge facing researchers in understanding the crypt and its role in gut health and disease.

5.4 Closing remarks

We have explored different aspects of the crypt within the morphoelastic rod framework. By focussing on different aspects of the crypts, from morphogenesis to homeostasis, we have developed several new models to understand the mechanisms governing key processes involved in crypt function. Many of these models can, in fact, be generalised to other biological systems. While there is still work to be done, we are confident that this framework can be further developed and the insights gained will advance not only the field of mathematical modelling of morphogenesis and epithelial growth, but also our understanding of the biomedical processes that regulate the crypt in health and disease.

Appendices

A

Supplementary information for post-buckling analysis

A.1 Determining the buckling amplitude

In this section, we introduce the functions that are needed to calculate the buckling amplitude C_1 for different values of k and L_0 (and hence γ^*). After unfolding the bifurcation with the ansatz (2.29) and considering $\mathcal{O}(\delta^2)$ terms, we obtain the system

$$x^{(2)'} - \gamma^* n_x^{(2)} = \frac{\gamma^{(1)}}{\gamma^*} - \frac{\gamma^*}{2}\left(y^{(1)'}\right)^2 - y^{(1)'}y^{(1)'''}, \tag{A.1}$$

$$y^{(2)'} - \theta^{(2)} = 0, \tag{A.2}$$

$$n_x^{(2)'} - kx^{(2)} = 0, \tag{A.3}$$

$$n_y^{(2)'} - ky^{(2)} = 0, \tag{A.4}$$

$$\theta^{(2)'} - \gamma^* m^{(2)} = 0, \tag{A.5}$$

$$m^{(2)'} + \frac{(\gamma^* - 1)}{\gamma^*}\theta^{(2)} + n_y^{(2)} = 0. \tag{A.6}$$

We note that we have used Equations (2.16)–(2.18) to express the inhomogeneities in terms of $y^{(1)}$ only, and have simplified the system further by substituting $x^{(1)} = n_x^{(1)} = 0$. As in Section 2.3.1, the system decouples into two ordinary differential

equations for $x^{(2)}$ and $y^{(2)}$ given by (2.33)–(2.34), with

$$\mathcal{L}x^{(2)} = H_{x^{(2)}} = -\gamma^* y^{(1)'} y^{(1)''} - \left(y^{(1)'} y^{(1)'''}\right)', \tag{A.7}$$

$$\mathcal{M}y^{(2)} = H_{y^{(2)}} = 0. \tag{A.8}$$

We recall the linear operators $\mathcal{L}$ and $\mathcal{M}$ are defined in Equations (2.33) and (2.34) respectively by $\mathcal{L}x = x'' - k\gamma^* x$ and $\mathcal{M}y = y'''' + (\gamma^* - 1)y'' + k\gamma^* y$. As $H_{y^{(2)}} = 0$, (2.34) is homogeneous for $n = 2$ and provides no information about the buckling amplitude C_1. However, considering Equations (2.33) and (A.7) in tandem with the solution (2.24) and the boundary conditions $x^{(2)}(0) = x^{(2)}(L_0) = 0$ allows us to define $\widehat{x} := C_1^{-2} x^{(2)}$.

At next order, we have

$$x^{(3)'} - \gamma^* n_x^{(3)} = -\gamma^* y^{(1)'} y^{(2)'} - y^{(1)'} y^{(2)'''} - y^{(1)'''} y^{(2)'}, \tag{A.9}$$

$$y^{(3)'} - \theta^{(3)} = \frac{1}{3}\left(y^{(1)'}\right)^3 + x^{(2)'} y^{(1)'}, \tag{A.10}$$

$$n_x^{(3)'} - k x^{(3)} = 0, \tag{A.11}$$

$$n_y^{(3)'} - k y^{(3)} = 0, \tag{A.12}$$

$$\theta^{(3)'} - \gamma^* m^{(3)} = \frac{\gamma^{(1)}}{\gamma^*} y^{(1)''}, \tag{A.13}$$

$$\begin{aligned} m^{(3)'} + \frac{(\gamma^* - 1)}{\gamma^*}\theta^{(3)} + n_y^{(3)} = {} & \frac{(\gamma^* + 2)}{6\gamma^*}\left(y^{(1)'}\right)^3 + \frac{1}{\gamma^*}\left(y^{(1)'}\right)^2 y^{(1)'''} + \frac{1}{\gamma^*} x^{(2)'} y^{(1)'} \\ & + \frac{1}{\gamma^*} x^{(2)'} y^{(1)'''} - \frac{\gamma^{(1)}}{\gamma^{*2}} y^{(1)'}. \end{aligned} \tag{A.14}$$

Equations (A.9)–(A.14) decouple into the two ordinary differential equations, in which the forcing terms $H_{x^{(n)}}$ and $H_{y^{(n)}}$ are given by:

$$\mathcal{L}x^{(3)} = H_{x^{(3)}} = -\left(\gamma^* y^{(1)'} y^{(2)'} + y^{(1)'''} y^{(2)'} + y^{(1)'} y^{(2)'''}\right)', \tag{A.15}$$

$$\begin{aligned} \mathcal{M}y^{(3)} = H_{y^{(3)}} = {} & 2\left(y^{(1)''}\right)^3 + \frac{3\gamma^*}{2}\left(y^{(1)'}\right)^2 y^{(1)''} + 2\left(y^{(1)'}\right)^2 y^{(1)''''} + 8 y^{(1)'} y^{(1)''} y^{(1)'''} \\ & + \gamma^*\left(x^{(2)'} y^{(1)'}\right)' + y^{(1)'} x^{(2)''''} + 2 x^{(2)'} y^{(1)''''} + 4 x^{(2)''} y^{(1)'''} \\ & + 3 x^{(2)'''} y^{(1)''} - \frac{\gamma^{(1)}}{\gamma^*}\left(y^{(1)''} - y^{(1)''''}\right). \end{aligned} \tag{A.16}$$

Using the Fredholm Alternative Theorem and considering (A.16) in powers of C_1, the constants K_1 and K_2 in Equation (2.37) are obtained by evaluating the

following integrals

$$K_1 = \int_0^{L_0} \Big[2\left(\widehat{y}''\right)^3 + \frac{3\gamma^*}{2}\left(\widehat{y}'\right)^2 \widehat{y}'' + 2\left(\widehat{y}'^2\widehat{y}'''\right)' + 4\widehat{y}'\widehat{y}''\widehat{y}''' + \gamma^*\left(\widehat{x}'\widehat{y}'\right)' + 2\left(\widehat{x}'\widehat{y}''\right)'' + \left(\widehat{x}'''\widehat{y}'\right)' \Big] \widehat{y} dS_0, \tag{A.17}$$

$$K_2 = -\frac{1}{\gamma^*}\int_0^{L_0} \left(\widehat{y}'' - \widehat{y}''''\right)\widehat{y} dS_0, \tag{A.18}$$

where $\widehat{x} := C_1^{-2}x^{(2)}$ and $\widehat{y} := C_1^{-1}y^{(1)}$. Applying integration by parts to (A.18) yields

$$K_2 = \frac{1}{\gamma^*}\int_0^{L_0} \left(\widehat{y}'\right)^2 + \left(\widehat{y}''\right)^2 dS_0. \tag{A.19}$$

Therefore $K_2 > 0$ for all parameter values, provided that $\widehat{y}$ is non-trivial. Hence, the sign of constant K_1 determines the nature of the pitchfork.

A.2 Pitchfork bifurcation on an infinite domain

We show that in the case of an infinitely-long rod, the value of k for which the system transitions from a supercritical pitchfork bifurcation to a subcritical pitchfork bifurcation can be calculated exactly. Moreover, we show that the transition occurs only once.

Recall that the linear stability analysis yields the ordinary differential equations equations (Equations (2.19)–(2.20))

$$\mathcal{L}x^{(1)} = x^{(1)''} - k\gamma x^{(1)} = 0, \qquad \mathcal{M}y^{(1)} = y^{(1)''''} + (\gamma-1)y^{(1)''} + k\gamma y^{(1)} = 0, \tag{A.20}$$

Seeking oscillatory modes $y^{(1)} \sim e^{i\omega S_0}$ yields the oscillation frequencies from Equation (2.23), $\omega_\pm^2 = \frac{\gamma-1}{2} \pm \left(\frac{(\gamma-1)^2}{4} - k\gamma\right)^{\frac{1}{2}}$. For oscillations to persist over the whole domain, we require that $(\gamma-1)^2 \geq 4k\gamma$. Hence the bifurcation occurs when $(\gamma-1)^2 = 4k\gamma$, which gives rise to γ^*_{inf}, defined by Equation (2.28). Enforcing boundedness and that the solution is real-valued leads to the solution

$$y^{(1)} = C_1\cos(\omega S_0), \tag{A.21}$$

where

$$\omega = \left(\frac{\gamma^*_{\text{inf}} - 1}{2}\right)^{\frac{1}{2}} = \left(k + \left(k + k^2\right)^{\frac{1}{2}}\right)^{\frac{1}{2}}. \tag{A.22}$$

As before, we unfold about the bifurcation point γ^*_{inf} by letting $\gamma = \gamma^*_{\text{inf}} + \delta^2\gamma^{(1)}$, where $\delta \ll 1$ is our perturbation expansion parameter, and $\gamma^{(1)}$ is the control parameter away from bifurcation.

At $O(\delta^2)$, we substitute (A.21) into (A.7) and, after solving the equation and imposing boundedness, obtain

$$x^{(2)} = C_1^2 \frac{\omega^3(\gamma^*_{\text{inf}} - 2\omega^2)}{8\omega^2 + 2k\gamma^*_{\text{inf}}} \sin(2\omega S_0). \tag{A.23}$$

At $O(\delta^3)$, we obtain the amplitude equation for C_1 by substituting (A.21) and (A.23) into (A.16) and impose that secular terms vanish. This leads to Equation (2.37), $K_1 C_1^3 + K_2 C_1 \gamma^{(1)} = 0$, where the constants K_1 and K_2 are given by

$$K_1 = \frac{k^2\left[7 + 100\left(k + k^2\right)^{\frac{1}{2}} + 8k\left(16 + 7k + 7\left(k + k^2\right)^{\frac{1}{2}}\right)\right] - 4k\left(8 + 9\left(k + k^2\right)^{\frac{1}{2}}\right)}{8\left(16 + 7k\right)}, \tag{A.24}$$

$$K_2 = \left(k + k^2\right)^{\frac{1}{2}}. \tag{A.25}$$

We note that we have substituted Equation (2.28) to express K_1 and K_2 in terms of k only. As $K_2 > 0 \; \forall \; k > 0$, the sign of K_1 completely determines the type of pitchfork bifurcation the system undergoes, as confirmed in Appendix A.1. Therefore, the value of $k > 0$ where the transition occurs is found by solving $K_1 = 0$, yielding

$$k^* = \frac{21\sqrt{89} - 137}{160} \approx 0.38196. \tag{A.26}$$

It can be verified easily that $K_1 < 0$ when $k < k^*$ and $K_1 > 0$ when $k > k^*$, indicating a transition from a supercritical pitchfork bifurcation to a subcritical pitchfork bifurcation, which is confirmed by dynamical stability analysis of the solution branches. Moreover, there is only one transition when the rod is of infinite length, in contrast to the multiple transitions that can occur when the rod length is finite.

A.3 Including parameter heterogeneity

Here, we list the additional inhomogeneities that appear in Equations (2.30)–(2.32) when we account for spatial heterogeneities. These inhomogeneities result in the subsequent change from the buckling amplitude equation for the homogeneous case (2.37) to Equation (2.41).

In the first case of foundation stiffness heterogeneity, the linearised equations at $O(\delta)$ are unchanged from the homogeneous case. At $O(\delta^2)$ and $O(\delta^3)$, we have the following system of equations:

$$\mathcal{L}x^{(2)} = H_{x^{(2)}}, \tag{A.27}$$

$$\mathcal{M}y^{(2)} = 0, \tag{A.28}$$

$$\mathcal{L}x^{(3)} = H_{x^{(3)}}, \tag{A.29}$$

$$\mathcal{M}y^{(3)} = H_{y^{(3)}} - \eta k_0 \gamma_0^* \xi y^{(1)}. \tag{A.30}$$

The linear operators $\mathcal{L}$ and $\mathcal{M}$ have been defined in Equations (2.33)–(2.34) and Appendix A.1, while the inhomogeneities $H_{x^{(2)}}$, $H_{x^{(3)}}$, and $H_{y^{(3)}}$ are given by Equations (A.7), (A.15) and (A.16). Thus the amplitude equation now satisfies (2.41), K_3 can be deduced by evaluating the solvability condition, (2.36).

When rod stiffness heterogeneity is considered, the equations at $O(\delta^2)$ are

$$\mathcal{L}x^{(2)} = H_{x^{(2)}} + \eta(\gamma_0^* - 1)\xi', \tag{A.31}$$

$$\mathcal{M}y^{(2)} = 0. \tag{A.32}$$

As Equation (A.31) is a linear ordinary differential equation, the superposition of particular solutions and the boundary conditions $x^{(2)}(0) = x^{(2)}(L_0) = 0$ imply that we can define $x^{(2)} := C_1^2\widehat{x} + \eta\widehat{x}_\xi$, where $\mathcal{L}\widehat{x}_\xi = (\gamma_0^* - 1)\xi'$. At the next order, we have

$$\mathcal{L}x^{(3)} = H_{x^{(3)}}, \tag{A.33}$$

$$\begin{aligned}\mathcal{M}y^{(3)} = H_{y^{(3)}} + \eta\Big[&\xi\left((1-\gamma_0^*)y^{(1)''} - y^{(1)''''}\right) \\ &+ \xi'\left((1-\gamma_0^*)y^{(1)'} - y^{(1)'''}\right) - \xi' y^{(1)'''} - \xi'' y^{(1)''}\Big].\end{aligned} \tag{A.34}$$

Therefore, K_3 is obtained by evaluating (2.36), yielding the amplitude equation (2.41).

For heterogeneous growth modelled by (2.39), considering $O(\delta^2)$ terms now yields

$$\mathcal{L}x^{(2)} = H_{x^{(2)}} + \eta\xi', \tag{A.35}$$

$$\mathcal{M}y^{(2)} = 0, \tag{A.36}$$

Therefore, by the linearity of (A.36), we can again write $x^{(2)} := C_1^2\widehat{x} + \eta\widehat{x}_\xi$ where, x_ξ satisfies $\mathcal{L}\widehat{x}_\xi = \xi'$. Furthermore,

$$\mathcal{L}x^{(3)} = H_{x^{(3)}}, \tag{A.37}$$

$$\mathcal{M}y^{(3)} = H_{y^{(3)}} - \eta\left[\xi\left(y^{(1)''} + y^{(1)''''}\right) + \xi'\left(y^{(1)'} + y^{(1)'''}\right)\right]. \tag{A.38}$$

Hence, evaluating (2.36) for growth heterogeneity yields the amplitude equation (2.41), with K_3 obtained by the Fredholm Alternative Theorem.

A.4 Stability analysis of buckled solutions

Despite the insights provided from the linear stability analysis and weakly nonlinear analysis on the growth-induced evolution of the rod, we have no information about the dynamic stability of the non-trivial solutions obtained, as we have only considered the static form of the model. In order to investigate the stability of the buckled solutions, we must consider the time-dependent behaviour of the system. We assume that there is no dynamic rotation in the system, and therefore only introduce time-dependence to the force balance. We scale time by the standard Kirchoff time scaling $T = (\rho I/EA)^{1/2}\widehat{T}$ [40, 76, 77]. In the initial configuration, the planar force balance equations (2.10) are

$$n_x' = k(x - S_0) + \gamma\ddot{x}, \tag{A.39}$$

$$n_y' = ky + \gamma\ddot{y}, \tag{A.40}$$

where $' = \partial/\partial S_0$ $\dot{} = \partial/\partial\widehat{T}$. Suppose that a known equilibrium solution to the full nonlinear system (2.9)–(2.13) is given by the solution vector

$$\mathbf{x}_{\text{eq}} = \left(x_{\text{eq}}(S_0), y_{\text{eq}}(S_0), \theta_{\text{eq}}(S_0), n_{x,\text{eq}}(S_0), n_{y,\text{eq}}(S_0), m_{\text{eq}}(S_0)\right)^T,$$

with fixed parameters k, L_0, and γ, and T denotes the matrix transpose. We perform a linear time-dependent perturbation in the arbitrarily small parameter δ as such

$$\begin{aligned}
x &= x_{\text{eq}}(S_0) + \delta x_{\text{dyn}}(S_0)e^{i\sigma T},\\
y &= y_{\text{eq}}(S_0) + \delta y_{\text{dyn}}(S_0)e^{i\sigma T},\\
\theta &= \theta_{\text{eq}}(S_0) + \delta \theta_{\text{dyn}}(S_0)e^{i\sigma T},\\
n_x &= n_{x,\text{eq}}(S_0) + \delta n_{x,\text{dyn}}(S_0)e^{i\sigma T},\\
n_y &= n_{y,\text{eq}}(S_0) + \delta n_{y,\text{dyn}}(S_0)e^{i\sigma T},\\
m &= m_{\text{eq}}(S_0) + \delta m_{\text{dyn}}(S_0)e^{i\sigma T}.
\end{aligned} \tag{A.41}$$

Substituting this perturbation into (2.9), (2.11), (A.39), and (A.40) yields the system, at $O(\delta)$:

$$\begin{aligned}
x'_{\text{dyn}} &= \frac{\gamma}{2}\Big(1+\cos(2\theta_{\text{eq}})\Big)n_{x,\text{dyn}} + \frac{\gamma}{2}\sin(2\theta_{\text{eq}})n_{y,\text{dyn}}\\
&\quad - \gamma\Big[\sin\theta_{\text{eq}} + \sin(2\theta_{\text{eq}})n_{x,\text{eq}} - \cos(2\theta_{\text{eq}})n_{y,\text{eq}}\Big]\theta_{\text{dyn}},
\end{aligned} \tag{A.42}$$

$$\begin{aligned}
y'_{\text{dyn}} &= \frac{\gamma}{2}\sin(2\theta_{\text{eq}})n_{x,\text{dyn}} + \frac{\gamma}{2}\Big(1-\cos(2\theta_{\text{eq}})\Big)n_{y,\text{dyn}}\\
&\quad - \gamma\Big[\cos\theta_{\text{eq}} + \cos(2\theta_{\text{eq}})n_{x,\text{eq}} - \sin(2\theta_{\text{eq}})n_{y,\text{eq}}\Big]\theta_{\text{dyn}},
\end{aligned} \tag{A.43}$$

$$n'_{x,\text{dyn}} = (k-\gamma\sigma^2)x_{\text{dyn}}, \tag{A.44}$$

$$n'_{y,\text{dyn}} = (k-\gamma\sigma^2)y_{\text{dyn}}, \tag{A.45}$$

$$\theta'_{\text{dyn}} = \gamma m_{\text{dyn}}, \tag{A.46}$$

$$\begin{aligned}
m'_{\text{dyn}} &= \gamma\Big[\sin\theta_{\text{eq}} + n_{x,\text{eq}}\sin(2\theta_{\text{eq}}) - n_{y,\text{eq}}\cos(2\theta_{\text{eq}})\Big]n_{x,\text{dyn}}\\
&\quad - \gamma\Big[\cos\theta_{\text{eq}} + n_{x,\text{eq}}\cos(2\theta_{\text{eq}}) - n_{y,\text{eq}}\sin(2\theta_{\text{eq}})\Big]n_{y,\text{dyn}}\\
&\quad + \gamma\Big[n_{x,\text{eq}}\cos\theta_{\text{eq}} + n_{y,\text{eq}}\sin\theta_{\text{eq}} + 2n_{x,\text{eq}}n_{y,\text{eq}}\sin(2\theta_{\text{eq}})\\
&\qquad + (n^2_{x,\text{eq}} - n^2_{y,\text{eq}})\cos(2\theta_{\text{eq}})\Big]\theta_{\text{dyn}},
\end{aligned} \tag{A.47}$$

We note that we have made use of the trigonometric double angle formulae to simplify the ordinary differential equations. The system (A.42)–(A.47) can be written in the form

$$\mathbf{x}'_{\text{dyn}} = \mathbf{A}\mathbf{x}_{\text{dyn}}, \tag{A.48}$$

where the vector $\mathbf{x}_{\text{dyn}} = (x_{\text{dyn}}, y_{\text{dyn}}, \theta_{\text{dyn}}, n_{x,\text{dyn}}, n_{y,\text{dyn}}, m_{\text{dyn}})^T$ and $\mathbf{A}$ is a matrix that is expressed solely in terms of $\mathbf{x}_{\text{eq}}$. As $\mathbf{x}_{\text{eq}}$ is known, for a given σ^2, $\mathbf{A}$ is constant for each $S_0 \in [0, L_0]$ and hence the system (A.42)–(A.47) is a system of first-order, linear ordinary differential equations with constant coefficients for a fixed value of S_0. Therefore, we can integrate the system over the interval $[0, L_0]$. However, observe that only the boundary conditions for x_{dyn}, y_{dyn} and θ_{dyn} are known; that is, they must vanish at the endpoints $S_0 = 0$ and $S_0 = L_0$. To overcome this, we use a method that has been used in previous buckling analyses [18, 119].

We seek a solution of the form $\mathbf{x}_{\text{dyn}} = b_1\mathbf{x}^{(1)}_{\text{dyn}} + b_2\mathbf{x}^{(2)}_{\text{dyn}} + b_3\mathbf{x}^{(3)}_{\text{dyn}}$, where, at $S_0 = 0$, $\mathbf{x}^{(1)}_{\text{dyn}}$, $\mathbf{x}^{(2)}_{\text{dyn}}$ and $\mathbf{x}^{(3)}_{\text{dyn}}$ satisfy

$$\mathbf{x}^{(1)}_{\text{dyn}}(0) = (0,0,0,1,0,0)^T, \quad \mathbf{x}^{(2)}_{\text{dyn}}(0) = (0,0,0,0,1,0)^T, \quad \mathbf{x}^{(3)}_{\text{dyn}}(0) = (0,0,0,0,0,1)^T. \tag{A.49}$$

Therefore, the solution components $\mathbf{x}^{(1)}_{\text{dyn}}$, $\mathbf{x}^{(2)}_{\text{dyn}}$ and $\mathbf{x}^{(3)}_{\text{dyn}}$ are linearly independent and thus each solution may be solved for independently as functions of σ^2. To determine b_1, b_2 and b_3 and consequently our final solvability condition, we impose the boundary condition that x_{dyn}, y_{dyn} and θ_{dyn} vanish at $S_0 = L_0$, leading to the matrix equation

$$\begin{pmatrix} x^{(1)}_{\text{dyn}} & x^{(2)}_{\text{dyn}} & x^{(3)}_{\text{dyn}} \\ y^{(1)}_{\text{dyn}} & y^{(2)}_{\text{dyn}} & y^{(3)}_{\text{dyn}} \\ \theta^{(1)}_{\text{dyn}} & \theta^{(2)}_{\text{dyn}} & \theta^{(3)}_{\text{dyn}} \end{pmatrix} \begin{pmatrix} b_1 \\ b_2 \\ b_3 \end{pmatrix} = \begin{pmatrix} 0 \\ 0 \\ 0 \end{pmatrix} \quad \text{at} \quad S_0 = L_0. \tag{A.50}$$

A solution to Equation (A.50) exists if and only if the determinant of the left hand side matrix is equal to zero for a given σ^2. Therefore, if there is a value of $\sigma^2 < 0$ such that the determinant vanishes, then the buckled solution $\mathbf{x}_{\text{eq}}$ is unstable, as the time perturbation grows exponentially as $T \to \infty$.

A.5 Energies

Here, we give the forms of the energy functionals that are considered in Sections 2.4.3. We then show how these defined energies change for heterogeneity in rod stiffness and growth, helping to elucidate the observed changes to rod shape in Figure 2.4.

The total energy of the system, $\mathcal{E}$, comprises contributions from bending, stretching, and the underlying foundation.

In the reference configuration, these dimensional individual energy densities may be written respectively as:

$$\mathrm{U^B} = \frac{EI}{2}\left(\frac{\partial\theta}{\partial S}\right)^2, \quad \mathrm{U^S} = \frac{EA}{2}(\alpha-1)^2, \quad \mathrm{U^F} = \frac{Ek_f}{2\gamma}\left[\left(x-\frac{S}{\gamma}\right)^2 + y^2\right]. \quad \text{(A.51)}$$

After nondimensionalisation, we write the energy densities as

$$\mathrm{U^B} = \frac{E_b}{2}\left(\frac{\partial\theta}{\partial S}\right)^2, \quad \mathrm{U^S} \quad = \frac{E_s}{2}(\alpha-1)^2, \quad \mathrm{U^F} = \frac{k}{2\gamma}\left[\left(x-\frac{S}{\gamma}\right)^2 + y^2\right], \quad \text{(A.52)}$$

where E_b, E_s, and k represent the dimensionless rod bending stiffness, rod stretching stiffnes, and foundation stiffness repectively (note that in the homogeneous case, $E_s = E_b = 1$). Therefore, the total energy density is given by

$$\mathrm{U^{total}} = \mathrm{U^B} + \mathrm{U^S} + \mathrm{U^F} + n_x\left(\frac{\partial x}{\partial S} - \alpha\cos\theta\right) + n_y\left(\frac{\partial y}{\partial S} - \alpha\sin\theta\right). \quad \text{(A.53)}$$

The latter two terms correspond to the geometric constraints placed on the rod, with the horizontal and vertical forces n_x and n_y acting as Lagrange multipliers. However, these contributions will vanish after energy minimisation. Hence, the total energy $\mathcal{E}^{\mathrm{total}}$ is given by

$$\mathcal{E}^{\mathrm{total}} = \mathcal{E}^{\mathrm{bend}} + \mathcal{E}^{\mathrm{stretch}} + \mathcal{E}^{\mathrm{foundation}}, \quad \text{(A.54)}$$

where

$$\mathcal{E}^{\mathrm{bend}} = \int_0^{L_0} \mathrm{U^B}\gamma dS_0, \quad \text{(A.55)}$$

$$\mathcal{E}^{\mathrm{stretch}} = \int_0^{L_0} \mathrm{U^S}\gamma dS_0, \quad \text{(A.56)}$$

$$\mathcal{E}^{\mathrm{foundation}} = \int_0^{L_0} \mathrm{U^F}\gamma dS_0. \quad \text{(A.57)}$$

A.6 The inverse problem

In this section, we describe our approach to the inverse problem discussed briefly in Section 3.5, and the method of producing Figure 2.10. We chose a candidate shape with embedded heterogeneity, in this case, foundation heterogeneity following Figure 2.4(b), and we tried to match that shape by varying the heterogeneity in

the rod stiffness and growth, in the form of (2.39), as well as the net growth γ_0, based on the results of Section 2.4.3. The baseline foundation stiffness k_0 and rod length L_0 were set to $k_0 = 0.04$ and $L_0 = 20$, respectively.

Figure 2.4(c) showed that when net growth is unchanged, growth heterogeneity redistributes the material of the rod away from regions of low growth to those with high growth. This suggests that in order to match the candidate shape, growth must be high in the middle region and low in the outer regions. For rod stiffness heterogeneity, we wanted to localise the buckling to regions of softened rod stiffness, but to counteract the enhanced compressed seen in Figure 2.4(b), we increased the net growth.

Here we have only explored this problem in a preliminary manner. An extensive search of the heterogeneity parameter space is intrinsically challenging and time-consuming, as the heterogeneity can in principle take any form, and the morphology produced for a given form can only be obtained as the result of numerical path continuation from a known solution. While a more detailed investigation would be a worthwhile focus for another paper, here we have chosen heterogeneities in the *ad hoc*, but intuitively guided, manner outlined above. Our prescribed heterogeneity choices were: for foundation stiffness heterogeneity, we set $\gamma = 1.9$, $\widehat{\epsilon} = 0.75$ and $\xi(S_0) = \cos(2\pi S_0/L_0))$; for rod stiffness heterogeneity, γ was increased to $\gamma = 2.45$, $\widehat{\epsilon} = 0.9$, and $\xi(S_0) = 1 - \exp\left(-16(S_0 - 0.5L_0)^2/L_0^2\right)$; and for growth heterogeneity, we prescribed $\gamma_0 = 1.9$, $\widehat{\epsilon} = 0.9$, and $\xi(S_0) = -\cos(2\pi S_0/L_0))$.

Once we had matched the shapes to a sufficient degree, we examined all other features, such as the bending moment m, force components n_x, n_y, etc, seeking distinguishing characteristics. From this, we identified two salient features: the axial stress n_3 in the outer region, where there was minimal growth (Fig. 2.10(b)); and the foundation energy density U^{F} in the middle section, where the foundation had been softened locally (Fig. 2.10(c)).

B

Self-contact derivations

The phenomenon of self-contact is a complex but possibly significant step towards a full crypt morphology. To understand how to best account for self-contact within the crypt, we consider the problem using a variational approach, minimising the variation of the total energy described in Appendix A, now with the addition of enforced contact conditions.

We assume symmetric, frictionless self-contact; therefore, we can reduce the problem of self-contact to the half-interval, $[0, 1/2]$. We first consider the case of self-contact at a point, before extending our analysis to the case of self-contact along a region. In each case, we derive the resulting equations for the case when the rod is tethered to a linear elastic foundation. The foundation can be replaced by other types, using subsequent force balance arguments.

B.1 Self-contact at a point

The contact point is assumed to occur an isolated point, $x(S_c) = x_0$, where x_0 describes the self-contact width. Following notation from Appendix A, we consider the total energy with respect to the reference configuration, now parametrised by the initial arc length, S_0, so that the domain is fixed. The total energy

functional to be minimised is

$$\mathcal{E} = \int_0^{\frac{1}{2}} \mathrm{U}^{\mathrm{total}} \gamma dS_0 + \lambda_c (x(S_c) - x_0), \tag{B.1}$$

where $\mathrm{U}^{\mathrm{total}}$ is the total energy of the rod in the absence of self-contact and the second term on the right-hand side of Equation (B.1) enforces the self-contact condition at $S_0 = S_c$, where the parameter λ_p acts as a Lagrange multiplier. Recall that $\mathrm{U}^{\mathrm{total}}$ is defined by Equation (B.2) as:

$$\begin{aligned} \mathrm{U}^{\mathrm{total}} = & \frac{E_b}{2}\left(\frac{\theta'}{\gamma}\right)^2 + \frac{E_s}{2}(\alpha - 1)^2 + \frac{k}{2\gamma}\left[(x - S_0)^2 + y^2\right] \\ & + \frac{n_x}{\gamma}(x' - \alpha\gamma\cos\theta) + \frac{n_y}{\gamma}(y' - \alpha\gamma\sin\theta), \end{aligned} \tag{B.2}$$

where the force components n_x and n_y are point-wise Lagrange multipliers to enforce the geometric planar constraints. Note that we may also express the total energy (B.1) as

$$\mathcal{E} = \int_0^{\frac{1}{2}} \mathrm{U}^{\mathrm{total}} \gamma + \lambda_c (x(S_0) - x_0)\delta(S_0 - S_c) dS_0, \tag{B.3}$$

where $\delta(S_0)$ is the Dirac delta function. The modified force balance equations are obtained by minimising the first variation of $\mathcal{E}$, defined as:

$$\delta\mathcal{E} = \frac{d}{d\varepsilon}\mathcal{E}[x + \varepsilon\bar{x}, y + \varepsilon\bar{y}, \theta + \varepsilon\bar{\theta}, \alpha + \varepsilon\bar{\alpha}, S_c + \varepsilon\bar{S}_c]\Big|_{\varepsilon=0}, \tag{B.4}$$

where ε is an arbitrarily small parameter, and $\bar{x}, \bar{y}, \bar{\theta}, \bar{\alpha}$, and $\bar{S}_c$ are the increments in their respective variables. Evaluating (B.13) yields

$$\begin{aligned} \delta\mathcal{E} = & \left[E_b\frac{\theta'\bar{\theta}}{\gamma} + n_x\bar{x} + n_y\bar{y}\right]_0^{\frac{1}{2}} \\ & + \int_0^{\frac{1}{2}} \Bigg[-\left(E_b\frac{\theta'}{\gamma}\right)'\bar{\theta} + \gamma E_s(\alpha - 1)\bar{\alpha} + k\left((x - S_0)\bar{x} + y\bar{y}\right) \\ & \quad - n_x'\bar{x} + n_x(\alpha\gamma\sin\theta\bar{\theta} - \gamma\cos\theta\bar{\alpha}) - n_y'\bar{y} - n_y(\alpha\gamma\cos\theta\bar{\theta} + \gamma\sin\theta\bar{\alpha}) \\ & \quad + \lambda_c(\bar{x} + x'\bar{S}_c)\delta(S_0 - S_c)\Bigg] dS_0, \end{aligned} \tag{B.5}$$

where we have applied integration by parts to eliminate terms that involve derivatives of the increments $\bar{x}, \bar{y}$, and $\bar{\theta}$. The first term on the right hand side of Equation

(B.5) vanishes after consideration of the boundary conditions. Recall that our left clamped boundary condition is:

$$x(0) = 0, \qquad y(0) = 0, \qquad \theta(0) = 0. \tag{B.6}$$

Therefore, at $S_0 = 0$, the increments $\bar{x}(0) = 0$, $\bar{y}(0) = 0$ and $\bar{\theta}(0) = 0$. As we are primarily interested in the growth and deformation of an intestinal crypt, we restrict ourselves to even solutions about $S_0 = 1/2$. Therefore, at $S_0 = 1/2$, we have that $x = 1/2$ and $\theta = 0$, leading to $\bar{x} = 0$ and $\bar{\theta} = 0$ at $S_0 = 1/2$. Hence, in order to ensure that the first term vanishes, we must impose that $n_y = 0$. Thus, the boundary conditions along the half-interval are:

$$x(0) = 0, \quad y(0) = 0, \quad \theta(0), \qquad x\left(\frac{1}{2}\right) = \frac{1}{2}, \quad \theta\left(\frac{1}{2}\right) = 0, \quad n_y\left(\frac{1}{2}\right) = 0. \tag{B.7}$$

Now, to ensure that $\delta\mathcal{E} = 0$, we impose that each the integral terms vanishes. As the increments are arbitrary functions, by the continuity lemma, we recover the familiar vertical force balance and angular momentum balance equations, Equations (2.10) and (2.11) respectively. However, we now obtain an modified horizontal force balance equation,

$$n_x' = k(x - S_0) + \lambda_c \delta(S_0 - S_c). \tag{B.8}$$

Integrating Equation (B.8) about $S_0 = S_c$ yields an expression for λ_c:

$$\lambda_c = n_x(S_c+) - n_x(S_c-). \tag{B.9}$$

That is, self-contact leads to a jump in resultant horizontal force about the self-contact point, S_c. Finally, an additional condition at the self-contact point is obtained:

$$x'(S_c) = 0. \tag{B.10}$$

Substituting (B.10) into the geometric balance (2.9) implies that $\theta = \pm\pi/2$. As we primarily consider downward invaginations, we obtain the condition

$$\theta(S_c) = \frac{\pi}{2}. \tag{B.11}$$

B.2 Self-contact along a region

Once the rod has undergone self-contact at a point, we expect that after further growth, the rod will transition from self-contact an isolated point to self-contact along a region of non-zero length. We denote the self-contact region endpoints by $S_c^{(1)}$ and $S_c^{(2)}$, which are defined such that $x(S_0) = x_0 \; \forall S_0 \in [S_c^{(1)}, S_c^{(2)}]$. Imposing this point-wise condition leads to a extension of the original energy defined in Equation (B.1). The total energy $\mathcal{E}$ is now defined as:

$$\mathcal{E} = \int_0^{\frac{1}{2}} \mathrm{U}^{\mathrm{total}}\gamma + \frac{\lambda_c(S_0)}{2}(x - x_0)\left[\mathrm{H}(S_0 - S_c^{(1)}) + \mathrm{H}(S_c^{(2)} - S_0)\right] dS_0. \tag{B.12}$$

The third term on the right-hand side of (B.12) imposes that self-contact holds along the region $[S_c^{(1)}, S_c^{(2)}]$, where $\lambda_c(S_0)$ is now a point-wise Lagrange multiplier and $\mathrm{H}(S_0)$ is the Heaviside step function. Minimising the first variation of $\mathcal{E}$, defined now by

$$\delta\mathcal{E} = \frac{d}{d\varepsilon}\mathcal{E}[x + \varepsilon\bar{x}, y + \varepsilon\bar{y}, \theta + \varepsilon\bar{\theta}, \alpha + \varepsilon\bar{\alpha}, S_c^{(1)} + \varepsilon\bar{S}_c^{(1)}, S_c^{(2)} + \varepsilon\bar{S}_c^{(2)}]\Big|_{\varepsilon=0}, \tag{B.13}$$

yields the familiar vertical force and moment balance equations, (2.10)–(2.11). However, the horizontal geometric and force balances are now given by:

$$x' = \cos\theta = 0, \tag{B.14}$$

$$n_x' = k(x - S_0) + \frac{\lambda_c}{2}\left[\mathrm{H}(S_0 - S_c^{(1)}) + \mathrm{H}(S_c^{(2)} - S_0)\right]. \tag{B.15}$$

Now λ_c acts as a force distribution that imposes pointwise self-contact over the region $[S_c^{(1)}, S_c^{(2)}]$, which is determined by the following conditions. First, integrating Equation (B.15) about $S_0 = S_c^{(1)}$ yields the first boundary condition:

$$\lambda_c(S_c^{(1)}) = 2\left[n_x(S_c^{(1)}+) - n_x(S_c^{(1)}-)\right]. \tag{B.16}$$

Next, integrating Equation (B.15) about $S_0 = S_c^{(2)}$ yields:

$$\lambda_c(S_c^{(2)}) = 2\left[n_x(S_c^{(2)}+) - n_x(S_c^{(2)}-)\right], \tag{B.17}$$

where $n_x(S_c^{(2)}-)$ is determined by integration over the self-contact region:

$$n_x(S_c^{(2)}-) = n_x(S_c^{(1)}+) + \int_{S_c^{(1)}+}^{S_c^{(2)}-} k(x - S_0) + \lambda(S_0)dS_0. \tag{B.18}$$

Additionally, note that Equation (B.14) implies the following conditions:

$$\theta(S_0) = \frac{\pi}{2} \qquad \Longrightarrow \qquad \theta'(S_0) = 0, \qquad \forall \qquad S_0 \in [S_c^{(1)}, S_c^{(2)}]. \tag{B.19}$$

Finally, we also obtain the two self-contact conditions for $x(S_0)$:

$$x(S_c^{(1)}) = x_0, \qquad x(S_c^{(2)}) = x_0. \tag{B.20}$$

B.3 Enforcing constant self-encapsulated area

We now discuss how the system (3.4)–(3.8) are altered if we impose that area enclosed by self-contact is fixed. By Green's theorem, this constraint is given by:

$$A = \int_{S_c}^{\frac{1}{2}} xy' dS_0 = \int_0^{\frac{1}{2}} xy' \mathrm{H}(S_0 - S_c) dS_0 = A_0, \tag{B.21}$$

where $A_0 > 0$ is constant. Note that for self-contact along a region, we would replace S_c by $S_c^{(2)}$. For self-contact at a single point, we modify (B.1) to include the constraint (B.21) as such:

$$\mathcal{E} = \int_0^{\frac{1}{2}} \mathrm{U}^{\mathrm{total}} \gamma dS_0 + \lambda_c(x(S_c) - x_0) + \lambda_A \int_{S_c}^{\frac{1}{2}} xy' dS_0. \tag{B.22}$$

For self-contact along the region $[S_c^{(1)}, S_c^{(2)}]$, we have:

$$\mathcal{E} = \int_0^{\frac{1}{2}} \mathrm{U}^{\mathrm{total}} \gamma dS_0 + \int_{S_c^{(1)}}^{S_c^{(2)}} \lambda_c(S_0)(x - x_0) dS_0 + \lambda_A \int_{S_c^{(2)}}^{\frac{1}{2}} xy' dS_0. \tag{B.23}$$

In both cases, λ_{A} is a Lagrange multiplier. Minimising the total variation of the functionals (B.22) and (B.23) yields the altered force balance equations:

$$n_x' = k(x - S_0) + \lambda_A y' \mathrm{H}(S_0 - S_c), \tag{B.24}$$

$$n_y' = ky - \lambda_A x' \mathrm{H}(S_0 - S_c), \tag{B.25}$$

while for self-contact along a region, S_c is simply replaced with $S_c^{(2)}$. These equations show the constant self-contact area is maintained by a normal force, modulated by the Lagrange multiplier λ_A, which is analogous to a hydrostatic pressure.

C

Homeostasis for a 2D morphology

We derive the resulting equations that describe homeostasis along a 2D morphology. In principle, this is the same as case for a 1D morphology, but we now must specify the homeostatic shape through the tangent angle, θ. Following notation in Chapter 4, we denote Lagrangian variables by $f(S_0, t)$ and Eulerian variables by $\hat{f}(s,t) := f(S_0(s,t),t)$. The 1D homeostasis is extended accordingly:

$$\frac{\dot{\gamma}}{\gamma} = \mathcal{G} := g(s), \qquad \hat{\theta} = \hat{\theta}(s). \tag{C.1}$$

That is, homeostasis in 2D is defined as the incremental growth $\dot{\gamma}\gamma^{-1}$ and the tangent angle θ (which defines the rod shape) being fixed with respect to the current arc length s and independent of time, where $g(s)$ is the homeostatic incremental growth profile.

In the Eulerian frame, the full set of 2D linear and angular momentum balance

equations is given by:

$$\frac{\partial \hat{S}_0}{\partial s} = \frac{1}{\hat{\alpha}\hat{\gamma}}, \tag{C.2}$$

$$\frac{\partial \hat{x}}{\partial s} = \cos\hat{\theta}, \tag{C.3}$$

$$\frac{\partial \hat{y}}{\partial s} = \sin\hat{\theta}, \tag{C.4}$$

$$\frac{\partial \hat{n}_x}{\partial s} = k(\hat{x} - \hat{p}_x), \qquad \frac{\partial \hat{p}_x}{\partial t} = \rho(\hat{x} - \hat{p}_x) + \hat{v}\frac{\partial \hat{p}_x}{\partial s}, \tag{C.5}$$

$$\frac{\partial \hat{n}_y}{\partial s} = k(\hat{y} - \hat{p}_y), \qquad \frac{\partial \hat{p}_y}{\partial t} = \rho(\hat{y} - \hat{p}_y) + \hat{v}\frac{\partial \hat{p}_y}{\partial s}, \tag{C.6}$$

$$\frac{\partial \hat{\theta}}{\partial s} = E_b^{-1}\hat{m}, \tag{C.7}$$

$$\frac{\partial \hat{m}}{\partial s} = \hat{n}_x \sin\hat{\theta} - \hat{n}_y \cos\hat{\theta}, \tag{C.8}$$

where $\hat{v}(s,t)$ is the flow velocity that arises from mapping Lagrangian variables to the Eulerian configuration,

$$\hat{v} = \hat{\alpha}\hat{\gamma}\frac{\partial \hat{S}_0}{\partial t}, \tag{C.9}$$

and $\hat{\alpha}(s,t)$ is the Eulerian elastic stretch, defined by the (nondimensional) constitutive relation,

$$\hat{\alpha} = 1 + \hat{n}_3, \qquad \text{where} \qquad \hat{n}_3 = \hat{n}_x \cos\hat{\theta} + \hat{n}_y \sin\hat{\theta}, \tag{C.10}$$

and $\hat{\gamma}(s,t)$ is the Eulerian growth stretch which evolves according to Equation (4.44):

$$\hat{\gamma}_t = g(s)\gamma + \hat{v}\hat{\gamma}_s. \tag{C.11}$$

The Equations (C.2)–(C.8) are solved subject to the clamped boundary conditions:

$$\hat{S}_0(0) = 0, \quad \hat{S}_0(l) = L_\mu, \quad \hat{x}(0) = 0, \quad \hat{x}(l) = 1, \quad \hat{y}(0) = \hat{y}(l) = 0, \tag{C.12}$$

where $l = \int_0^{L_\mu} \alpha\gamma dS_0$ is the total rod length.

We recall from Equation (4.47) that in the Eulerian configuration, the initial arc length $\hat{S}_0(s,t)$ must satisfy the following compatibility condition:

$$\frac{\partial^2 \hat{S}_0}{\partial s \partial t} = \frac{\partial^2 \hat{S}_0}{\partial t \partial s} \qquad \Longleftrightarrow \qquad \frac{\partial}{\partial s}\left(\frac{\hat{v}}{\hat{\alpha}\hat{\gamma}}\right) = \frac{\partial}{\partial t}\left(\frac{1}{\hat{\alpha}\hat{\gamma}}\right). \tag{C.13}$$

We now proceed in the same manner as Chapter 4, where we make a number of simplifying assumptions based on the homeostasis definition (C.1). First, observe that if $\theta = \theta(s)$, then we can define the equivalent Eulerian tangent angle by $\hat{\theta} = \hat{\theta}(s)$. Therefore, the homeostatic morphology, $(\hat{x}(s), \hat{y}(s))$, can be obtained straightforwardly:

$$\hat{\theta} = \hat{\theta}(s) \qquad \Longleftrightarrow \qquad \hat{x}(s) = \int_0^s \cos\hat{\theta}(s')ds', \qquad \hat{y}(s) = \int_0^s \sin\hat{\theta}(s')ds'. \quad \text{(C.14)}$$

Furthermore, by Equation (C.7), the bending moment $\hat{m} = \hat{m}(s)$.

Now, if $\mathcal{G} = \mathcal{G}(W(s), \hat{n}_3)$, then $\hat{n}_3$ is independent of time:

$$\mathcal{G}(W(s), \hat{n}_3) = g(s) \qquad \Longleftrightarrow \qquad \hat{n}_3 = \hat{n}_3(s). \quad \text{(C.15)}$$

As $\hat{\theta} = \hat{\theta}(s)$, then by definition of the axial stress, $\hat{n}_3$, the individual force components, $\hat{n}_x$ and $\hat{n}_y$, are also independent of time:

$$\hat{n}_3 = \hat{n}_3(s), \quad \hat{\theta} = \hat{\theta}(s), \qquad \Longrightarrow \qquad \hat{n}_x = \hat{n}_x(s), \quad \hat{n}_y = \hat{n}_y(s). \quad \text{(C.16)}$$

By the constitutive relation (C.10), the Eulerian elastic stretch $\hat{\alpha}$ is also independent of time:

$$\hat{\alpha}(s) = 1 + \hat{n}_3(s). \quad \text{(C.17)}$$

If $\hat{n}_x = \hat{n}_x(s)$ and $\hat{n}_y = \hat{n}_y(s)$, then by Equations (C.5)–(C.6), in turn, implies that $\hat{p}_x = \hat{p}_x(s)$ and $\hat{p}_y = \hat{p}_y(s)$. Accordingly, the time derivatives, $\partial\hat{p}_x/\partial t$ and $\partial\hat{p}_y/\partial t$, vanish. This leads to two equivalent expressions for the flow velocity $\hat{v}$, which is also a function of s only:

$$\hat{v}(s) = -\frac{\rho(\hat{x} - \hat{p}_x)}{\frac{\partial\hat{p}_x}{\partial s}} = -\frac{\rho(\hat{y} - \hat{p}_y)}{\frac{\partial\hat{p}_y}{\partial s}}. \quad \text{(C.18)}$$

Hence, the homeostatic system of equations in 2D is given by:

$$\frac{d\hat{n}_x}{ds} = k(\hat{x} - \hat{p}_x), \tag{C.19}$$

$$\frac{d\hat{n}_y}{ds} = k(\hat{y} - \hat{p}_y), \tag{C.20}$$

$$\frac{d\hat{p}_x}{ds} = -\frac{\rho(\hat{x} - \hat{p}_x)}{\hat{v}}, \tag{C.21}$$

$$\frac{d\hat{p}_y}{ds} = -\frac{\rho(\hat{y} - \hat{p}_y)}{\hat{v}}, \tag{C.22}$$

$$\frac{d\hat{v}}{ds} = \frac{\left(k(\hat{x} - \hat{p}_x)\cos\hat{\theta} + k(\hat{y} - \hat{p}_y)\sin\hat{\theta} + \hat{\theta}_s(-\hat{n}_x\sin\hat{\theta} + \hat{n}_y\cos\hat{\theta}\right)\hat{v}}{E_s + \hat{n}_x\cos\hat{\theta} + \hat{n}_y\sin\hat{\theta}} - g(s;\hat{n}_3), \tag{C.23}$$

subject to the boundary conditions

$$\hat{p}_x(0) = 0, \qquad \hat{p}_y(0) = \hat{y}(0), \qquad \hat{v}(0) = 0. \tag{C.24}$$

The sloughing boundary $L_\mu(t)$ is finally determined by integrating Equation (C.2) over $s \in [0,1]$:

$$L_\mu(t) = \int_0^1 \frac{1}{\hat{\alpha}(s)\hat{\gamma}(s,t)} ds, \tag{C.25}$$

where $\hat{\gamma}(s,t)$ evolves in homeostasis according to Equation (4.62):

$$\hat{\gamma}_t = g(s;\hat{n}_3)\hat{\gamma} + \hat{v}(s)\hat{\gamma}_s. \tag{C.26}$$

References

[1] B. Alberts, A.D. Johnson, J. Lewis, M. Raff, K. Roberts, and P. Walter, *Molecular Biology of the Cell*, Garland Science, New York, 2002.

[2] A.A. Almet, H.M. Byrne, P.K. Maini, and D.E. Moulton, *Post-buckling behaviour of a growing elastic rod*, Journal of Mathematical Biology **78** (2019), 777–814.

[3] A.A. Almet, P.K. Maini, D.E. Moulton, and H.M. Byrne, *Modelling perspectives on the intestinal crypt, a canonical system for growth, mechanics, and remodelling*, Submitted to Current Opinion in Biomedical Engineering (2019).

[4] J.C. Amazigo, B. Budiansky, and G.F. Carrier, *Asymptotic analyses of the buckling of imperfect columns on nonlinear elastic foundations*, International Journal of Solids and Structures **6** (1970), no. 10, 1341–1356.

[5] D. Ambrosi, G.A. Ateshian, E.M. Arruda, S.C. Cowin, J. Dumais, A. Goriely, G.A. Holzapfel, J.D. Humphrey, R. Kemkemer, E. Kuhl, J.E. Olberding, L.A. Taber, and K. Garikipati, *Perspectives on biological growth and remodeling*, Journal of the Mechanics and Physics of Solids **78** (2011), no. 6, 1–16.

[6] D. Ambrosi, M. Ben Amar, C.J. Cyron, A. DeSimone, A. Goriely, J.D. Humphrey, and E. Kuhl, *Growth and remodelling of living tissues: perspectives, challenges and opportunities*, Journal of the Royal Society Interface **16** (2019), no. 157, 20190233.

[7] M. Aragona, T. Panciera, A. Manfrin, S. Giulitti, F. Michielin, N. Elvassore, S. Dupont, and S. Piccolo, *A mechanical checkpoint controls multicellular*

growth through YAP/TAZ regulation by actin-processing factors, Cell **154** (2013), no. 5, 1047–1059.

[8] A. Araujo, A. Rübben, P.J. Bentley, and D. Basanta, *Testing three hypotheses of the contribution of geometry and migration dynamics to intestine crypt evolution*, Artificial Life Conference Proceedings, MIT Press, 2018, pp. 420–427.

[9] F. Aurenhammer, R. Klein, and D.-T. Lee, *Voronoi diagrams and Delaunay triangulations*, vol. 8, World Scientific, 2013.

[10] D.E. Axelrod, S. Vedula, and J. Obaniyi, *Effective chemotherapy of heterogeneous and drug-resistant early colon cancers by intermittent dose schedules: a computer simulation study*, Cancer Chemotherapy and Pharmacology **79** (2017), no. 5, 889–898.

[11] L. Azzolin, T. Panciera, S. Soligo, E. Enzo, S. Bicciato, S. Dupont, S. Bresolin, C. Frasson, G. Basso, V. Guzzardo, A. Fassina, M. Cordenonsi, and S. Piccolo, *YAP/TAZ incorporation in the β-catenin destruction complex orchestrates the Wnt response*, Cell **158** (2014), no. 1, 157–170.

[12] L. Azzolin, F. Zanconato, S. Bresolin, M. Forcato, G. Basso, S. Bicciato, M. Cordenonsi, and S. Piccolo, *Role of TAZ as mediator of Wnt signaling*, Cell **151** (2012), no. 7, 1443–1456.

[13] A.M. Baker, B. Cereser, S. Melton, A.G. Fletcher, M. Rodriguez-Justo, P.J. Tadrous, A. Humphries, G. Elia, S.A.C. McDonald, N.A. Wright, B.D. Simons, M. Jansen, and T. A. Graham, *Quantification of crypt and stem cell evolution in the normal and neoplastic human colon*, Cell Reports **8** (2014), no. 4, 940–947.

[14] V. Balbi and P. Ciarletta, *Morpho-elasticity of intestinal villi*, Journal of the Royal Society Interface **10** (2013), no. 82, 20130109.

[15] E.D. Bankaitis, A. Ha, C.J. Kuo, and S.T. Magness, *Reserve stem cells in intestinal homeostasis and injury*, Gastroenterology (2018).

[16] N. Barker, R.A. Ridgway, J.H. van Es, M. van de Wetering, H. Begthel, M. van den Born, E. Danenberg, A.R. Clarke, O.J. Sansom, and H. Clevers, *Crypt stem cells as the cells-of-origin of intestinal cancer*, Nature **457** (2009), no. 7229, 608.

[17] E.R. Barry, T. Morikawa, B.L. Butler, K. Shrestha, R. De La Rosa, K.S. Yan, C.S. Fuchs, S.T. Magness, R. Smits, S. Ogino, C.J. Kuo, and F.D. Camargo, *Restriction of intestinal stem cell expansion and the regenerative response by YAP*, Nature **493** (2013), no. 7430, 106.

[18] M. Ben Amar and A. Goriely, *Growth and instability in elastic tissues*, Journal of the Mechanics and Physics of Solids **53** (2005), no. 10, 2284–2319.

[19] M. Ben Amar and F. Jia, *Anisotropic growth shapes intestinal tissues during embryogenesis*, Proceedings of the National Academy of Sciences **110** (2013), no. 26, 10525–10530.

[20] T.K. Berdyyeva, C.D. Woodworth, and I. Sokolov, *Human epithelial cells increase their rigidity with ageing in vitro: direct measurements*, Physics in Medicine & Biology **50** (2004), no. 1, 81.

[21] M. Bienz and H. Clevers, *Linking colorectal cancer to Wnt signaling*, Cell **103** (2000), no. 2, 311–320.

[22] M.A. Biot, *Bending of an infinite beam on an elastic foundation*, Journal of Applied Mechanics (1937), A1–7.

[23] A. Bollas and L. Shahriyari, *The role of backward cell migration in two-hit mutants' production in the stem cell niche*, PLoS ONE **12** (2017), no. 9, e0184651.

[24] L.G. Bowden, H.M. Byrne, P.K. Maini, and D.E. Moulton, *A morphoelastic model for dermal wound closure*, Biomechanics and Modeling in Mechanobiology **15** (2016), no. 3, 663–681.

[25] R. Bravo and D.E. Axelrod, *A calibrated agent-based computer model of stochastic cell dynamics in normal human colon crypts useful for in silico experiments*, Theoretical Biology and Medical Modelling **10** (2013), no. 1, 66.

[26] V. Breña-Medina and A. Champneys, *Subcritical Turing bifurcation and the morphogenesis of localized patterns*, Physical Review E **90** (2014), no. 3, 170–6.

[27] N.F. Britton, N.A. Wright, and J.D. Murray, *A mathematical model for cell population kinetics in the intestine*, Journal of Theoretical Biology **98** (1982), no. 3, 531–541.

[28] S. Budday, E. Kuhl, and J.W Hutchinson, *Period-doubling and period-tripling in growing bilayered systems*, Philosophical Magazine **6435** (2015), no. June, 1–17.

[29] S. Budday, P. Steinmann, and E. Kuhl, *The role of mechanics during brain development*, Journal of the Mechanics and Physics of Solids **72** (2014), 75–92.

[30] P. Buske, J. Galle, N. Barker, G. Aust, H. Clevers, and M. Loeffler, *A comprehensive model of the spatio-temporal stem cell and tissue organisation in the intestinal crypt*, PLoS Computational Biology **7** (2011), no. 1.

[31] A.B. Cairnie and B.H. Millen, *Fission of Crypts in the Small Intestine of the Irradiated Mouse*, Cell Proliferation **8** (1975), no. 2, 189–196.

[32] Y. Cao and J.W. Hutchinson, *From wrinkles to creases in elastomers: the instability and imperfection-sensitivity of wrinkling*, Proceedings of the Royal Society A **468** (2011), no. 2137, 94–115.

[33] ———, *Wrinkling Phenomena in Neo-Hookean Film/Substrate Bilayers*, Journal of Applied Mechanics **79** (2017), no. May 2012, 1–9.

[34] T.D Carroll, A.J Langlands, J.M Osborne, I.P Newton, P.L Appleton, and I.S. Näthke, *Interkinetic nuclear migration and basal tethering facilitates post-mitotic daughter separation in intestinal organoids*, Journal of Cell Science **130** (2017), no. 22, 3862–3877.

[35] T.D Carroll, I.P Newton, Y. Chen, J.J. Blow, and I.S. Näthke, *Lgr5$^+$ intestinal stem cells reside in an unlicensed g1 phase*, Journal of Cell Biology **217** (2018), no. 5, 1667–1685.

[36] A.R. Champneys, T.J. Dodwell, R.M.J. Groh, G.W. Hunt, R.M. Neville, A. Pirrera, A.H. Sakhaei, M. Schenk, and M. Ahmer Wadee, *Happy catastrophe: recent progress in analysis and exploitation of elastic instability*, Frontiers in Applied Mathematics and Statistics **5** (2019), 34.

[37] R. Chirat, D.E. Moulton, and A. Goriely, *Mechanical basis of morphogenesis and convergent evolution of spiny seashells.*, Proceedings of the National Academy of Sciences **110** (2013), no. 15, 1–6.

[38] C.-J. Chuong and Y.-C. Fung, *Residual stress in arteries*, Frontiers in Biomechanics, Springer, 1986, pp. 117–129.

[39] H. Clevers, *Wnt/β-catenin signaling in development and disease*, Cell **127** (2006), no. 3, 469–480.

[40] B.D. Coleman, E.H. Dill, M. Lembo, L. Zheng, and I. Tobias, *On the Dynamics of Rods in the Theory of Kirchhoff and Clebsch*, Archive for Rational Mechanics and Analysis **121** (1993), 339–359.

[41] B.D. Coleman and D. Swigon, *Theory of self–contact in Kirchhoff rods with applications to supercoiling of knotted and unknotted DNA plasmids*, Philosophical Transactions of the Royal Society A **362** (2004), no. 1820, 1281–1299.

[42] S.C. Cowin, *Tissue growth and remodeling*, Annual Reviews in Biomedical Engineering **6** (2004), 77–107.

[43] C.J. Cyron and J.D. Humphrey, *Vascular homeostasis and the concept of mechanobiological stability*, International Journal of Engineering Science **85** (2014), 203–223.

[44] P. De Santa Barbara, G.R. Van Den Brink, and D.J. Roberts, *Development and differentiation of the intestinal epithelium*, Cellular and Molecular Life Sciences **60** (2003), no. 7, 1322–1332.

[45] B. Degirmenci, T. Valenta, S. Dimitrieva, G. Hausmann, and K. Basler, *GLI1-expressing mesenchymal cells form the essential Wnt-secreting niche for colon stem cells*, Nature **558** (2018), no. 7710, 449.

[46] V. Démery, B. Davidovitch, and C.D. Santangelo, *Mechanics of large folds in thin interfacial films*, Physical Review E **90** (2014), no. 4, 042401.

[47] J. Dervaux and M. Ben Amar, *Localized growth of layered tissues*, IMA Journal of Applied Mathematics **75** (2010), 571–580.

[48] J. Dervaux, P. Ciarletta, and M. Ben Amar, *Morphogenesis of thin hyperelastic plates: A constitutive theory of biological growth in the Foppl-von Karman limit*, Journal of the Mechanics and Physics of Solids **57** (2009), 458–471.

[49] E.J Doedel, T.F Fairgrieve, B. Sandstede, A.R Champneys, Y.A Kuznetsov, and X. Wang, *AUTO-07P: Continuation and bifurcation software for ordinary differential equations*, (2007).

[50] D. Drasdo and M. Loeffler, *Individual-based models to growth and folding in one-layered tissues: Intestinal crypts and early development*, Nonlinear Analysis, Theory, Methods and Applications **47** (2001), no. 1, 245–256.

[51] H. Du, Q. Nie, and W.R. Holmes, *The Interplay between Wnt Mediated Expansion and Negative Regulation of Growth Promotes Robust Intestinal Crypt Structure and Homeostasis*, PLoS Computational Biology **11** (2015), no. 8, 1–23.

[52] S.-J.N. Dunn, P.L. Appleton, S.A. Nelson, I.S. Näthke, D.J. Gavaghan, and J.M. Osborne, *A two-dimensional model of the colonic crypt accounting for the role of the basement membrane and pericryptal fibroblast sheath*, PLoS Computational Biology **8** (2012), no. 5.

[53] S.-J.N. Dunn, I.S. Näthke, and J.M. Osborne, *Computational models reveal a passive mechanism for cell migration in the crypt*, PLoS ONE **8** (2013), no. 11, 1–18.

[54] S.-J.N. Dunn, J.M. Osborne, P.L. Appleton, and I.S. Näthke, *Combined changes in Wnt signaling response and contact inhibition induce altered proliferation in radiation-treated intestinal crypts*, Molecular Biology of the Cell **27** (2016), no. 11, 1863–1874.

[55] S. Dupont, L. Morsut, M. Aragona, E. Enzo, S. Giulitti, M. Cordenonsi, F. Zanconato, J. Le Digabel, M. Forcato, S. Bicciato, N. Elvassore, and S. Piccolo, *Role of YAP/TAZ in mechanotransduction*, Nature **474** (2011), no. 7350, 179.

[56] C.M. Edwards and S.J. Chapman, *Biomechanical modelling of colorectal crypt budding and fission*, Bulletin of Mathematical Biology **69** (2007), no. 6, 1927–1942.

[57] G.T. Eisenhoffer, P.D Loftus, M. Yoshigi, H. Otsuna, C.-B. Chien, P.A Morcos, and J. Rosenblatt, *Crowding induces live cell extrusion to maintain homeostatic cell numbers in epithelia*, Nature **484** (2012), no. 7395, 546.

[58] A.J Engler, S. Sen, H.L. Sweeney, and D.E. Discher, *Matrix elasticity directs stem cell lineage specification*, Cell **126** (2006), no. 4, 677–689.

[59] A. Erlich, D.E. Moulton, and A. Goriely, *Are homeostatic states stable? Dynamical stability in morphoelasticity*, Bulletin of Mathematical Biology **81** (2019), no. 8, 3219–3244.

[60] L. Euler, *Methodus inveniendi lineas curvas maximi minimive proprietate gaudentes*, apud Marcum-Michaelem Bousquet, 1744.

[61] H.F Farin, I. Jordens, M.H. Mosa, O. Basak, J. Korving, D.V.F Tauriello, K. de Punder, S. Angers, P.J. Peters, M.M. Maurice, and H. Clevers, *Visualization of a short-range Wnt gradient in the intestinal stem-cell niche*, Nature **530** (2016), no. 7590, 340.

[62] I.N. Figueiredo, C. Leal, G. Romanazzi, and B. Engquist, *Homogenization Model for Aberrant Crypt Foci*, SIAM Journal on Applied Mathematics **76** (2016), no. 3, 1152–1177.

[63] J.E. Flaherty, J.B. Keller, and S.I. Rubinow, *Post buckling behavior of elastic tubes and rings with opposite sides in contact*, SIAM Journal on Applied Mathematics **23** (1972), no. 4, 446–455.

[64] A.G. Fletcher, C.J.W. Breward, and S.J. Chapman, *Mathematical modeling of monoclonal conversion in the colonic crypt*, Journal of Theoretical Biology **300** (2012), 118–133.

[65] A.M Freddo, S.K Shoffner, Y. Shao, K. Taniguchi, A.S. Grosse, M.N. Guysinger, S. Wang, S. Rudraraju, B. Margolis, K. Garikipati, S. Schnell, and D.L. Gumucio, *Coordination of signaling and tissue mechanics during morphogenesis of murine intestinal villi: a role for mitotic cell rounding*, Integrative Biology **8** (2016), no. 9, 918–928.

[66] Y-C. Fung, *Biomechanics: mechanical properties of living tissues*, Springer Science & Business Media, 2013.

[67] C. Gaspar and R. Fodde, *Apc dosage effects in tumorigenesis and stem cell differentiation*, International Journal of Developmental Biology **48** (2004), no. 5-6, 377–386.

[68] U. Gat, R. DasGupta, L. Degenstein, and E. Fuchs, *De novo hair follicle morphogenesis and hair tumors in mice expressing a truncated β-catenin in skin*, Cell **95** (1998), no. 5, 605–614.

[69] H. Gehart and H. Clevers, *Tales from the crypt: new insights into intestinal stem cells*, Nature Reviews Gastroenterology & Hepatology (2018), 1.

[70] T.G. Gerike, U. Paulus, C.S. Potten, and M. Loeffler, *A dynamic model of proliferation and differentiation in the intestinal crypt based on a hypothetical intraepithelial growth factor*, Cell Proliferation **31** (1998), no. 2, 93–110.

[71] N. Gjorevski, N. Sachs, A. Manfrin, S. Giger, M.E. Bragina, P. Ordóñez-Morán, H. Clevers, and M.P. Lutolf, *Designer matrices for intestinal stem cell and organoid culture*, Nature **539** (2016), no. 7630, 560.

[72] R.E. Goldstein and A. Goriely, *Dynamic buckling of morphoelastic filaments*, Physical Review E **74** (2006), no. 1, 010901.

[73] O. Gonzalez, J.H. Maddocks, F. Schuricht, and H. von der Mosel, *Global curvature and self-contact of nonlinearly elastic curves and rods*, Calculus of Variations and Partial Differential Equations **14** (2002), no. 1, 29–68.

[74] A. Goriely, *The mathematics and mechanics of biological growth*, vol. 45, Springer, 2017.

[75] A. Goriely, M.G.D. Geers, G.A. Holzapfel, J. Jayamohan, A. Jérusalem, S. Sivaloganathan, W. Squier, J.A.W. Dommelen, S.L. Waters, and E. Kuhl, *Mechanics of the brain: perspectives, challenges, and opportunities*, Biomechanics and Modeling in Mechanobiology (2015), 1–35.

[76] A. Goriely and M. Tabor, *Nonlinear dynamics of filaments I. Dynamical instabilities*, Physica D **105** (1997), 20–44.

[77] ———, *Nonlinear dynamics of filaments II. Nonlinear analysis*, Physica D **105** (1997), no. 1-3, 45–61.

[78] ———, *Spontaneous helix hand reversal and tendril perversion in climbing plants*, Physical Review Letters **80** (1998), no. 7, 1564.

[79] Alain Goriely, *The Mathematics and Mechanics of Biological Growth*, Springer, 2016.

[80] S. Goyal, N.C. Perkins, and C.L. Lee, *Non-linear dynamic intertwining of rods with self-contact*, International Journal of Non-Linear Mechanics **43** (2008), no. 1, 65–73.

[81] F. Graner and J.A. Glazier, *Simulation of biological cell sorting using a two-dimensional extended potts model*, Physical Review Letters **69** (1992), no. 13, 2013.

[82] A. Graudenzi, G. Caravagna, G. De Matteis, and M. Antoniotti, *Investigating the relation between stochastic differentiation, homeostasis and clonal expansion in intestinal crypts via multiscale modeling*, PLoS ONE **9** (2014), no. 5.

[83] A. Gregorieff, Y. Liu, M.R. Inanlou, Y. Khomchuk, and J.L. Wrana, *Yap-dependent reprogramming of Lgr5+ stem cells drives intestinal regeneration and cancer*, Nature **526** (2015), no. 7575, 715.

[84] J. Guiu, E. Hannezo, S. Yui, S. Demharter, S. Ulyanchenko, M. Maimets, A. Jørgensen, S. Perlman, L. Lundvall, L.S. Mamsen, A. Larsen, R.H. Olesen, C.Y. Andersen, L.L. Thuesen, K.J. Hare, T.H. Pers, K. Khodosevich, B.D. Simons, and K.B. Jensen, *Tracing the origin of adult intestinal stem cells*, Nature **570** (2019), no. 7759, 107.

[85] E. Hannezo, J. Prost, and J.F. Joanny, *Instabilities of monolayered epithelia: Shape and structure of villi and crypts*, Physical Review Letters **107** (2011), no. 7, 1–5.

[86] P. Howell, G. Kozyreff, and J. Ockendon, *Applied Solid Mechanics*, 1st ed., Cambridge University Press, 2009.

[87] J.D. Humphrey, *Continuum biomechanics of soft biological tissues*, Proceedings of the Royal Society of London A **459** (2003), no. 2029, 3–46.

[88] A. Humphries and N.A. Wright, *Colonic crypt organization and tumorigenesis.*, Nature Reviews Cancer **8** (2008), no. 6, 415–24.

[89] J.W. Hutchinson, *The role of nonlinear substrate elasticity in the wrinkling of thin films*, Philosophical Transactions of the Royal Society A **37** (2013).

[90] J.W. Hutchinson and W.T. Koiter, *Postbuckling theory*, Applied Mechanics Reviews **23** (1970), no. 12, 1353–1366.

[91] M. Imajo, M. Ebisuya, and E. Nishida, *Dual role of YAP and TAZ in renewal of the intestinal epithelium*, Nature cell biology **17** (2015), no. 1, 7.

[92] T. Ingham-Dempster, D.C. Walker, and B.M. Corfe, *An agent-based model of anoikis in the colon crypt displays novel emergent behaviour consistent with biological observations*, Royal Society Open Science **4** (2017), no. 4.

[93] S. Itzkovitz, I.C. Blat, T. Jacks, H. Clevers, and A. van Oudenaarden, *Optimality in the development of intestinal crypts*, Cell **148** (2012), no. 3, 608–619.

[94] E. Jambon-Puillet, D. Vella, and S. Protière, *The compression of a heavy floating elastic film*, Soft matter **12** (2016), no. 46, 9289–9296.

[95] Y. Jin, L.and Liu and Z. Cai, *Post-buckling analysis on growing tubular tissues: A semi-analytical approach and imperfection sensitivity*, International Journal of Solids and Structures **162** (2019), 121–134.

[96] M.D. Johnston, C.M. Edwards, W.F. Bodmer, P.K. Maini, and S.J. Chapman, *Mathematical modeling of cell population dynamics in the colonic crypt and in colorectal cancer*, Proceedings of the National Academy of Sciences **104** (2007), no. 10, 4008–4013.

[97] Z. Kabiri, G. Greicius, B. Madan, S. Biechele, Z. Zhong, H. Zaribafzadeh, J. Aliyev, Y. Wu, R. Bunte, B.O. Williams, J. Rossant, and D.M. Virshup, *Stroma provides an intestinal stem cell niche in the absence of epithelial wnts*, Development **141** (2014), no. 11, 2206–2215.

[98] M. Karin and H. Clevers, *Reparative inflammation takes charge of tissue regeneration*, Nature **529** (2016), no. 7586, 307.

[99] P. Kaur and C.S. Potten, *Cell migration velocities in the crypts of the small intestine after cytotoxic insult are not dependent on mitotic activity*, Cell Proliferation **19** (1986), no. 6, 601–610.

[100] S.K. Kershaw, H.M. Byrne, D.J. Gavaghan, and J.M. Osborne, *Colorectal cancer through simulation and experiment*, IET Systems Biology **7** (2013), no. 3, 57–73.

[101] J. Kierzenka and L.F. Shampine, *A BVP solver based on residual control and the Matlab PSE*, ACM Transactions on Mathematical Software **27** (2001), no. 3, 299–316.

[102] C-K. Kim, V.W. Yang, and A.B. Bialkowska, *The role of intestinal stem cells in epithelial regeneration following radiation-induced gut injury*, Current Stem Cell Reports **3** (2017), no. 4, 320–332.

[103] J. Kinchen, H.H. Chen, K. Parikh, A. Antanaviciute, M. Jagielowicz, D. Fawkner-Corbett, N. Ashley, L. Cubitt, E. Mellado-Gomez, M. Attar, E. Sharma, Q. Wills, R. Bowden, F.C. Richter, D. Ahern, K.D. Puri, J. Henault, F. Gervais, H. Koohy, and A. Simmons, *Structural remodeling of the human colonic mesenchyme in inflammatory bowel disease*, Cell **175** (2018), no. 2, 372–386.

[104] S. Koch, *Extrinsic control of Wnt signaling in the intestine*, Differentiation **97** (2017), 1–8.

[105] W.T. Koiter, *The stability of elastic equilibrium*, Tech. report, Stanford Univ Ca Dept of Aeronautics and Astronautics, 1970.

[106] N.L Komarova, C. Lengauer, B. Vogelstein, and M.A. Nowak, *Dynamics of genetic instability in sporadic and familial colorectal cancer*, Cancer Biology & Therapy **1** (2002), no. 6, 685–692.

[107] D. Krndija, F. El Marjou, B. Guirao, S. Richon, O. Leroy, Y. Bellaiche, E. Hannezo, and D.M. Vignjevic, *Active cell migration is critical for steady-state epithelial turnover in the gut*, Science **365** (2019), no. 6454, 705–710.

[108] C.R. Laing, W.C. Troy, B. Gutkin, and G.B. Ermentrout, *Multiple bumps in a neuronal model of working memory*, SIAM Journal on Applied Mathematics **63** (2002), no. 1, 62–97.

[109] R.S. Lakes, *Viscoelastic solids*, vol. 9, CRC press, 1998.

[110] M. Loeffler, Christopher S. Potten, U. Paulus, J. Glatzer, and S. Chwalinski, *Intestinal crypt proliferation. II. Computer modelling of mitotic index data provides further evidence for lateral and vertical cell migration in the absence of mitotic activity*, Cell Proliferation **21** (1988), no. 4, 247–258.

[111] M. Loeffler, R. Stein, H.-E. Wichmann, C.S Potten, P. Kaur, and S. Chwalinski, *Intestinal cell proliferation. I. a comprehensive model of steady-state proliferation in the crypt*, Cell Proliferation **19** (1986), no. 6, 627–645.

[112] C. Lopez-Garcia, A.M. Klein, B.D. Simons, and D.J. Winton, *Intestinal stem cell replacement follows a pattern of neutral drift*, Science **330** (2010), no. 6005, 822–825.

[113] A. Magnusson, M. Ristinmaa, and C. Ljung, *Behaviour of the extensible elastica solution*, International Journal of Solids and Structures **38** (2001), no. 46-47, 8441–8457.

[114] E. Marshman, C. Booth, and C.S. Potten, *The intestinal epithelial stem cell*, BioEssays **24** (2002), no. 1, 91–98.

[115] F. A. Meineke, C. S. Potten, and M. Loeffler, *Cell migration and organization in the intestinal crypt using a lattice-free model*, Cell Proliferation **34** (2001), no. 4, 253–266.

[116] F. Michor, Y. Iwasa, H. Rajagopalan, C. Lengauer, and M.A. Nowak, *Linear model of colon cancer initiation*, Cell Cycle **3** (2004), no. 3, 356–360.

[117] G.R. Mirams, A.G. Fletcher, P.K.. Maini, and H.M. Byrne, *A theoretical investigation of the effect of proliferation and adhesion on monoclonal conversion in the colonic crypt*, Journal of Theoretical Biology **312** (2012), 143–156.

[118] H. Miyoshi, R. Ajima, C.T. Luo, T.P. Yamaguchi, and T.S. Stappenbeck, *Wnt5a potentiates TGF-β signaling to promote colonic crypt regeneration after tissue injury*, Science **338** (2012), no. 6103, 108–113.

[119] D.E Moulton and A. Goriely, *Circumferential buckling instability of a growing cylindrical tube*, Journal of the Mechanics and Physics of Solids **59** (2011), no. 3, 525–537.

[120] D.E. Moulton, T. Lessinnes, and A. Goriely, *Morphoelastic rods. Part I: A single growing elastic rod*, Journal of the Mechanics and Physics of Solids **61** (2013), no. 2, 398–427.

[121] J.J. Muñoz and S. Albo, *Physiology-based model of cell viscoelasticity*, Physical Review E **88** (2013), no. 1, 012708.

[122] P.J. Murray, A. Walter, A.G. Fletcher, C.M. Edwards, M.J. Tindall, and P.K. Maini, *Comparing a discrete and continuum model of the intestinal crypt.*, Physical Biology **8** (2011), no. 2, 026011.

[123] G. Napoli and S. Turzi, *Snap buckling of a confined thin elastic sheet*, Proceedings of the Royal Society A **471** (2015), no. 2183, 20150444.

[124] M.R. Nelson, D. Howard, O.E. Jensen, J.R. King, F.R.A.J. Rose, and S.L. Waters, *Growth-induced buckling of an epithelial layer*, Biomechanics and Modeling in Mechanobiology **10** (2011), no. 6, 883–900.

[125] M.R. Nelson, J.R. King, and O.E. Jensen, *Buckling of a growing tissue and the emergence of two-dimensional patterns*, Mathematical Biosciences **246** (2013), no. 2, 229–241.

[126] W.J. Nelson and R. Nusse, *Convergence of Wnt, β-catenin, and cadherin pathways*, Science **303** (2004), no. 5663, 1483–1487.

[127] M.A. Nowak, N.L. Komarova, A. Sengupta, P.V. Jallepalli, I.-M. Shih, B. Vogelstein, and C. Lengauer, *The role of chromosomal instability in tumor initiation*, Proceedings of the National Academy of Sciences **99** (2002), no. 25, 16226–16231.

[128] M.A. Nowak, F. Michor, and Y. Iwasa, *The linear process of somatic evolution*, Proceedings of the National Academy of Sciences **100** (2003), no. 25, 14966–14969.

[129] R.D. O'Dea and J.R. King, *Multiscale analysis of pattern formation via intercellular signalling*, Mathematical Biosciences **231** (2011), no. 2, 172–185.

[130] ———, *Continuum limits of pattern formation in hexagonal-cell monolayers*, Journal of Mathematical Biology **64** (2012), no. 3, 579–610.

[131] S.G. O'Keeffe, D.E. Moulton, S.L. Waters, and A. Goriely, *Growth-induced axial buckling of a slender elastic filament embedded in an isotropic elastic matrix*, International Journal of Non-Linear Mechanics **56** (2013), no. C, 94–104.

[132] O.M. O'Reilly and T.N. Tresierras, *On the evolution of intrinsic curvature in rod-based models of growth in long slender plant stems*, International Journal of Solids and Structures **48** (2011), no. 9, 1239–1247.

[133] James M. Osborne, Alexander G. Fletcher, Joe M. Pitt-Francis, Philip K. Maini, and David J. Gavaghan, *Comparing individual-based approaches to modelling the self-organization of multicellular tissues*, PLoS Computational Biology **13** (2017), no. 2, e1005387.

[134] J.M. Osborne, A. Walter, S.K. Kershaw, G.R. Mirams, A.G. Fletcher, P. Pathmanathan, D.J. Gavaghan, O.E. Jensen, P.K. Maini, and H.M. Byrne, *A hybrid approach to multi-scale modelling of cancer.*, Philosophical Transactions of the Royal Society A **368** (2010), no. 1930, 5013–5028.

[135] M.J. Oudhoff, M.J.S. Braam, S.A. Freeman, D. Wong, D.G. Rattray, J. Wang, F. Antignano, K. Snyder, I. Refaeli, M.R. Hughes, K.M. McNagny, M.R. Gold, C.H. Arrowsmith, T. Sato, F.M.V. Rossi, J.H. Tatlock, D.R. Owen, P.J. Brown, and C. Zaph, *SETD7 controls intestinal regeneration and tumorigenesis by regulating Wnt/β-catenin and Hippo/YAP signaling*, Developmental Cell **37** (2016), no. 1, 47–57.

[136] C. Pin, A.J.M. Watson, and S.R. Carding, *Modelling the spatio-temporal cell dynamics reveals novel insights on cell differentiation and proliferation in the small intestinal crypt*, PLoS ONE **7** (2012), no. 5.

[137] D. Pinto and H. Clevers, *Wnt control of stem cells and differentiation in the intestinal epithelium*, Experimental Cell Research **306** (2005), no. 2, 357–363.

[138] L. Pocivavsek, R. Dellsy, A. Kern, S. Johnson, B. Lin, K.Y.C. Lee, and E. Cerda, *Stress and fold localization in thin elastic membranes*, Science **320** (2008), no. 5878, 912–916.

[139] W.J. Polacheck and C.S. Chen, *Measuring cell-generated forces: a guide to the available tools*, Nature Methods **13** (2016), no. 5, 415.

[140] C.S. Potten, M. Kellett, S.A. Roberts, D.A. Rew, and G.D. Wilson, *Measurement of in vivo proliferation in human colorectal mucosa using bromodeoxyuridine.*, Gut **33** (1992), no. 1, 71–78.

[141] C.S. Potten and M. Loeffler, *Stem cells: attributes, cycles, spirals, pitfalls and uncertainties. lessons for and from the crypt*, Development **110** (1990), no. 4, 1001–1020.

[142] D.W. Powell, I.V. Pinchuk, J.I. Saada, X. Chen, and R.C. Mifflin, *Mesenchymal cells of the intestinal lamina propria*, Annual Review of Physiology **73** (2011), 213–237.

[143] S.L. Preston, W.M. Wong, A.O.O Chan, R. Poulsom, R. Jeffery, R.A. Goodlad, N. Mandir, G. Elia, M. Novelli, W.F. Bodmer, I.P. Tomlinson, and N.A. Wright, *Bottom-up histogenesis of colorectal adenomas: Origin in the monocryptal adenoma and initial expansion by crypt fission*, Cancer Research **63** (2003), no. 13, 3819–3825.

[144] S.P. Preston, O.E. Jensen, and G. Richardson, *Buckling of an axisymmetric vesicle under compression: the effects of resistance to shear*, The Quarterly Journal of Mechanics and Applied Mathematics **61** (2008), no. 1, 1–24.

[145] P. Recho, A. Jerusalem, and A. Goriely, *Growth, collapse, and stalling in a mechanical model for neurite motility*, Physical Review E **93** (2016), no. 3, 032410.

[146] T. Reya and H. Clevers, *Wnt signalling in stem cells and cancer*, Nature **434** (2005), no. 7035, 843.

[147] E.K. Rodriguez, A. Hoger, and A.D. McCulloch, *Stress-dependent finite growth in soft elastic tissues.*, Journal of Biomechanics **27** (1994), no. 4, 455–67.

[148] M.E. Rothenberg, Y. Nusse, T. Kalisky, J.J. Lee, P. Dalerba, F. Scheeren, N. Lobo, S. Kulkarni, S. Sim, D. Qian, P.A. Beachy, P.J. Pasricha, S.R. Quake, and M.F. Clarke, *Identification of a cKit$^+$ colonic crypt base secretory cell*

that supports Lgr5$^+$ stem cells in mice, Gastroenterology **142** (2012), no. 5, 1195–1205.

[149] S.G. Ruan and W.D. Wang, *Dynamical behavior of an epidemic model with a nonlinear incidence rate*, Journal of Differential Equations **188** (2003), no. 1, 135–163.

[150] T. Sato, J.H. Van Es, H.J. Snippert, D.E. Stange, R.G. Vries, M. Van Den Born, N. Barker, N.F. Shroyer, M. Van De Wetering, and H. Clevers, *Paneth cells constitute the niche for Lgr5 stem cells in intestinal crypts*, Nature **469** (2011), no. 7330, 415.

[151] T. Sato, R.G. Vries, H.J. Snippert, M. Van De Wetering, N. Barker, D.E. Stange, J.H. Van Es, A. Abo, P. Kujala, P.J. Peters, and H. Clevers, *Single lgr5 stem cells build crypt–villus structures in vitro without a mesenchymal niche*, Nature **459** (2009), no. 7244, 262.

[152] F. Schuricht and H. Von Der Mosel, *Euler-Lagrange equations for nonlinearly elastic rods with self-contact*, Archive for Rational Mechanics and Analysis **168** (2003), no. 1, 35–82.

[153] N.A.F. Senan, O.M. O'Reilly, and T.N. Tresierras, *Modeling the growth and branching of plants: a simple rod-based model*, Journal of the Mechanics and Physics of Solids **56** (2008), no. 10, 3021–3036.

[154] H. Seno, H. Miyoshi, S.L. Brown, M.J. Geske, M. Colonna, and T.S. Stappenbeck, *Efficient colonic mucosal wound repair requires Trem2 signaling*, Proceedings of the National Academy of Sciences **106** (2009), no. 1, 256–261.

[155] D. Serra, U. Mayr, A. Boni, I. Lukonin, M. Rempfler, L.C. Meylan, M.B. Stadler, P. Strnad, P. Papasaikas, D. Vischi, A. Waldt, G. Roma, and P. Liberali, *Self-organization and symmetry breaking in intestinal organoid development*, Nature (2019), 1.

[156] L.F. Shampine, J. Kierzenka, and M.W. Reichelt, *Solving boundary value problems for ordinary differential equations in MATLAB with bvp4c*, Tutorial Notes **2000** (2000), 1–27.

[157] B.I. Shraiman, *Mechanical feedback as a possible regulator of tissue growth*, Proceedings of the National Academy of Sciences **102** (2005), no. 9, 3318–3323.

[158] A.E. Shyer, T. Tallinen, N.L. Nerurkar, Z. Wei, E.S. Gil, D.L. Kaplan, C.J. Tabin, and L. Mahadevan, *Villification: how the gut gets its villi*, Science **342** (2013), no. 6155, 212–218.

[159] R. Skalak, D.A. Farrow, and A. Hoger, *Kinematics of surface growth*, Journal of Mathematical Biology **35** (1997), no. 8, 869–907.

[160] H.J. Snippert, L.G. Van Der Flier, T. Sato, J.H. Van Es, M. Van Den Born, C. Kroon-Veenboer, N. Barker, A.M. Klein, J. Van Rheenen, B.D. Simons, and H. Clevers, *Intestinal crypt homeostasis results from neutral competition between symmetrically dividing Lgr5 stem cells*, Cell **143** (2010), no. 1, 134–144.

[161] S.J. Spechler and R.K. Goyal, *Barrett's esophagus*, New England Journal of Medicine **315** (1986), no. 6, 362–371.

[162] M. Spit, B.-K. Koo, and M.M. Maurice, *Tales from the crypt: intestinal niche signals in tissue renewal, plasticity and cancer*, Open Biology **8** (2018), no. 9, 180120.

[163] E.L. Starostin, *Symmetric equilibria of a thin elastic rod with self-contacts*, Philosophical Transactions of the Royal Society A **362** (2004), no. 1820, 1317–1334.

[164] T. Stylianopoulos, J.D. Martin, V.P. Chauhan, S.R. Jain, B. Diop-Frimpong, N. Bardeesy, B.L. Smith, C.R. Ferrone, F.J. Hornicek, Y. Boucher, L.L. Munn, and R.K. Jain, *Causes, consequences, and remedies for growth-induced solid*

stress in murine and human tumors, Proceedings of the National Academy of Sciences **109** (2012), no. 38, 15101–15108.

[165] I. Stzepourginski, G. Nigro, J.-M. Jacob, S. Dulauroy, P.J. Sansonetti, G. Eberl, and L. Peduto, *CD34+ mesenchymal cells are a major component of the intestinal stem cells niche at homeostasis and after injury*, Proceedings of the National Academy of Sciences **114** (2017), no. 4, E506–E513.

[166] K. Sugimura, P-F. Lenne, and F. Graner, *Measuring forces and stresses in situ in living tissues*, Development **143** (2016), no. 2, 186–196.

[167] K.D. Sumigray, M. Terwilliger, and T. Lechler, *Morphogenesis and compartmentalization of the intestinal crypt*, Developmental Cell **45** (2018), no. 2, 183–197.

[168] L.A. Taber, *Towards a unified theory for morphomechanics*, Philosophical Transactions of the Royal Society A **367** (2009), no. 1902, 3555–3583.

[169] Koji Taniguchi, Li-Wha Wu, Sergei I Grivennikov, Petrus R De Jong, Ian Lian, Fa-Xing Yu, Kepeng Wang, Samuel B Ho, Brigid S Boland, John T Chang, et al., *A gp130–src–yap module links inflammation to epithelial regeneration*, Nature **519** (2015), no. 7541, 57.

[170] R.W. Taylor, M.J. Barron, G.M. Borthwick, A. Gospel, P.F. Chinnery, D.C. Samuels, G.A. Taylor, S.M. Plusa, S.J. Needham, L.C Greaves, T.B.L. Kirkwood, and D.M. Turnbull, *Mitochondrial DNA mutations in human colonic crypt stem cells*, The Journal of Clinical Investigation **112** (2003), no. 9, 1351–1360.

[171] T. Thalheim, P. Buske, J. Przybilla, K. Rother, M. Loeffler, and J. Galle, *Stem cell competition in the gut: insights from multi-scale computational modelling*, Journal of The Royal Society Interface **13** (2016), no. 121, 20160218.

[172] J.M.T Thompson, G.H.M van der Heijden, and S. Neukirch, *Supercoiling of DNA plasmids: mechanics of the generalized ply*, Proceedings of the Royal Society of London A: Mathematical, Physical and Engineering Sciences **458** (2002), no. 2020, 959–985.

[173] S. Timoshenko, *Analytis of bi-metal thermostats*, Journal of the Optical Society of America **11** (1925), no. 3, 233–255.

[174] A. Totaro, M. Castellan, D. Di Biagio, and S. Piccolo, *Crosstalk between YAP/TAZ and Notch signaling*, Trends in Cell Biology **28** (2018), no. 7, 560–573.

[175] J.S. Trier, C.H. Allan, D.R. Abrahamson, and S.J. Hagen, *Epithelial basement membrane of mouse jejunum. Evidence for laminin turnover along the entire crypt-villus axis.*, The Journal of Clinical Investigation **86** (1990), no. 1, 87–95.

[176] L. Truskinovsky and G. Zurlo, *Nonlinear elasticity of incompatible surface growth*, Physical Review E **99** (2019), no. 5, 053001.

[177] G.H.M. Van der Heijden, S. Neukirch, V.G.A. Goss, and J.M.T. Thompson, *Instability and self-contact phenomena in the writhing of clamped rods*, International Journal of Mechanical Sciences **45** (2003), no. 1, 161–196.

[178] I.M.M. Van Leeuwen, G.R. Mirams, A. Walter, A.G. Fletcher, P.J. Murray, J.M. Osborne, S. Varma, S.J. Young, J. Cooper, B. Doyle, J. Pitt-Francis, L. Momtahan, P. Pathmanathan, J.P. Whiteley, S.J. Chapman, D.J. Gavaghan, O.E. Jensen, J.R. King, P.K. Maini, S.L. Waters, and H.M. Byrne, *An integrative computational model for intestinal tissue renewal*, Cell Proliferation **42** (2009), no. 5, 617–636.

[179] P. Van Liedekerke, M.M. Palm, N. Jagiella, and D. Drasdo, *Simulating tissue mechanics with agent-based models: concepts, perspectives and some novel results*, Computational Particle Mechanics **2** (2015), no. 4, 401–444.

[180] L. Vermeulen, E. Morrissey, M. Van Der Heijden, A.M. Nicholson, A. Sottoriva, S. Buczacki, R. Kemp, S. Tavaré, and D.J. Winton, *Defining stem cell dynamics in models of intestinal tumor initiation*, Science **342** (2013), no. 6161, 995–998.

[181] K.D. Walton, M. Whidden, Å. Kolterud, S.K. Shoffner, M.J. Czerwinski, J. Kushwaha, N. Parmar, D. Chandhrasekhar, A.M. Freddo, S. Schnell, and D.L. Gumucio, *Villification in the mouse: Bmp signals control intestinal villus patterning*, Development **143** (2016), no. 3, 427–436.

[182] A.J.M. Watson, C.A. Duckworth, Y. Guan, and M.H. Montrose, *Mechanisms of epithelial cell shedding in the Mammalian intestine and maintenance of barrier function*, Annals of the New York Academy of Sciences **1165** (2009), no. 1, 135–142.

[183] N.A. Wright and M. Alison, *The Biology of Epithelial Cell Populations*, vol. 1–2, Oxford University Press, USA, 1984.

[184] W. Xu, R. Mezencev, B. Kim, L. Wang, J. McDonald, and T. Sulchek, *Cell stiffness is a biomarker of the metastatic potential of ovarian cancer cells*, PloS ONE **7** (2012), no. 10, e46609.

[185] K.S Yan, L.A. Chia, X. Li, A. Ootani, J. Su, J.Y. Lee, N. Su, Y. Luo, S.C. Heilshorn, M.R. Amieva, E. Sangiorgi, M.R. Capecchi, and C.J. Kuo, *The intestinal stem cell markers Bmi1 and Lgr5 identify two functionally distinct populations*, Proceedings of the National Academy of Sciences **109** (2012), no. 2, 466–471.

[186] S. Yui, L. Azzolin, M. Maimets, M.T. Pedersen, R.P. Fordham, S.L. Hansen, H.L. Larsen, J. Guiu, M.R.P. Alves, C.F. Rundsten, J.V. Johansen, Y. Li, C.D. Madsen, T. Nakamura, M. Watanabe, O.H. Nielsen, P.J. Schweiger, S. Piccolo, and K.B. Jensen, *YAP/TAZ-dependent reprogramming of colonic epithelium links ECM remodeling to tissue regeneration*, Cell Stem Cell **22** (2018), no. 1, 35–49.

[187] L. Zhang, A.D. Lander, and Q. Nie, *A reaction-diffusion mechanism influences cell lineage progression as a basis for formation, regeneration, and stability of intestinal crypts*, BMC Systems Biology **6** (2012).

[188] R. Zhao and F. Michor, *Patterns of proliferative activity in the colonic crypt determine crypt stability and rates of somatic evolution*, PLoS Computational Biology **9** (2013), no. 6, e1003082.

[189] G. Zurlo and L. Truskinovsky, *Printing non-euclidean solids*, Physical Review Letters **119** (2017), no. 4, 048001.

[190] ———, *Inelastic surface growth*, Mechanics Research Communications **93** (2018), 174–179.